UNIVERSIDAD DE CHILE
FACULTAD DE CIENCIAS FÍSICAS Y MATEMÁTICAS
DEPARTAMENTO DE FÍSICA

PERMANENT DYNAMICS OF PARTICLE-LIKE SOLUTIONS IN OUT-OF-EQUILIBRIUM SYSTEMS

TESIS PARA OPTAR AL GRADO DE
DOCTOR EN CIENCIAS, MENCIÓN FÍSICA

ALEJANDRO JOSE ALVAREZ SOCORRO

PROFESOR GUÍA:
MARCEL CLERC GAVILAN

MIEMBROS DE LA COMISIÓN:
MUSTAPHA TLIDI
DANIEL ESCAFF DIXON
MARIO WILSON HERRÁN
CARLA HERMANN AVIGLIANO

Este trabajo ha sido parcialmente financiado por Becas Conicyt 2015. Folio No. 21151618

SANTIAGO DE CHILE
2021

RESUMEN DE LA MEMORIA PARA OPTAR
AL TÍTULO DE DOCTOR EN CIENCIAS, MENCIÓN FÍSICA
POR: ALEJANDRO JOSE ALVAREZ SOCORRO
FECHA: 2021
PROF. GUÍA: MARCEL CLERC GAVILAN

PERMANENT DYNAMICS OF PARTICLE-LIKE SOLUTIONS IN OUT-OF-EQUILIBRIUM SYSTEMS

This dissertation aims to understand how nonvariational effects affect the dynamics of particle-type solutions in spatially extended systems. In the first part of our research, we study nonvariational perturbations on the dynamics of fronts and localized structures that can be understood as particle-like solutions associating continuous variables such as position, velocity, and size. In Chapter 1, we explain some preliminary concepts useful to understand the results of this thesis. Chapter 2 is dedicated to understanding how nonvariational effects can affect the dynamics of fronts connecting a stable state with an unstable one. From an analytical and numerical point of view, we show how the nonvariational effect can induce a pulled-pushed transition in this kind of front and show experimental evidence of our results in a LCLV setup with optical feedback. Chapter 3 reveals how nonvariational effects induce propagation in normal fronts, obtaining in such a way a new propagation mechanism caused only by the shape of the front connecting the stable states that the nonvariational parameters can control. In addition, we verify our theoretical findings by studying the LCLV setup with optical feedback in the regime where the system is multistable. Chapter 4 shows a transition from motionless to traveling localized states due to a spontaneous symmetry breaking in the nonvariational Turing-Swift-Hohenberg equation as an archetypical model of pattern-forming systems. A nonvariational effect drives such transition, and it is characterized numerically and analytically. Moreover, we generalize such kinds of states in higher dimensions. Chapter 5 and 6 explores a new kind of chimera states in continuous media, namely, traveling and wandering chimera states, respectively. Chimera states are characterized by the coexistence of coherent and incoherent spatiotemporal dynamics. Traveling chimeras propagates in a specific direction with a well-defined average speed; meanwhile, wandering chimeras exhibit an erratic motion resembling a random walk. We characterize its statistical and dynamical properties and give numerical insights about its bifurcation diagram. In chapter 7, we study the dynamics of fronts but consider another kind of nonvariational perturbation, namely, deterministic fluctuations englobing chaotical and spatiotemporal chaotical dynamics. We show that despite these fluctuations, a front may remain pinned, in contrast to fronts in systems with Gaussian white noise fluctuations, and explore the pinning-depinning transition. We describe this transition by deriving an equation for the front position, which takes the form of an overdamped system with a ratchet potential and chaotic forcing; this equation can, in turn, be transformed into a linear parametrically driven oscillator with a chaotically oscillating frequency. Finally, in chapter 8, we extend our study of deterministic perturbations to localized structures. Mobility properties of spatially localized structures arising from chaotic but deterministic forcing of the bistable Swift-Hohenberg equation are compared with the corresponding results when the chaotic forcing is replaced by white noise. For the family of LS studied, we found that shorter structures are more fragile than longer ones, and their stability region can be displaced outside the pinning region for constant forcing. In addition, we discuss the nature of randomness and how it can emerge from deterministic dynamics.

RESUMEN DE LA MEMORIA PARA OPTAR
AL TÍTULO DE DOCTOR EN CIENCIAS, MENCIÓN FÍSICA
POR: ALEJANDRO JOSE ALVAREZ SOCORRO
FECHA: 2021
PROF. GUÍA: MARCEL CLERC GAVILAN

PERMANENT DYNAMICS OF PARTICLE-LIKE SOLUTIONS IN OUT-OF-EQUILIBRIUM SYSTEMS

Esta disertación tiene como objetivo comprender cómo los efectos no variacionales afectan la dinámica de las soluciones tipo partícula en sistemas espacialmente extendidos. En la primera parte de nuestra investigación, estudiamos perturbaciones no variacionales en la dinámica de frentes y estructuras localizadas, las cuales pueden entenderse como soluciones tipo partícula, es decir, pueden describirse a través de variables continuas tales como la posición, la velocidad y el tamaño. En el Capítulo 1, explicamos algunos conceptos preliminares necesarios para comprender los resultados de esta tesis. El capítulo 2 está dedicado a vislumbrar cómo los efectos no variacionales pueden afectar la dinámica de los frentes que conectan un estado estable con uno inestable. Desde un punto de vista analítico y numérico, mostramos cómo los efectos no variacionales pueden inducir una transición tipo pulled-pushed en esta clase de frentes. Adicionalmente, mostramos evidencia experimental de nuestros resultados en un setup compuesto por una válvula de luz de cristal líquido (LCLV) con retroinyección óptica. En el Capítulo 3 revelamos cómo los efectos no variacionales pueden inducir propagación en frentes normales, obteniendo un nuevo mecanismo de propagación que depende exclusivamente de la forma del frente que conecta los estados estables, la cual es modulada por los parámetros no variacionales. Nuestros hallazgos teóricos son verificados mediante el estudio de este tipo de frentes en la LCLV con retroinyección óptica en el régimen en el que este sistema es multiestable. En el capítulo 4 se muestra una transición de estados localizados inmóviles a propagativos en la ecuación no variacional de Turing-Swift-Hohenberg, como consecuencia de una ruptura espontánea de simetría. Dicha transición es conducida por efectos no variacionales y se logra caracterizar numérica y analíticamente. Además, generalizamos este tipo de estados en dimensiones superiores. Los capítulos 5 y 6 exploran un nuevo tipo de estados de quimera en medios continuos, a saber, estados de quimera viajeros y errantes, respectivamente. Los estados de quimera se caracterizan por la coexistencia de dinámicas espacio-temporales coherentes e incoherentes. Las quimeras viajeras se propagan en una dirección preferencial con una velocidad media bien definida; mientras tanto, las quimeras errantes exhiben un movimiento errático que se asemeja a un caminante aleatorio. Caracterizamos sus propiedades estadísticas y dinámicas y brindamos información numérica sobre sus diagramas de bifurcación. En el capítulo 7, estudiamos la dinámica de los frentes, sujetos a fluctuaciones determinísticas que incluyen a comportamientos caóticos y caóticos espacio-temporales. Mostramos que a pesar de estas fluctuaciones, un frente puede permanecer anclado (o pinned), en contraste con la aplicación de fluctuaciones estocásticas. Para explorar la transición de pinning-depinning, se deriva una ecuación para la posición del frente, que toma la forma de un sistema sobreamortiguado con un potencial tipo ratchet y un forzamiento caótico. En el capítulo 8, ampliamos nuestro estudio de perturbaciones determinísticas a estructuras localizadas comparando el efecto de las fluctuaciones determinísticas con el de las estocásticas. Finalmente, se discute la naturaleza de la aleatoriedad y cómo esta puede surgir de una dinámica determinística.

A Sofía

Agradecimientos

I am grateful to my wife and daughter. They, throughout the doctorate, have encouraged me unconditionally despite the very high level of commitment, effort, and sacrifice implicit in the completion of a Ph.D. in Physics at the University of Chile. It has been a complex journey that we started as a couple and ended as a family.

I would like to thank my mother, from Venezuela, who was always happy with each achievement reached. Despite the distance and call after call, she followed my entire road through the doctorate.

I would like to mainly thank my mentor and doctoral thesis supervisor, Professor Marcel Clerc. Until I joined his student group, he always supported, motivated, and taught me how only the best of mentors can teach his disciples. His way of doing science is amazing and inspiring. I will never forget the hours spent in his office, in which, through questions, discussions, and calculations on his chalkboard, step by step, we approach the frontier of our scientific discipline, obtaining valuable contributions. Moreover, my "doctoral thesis" path journey gave me quite solid theoretical, experimental and computational training. Before finishing it, I received several achievements, awards, and interesting position offers.

I am also deeply grateful to Professor Mustapha Tlidi, who allowed me to intern in his research group at the Université Libre de Bruxelles ULB. This internship ended with one of the key works of my doctoral thesis, and it opened the doors to future projects that I hope to continue. During my stay in Brussels, I felt at home because I was literally adopted as one of his students. Thanks to this, I discovered how delay as a feedback mechanism can become responsible for emergent behaviors in complex systems, such as forming localized structures and motion as a dissipative mechanism. This gave me an alternative vision in the study of localized dissipative structures. My passage through the laboratory of robust phenomena in optics left me with great friendships and collaborations that gave me a much deeper vision of scientific work. I particularly thank Gregorio González (doctoral student) and Dr. Mario Wilson (postdoc), with whom I had the privilege of sharing and discussing ideas and collaborating on my first research articles. I am not exaggerating when I say that I was introduced to the world of experimental physics. I also thank Dr. Michel Ferré (postdoc), with whom I also had the privilege of collaborating on several of the works developed in this thesis. His vision as a theoretical physicist, knowledge, and motivations generated learning instances that undoubtedly improved my skills as a scientist and collaborator. Also, I would like to thank Camila Castillo, with whom I was fortuitously lucky to collaborate on one of the works compiled in this thesis. Her attitude and commitment to research and her mastery of

the experimental layers of our research were powerful, accelerating, and motivating factors. This enabled us the achieve with extreme efficiency the article that we were able to publish the fastest.

I would like to thank Alejandro Leon, Gladys Jara, Valeska Zambra, Fabian Alvarez, Mauricio Morel, Ignacio Andrade, Ernesto Berrios, David Pinto, Nicolás Verschueren, Enrique Calisto, Nicolás Perinet, Karin Alfaro, all members of LAFER, with whom I shared knowledge, ideas and, religiously, lunch meetings every Friday.

I would also like to thank the professors who collaborated with my thesis supervisor in my training as a physicist, mainly Hugo Arellano, Enrique Tirapegui, Mario Molina, Fernando Lund, Diana Dulic, Felipe Barra, Rodrigo Soto, Mario Riquelme. Through their classes, they managed to inspire me, motivate me, and keep me asking questions. With extreme generosity, I feel that they introduce me in their respective disciplines, and I hope to contribute to them.

Finally, I cannot leave out of this gratitude the rest of the colleagues with whom I had the privilege of sharing at the university and outside of it, among them Pablo Mardones, Nelson Adriazola, Verónica Gaete, Camila Horvath, Bastián Pradenas, Boris Jara, Tomás Vera, and Henry Rosales.

To all of you, thank you very much.

Contents

List of Figures

Introducción

Nature is full of peculiar phenomena emerging as a consequence of injection and dissipation of energy, and it is the job of physicists to classify, characterize, understand and predict the occurrence and dynamics of such phenomena. In this thesis, we are interested in a particular type of phenomenon that we can associate with the concept of a particle in its most elementary form, i.e., phenomena that can be characterized by continuous parameters such as position, size, field, speed, among others. For example, the propagation of a flame in an elongated strip of paper (quasi-one-dimensional system) can be understood as a particle propagating in a one-dimensional space. Here, its position is given by the center of the combustion reaction region; the size of the particle would be associated with the size of the combustion zone. Its speed would be the speed with which the center of the zone where the combustion occurs moves concerning time. Another example of interest for the present manuscript would be the propagation of localized structures, e.g., a non-linear wave, where the position, size, amplitude, and velocity can be defined almost directly, establishing an immediate link with the concept of particle. It should be noted that this is just one way of interpreting and understanding this type of phenomenon. Furthermore, our theoretical frame of reference is a consequence of the interaction between various disciplines, mainly classical mechanics, statistical physics, optics, fluid dynamics, physics out of equilibrium, non-linear dynamics, dynamic systems, so it could be said that it is a modern approach to problems that escape a purely relaxational dynamic.

In this sense, we will be mainly interested in two types of phenomena that can be associated with the concept of a particle, namely,

- Fronts, domain walls, interfaces.
- Localized structures, dissipative solitons, localized patterns, defects.

Fronts and localized structures themselves appear in a wide range of systems coming from optics, mechanics, combustion, chemical reactions, liquid crystals, granular media, hydrodynamics, plasmas, among many others. Moreover, these phenomena appear in more far topics like population dynamics, genetics, cancer disease, brain dynamics, opinion dynamics in societies, to mention a few. Such phenomena that appears in several systems independently of the underlying physics are called robust phenomena. Fig. 1 exhibits some examples of fronts and localized structures in several physical systems. Figure 1(a) it is shown a pendulum chain with dissipation and parametrically forced, where emerges, in a range of parameters, a solution that connects the equilibria $\theta = 0$ and $\theta = \pi$, making that it coexist in space. Other examples of fronts illustrated in Fig.1 appears in (b) fluidized granular media, (c) interface

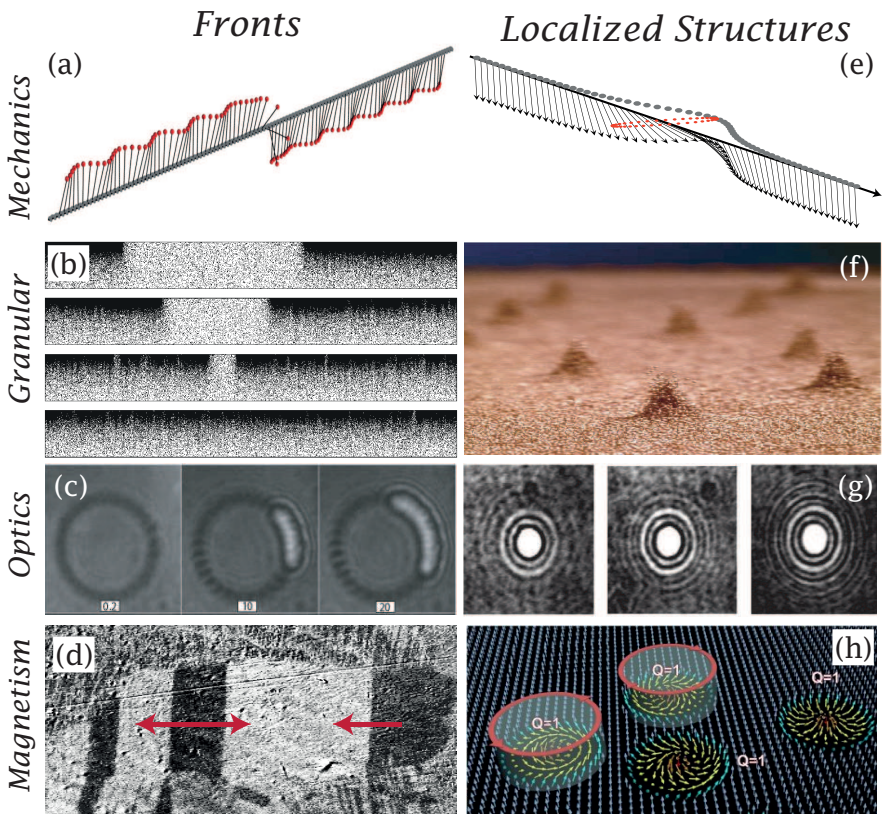

Figure 1: In this figure, we can observe several examples of particle-like solutions. In the left panel, we can see fronts solutions in (a) an array of pendulums, (b) fluidized granular media, (c) optical media and (d) magnetical media. The corresponding localized solutions at each of the before mentioned media are shown in (e),(f),(g), and (h).

connecting two domains with different average molecular orientation in optical media, and (d) domain walls in magnetical media. In the same spirit, the right panels exhibit some examples of localized states. Particularly, Fig.1 (e) show localized structures in a pendulum chain, and (f) in fluidized granular media, (g) in optical media and (h) in magnetical media.

Additionally, fronts and localized structures are non-linear phenomena; that is, the laws of evolution that describe such phenomena are non-linear, and typically their solutions do not satisfy the principle of superposition, or in other words, the Linear combination solutions is not a solution, what if it occurs in linear systems.

Going deeper into the universe of spatially extended non-linear systems, we have those approaching equilibrium through purely relaxational type dynamics, i.e., their asymptotic behavior ends in a stable equilibrium or a periodic orbit. For these so-called variational systems, an energy functional can be found whose minimization describes its asymptotic dynamics. On the other hand, we have the so-called non-variational ones, characterized by permanent dynamics, and from the theoretical point of view, their laws of evolution do not follow the minimization of functional energy. Unfortunately, while there are methods to study variational systems, general literature for non-variational systems is absent, and there are few research papers in the area.

Contradictory to what one might think based on classical literature, non-variational systems are generic and commonly appear when is searched for laws of evolution of macroscopic systems out of equilibrium. Variationality, as a mathematical property, surrenders to coarse-grained hypotheses and mean-field approaches. Although variationality could be recovered by considering the entire system from a microscopic point of view as well as all the interaction between its constituents, this would render the model theoretically and numerically intractable. Hence the great relevance of non-variational systems.

Precisely this thesis tries to give a broad panorama of the dynamics of particle-type solutions in non-variational spatially extended systems, addressing how non-variational effects affect the dynamics of fronts and localized structures. Nevertheless, only front and localized structure dynamics themselves are topics of broad interest in the scientific community.

0.1 Objetives

The main objective of this thesis is to understand how nonvariational effects can affect the dynamics of particle-like solutions, in particular, fronts and localized structures.

0.1.1 Specific Objetives

We are particularly interested in

- Understand how nonvariational effects could affect the dynamics of normal and FKPP fronts or interfaces and characterize its transitions.
- Give numerical and analytical insights about the modification of propagation direction of speed when nonvariational terms are considered.
- Understand how nonvariational effects can modify direction and propagation speed in localized structures and characterize its dynamical transitions.
- Generalize the results for higher dimensions.
- Validate the theoretical results developed in this thesis by experiments whose mathematical model corresponds to a nonvariational system.
- Study the emergence of new dynamical behaviors driven by nonvariational effects, motivated by the existence of chimera (or chaoticons) for the nonvariational Turing-Swift-Hohenberg equation.
- Answer the question, can chaoticons propagate? Furthermore, what kind of propagation dynamics can exhibit these.
- Explore how deterministic fluctuations as another example of nonvariational perturbations can affect the dynamics of fronts and localized structures.
- Show how deterministic fluctuations could drive the system to different transitions comparing with stochastic fluctuations.
- Give insights about how deterministic systems can reach randomness.
- Propose new methods to approach nonvariational systems.

0.2 Content of the thesis

This thesis is divided as follows.

The chapter 1 contains the theoretical framework with the necessary concepts to understand the rest of the chapters of the thesis. For this purpose, definitions from non-linear physics, pattern formation, and spatially extended systems are systematically addressed. The concepts of robust phenomena, fronts, localized structures, localized patterns, chaos, space-time chaos, and chimera states are also presented. We also explain the concept of variational and non-variational systems, understanding the latter as systems whose dynamics are not purely relaxation and can not minimize an energy functional. Nonvariationality will be crucial because one of the pillars of this thesis is understanding how non-variational effects affect the dynamics of robust phenomena such as localized structures and interfaces or fronts. Finally, we explain the details of a liquid crystal light valve experimental setup that can be variational or non-variational, depending on the tuning, which will serve as a validation laboratory for a large part of the results presented in this thesis.

In the chapter 2 we begin the study of the non-variational effects in the dynamics of fronts of FKPP type, that is, fronts that connect a stable state with an unstable one. This type of front allows describing physical processes such as combustion, the dynamics of a population, and, as we show in this chapter, the dynamics of a liquid crystal light valve with optical feedback under certain experimental conditions.

In the chapter 3 we try to explore the non-variational effects on another type of front, called normal fronts, characterized by connecting two stable states. As in the previous case, these fronts allow describing physical processes such as combustion (when the material has a sufficiently high ignition point), competition between populations in population dynamics, and dynamics in magnetic and optical media. In particular, we show an application in the control of fronts in the liquid crystal light valve presented in the previous chapters.

In the chapter 4 we seek to understand how non-variational effects can affect the dynamics of localized dissipative structures, showing that both the speed of propagation and the direction can be controlled via the adjustment of the non-variational parameters. Additionally, we try to extend the results obtained to larger dimensions, finding a family of bounded localized structures (which we call catamarans because they resemble boats with two parallel hulls), emerging as a consequence of the non-variational terms and whose dynamics and transitions were characterized. Later, this kind of solution was reported in [1, 2] on another setup based on liquid crystals.

In chapter 5 we show a paradigmatic phenomenon in the chimera literature. Although the emergence of chimera-type states (or chaoticons) in continuous media due to the effect of non-variational terms was reported in [3, 4], we show that there exists a family of chimeras that breaks its symmetry and travels in a wide range of parameters with well-defined direction and speed. The propagation mechanism is the consequence of the collective oscillations or modes within the localized structure. In this sense, we show their dynamics, emergence, and zoology and numerically illustrate their interaction and the formation of bound states.

In chapter 6, we show the emergence of an extremely curious phenomenon that we called

wandering chimeras in spatially continuous systems. These wandering chimeras are characterized by behavior resembling the Brownian movement; however, as we demonstrated in the chapter, they are statistically and dynamically different. Additionally, we evidenced the existence of this type of state through data obtained from the liquid crystal light valve setup with optical feedback.

In the chapter 7, we explore a different type of non-variational effect, this time given by the perturbation of a system by deterministic or chaotic fluctuations. The motivation of our research was to discover how deterministic fluctuations affect the dynamics of fronts by considering the coupling of the Nagumo Kuramoto equation with the Kuramoto-Sivashinsky equation as a source of spatiotemporal chaos. In this sense, we find important differences between chaotic and stochastic perturbations. Perhaps the most important result is that, unlike noise, deterministic perturbations preserve the pinning zone due to the forbidden transitions typical of deterministic dynamics. Finally, this work opens the doors to understanding how noise can emerge from chaotic dynamics in spatially extended systems, as we illustrate by measuring macroscopic variables such as average behavior, thus obtaining the main ingredients of noise.

In chapter 8 we continue investigating the effect of deterministic fluctuations, in this case in the dynamics of localized structures through the study of a system composed of the non-variational Turing-Swift-Hohenberg equation coupled with the Kuramoto-Sivashinsky equation to be able to elucidate the effect of the spatiotemporal chaotic perturbations in the dynamics of the localized structures that the Turing-Swift-Hohenberg equation exhibits. In a wide range of parameters, we find that the position and speed of the localized structures present a sustained chaotic behavior, without transitions to the homogeneous state or to another localized structure, which does not occur when considering stochastic perturbations. Together with the previous one, this work opens the doors to an interesting line of research, given by the transitions induced by chaos.

Along with our research, we were trying to understand how robust phenomena like fronts and localized structures emerge and modify their dynamics when non-variational effects are present due to when macroscopic phenomena in nature are modeled; typically, such models are non-variational. The common thread throughout our research was precisely to understand how non-variational effects affect the dynamics of fronts and localized structures encompassed within the concept of particle-type solution. In this sense, in chapter 9, we summarize all the findings as conclusions of our research.

Chapter 1

Theoretical Framework

In this chapter we develop all the theoretical background needed to understand the results presented in this thesis.

1.1 Robust phenomena and out-of-equilibrium systems

A phenomenon is called robust if it emerges in a wide variety of systems, independently of the underlying physics. Some examples are

- The interfaces between states, also called *fronts*. They are found in various systems, e.g., in chemical reactions like combustion, where the burned state is separated from the unburned state by an interface where the reaction occurs. We can also find fronts in others physical systems such as domain walls in (i) magnetic media defined as an interface separating magnetic domains, or the region where the transition between the different magnetic moments, (ii) optical media (interfaces between regions with different molecular orientation), (iii) climatic fronts (interfaces between masses of cold air and hot air, where typically are formed cumulus clouds or cumulonimbus) and even in (iv) social systems, with groups of people separated by their opinions. Some excellent books and reviews about fronts dynamics are [5, 6, 7]
- *Localized structures* are also found in various systems and often appear as localized spots or patterns in the media. They are shown in magnetic and optical media as areas or spots with well-defined properties such as position, speed, and size and differentiated from the surrounding environment. Particularly in liquid crystals, they can be seen as areas with molecular orientation different from that of the medium, so that observing them using crossed polarizers, we can see them as "bright" points of light on a "dark" background depending on whether the molecular orientation of the base state allows do not pass the light. A good review in localized structures can be found in [8, 9]
- *Chaotic behavior*, although possibly many, is mistaken for chance; it is also robust. Phenomena such as the toss of a coin or dice, the weather, the stock market, and even a double pendulum exhibit the main properties of chaos, which are the apparently random like behavior with a marked sensitivity to the initial conditions [10, 11].

Other examples are the waves, synchronization of coupled systems [12, 13], spatial pattern formation [14], hysteresis [15], among many others [16].

Robust phenomena are usually understood from a mathematical perspective via the theory of normal forms within dynamical systems theory [17, 18]. It is sought to find the most straightforward equation that allows describing the behavior of the phenomenon qualitatively. These equations, models, or laws of evolution called normal forms can come in many flavors, typically as differential equations, partial derivative equations, discrete maps, and cellular automata. In this sense, the emergence of robust phenomena in normal forms is usually linked to the change in some system parameter, and the specific value of the parameter in which said emergence occurs is usually called the bifurcation point.

1.2 Dynamical Systems and Evolution Laws

From the above, a dynamical system can be understood as a rule or law of evolution over state space. More formally, a dynamical system consists of an abstract space, called phase space or state space, whose coordinates (called state variables) describe the state of a system at any moment, and the evolution law allows the absolute determination of the future of all state variables, given only the initial state or condition of the system.

Some examples of dynamical systems are:

- The state of a simple pendulum, described by its angle and speed, is given by Newton's law $F = ma$, or more explicitly $\mathrm{d}^2\theta/\mathrm{d}t^2 + (g/L)\sin\theta = 0$.
- The temperature of a metal rod of a sufficiently small radius at a point x, and at an instant t is given by $\partial_t u = c\partial_{xx} u$.
- The population of a self-limited population of bacterias in a petri dish through a generation time window could be described by the map $x_{t+1} = \mu x_t(1 - x_t)$.

1.3 Spatially Extended Systems

Physical systems are tipically spatially extended, i.e., the dynamical behavior in any point of the space depends on the state of the whole space or at least of part of it. From a mathematical point of view these equations that determine the evolution laws of the systems are in general described as partial differential equations.

In the following, we will discuss about some models that will be explored and used throughout the development of this thesis. In general, all will be described by:

$$\partial_t u = F(u) + \nu\partial_{xx} u + \xi\partial_{xxxx} u + bu\partial_x xu + c(\partial_x u)^2, \tag{1.1}$$

that represent a generalization of the classical reaction-diffusion equation, recovered taking $\xi = b = c = 0$.

Fisher, Kolmogorov, Petrovsky and Piskunov Equation

In the world of reaction diffusion equations, the Fisher, Kolmogorov, Petrovsky and Piskunov equation, denoted by FKPP, is maybe one of the most explored models. It is given by the following equation

$$\partial_t u = ru(1-u) + \nu \partial xxu. \tag{1.2}$$

It was introduced in 1937 in a seminal work of R. A. Fisher [19] and in parallel but A. N. Kolmogorov, together with I. G. Petrovsky and N. S. Piskunov [20] as a model to describe the advantageous of a gene. In addition, investigating the propagation this model in the context of combustion theory. This is maybe the simplest and most known equation that describe a traveling wave.

Turing-Swift-Hohenberg Equation

This equation was studied by A. Turing in the 1970s in the context of the problem of morphogenesis, as was reported in posthumously reported in [21, 22] and by J. Swift and P. Hohenberg in [23] in the context of hidrodynamic fluctuations. Since it, this equation has been a topic of intensive research [24, 25, 26, 27] as archetypical model for fronts, localized states and pattern formation. It can be written as

$$\partial_t u = \eta + \mu u - u^3 - \nu \partial_{xx} u - \partial_{xxxx} u \tag{1.3}$$

depending of the region of parameters, this equation presents fronts solutions, localized states and patterns [24, 25].

Kuramoto-Sivashinsky Equation

This equation is one of the most simple equations where spatio-temporal chaos emerges. Was derived by Kuramoto in the context of coupled oscillators [28] and by Sivashinky in the context of flame dynamics [29]. It can be written in the following way

$$\partial_t \psi = -\mu \partial_{xx} \psi - (\partial_x \psi)^2 - \partial_{xxxx} \psi \tag{1.4}$$

This equation exhibit a rich and complex dynamics and will be studied with more details in the following sections.

1.3.1 Variational and Nonvariational Systems

Physics in equilibrium deals with systems for which its asymptotic behavior is known, either that reach the stable equilibrium state through energy dissipation, or that from the macroscopic point of view it is in a well defined state without any permanent dynamics in the macroscopic variables defining it. In this scenario, the evolution laws are tipically described by the extremization of a conservated quantity, tipically the energy. These systems are called

variational. More formally, from a mathematical point of view, a variational system is defined as a system whose dynamics comes from the derivative of a functional, i.e.,

$$\partial_t u = -\frac{\delta F}{\delta u} \tag{1.5}$$

These kind of system follow a relaxational dynamics, and can not show any kind of permanent dynamics nor spatio-temporal complexity. On the other hand, a nonvariational or nongradient system [30, 31, 32, 33, 34, 35] are those that can not be written as Eq. (1.5). Such systems tipically describes more rich and interesting dynamics, and are permanent in time and appears frequently in the modelling of macroscopic systems due to the corse-grain and mean-field approaches envolved in the deduction of the evolution laws. Thus, we will mainly interested in robust phenomena like fronts and localized structures in nonvariational system. In models, fronts and localized structures can be described as particle like solutions.

1.3.2 Particle-Like Solutions

Phenomena that can be described by particle like solutions are robust in nature. We can identify propagative localized structures in macroscopic systems that preserve its shape and can be characterized by macroscopic variables like position, speed, withd, height, charge, mass, etc. Thus, phenomena like a pulse propagation or a domain wall in a magnetic media can be understood in the framework of particle-like phenomena.

1.4 Fronts or domain walls

We can define a front as a nonlinear wave, joining two steady states of the system. Such states can be static or dynamical states. Maybe the most general definition of front is the following. A front can be defined as a solution that connect two steady states in a spatially extended systems. It can be motionless or traveling. In this thesis we will interested in the later scenario. Consider a traveling front that propagates with a well defined speed v. We can write the solution in the co-mobile frame putting $z = x - vt$, obtaining in this way

$$u(x,t) = u(x - vt) = u(z) \tag{1.6}$$

A studyed the scenario is a front connecting two stationary states, $u(x,t) = u_0$ and $u(x,t) = u_1$, where $F(u) = 0$. In the following we will explore the properties of fronts connecting a stable state with an unsable one.

1.5 FKPP fronts

One of the most simplest systems exhibiting fronts is the FKPP equation,

$$\partial_t u = ru(1-u) + \partial_{xx} u.$$

It have two steady states, $u_0 = 0$ and $u_1 = 1$. Kolmogorov *et al.* [20] show how to get the direction of propagation, obtaining that the unstable state always invades the stable one for

this equation. Thus, to get the front propagation direction it is only needed evaluate the stability of the steady states. In this case, for $r > 0$ we have

$$\partial_u F(0) = r - 2ru|_{u_0=0} = r > 0$$

and,

$$\partial_u F(1) = r - 2ru|_{u_1=1} = -r < 0$$

then, u_0 is unstable and u_1 is stable.

1.5.1 Propagation speed: pulled and pushed fronts

Consider a slightly general scenario than the FKPP equation by taking a bistable reaction-diffusion equation

$$\partial_t u = F(u) + D\partial_{xx} u \tag{1.7}$$

with $F(0) = F(1) = 0$ and $F(u) > 0$ for $0 < u < 1$. In the equation 1.7. Putting the system in the co-moving frame and linearizing the front solution around the unstable state, we obtain

$$D\partial_{zz} u + v\partial_z u + F'(0)u = 0 \tag{1.8}$$

Note that it is an homogeneous second order differential equation with constant coefficients, therefore its solutions can be found by using the exponential ansatz $u(z) \approx \mathrm{e}^{\lambda z}$, obtaining

$$(D\lambda^2 + v\lambda + F'(0))\mathrm{e}^{\lambda z} = 0 \tag{1.9}$$

where $\mathrm{e}^{\lambda z} \neq 0$ always. Therefore,

$$D\lambda^2 + v\lambda + F'(0) = 0 \tag{1.10}$$

whose solutions are given by

$$\lambda_{\pm} = \frac{-v \pm \sqrt{v^2 - 4DF'(0)}}{2D} \tag{1.11}$$

and to obtain the associated real solutions, it must satisfy

$$v^2 - 4DF'(0) \geq 0 \tag{1.12}$$

But to obtain solutions with physical meaning is needed that

$$v \geq \sqrt{4DF'(0)} \tag{1.13}$$

because in other case the solution will oscillate arround $u = 0$, driving to negative values for the density u. We can find the minimal front speed using a linear criteria in a similar way showed for the FKPP system in the above section. Thus, we consider an exponential ansatz $u(z) \approx \mathrm{e}^{-\lambda z}$ in Eq. (1.8), obtaining

$$v(\lambda) = D\lambda + \frac{F'(0)}{\lambda} \tag{1.14}$$

and to find the minimun we derivate with respect to λ and set it equal to zero to get

$$v'(\lambda) = D - \frac{F'(0)}{\lambda^2} = 0 \tag{1.15}$$

and solving for λ, give us

$$\lambda = \sqrt{\frac{F'(0)}{D}} \tag{1.16}$$

and substituting in Eq. (1.14) we obtaing

$$v^* = \min_{\lambda}[v(\lambda)] = 2\sqrt{DF'(0)} \tag{1.17}$$

In addition, Aronson and Weinberger [36] obtain in addition and upper bound for the speed, so that

$$2\sqrt{DF'(0)} \leq v^* \leq 2\sqrt{DSup_u\Big[\frac{F(u)}{u}\Big]}, \tag{1.18}$$

for any positive and sufficiently localized initial condition $u(x, 0)$, with $u(x, 0) \in [0, 1]$. Moreover, for any function satisfying $F(u) \leq uF'(0)$, the upper and lower bounds agree and the asymptotic front speed is uniquely determined and given by Eq. (1.17).

Note that in the above scenario the fron speed can be calculated by a linear criteria and only depends on the region where the front vanishes, i.e., the front tail $u \approx 0$. This

propagation mechanism is called pulled (also pulled fronts) because the front propagations is pulled by its leading edge.

On the other hand, when the upper and lower bounds does not coincide and the asymptotic front speed is larger than the given by the lower bound (linear criteria), the front propagation mechanism is called of pushed type, because the front is pushed by its interior part. In the following section we will show an example of a system exhibiting a pulled pushed transition in the front dynamics.

1.5.2 Pulled-Pushed Transition

Consider the following system

$$\partial_t u = u(1-u)(1+au), \ (a>0) \tag{1.19}$$

The above equation have two steady states given by $u \equiv 1$ and $u \equiv 0$ that are stable and unstable one respectively. Nevertheless, the asymptotic front speed changes when the a parameter is increased over a critical value. In fact, [37] shows that the front speed is described by

$$v = \begin{cases} 2\sqrt{D} & a \leq 2 \\ (\sqrt{a} + 2/\sqrt{a})\sqrt{D/2} & a > 2 \end{cases} \tag{1.20}$$

1.6 Normal fronts

Another interesting kind of front is given by those connecting two stables states, called normal fronts. A simple example is given by a generic bistable system, whose potential is depicted in figure (a). In order to have an expresion for this system, consider

$$\partial_t u = F(u) + \partial_{xx} u \tag{1.21}$$

where $u = u(x,t)$ and $u = u_0$, $u = u_1$ are stable states, i.e., $\partial_u F(u) < 0$ for $u = u_0, u_1$.

The propagation direction and speed of these kind of fronts depends on the sign and magnitude of the difference of energy. Following the Pomeau work [38] we get to the following expresion for the front propagation speed

$$v \propto \Delta V(u) = \int_{u_0}^{u_1} F(u) \mathrm{d}u \tag{1.22}$$

A detailed calculation for a specific bistable system is done in the chapter 3.

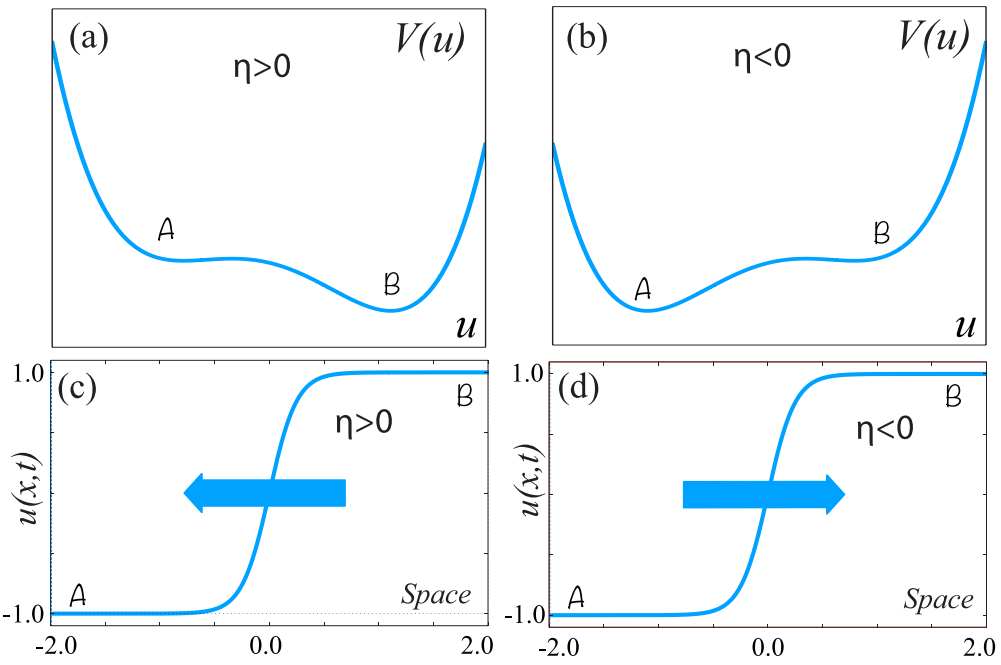

Figure 1.1: Panels (a) and (b) show a generic bistable potential where the asymmetry is controlled by η parameter, having in (a) that the state B minimizes the energy potential corresponding to $\eta > 0$ and in (b) the contrary scenario, i.e., A minimize the energy potential. In panel (c) is depicted how the state B invades A when B minimizes the energy potential, and in panel (c) the complementary case.

1.7 Dissipative Localized Structures

Out-of-equilibrium systems are typically described through non-linear dynamical systems. In turn, these can be understood qualitatively through simplified equations called normal forms. Therefore, one of the most straightforward and most interesting generic transitions can be observed through the birth of a homoclinic tangency; described connection occurs between one of the stable varieties and one of the unstable manifolds of the equilibria.

From a purely mathematical point of view, these homoclinic tangles give rise to the so-called localized structures [24, 39]. However, from the physical perspective, localized strictures are characterized by the coexistence between injection and energy dissipation, typically represented through non-linear focusing terms (injection) and differential operators, among which the Laplacian (diffusion). The balance between injection and energy dissipation in effect allows stabilization of localized structures against small disturbances. These out of equilibrium structures are called self-organized dissipative localized structures [14, 8, 40]. It is also worth mentioning that we can also understand the spatial variation of a front connecting two homogeneous states as a localized structure because in that case, we will have a solution that will connect the zero homogeneous state with itself through a path that describes the variation of the solution in the heart of the front (interface).

It should be noted that this type of structure emerges in both natural systems and those derived from technological devices, the latter being of particular interest given the possibility of its reproduction and study through experimental setup within a laboratory. Other examples of dissipative localized structures are spirals and, in general, localized patterns, typically the product of the coexistence between homogeneous states and patterns.

In addition to the term localized dissipative structure, in the literature, we can find synonyms such as:

- Dissipative soliton[8, 41], which refers to its similarity to localized waves in conservative systems, also called solitons, which can typically be found in the study of surface waves in fluids or through solutions of the non-linear Schrödinger equation, the Sine-Gordon equation, and variational variants.
- Pulse, used throughout the literature on optical systems as light pulses in setups composed of optical fibers [42, 43] and in neurodynamics, when studying the propagation of electrical stimuli in neuronal tissues [44].
- Spots, mainly used in the literature of optical systems [45, 46], especially in liquid crystals [47, 48, 49], since these localized structures typically emerge as spots of light or absence of light in said systems. However, recently it has also been applied in the emergence of structures located in vegetation [50].

1.8 Patterns and localized patterns

In natural and technological systems, patterns tend to emerge from a homogeneous state due to a destabilization of the stable state via spatial modulation. Examples of these can be found in the "sand-ripples" on the sea surface, the Faraday waves that emerge in vertically forced systems, or the convective Rayleigh-Benard rolls. An example of particular interest

throughout this manuscript will be the standard states in the Swift-Hohenberg equation [24]. As mentioned in the previous chapter, a localized structure can be seen as a homoclinic orbit in the associated Newton-like system. Thus, a localized pattern can be understood similarly, with the difference that the type of connection performs more complex explorations or tours in phase space. To review more details about pattern formation systems and its dynamics there are excellent books and reviews, e.g., [40, 14, 51, 52, 53, 54] and references therein.

1.9 Dynamical Complexity

From classical mechanics, we know that a simple pendulum can show us solutions that, due to the friction (dissipation of energy mechanism), it ends asymptotically in a state of equilibrium without oscillations. A little more sophisticated systems such as the magnetic pendulum or the double pendulum can present highly complex orbits. Nevertheless, the dissipation will play its role in both scenarios, bringing the system to a stable and homogeneous equilibrium over time. We also know that a simple pendulum leads at most to periodic behaviors under ideal conditions (without friction or energy dissipation). However, in general, its dynamics can become aperiodic and even qualitatively similar to randomness. For example, from a numerical and experimental point of view, the double pendulum has been studied, either assuming the absence of dissipation in the numerical case or by injecting energy to replace the loss naturally. In both scenarios, the existence of aperiodic orbits is shown [55, 56]. In the following will be explored what kinds of dynamical behaviors continue after the periodic behavior.

1.9.1 Quasiperiodicity

After periodicity, the dynamical behavior that follows in complexity is quasi-periodicity, distinguished from periodicity through a translation by excess or defect in the period, i.e., there does not exist a period. A simple example is the following:

$$\partial_{tttt} y + 3\partial_{tt} y + 2y = 0, \tag{1.23}$$

whose solution

$$y(t) = A\cos(t) + B\sin(t) + C\cos\left(\sqrt{2}t\right) + \sin\left(\sqrt{2}t\right),\ A, B, C, D \in \mathcal{R}, \tag{1.24}$$

gives rise to aperiodic trajectories, since the function $t\ tocos(t) +\ cos(\ sqrt2t)$ is not periodic and is a solution of the differential equation.

A more straightforward example in discrete dynamical systems is given by the rotation maps of the circle, i.e.,

$$x_{t+1} = (x_t + \lambda) \mod 1, \tag{1.25}$$

whose solutions or trajectories are always periodic if λ is a rational number because in that case $\lambda = p/q$ and by iterating q times, we would obtain

$$\{x_0, x1 = \left(x_0 + \frac{p}{q}\right) \mod 1, x_2 = \left(x_0 + 2\frac{p}{q}\right) \mod 1, \ldots, x_p = \left(x_0 + q\frac{p}{q}\right) \mod 1 = x_0.\} \tag{1.26}$$

Note that if *lambda* is irrational, the situation is quite different since it is impossible to find a q such that the q -th iterated allows generating a periodic orbit. This result is known as Jacobi's theorem [11].

It should be noted that the quasi-periodicity finally keeps the solution close to a periodic solution so that from the physical point of view, it allows making predictions with an error margin limited by the maximum translation concerning the periodic orbit that the system allows. A more interesting aperiodic behavior is the so-called deterministic chaos, or simply chaos explained in the next section.

1.9.2 Chaos

We have mentioned that systems out of equilibrium can present highly complex and aperiodic behaviors over time as energy dissipation mechanisms. Such behavior is called chaos and is mainly characterized by the property of having sensitivity to initial conditions. We will evidence this robust dynamical behavior through two generic and well-known examples, one in discrete systems and the other in continuous systems.

Logistic Map

Maybe the most simple example of chaotic dynamics is given by the logistic map, given by

$$x_{t+1} = f(x_t) = \mu x_t(1 - x_t).$$

Geometrically, it is described by a concave parabola that cross the x-axis at $x = 0$ and $x = 1$, as we can see in figure 1.2.

Note that, from the Figure 1.2, this map has two fixed points, given by the solutions of the equation: $f(x) = x$, one of them is trivial $f(0) = 0$ and the other one is easily calculated by:

$$\begin{aligned} & \mu x(1-x) &=& x \\ \Longrightarrow \quad & (\mu-1)x - \mu x^2 &=& 0 \\ \Longrightarrow \quad & x &=& (\mu-1)/\mu. \end{aligned}$$

In particular, for $\mu = 4$, we obtain that $x = 3/4$ is a fixed point. Realizing a linear stability analysis we get that

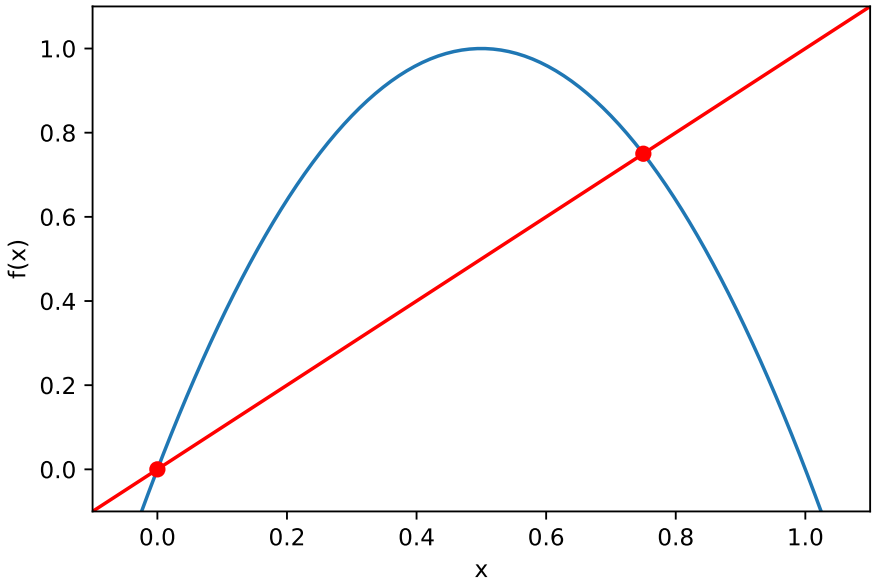

Figure 1.2: Logistic map. Fixed points (equivalent to steady state in continuous time systems are given by the intersection between the parabola described by the map and the identity function.)

$$f'(x) = \mu - 2\mu x$$

Note that $x = 0$ is always unstable for $\mu > 0$. On the other hand, evaluating the other one equilibrium, we get

$$f'\Big(\frac{\mu - 1}{\mu}\Big)x = \mu - 2\mu\frac{\mu - 1}{\mu}$$

or simplifying

$$\Big|f'\Big(\frac{\mu - 1}{\mu}\Big)\Big| = |2 - \mu|$$

thus, $x = (\mu - 1)/\mu$ is stable for $1 < \mu < 3$ and loose it stability for $\mu \geq 3$, where start the first period-doubling phenomena.

To understand more in deep the dynamics of this map, we will study its periodic orbits. Thus, x_0 define a periodic orbit of n-period if

$$x_0, x_1 = f(x_0), x_2 = f^2(x_0) = f(f(x_0)), \ldots, x_n = f^n(x_0) = 0$$

where n is the smallest integer that $f^n(x_0) = x_0$. Note that fixed points are periodic orbits of 1-period. We can calculate numerically the periodic orbits for this map in function of the parameter μ, obtaining the bifurcation diagram shown in figure 1.3

From the figure 1.3 we can get some intuition about where is borning the dynamical complexity, and we can observe a sort of branching of the period orbits. This phenomena is known as a period-doubling cascade, and the logistic map is maybe the most simple dynamical system exhibit it. Note the self-similarity of the bifurcation diagram. Tipically, bifurcation diagrams over regions where the dynamics is chaotic have this property, known as fractal branching due to period doubling. In this point we will see how period orbits evolve and duplicate its period through increasing the bifurcation parameter. Nevertheless we do not see yet how chaos looks. Figure 1.4 show a generic orbit of the logistic map in the chaotical regime.

Sensibility to initial conditions

We mention in the first part of this manuscript that the sensibility to initial conditions is one of the most important ingredients of chaos. In the following we will characterize such property for the logistic map. In order to illustrate it consider the logistic map at $\mu = 4$ and the following two initial conditions $x_0 \in (0, 1)$ and a small perturbation of it, e.g., $x_0' = x_0 + \varepsilon$ with ε arbitrarily small but ensuring that $x_0' \in (0, 1)$. Simulating this scenario, we obtain the behabiour ilustrated in figure 1.5

As we can see in figure 1.5, after close to 20 iterations, both solutions separates with a poor correlated behabior. The instantaneous and cumulative difference between the two orbits is ilustrated in figure 1.6. This give us and idea about how both orbits separates in time. In fact, one can calculate the rate of (exponential) separation between orbits that starts arbitrarily close. This drive us to the concept of Lyapunov exponent, that is maybe the most popular chaos quantifier. It will be presented later.

Instead of the simplicity of the logistic map, there are a lot of research associated with it. A good reference about the importance and the applications related to the logistic map can be found in [57]

Lorenz Equations

In a seminal paper published in 1963, Edward Lorenz discovered that simple deterministic systems could give rise to extremely complex dynamic behaviors. His famous equations can be deduced from a drastic simplification of atmospheric convection roll equations. However, the same equations have been also deduced in optical [58] and mechanical [59] systems.

The Lorenz equations are given by

$$\begin{aligned} \dot{x} &= \sigma(x - y) \\ \dot{y} &= \rho x - y - xz \\ \dot{z} &= xy - \beta z \end{aligned} \tag{1.27}$$

here σ, ρ and β are parameters that in the Lorenz model correspond to the Prandtl number,

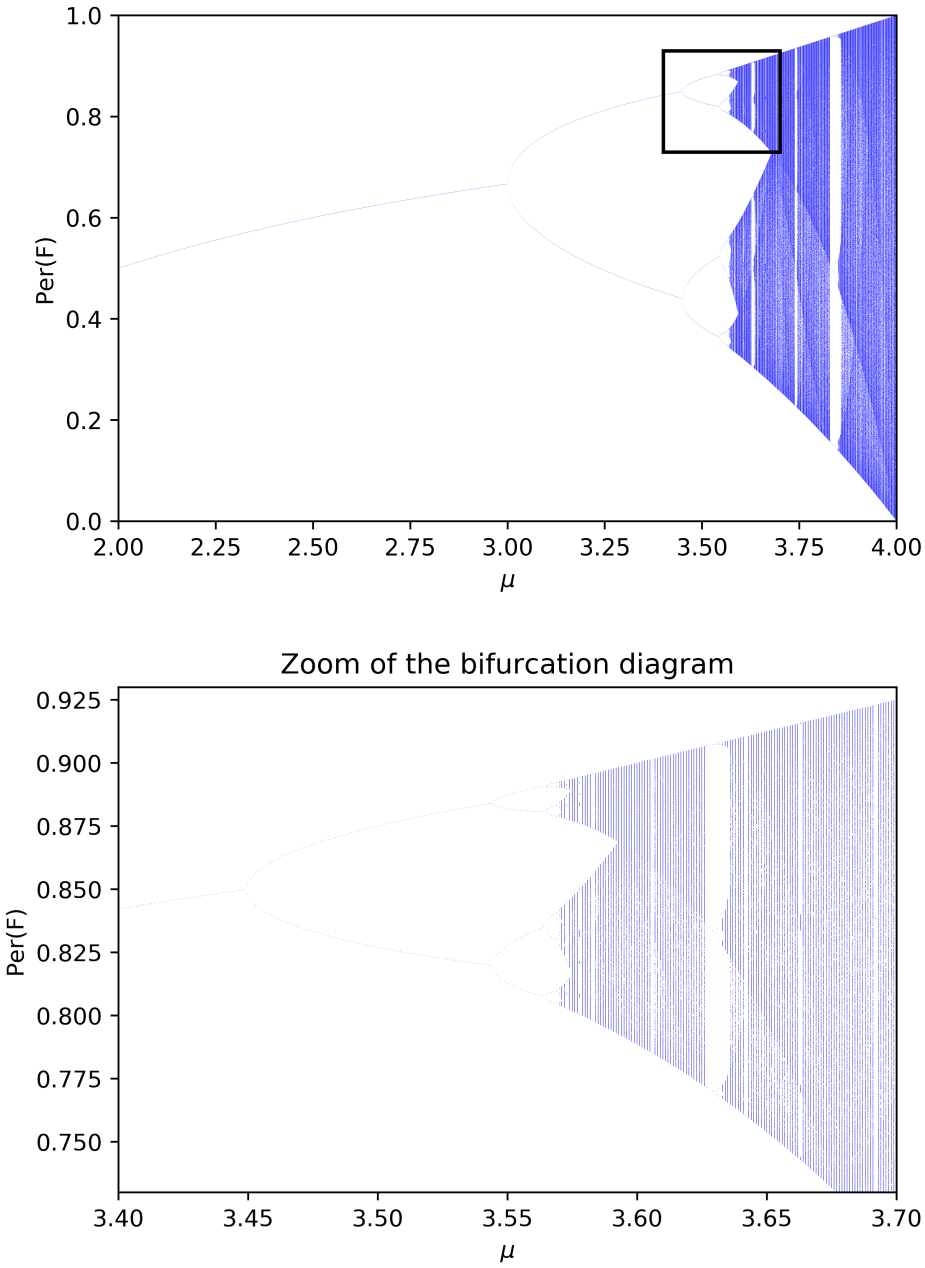

Figure 1.3: Bifurcation diagram for the logistic map in terms of the bifurcation parameter μ. Here we can see the stable periodic orbits for each μ value as well as the doubling-period effect. The black box indicated in the top of this figure corresnpond to the plot located at the bottom)

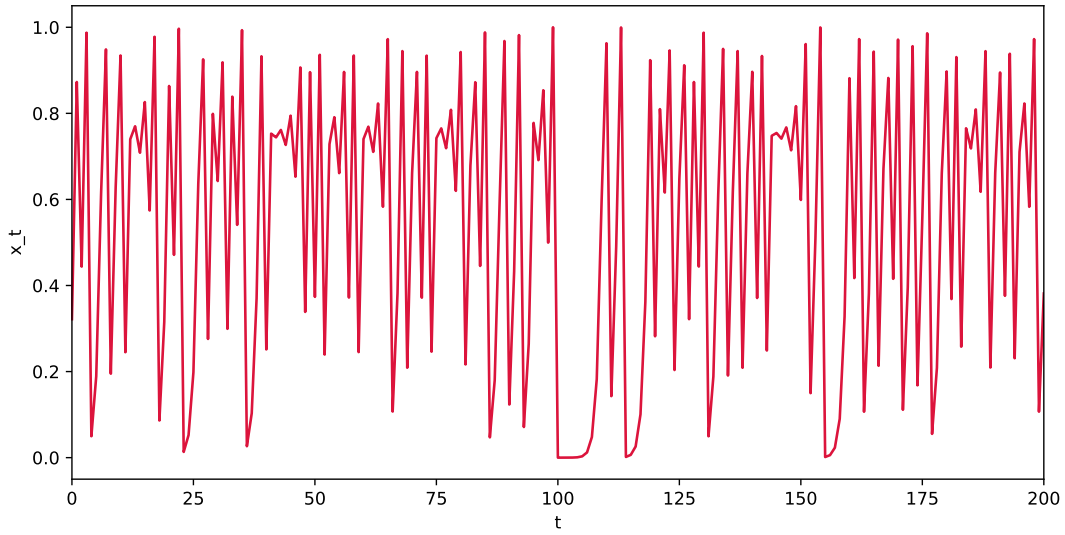

Figure 1.4: Generic orbit of the logistic map, for $\mu = 4$

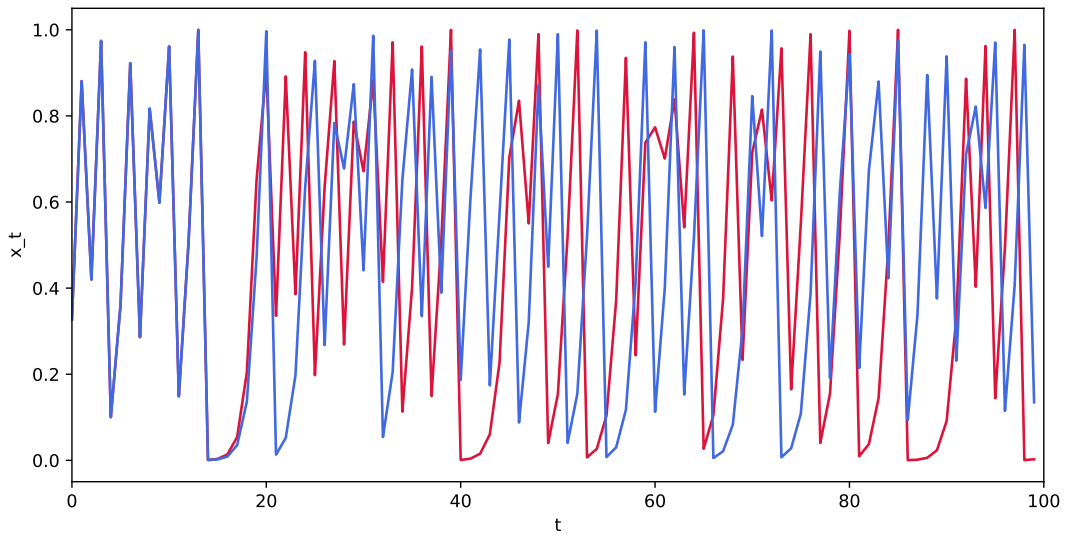

Figure 1.5: Sensibility to initial conditions illustrated to two initial conditions starting close to $x_0 = 0.3274$ with a distance of order 10^{-8}

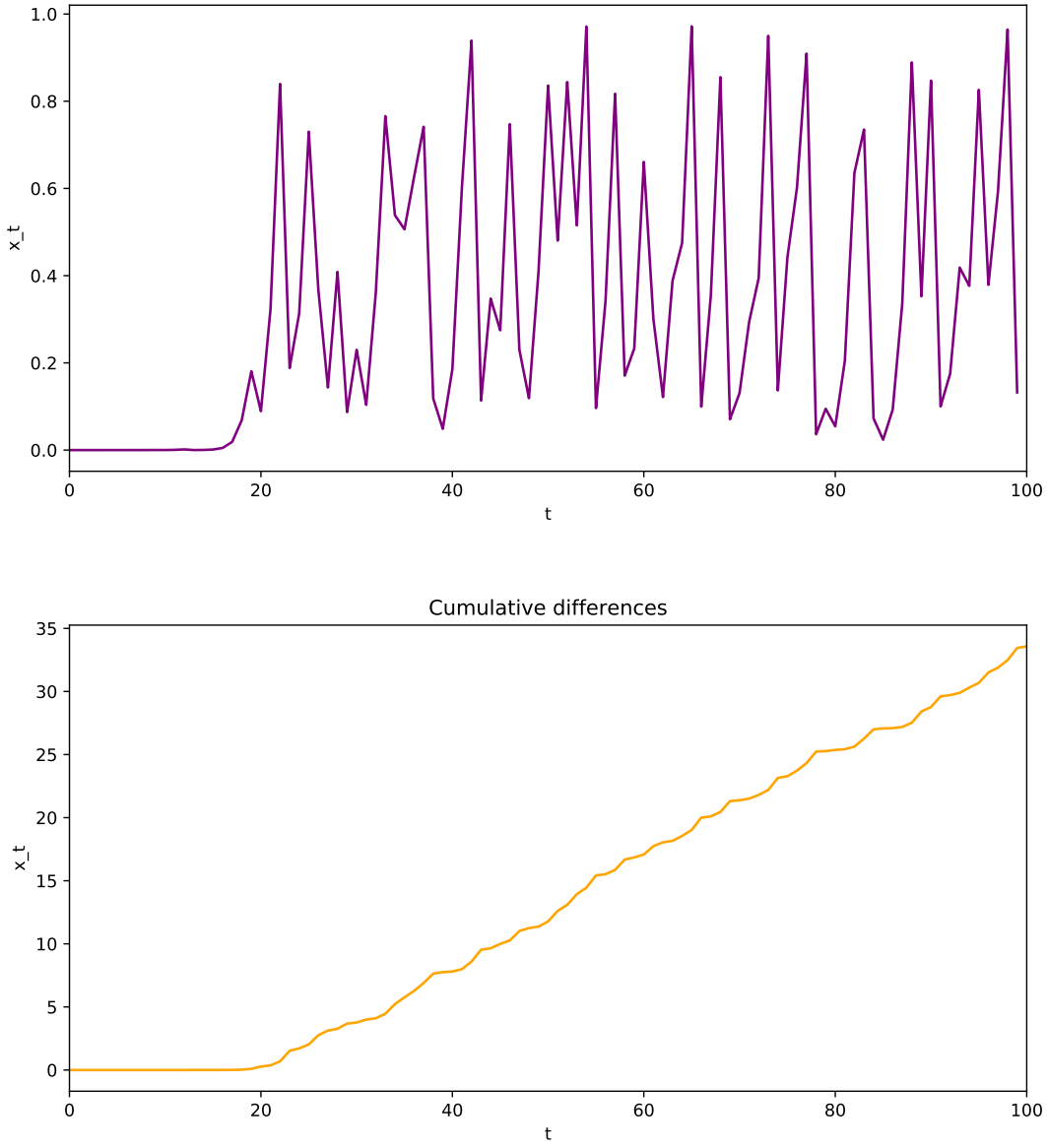

Figure 1.6: Instantaneous and cumulative difference between the orbits shown in figure 1.5

the Rayleigh number, and the ρ parameter is related to the aspect ratio of the rolls.

This system has only two nonlinear terms, given by the quadratic terms xy and xz, it is symmetric $(x, y) \to (-x, -y)$ so that, if $(x(t)y(t), z(t))$ is solution, then $(-x(t), -y(t), -z(t))$ is also solution. Additionally it is also dissipative, i.e., the volumes in the phase space contract under time evolution of the system. This system exhibits chaos for a wide range of parameters, and in Fig. 1.7 we can see the chaotic behabior of each component as well as the interesting geometry of the attractor.

There are book dedicated to the study of this equation [60] and there exist several open problems related to it.

1.9.3 Spatio-temporal chaos

When we speak of space-time chaos, we are in the world of spatially extended systems, typically described through partial derivative equations or through systems of differential equations where the spatial variable has been discretized. In this scenario and the sensitivity to the initial conditions, typically shown through the exponential separation of the trajectories over time, there is a loss of spatial correlation. Perhaps the simplest example of a system exhibiting space-time chaos is given by the PDE.

$$\partial_t \psi = -\mu \partial_{xx} \psi - (\partial_x \psi)^2 - \partial_{xxxx} \psi \tag{1.28}$$

known as the Kuramoto-Sivashinky system, which exhibits spatiotemporal chaos and loss of spatial correlation, as is shown in [28, 29].

Another example, just as paradigmatic, is given by the coupled map system.

$$x_n^{t+1} = (1 - \varepsilon) f(x_n^{t+1}) + \frac{\varepsilon}{2}(f(x_{n-1}^t + f(x_{n+1}^t)),\ n = 1, \ldots, N \tag{1.29}$$

where the map $f : \mathbb{R} \to \mathbb{R}$ is given by

$$f(x) = ax^2 - 1, \tag{1.30}$$

where a is a real number, studied by Kuramoto in [61]. It exhibits also a complex spatiotemporal dynamics characterized by a sensitivity to initial conditions and loss of spatial correlationm as we can see in figure 1.9.

A more formal way of characterizing chaotic behavior is given by calculating the Lyapunov exponents for chaos and the Lyapunov spectrum for space-time chaos. The following sections explain the details for determining it.

1.9.4 Lyapunov Exponents

Consider the following dyamical system

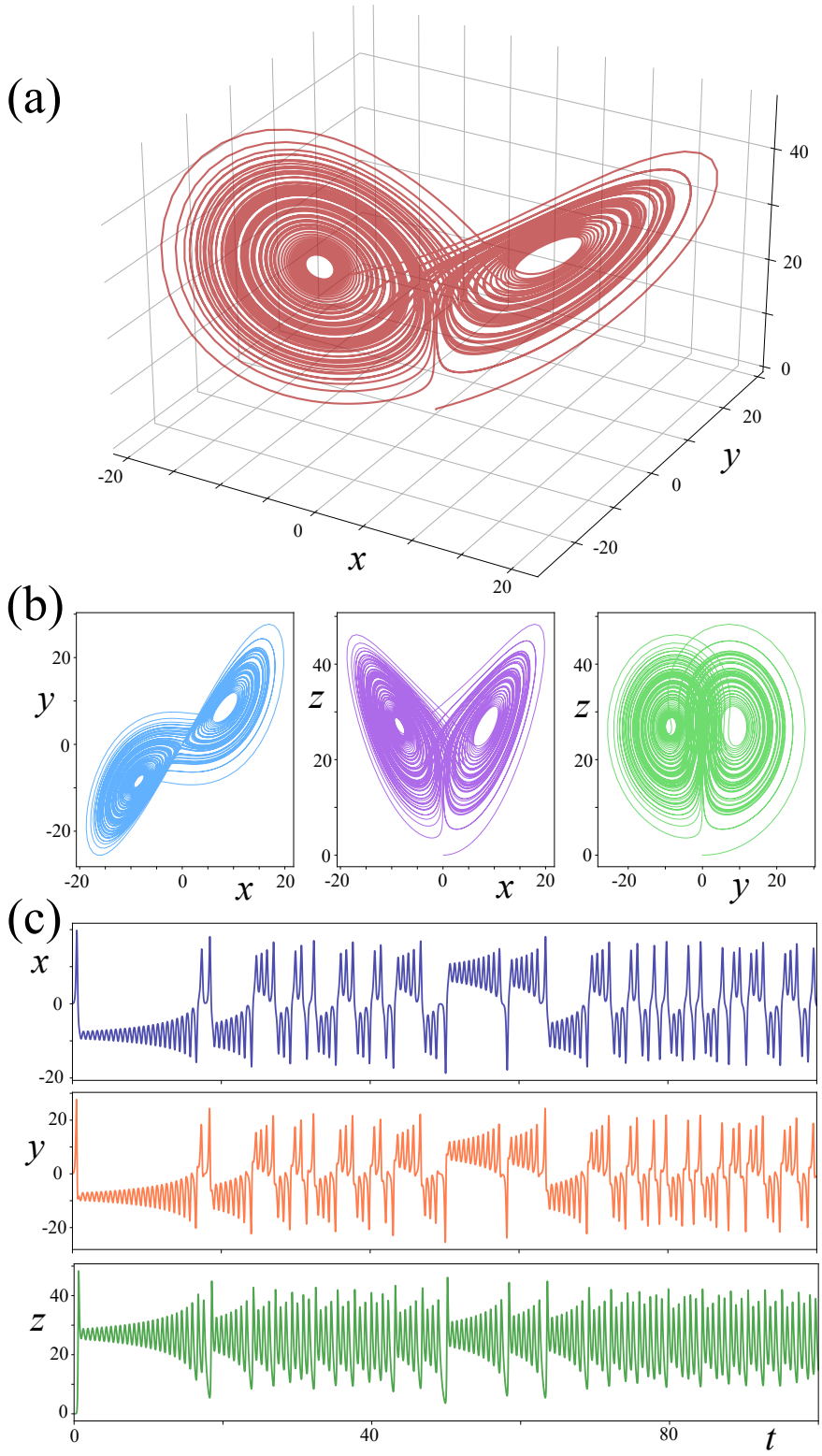

Figure 1.7: Panel (a) shows the attractor of the Lorenz system. Panel (b) depicts its different phase planes and (c) evidence the behavior of each component of the system with respect to time.

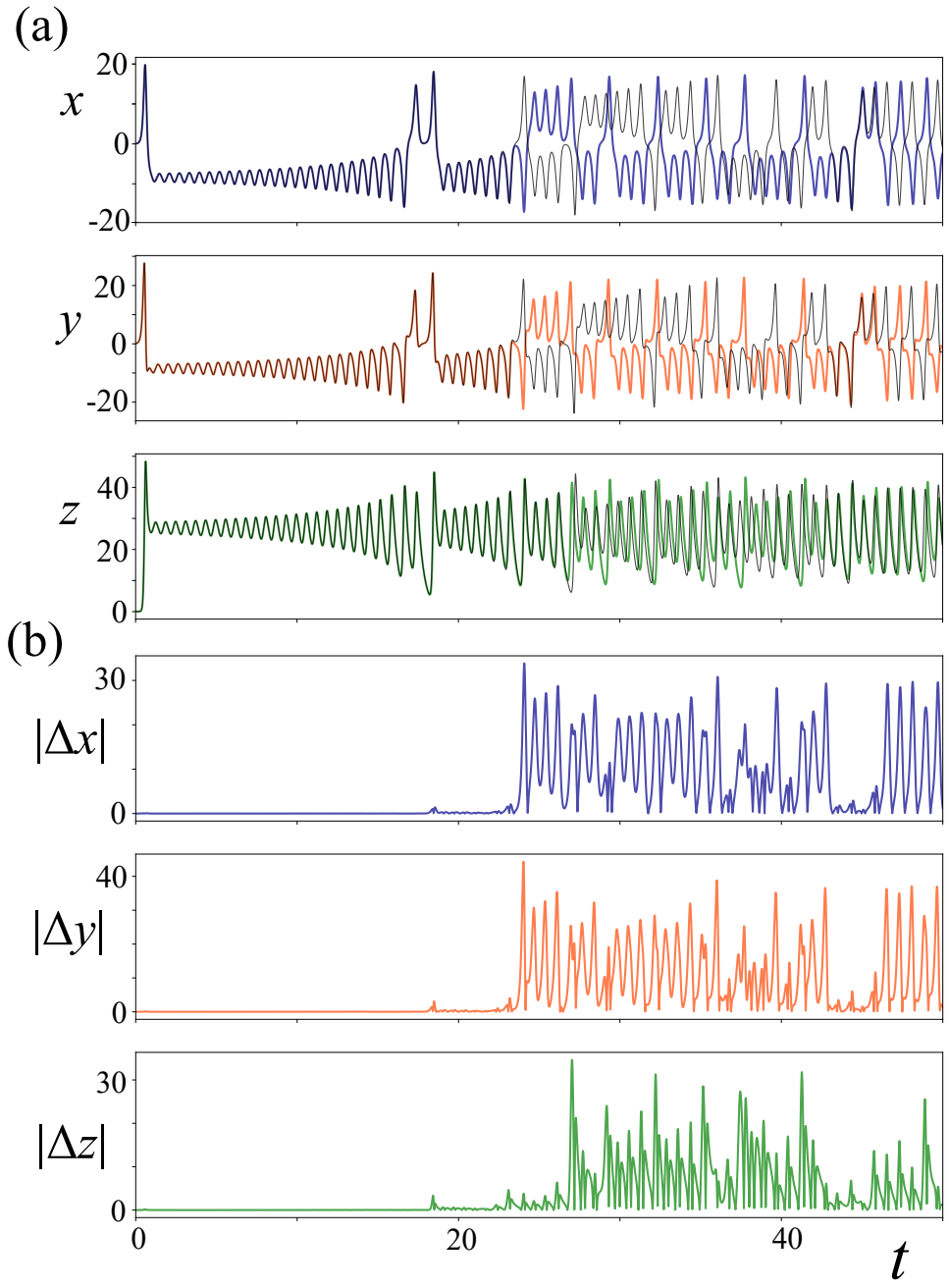

Figure 1.8: Panel (a) show the evolution of two initial conditions with a slightly difference of order 10^{-3} between them at each component. Panel (b) represent the differences $|\Delta x|$, $|\Delta y|$ and $|\Delta z|$, between the two solutions emphasize the separation of both solutions.

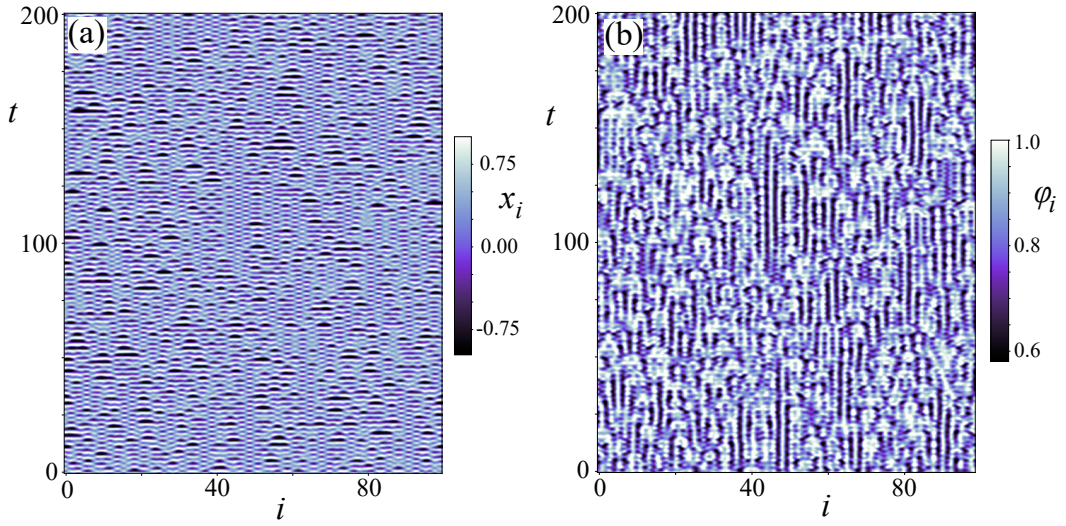

Figure 1.9: Figure show spatio-temporal chaos for the Kaneko coupled map lattice given by the Eq. 1.38

$$\dot{x} = f(x) \tag{1.31}$$

where x stands for the $N-$dimensional state vector. Consider now two points $x_0(0)$ and $x_1(0)$ as a initial condition for the trajectories $x_0(t)$ and $x_1(t)$ respectively. We can measure the separation or distance between the two corresponding points of these trajectories when we let evolving the time, throught

$$\mathrm{d}(t) = |x_1(t) - x_0(t)| \tag{1.32}$$

if the dynamics of the equation (1.31) is chaotic, then $\mathrm{d}(t)$ increases exponentially in time, i.e.,

$$\mathrm{d}(t) \approx \mathrm{d}(0)\mathrm{e}^{kt} \tag{1.33}$$

and this give us the average velocity of the exponential divergence of the trajectories through

$$k \approx \ln \frac{\left[\dfrac{\mathrm{d}(t)}{\mathrm{d}(0)}\right]}{t} \tag{1.34}$$

and taking the limit $\mathrm{d}(0) \to 0$ and $t \to \infty$, we obtain a exact definition of the *maximum characteristic Lyapunov exponent*, i.e.,

$$\lambda = \lim_{\substack{\mathrm{d}(0)\to 0 \\ t\to\infty}} \ln \frac{[\mathrm{d}(t)/\mathrm{d}(0]}{t} \tag{1.35}$$

Characterizing the dynamics in the following way:

- If $\lambda < 0$ then the dynamics tends to a stable fixed point.
- If $\lambda = 0$ then we have a periodic or quasi-periodic behevior.
- If $\lambda > 0$ one deals with a chaotic behabior.

Is nothewortly that the maximum characteristic Lyapunov exponent give us the velocity of information lost with respect to the initial system state.

1.9.5 Spectrum of Lyapunov Exponents

The Lyapunov spectrum is a more detailed measure than the maximum characteristic Lyapunov exponent. To understand it, consider again a trajectory $x(t)$ for the Eq. (1.31) with initial condition $x(0)$, and consider the neighborhood of trajectories $x_\varepsilon(t)$ by

$$x_\varepsilon = x(t) + \varepsilon\vec{(t)} \tag{1.36}$$

where $\varepsilon(t)$ is the distance between $x_\varepsilon(t)$ and $x(t)$. Thus, we can define the function

$$\lambda[\vec{\varepsilon}(0)] = \lim_{t\to\infty} \ln \frac{[\vec{\varepsilon}(t)/\vec{\varepsilon}(0]}{t} \tag{1.37}$$

whose argument is the vector of initial displacement $\vec{\varepsilon}(0)$ such that $|\vec{\varepsilon}(0)| = \varepsilon$ and $\varepsilon \to 0$.

Note that we can consider $\vec{\varepsilon}$ at the $N-$direction of the state space, obtaining in such a way a finite serie of values $\lambda_1, \lambda_2, \ldots, \lambda_n$. These values of the function λ are called the Lyapunov exponents (LEs), and the positive/negative values of the LEs can be viewed as a measure of the averaged exponential divergence/convergence of the neighborhood trajectories. In this work, LEs will be presented as a sequence of values in decreasing order, so that the first Lyapunov exponent is the greatest one. In this work we will focus in the algorithms based on Benettin method [62] and Jacobian method [63] to find the Lyapunov spectrum.

1.10 Chimera states

Chimera states are usually defined as spatio-temporal patterns exhibiting coexistence of coherent and inchoherent domains are ubicuous from out-of-equilibrium systems. They can be understood as localized spatiotemporal patters resulting from a symmetry breaking [64]. Although the chimera states has been extensively reported in discrete-space systems of oscillators, and there exist a lot of evidence that such behaviour also occurs in continuous systems. Experimentally, It has been reported in several systems ranging from nature to technological

devices. Since the seminal work of Kuramoto [65], the phenomena of chimera states has been increasing attention due to its robustness and universality. In neurodynamics, has been reported has spatio-temporal neuron firing patterns in experiments with cortinal neurons [66, 67, 68] In semiconductor lasers, chimera states has been observed has states with coherent and incoherent domains in terms of light intensity [69, 70, 71] and in coupled waveguide resonators appears reported as domains with coherent and incoherent light emission [72]. Nevertheless, in continuous media, the chimera states has been less explored. From the theoretical point of view, one of the first examples of this kind of chimera-like states in continuous systems is the chaoticon, given by [3, 4], showing coexistence of a coherent domain defined by a homogeneous state and an incoherent domain of spatiotemporal chaos in the nonvariational real Swift-Hohenberg model and the one-dimensional Nagumo Kuramoto model. In addition, recently has been reported an exciting example of coexistence of a homogeneous domain defined by a frozen spiral coexisting with a background of amplitude turbulence in the complex Ginzburg-Landau equation [73].

Some experimental examples in the continuous media scenario can be seen in fluid and optical systems. In fluid dynamics has been reported in the experiment of Faraday waves, parametrically forced by an oscillating, the coexistence of domains of regular stripes (coherent state) and chaotical surface waves (incoherent state) [74, 75]. In the Taylor-Couette flow, given by a fluid constrained between two rotating cylinders, we have that when the rate of rotation increases, the dynamics changes from an orderly laminar regime to a turbulent one through a series of intermediate dynamical states. In such intermediate states, we can find the coexistence of a coherent state given by the laminar regime coexist with an incoherent state of turbulence, see for example [76], and references therein.

1.10.1 Chimera states in a discrete time system

An exciting model to looking for chimeras in discrete systems is the famous coupled system of coupled logistic maps studied by Kaneko [61], and given by:

$$x_n^{t+1} = (1-\varepsilon)f(x_n^{t+1}) + \frac{\varepsilon}{2}(f(x_{n-1}^t + f(x_{n+1}^t)),\ n = 1, \ldots, N \tag{1.38}$$

where the map $f : \mathbb{R} \to \mathbb{R}$ is given by

$$f(x) = ax^2 - 1, \tag{1.39}$$

where a is a real number. The above map exhibits a transition to chaos driven by a doubling period cascade similar to that exhibited by the logistic map. Moreover, both maps are topologically conjugated (dynamically equivalent). In order to measure the syncronization, we can calculate a spatial phase by site

$$\theta_{\mathrm{i}}(t) = \mathrm{e}xp(-|x_{\mathrm{i}} + 1(t) - x_{\mathrm{i}-1}(t))/2|), \tag{1.40}$$

capturing the spatial variation arround the i-th site in the lattice. Note that if all the system

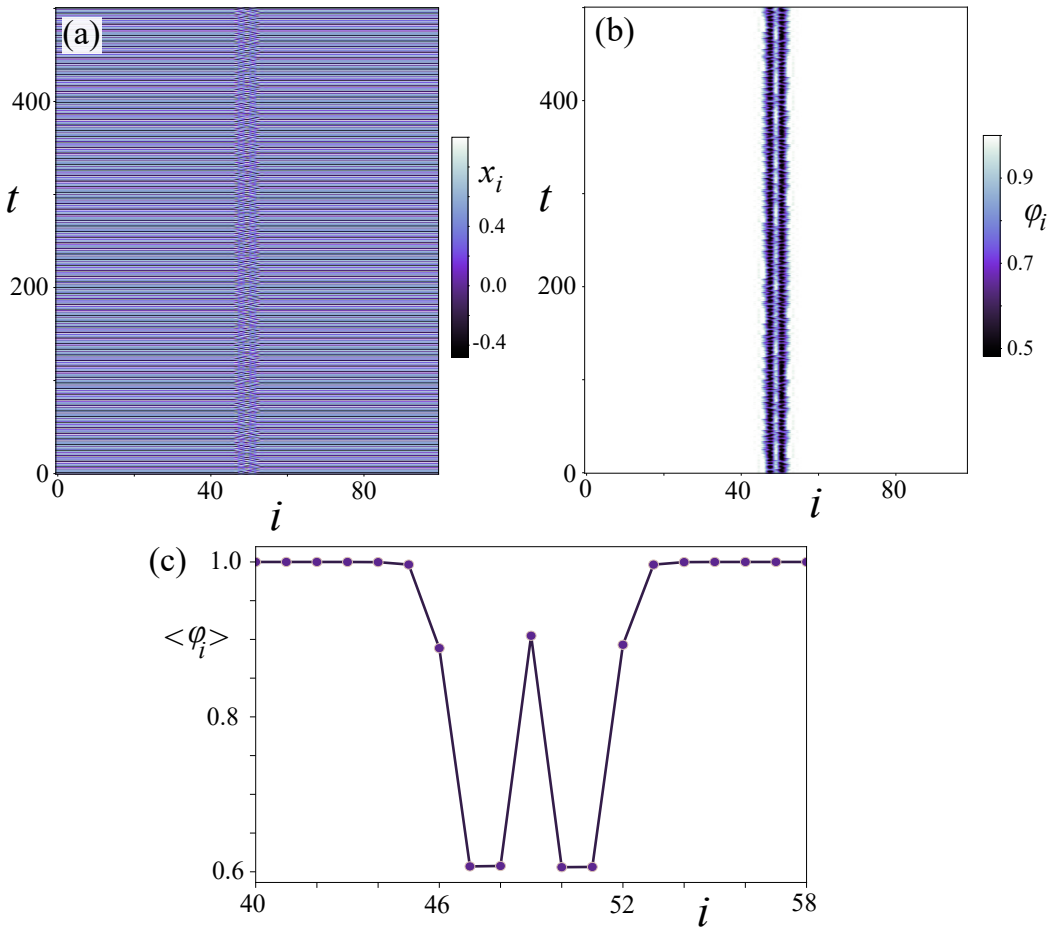

Figure 1.10: Panel (a) shows spatiotemporal diagram for Eq. (1.38). Panel (b) the spatio-temporal evolution of the phase calculated using Eq. (1.10.1. Panel (c) considers the temporal average of the phase at each site.

is synchronized, the phase $\theta_{\mathrm{i}}(t)$ of each site will be 1 for all $\mathrm{i} = 1, \ldots, N$ and time t. Thus, we can calculate the level of synchronization of the system by taking the Kuramoto order parameter

$$R = \frac{1}{N} \sum_{\mathrm{i}=1}^{N} \theta_{\mathrm{i}}(t) \tag{1.41}$$

or plot directly the spatio-temporal diagram given by Eq. () to identify asynchronous (or incoherent) domains or chimera states, as we can observe in figure 1.10(b).

1.10.2 Chimera states in a continuous time system

In the literature, we can find a great variety of chimeras in continuous systems. However, most appear thanks to combining systems with complex dynamics and typically non-local or complex couplings (through complex networks). However, a much simpler and more paradigmatic example is given by the Duffing oscillator system coupled to first neighbors

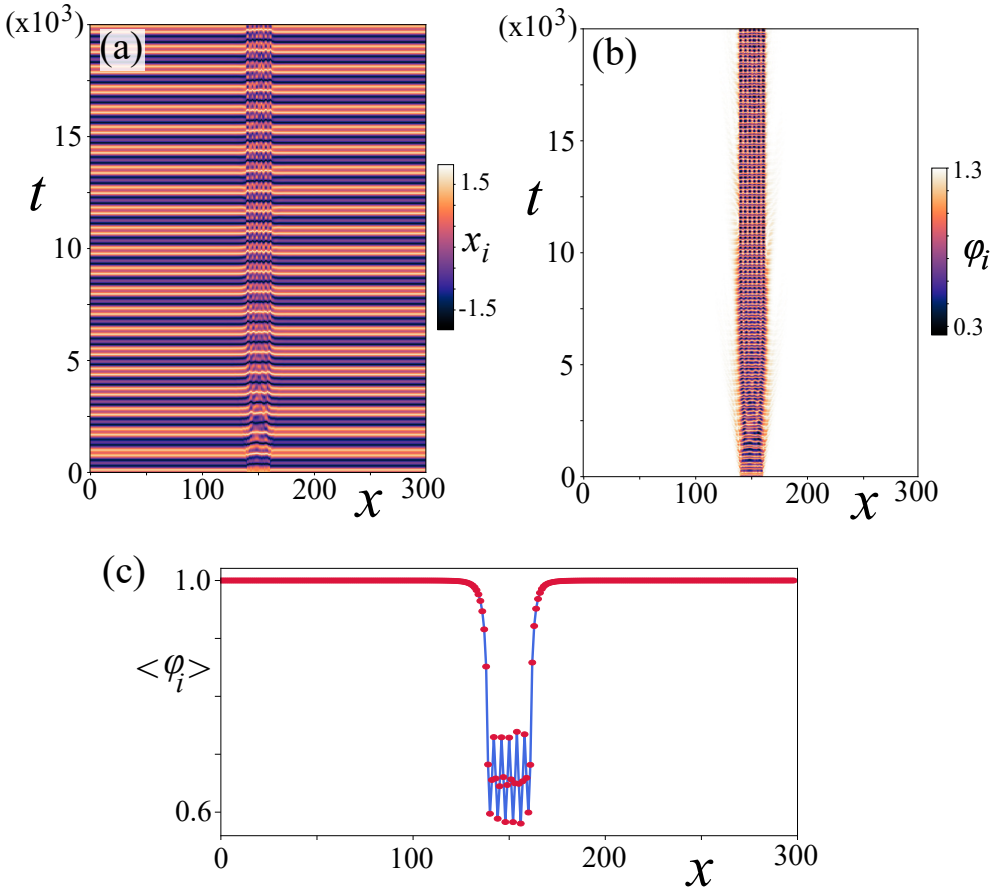

Figure 1.11: Chimera states exhibited by the Duffing system given by Eq. (1.42)

and reported in [77]. Such a system is defined by

$$\frac{\mathrm{d}}{\mathrm{d}t^2}x_n(t) = -x_n + \alpha x_n^3 - x_n^5 - \mu\frac{\mathrm{d}}{\mathrm{d}t}x_n + \gamma\cos(\omega t) + \kappa(x_{n+1} - 2x_n + x_{n-1}), \tag{1.42}$$

where $x_n(t)$ accounts for the displacement of the n-th oscillator with a unit natural frequency, $n = 1, \ldots, N$ characterizes the number of oscillators, μ is the friction coefficient, γ defines the amplitude of the periodic external forcing of frequency ω and κ is the coupling parameter. A chimera state for the YYY parameter values is shown in Figure 1.11.

1.11 LCLV Experiment: A nonvariational setup

Through all the research devoted to the realization of the present manuscript, an experimental setup protagonize almost all application of our theoretical work. Such setup is composed by a liquid cristal light valve (LCLV) with an optical feedback, characterized extensively by [78, 79, 80]. This setup contains a LCLV inserted in an optical feedback loop as is shown in Figure 1.13.

At the same time, the LCLV is composed by a nematic liquid–crystal film sandwiched in

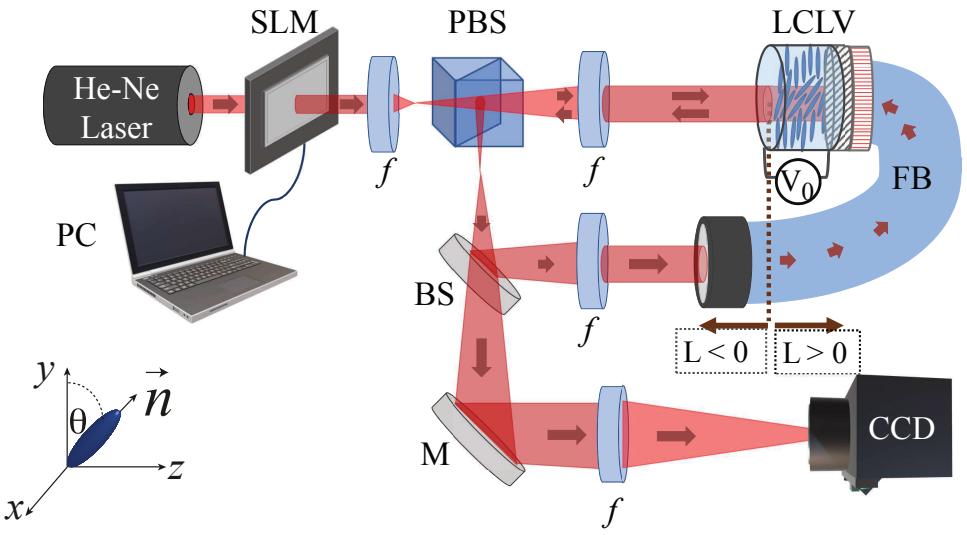

Figure 1.12: Schematic representation of a liquid crystal light valve with optical feedback. SLM denotes the spatial light modulator. PBS corresponds to the polarizing beam splitter, LCLV is the liquid cristal light valve, FB is the fiber bundle that reinject the light reaching the photoconductor. BS accounts for the beam splitter, M for a mirror, each f in a lense, L accounts for the difraction lenght and the camera that capture all the liquid crystal dynamics is denoted by CCD.

between a glass and a photoconductive plate over which a dielectric mirror is deposed. The liquid–crystal film under consideration is a nematic LC-654, produced by NIOPIK and is characterized by a planarly aligned (nematic director $\vec{n}$ parallel to the walls). It is a mixture of cyano-biphenyls, with a positive dielectric anisotropy $\Delta\varepsilon = \varepsilon_{\parallel} - \varepsilon_{\perp} = 10.7$ and large optical birefringence, $\Delta n = n_{\parallel} - n_{\perp} = 0.2$, where $\varepsilon_{\parallel}$ and $\varepsilon_{\perp}$ are the dielectric permittivities $\parallel$ and $\perp$ to $\vec{n}$, respectively, and $n_{\parallel}$ and are $n_{\perp}$ are the extraordinary ($\parallel$ to $\vec{n}$) and ordinary ($\perp$ to $\vec{n}$) refractive index. The cell have a thickness of d = 15 μm.

The feedback loop is closed by an optical fiber bundle (FB) and is designed in such a way that diffraction and polarization interference are simultaneously present. The optical free propagation length is given by L and it can be varied by a rail system with precision motors installed over the optical table.

Transparent electrodes over the glass plates allow the application of an electrical voltage V_0 across the nematic layer. The photoconductor behaves like a variable resistance, which decreases for increasing illumination.

The light injected in the optical look comes from an expanded He-Ne laser beam, with $\lambda = 633\ nm$, $1\ cm$ transverse diameter and power $I_{in} = 6.5\ mW/cm^2$, linearly polarized along the vertical y-axis. A spatial light modulator (SLM, controlled through an external computer) was placed in the input beam in order to carry out one-dimensional experiments and control the iluminated domain to study for two-dimensional phenomena.

The light which has passed through the liquid–crystal layer and has been reflected by the dielectric mirror experiences a phase shift which depends on the liquid–crystal molecular

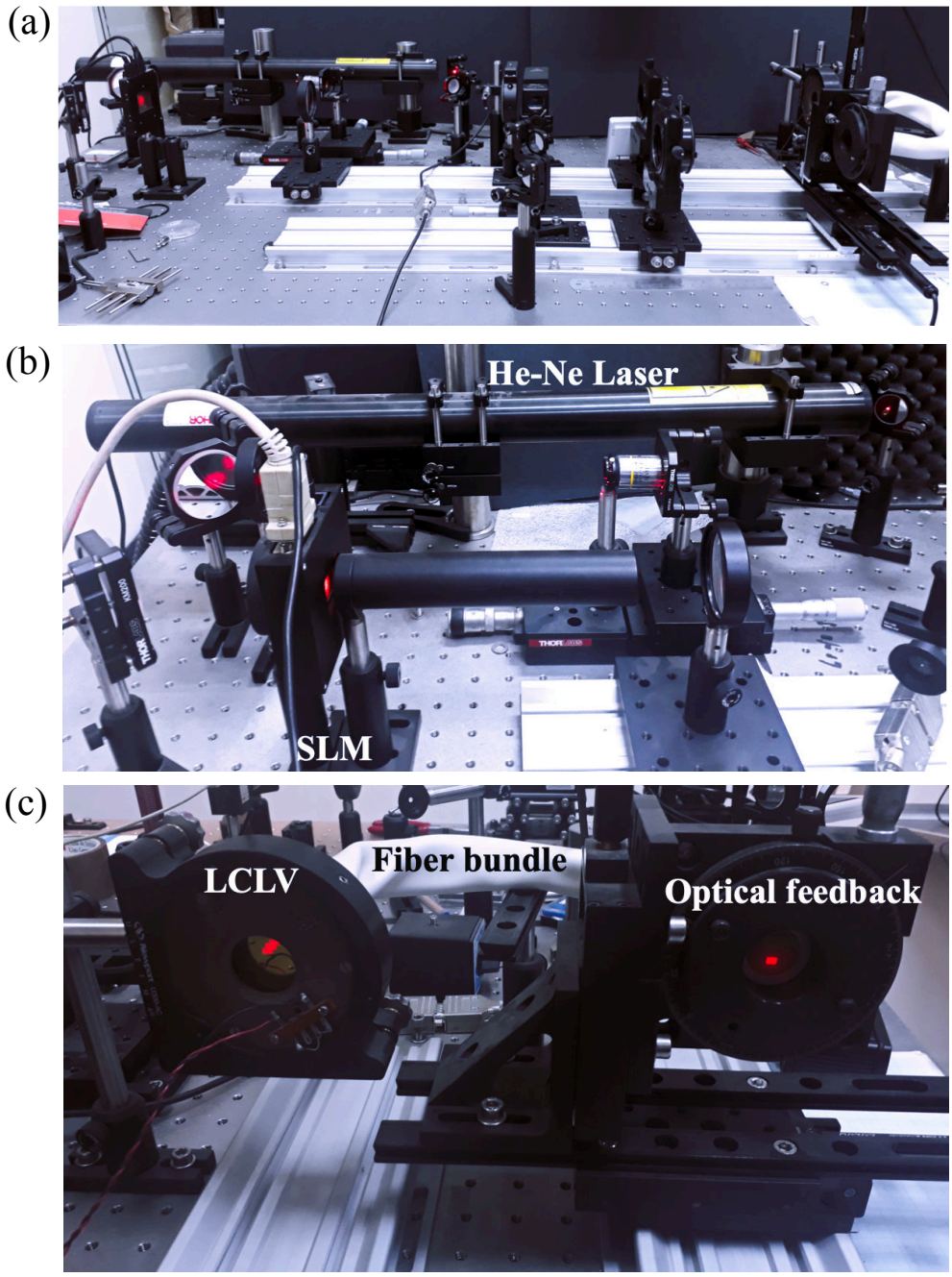

Figure 1.13: Setup pictures.

orientation and, on its turn, modulates the effective voltage that is locally applied to the liquid–crystal sample. Over a critical voltage, molecules tend to orient along the direction of the applied electric field, which changes local and dynamically following the illumination spatial distribution present in the photoconductor wall of the cell. When liquid–crystal molecules reorient, due to their birefringent nature, they induce a refractive index change. Thus, the LCLV acts as a manageable Kerr medium, causing a phase variation $\phi = \beta \cos^2 \theta \equiv 2k\mathrm{d}\Delta n \cos^2 \theta$ in the reflected beam proportional to the intensity of the incoming beam I_w on the photoconductive side, where θ is the longitudinal average of molecular reorientation. Here, $k = 2\pi/\lambda$ is the optical wave number. The system dynamics is controlled by adjusting the external voltage V_0 and free propagation length L.

Chapter 2

Nonvariational Effects in FKPP Fronts

2.1 Introduction

Unlike fronts in variational systems, the propagation of a front in a non-variational one does not follow the minimization of a free energy functional. In this chapter, we want to understand how the propagation of a front that connects a stable state with an unstable one is affected when it is considering non-variational effects. For this purpose, we started by studying the FKPP model, developed in section 1.3, equipped with two non-variational terms, nonlinear advection and nonlinear diffusion. Depending on the parameters that weight the non-variational terms, we show that the propagation speed of the front exhibits a supercritical transition of pulled-pushed type, in a similar way that the reported by [37], and explained in 1.5.2, but in this case driven by non-variational effects.

Then, we consider a theoretical and experimental approach to the results obtained in the nonvariational FKPP model, considering the liquid crystal light valve with an optical feedback setup and model, commented in section 1.11. In this case, the non-variational terms are related to the free diffraction length (or free propagation length). We found that theoretical and experimental results are in good agreement, obtaining a theoretical explanation of the behaviour of FKPP front in this experiment.

2.2 Nonvariational Fisher-Kolmogorov-Petrovskii-Piskunov model

The dynamics of FKPP fronts has been well studyed in the variational scenario, however, it is not the case of nonvariational systems. In order to have a first approach to the nonvariational effects in FKPP fronts, we will consider the following model:

$$\partial_t u = \mu u(1-u) + \nu \partial_{xx} u + bu\partial_{xx} u + c(\partial_x u)^2, \tag{2.1}$$

where b weights the nonlinear diffusion and c the nonlinear advection term. Note that for

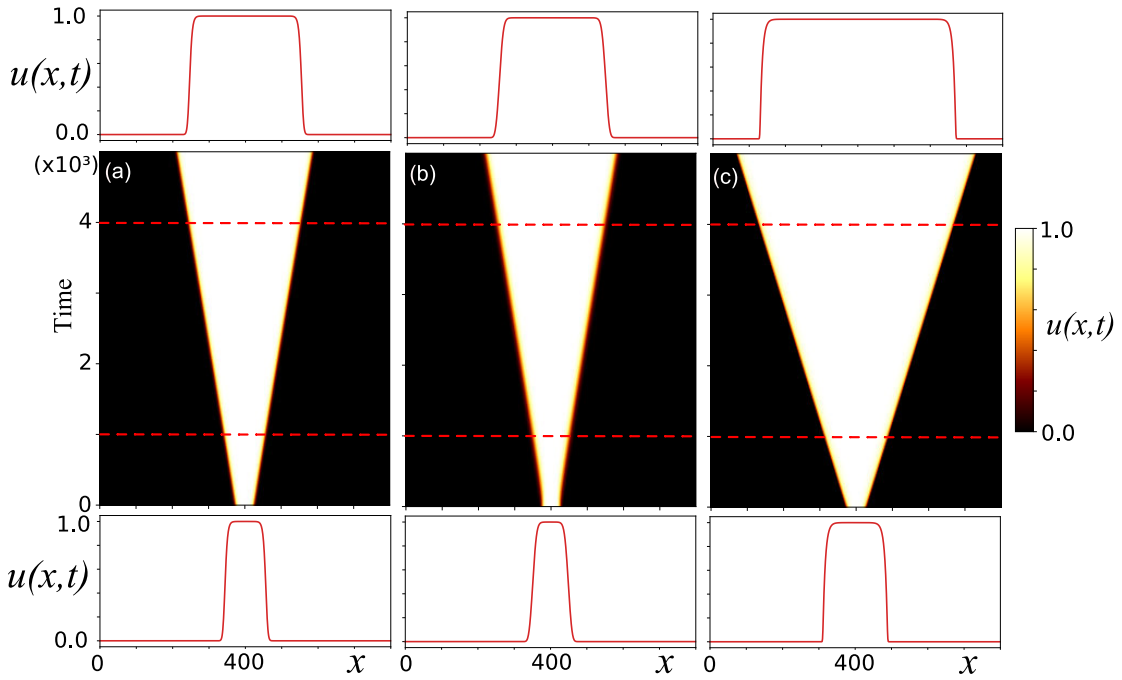

Figure 2.1: Spatiotemporal propagation of fronts solutions into an unstable state for three different values of c. Bottom panels accounts for the same initial condition, and upper panel for the final state, for number of iteration steps $T = 5000$. The nonlinear advection weight take the value $c = 0$ for (a), $c = -15$ for (b) and $c = 15$ for (c).

$b = c = 0$ we recover the classical Fisher equation 1.2, and for $b = 2c$ Eq. 2.1 is variational. In a first approach, we realize a numerical exploration of this model, taking central derivatives to approximate the spatial differential operators, and Runge-Kutta of fourth-order for time integration. To simplify the simulations we take $b = 0$ and let only varying c.

The effects in the front shape are illustrated in figure 2.1. To reveal the effect of non-variational terms in the propagation speed of this kind of fronts we realize a in-depth numerical exploration of equation 2.1 for $b = 0$ and c in range $[-10, 10]$. Obtaining the bifurcation diagram shown in Fig. 2.2

This result reensembles the pulled-pushed transition reported in [37], but unlike this one, our result is driven by non-variational effects. To explain and validate our numerical findings, we develop a theoretical framework based on the perturbation theory. Thus, consider a small nonvariational perturbation, i.e.,

$$\partial_t u = \mu u(1-u) + \nu \partial_{xx} u + \varepsilon(bu\partial_{xx} u + c(\partial_x u)^2) \tag{2.2}$$

where ε small weights the perturbation. From section 1.5.1, we known that the asymptotic speed for the FKPP equation is given by

$$v_{\text{fkpp}} = 2\sqrt{\mu\nu} \tag{2.3}$$

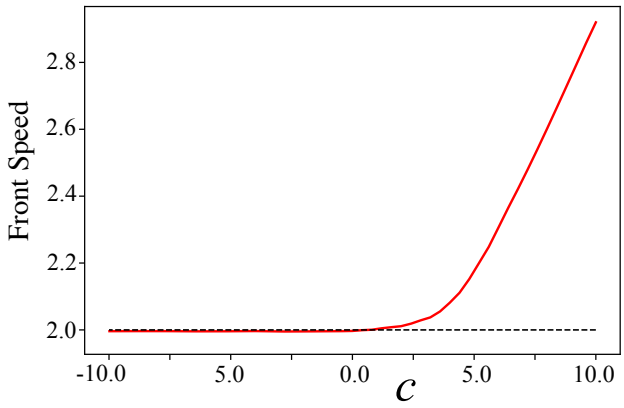

Figure 2.2: Pulled-pushed transition. The figure ilustrates a bifurcation diagram of speed depending on parameter c.

For the nonvariational scenario, $\varepsilon \neq 0$, we consider the system in the comobile system of reference and based on parameter variation method we put the following ansatz,

$$u(x,t) = u_f(x - vt - p(t)) + w(x - vt - p(t)) \tag{2.4}$$

where $v = v_{fkpp}$ is the asymptotic speed, $p(t)$ is a small correction for the position of the front, promoted to a time variable function, and w is a small correction function for the whole shape solution. Putting the system in the co-mobile frame and introducing the ansatz (2.4) in Eq. (2.2) we get from the left side

$$\partial_t u = -\dot{p}(t)\partial_z u_f - v\partial_z u_f - \nu\partial_z w \tag{2.5}$$

and from the right side,

$$\begin{aligned} \partial_t u \;\; = \;\; & \mu u_f - \mu u_f^2 - 2\mu u_f w + \mu w - \mu w^2 + \nu\partial_{zz} u + \nu\partial_{zz} w \\ & + b(u_f\partial_{zz} u_f + u_f\partial_{zz} w + w\partial_{zz} u_f + w\partial_{zz} w \\ & + c((\partial_z u_f)^2 + 2\partial_z u_f\partial_z w + (\partial_z w)^2) \end{aligned} \tag{2.6}$$

Taking up to linear terms in ε and factorizing in w, from Eqs. (2.5) and (2.6) we get

$$[-2\mu u_f + \mu + \nu\partial_{zz} + v\partial_z]w = -[\mu u_f(1 - u_f) + v\partial_z u_f] - \dot{p}(t)\partial_z u_f - b u_f\partial_{zz} u_f - c(\partial_z u_f)^2 \tag{2.7}$$

using the standar ket notation of functional spaces and calling $\mathcal{L} = -2\mu u_f + \mu + \nu\partial_{zz} + v\partial_z$, we obtain

$$\mathcal{L}\,|w\rangle = -b\,|u_f\partial_{zz} u_f\rangle - cket(\partial_z u_f)^2 - \dot{p}(t)\partial_z u_f \tag{2.8}$$

and considering the inner product

$$\langle f | \, g \rangle = \int_{-\infty}^{+\infty} f(z) g(z) \mathrm{d}z \tag{2.9}$$

we can apply the Fredholm alternative or solvability condition we obtain,

$$v_{NV}(b,c) = -b \frac{\langle \phi | \, u_f \partial_{zz} u_f \rangle}{\langle \phi | \, \partial_z u_f} - c \frac{\langle \phi | \, (\partial_z u_f)^2 \rangle}{\langle \phi | \, \partial_z u_f} \tag{2.10}$$

where $\phi := \phi(z) \in \mathrm{Ker}(\mathcal{L}^\dagger)$.

Note that $\mathcal{L}$ is not self adjoint, but we can calculate the adjoint in a straightforward manner, exploring the only one part of $\mathcal{L}$ that is not self-adjoint, obtaining

$$\mathcal{L} = \mathcal{L} - 2\nu \partial_z u_f \tag{2.11}$$

To evaluate numerically the Eq. 2.10, the kernel element ϕ is numerically calculated.

Finally, from Eq. (2.3) and (2.10) we get that the FKPP fronts in Eq. (2.1) there are two contributions for the speed

$$\begin{aligned} v &= v_{FKPP} + v_{NV} \\ &= 2\sqrt{\mu\nu} + v_{NV}(b,c) \end{aligned} \tag{2.12}$$

Note that μ and ν doest not appear explicitly in the expresion for v_{NV}, so we can think that the control of speed in the FKPP fronts can be increased taking $\mu \sim \nu \sim \varepsilon^2$.

The theory above developed is applied then to explain an experimental result showing a front propagation transition induced by diffraction in the liquid crystal light value setup with optical feedback. The diffraction is produced by the free propagation length that we can control by moving the fiber bundle in the light propagation axis, as we can see in Figure.

2.3 Outlook

- The robustness of the FKPP fronts enable us to extend these results to other contexts such as population dynamics, combustion theory.
- In particular, we are interested in understand the non-variational effect in discrete and heterogeneous media.
- These result can be applied in the design of optical switches based on FKPP fronts, but with a faster response due to diffractive effects.
- Control of LCLV displays could be improved, considering nonvariational perish.

Research Article | Vol. 27, No. 9 | 29 Apr 2019 | OPTICS EXPRESS 12391
Optics EXPRESS

Front propagation transition induced by diffraction in a liquid crystal light valve

ALEJANDRO J. ÁLVAREZ-SOCORRO,[1] CAMILA CASTILLO-PINTO,[1] MARCEL G. CLERC,[1] GREGORIO GONZÁLEZ-CORTES,[1] AND MARIO WILSON[2,*]

[1]*Departamento de Física and Millennium Institute for Research in Optics, FCFM, Universidad de Chile, Casilla 487–3, Santiago, Chile*
[2]*CONACYT–CICESE, Carretera Ensenada-Tijuana 3918, Zona Playitas, CP 22860, Ensenada, México*
[*] *mwilson@cicese.mx*

Abstract: Driven optical systems can exhibit coexistence of equilibrium states. Traveling waves or fronts between different states present complex spatiotemporal dynamics. We investigate the mechanisms that govern the front spread. Based on a liquid crystal light valve experiment with optical feedback, we show that the front propagation does not pursue a minimization of free energy. Depending on the free propagation length in the optical feedback loop, the front speed exhibits a supercritical transition. Theoretically, from first principles, we use a model that takes it into account, characterizing the speed transition from a plateau to a growing regime. The theoretical and experimental results show quite fair agreement.

1. Introduction

Front propagation occurs in a wide range of physical contexts such as optics, liquid crystals, granular matter, combustion, population dynamics, chemical reactions, industrial deposition processes, among others [1]. Since the seminal works of Fisher [2] and Kolmogorov, Petrovsky, and Piskunov [3] in genetics and population dynamics, respectively, on traveling fronts (called FKPP fronts) there has been an increasing interest in the study of this phenomenon. The FKPP front solutions are peculiar of connecting a stable state with an unstable one. The propagation speed of these fronts depends on the initial conditions. When the disturbance of the unstable state is bounded, the fronts always propagate with a minimal speed [1]. In liquid crystals, these fronts have been subject of intense research [4–12], since they play a fundamental role in understanding and applicating average molecular reorientations through light.

Theoretically, the interface dynamics is well understood for variational systems, i.e., systems whose dynamics is described in terms of the minimization of a physical quantity (free energy, entropy, and so forth). In contrast, nonvariational systems do not pursue a minimization of a free energy. Indeed, front propagation into an unstable state does not follow a minimization principle and its dynamics is less explored. However, front propagation between two stable states in nonvariational systems has been analyzed by Álvarez-Socorro et al [11]. The non-variationality is a generic characteristic of nonequilibrium systems [13, 14].

This work aims to investigate the effect of diffraction in the front propagation between two domains of average molecular orientations in a liquid crystal light valve (LCLV) with optical feedback. The diffraction produced by the free propagation length L governs the nonvariational effects. Based on a LCLV subjected to optical feedback experiment, front propagation into an unstable state is studied. Depending on diffraction, front speed exhibits a supercritical transition. Theoretically, using the nonlinear elasticity and optics theory, a model that accounts for this transition is inferred. The front speed exhibits a transition from a plateau to a growing regime. The theoretical and experimental results show a quite fair agreement.

#360003 https://doi.org/10.1364/OE.27.012401
© 2019 Received 12 Feb 2019; revised 14 Mar 2019; accepted 14 Mar 2019; published 17 Apr 2019

Optics EXPRESS

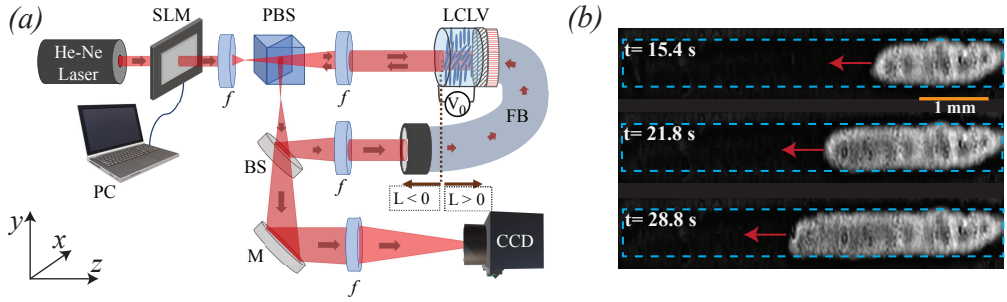

Fig. 1. Liquid crystal light valve with optical feedback. (a) Schematic representation of the experimental setup. The LCLV is composed of a nematic liquid crystal film sandwiched in between a glass and a photoconductive plate-over with a dielectric mirror. The light is injected through a He-Ne laser beam, f stands for lenses with a focal length of 25 cm, PBS represents a polarizer beam splitter, BS a beam splitter, and SLM is a spatial light modulator controlled by a computer (PC). The feedback loop is closed by an optical fiber bundle (FB). The free propagation length is denoted by L and the image in the LCLV is captured through a CCD camera. (b) Temporal snapshots sequence of the front propagation showed in the LCLV taken at $L = 0$ mm, $\nu = 1$ KHz, and $V_0 = 2.62\ V_{rms}$. Dark and light area account for different average molecular orientations, respectively. The dashed rectangles mark the illuminated region.

2. Experimental setup

A simple optical system that presents multistability and nonvariational dynamics is the LCLV with optical feedback [5–11]. Figure 1 schematically shows the used experimental setup. This setup consists in a liquid crystal cell with a photo-sensitive wall inserted in an optical feedback loop closed by an optical fiber bundle (FB). This experimental array has been designed in order to have coexisting diffraction and polarization interferences. The LCLV structure is composed by a nematic liquid crystal film between a glass with transparent electrodes (ITO) and a photoconductive plate with a deposited dielectric mirror. The liquid crystal film under consideration is a nematic LC-654, produced by NIOPIK, planar aligned, with thickness $d = 15\mu m$. It is a mixture of cyanobiphenyls, with a positive dielectric anisotropy. The optical free propagation length L drives the nonvariational effects. ITO electrodes are used to apply an external voltage V_0 across the nematic layer. The photoconductor resistance is inversely proportional to applying illumination [6].

Light suffers a phase shift while crossing the LCLV depending on the nematic director state (i.e., the average liquid crystal molecular orientation), which, in its time, modulates the effective local voltage applied to the nematic sample. Once a critical voltage is passed, the director tends to orient along the direction of the applied electric field, this reorientation changes local and dynamically, following the spatial distribution of light present in the photoconductor. Another effect of this molecular change, due to the liquid crystal birefringent nature, is an induced effective refractive index change. Thus, the LCLV can be seen as an active Kerr medium, causing a phase variation $\phi = \beta cos^2\theta = 2kd\Delta ncos^2\theta$ in the reflected beam proportional to the incoming beam intensity I_w on the photoconductive side, θ stands for the longitudinal average of the molecular reorientation [6] and $k = 2\pi/\lambda$ represents the wavenumber. An expended He-Ne laser beam, $\lambda = 633$ nm and power $I_{in} = 6.5$ mW/cm^2, linearly polarized along the vertical y axis is used as light source to illuminate the LCLV. Quasi-one-dimensional conditions are reached thanks to a computer controlled spatial light modulator (SLM) placed in the input beam. All experiments were conducted at a working temperature of 28°C. The voltage V_0 and free propagation length L are the control parameters.

Optics EXPRESS

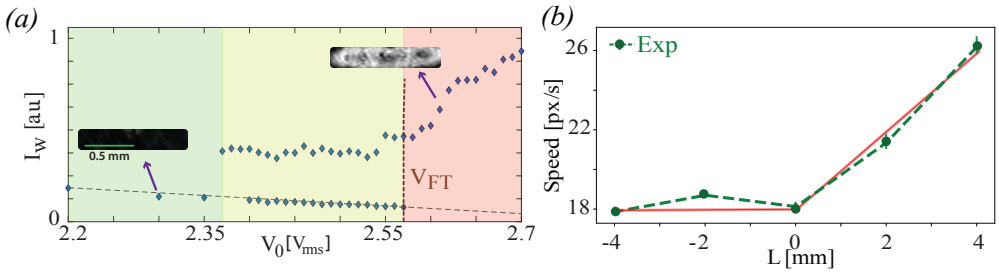

Fig. 2. Experimental characterization of the bifurcation diagram and the front propagation transition. (a) Bifurcation diagram observed in the LCLV with optical feedback constructed at $L = 0$ mm. The points account for the intensity of the reflected light by the LCLV as a function of the applied voltage V_0. The system exhibits three regions, two monostable and one bistable between the planar and reoriented state. V_{FT} accounts for the critical value of the reorientation instability, *the Fréedericksz transition*. The insets stand for respective snapshots obtained in the indicated voltages. (b) Front speed as a function of free propagation length L at $V_0 = 2.62V_{rms}$. The points account for the front speed measured in pixels per second. The dashed line is the union between consecutive experimental points. The continuous curve stands for the trend line of the experimental points.

2.1. *Experimental characterization of front propagation into an unstable state*

Thanks to the use of the spatial light modulator, a bidimensional channel is illuminated on the liquid crystal light valve of dimensions 6 mm long by 0.9 mm wide [cf. Fig. 1(b)]. By changing the voltage V_0 applied to the liquid crystal film and monitoring the evolution of light intensity that goes through the LCLV employing a CCD camera, we characterize the bifurcation diagram of the director reorientation transition. Figure 2(a) shows the bifurcation diagram obtained. For small voltage $V_0 < V_{FT}$, when the molecules are not reoriented, a little light is transmitted in the optical feedback, which corresponds to the channel being dark [see inset in Fig. 2(a)]. The critical voltage from which the molecules begin to reorient is designated by V_{FT}. On the contrary, when the director is reoriented, the transmitted light increases and then the channel turns light gray. Note that the transition of average molecular reorientation of the LCLV with optical feedback is of the first order type [4, 8]. Indeed, the transition exhibits an abrupt color change. Besides, when the voltage is varied, a hysteresis loop is observed between the average molecular configurations. The hysteresis region is between the two monostable regions.

To study the front propagation into an unstable state, we follow the strategy: initially applied voltage is small ($V_0 \ll V_{FT}$). Hence, the initial configuration is planar, and it is stable. Subsequently, the applied voltage is increased above a critical value of reorientation bifurcation ($V_0 = 2.62V_{rms} > V_{FT}$). Then the planar state becomes unstable, and the reoriented alignment is stable. The reoriented state (light color) starts to invade the planar alignment from the edges or imperfections of the channel. Figure 1(b) shows a sequence of snapshots of the observed front propagation. From the recording of the front propagation, its speed is determined. Subsequently, by changing the position of the optical fibers bundle, we can change the value of the free propagation length L, which is the distance where light diffraction occurs in our experimental setup. Figure 2(b) shows the front speed as a function of the free propagation length L at fixed applied voltage V_0. Unexpectedly, we infer that for small and negative L, the front speed is modified slightly, but for L positive this speed increases and is significantly modified. Therefore, we experimentally observe that the front speed exhibits a transition between a plateau and a growing regime. It is worthy to note that L does not change the relative stability between the director configurations, but rather changes the coupling between the molecular arrangements.

Optics EXPRESS

The origin of the front propagation transition will be elucidated in the next section.

3. Theoretical model of the LCLV with optical feedback

Based on the elastic theory, dielectric effects, and optical feedback, close to the Fréedericksz transition V_{FT}, the average molecular reorientation is given by the dimensionless model [4, 8, 11]

$$\partial_t u = \mu u + \beta u^2 + \gamma u^3 - u^5 + \partial_{xx} u + b u \partial_{xx} u + c(\partial_x u)^2, \tag{1}$$

where x and t, respectively, account for the spatial transverse coordinate and time. The order parameter $u(x,t)$ is the amplitude of the critical mode of the average molecular reorientation. μ is the bifurcation parameter, $\mu \ll 1$, that accounts for the competition between the electric and elastic force, which is proportional to $(V_0 - V_{FT})/V_{FT}$. β is a phenomenological parameter that accounts for the pretilt induced by the anchoring in the walls of the liquid crystal layer. The cubic and quintic terms stand for the competition between elastic and electrical forces induced by optical feedback [8]. The diffusion term $\partial_{xx} u$ describes the transverse elastic coupling. The coefficients b and c account, respectively, for the diffusion and the nonlinear advection. These two terms are proportional to the free propagation length L and have the same sign. Indeed, when $L = 0$, $b = c = 0$. Higher-order terms in Eq. (1) are ruled out by the scaling analysis, since $u \sim \mu^{1/4}$, $\gamma \sim \mu^{1/2}$, $\beta \sim \mu^{3/4}$, $\partial_x \sim \mu^{1/2}$, and $b \sim c \sim 0$. The previous model (1) satisfies an equation that is governed by the minimization of free energy $\mathcal{F}[u, \partial_x u]$ at $L = 0$, that is,

$$\partial_t u = -\frac{\partial \mathcal{F}}{\partial u}, \tag{2}$$

where $\mathcal{F} = \int dx[-\mu u^2/2 - \beta u^3/3 - u^4/4 + u^6/6 + (\partial_x u)^2/2]$. However, the diffraction effect generates that the diffusion and the nonlinear advection allow the emergence of permanent dynamics, such as spatiotemporal chaos [15] or oscillatory behaviors [7]. This type of behaviors is incompatible with a dynamic governed by a principle of minimization. The methodology of how to derive the parameters $\{\mu, \beta, b, c\}$ and the relation with the physical parameters are given by Clerc et al [8, 11].

The term proportional to β breaks the reflection symmetry of the amplitude u. This effect always renders the reorientation transition into a discontinuous instability with a small hysteresis. Note that positive and negative equilibria exist for $\beta, \mu > 0$. Besides, the negative values of the amplitude $u(x,t)$ has no physical sense. Figure 3 shows the bifurcation diagram of model Eq. (1). This model is characterized by exhibiting a first-order bifurcation when $\mu = 0$. Then the system presents a hysteresis region between two monostable regions. Note that this bifurcation diagram is qualitatively similar to that observed experimentally [cf. Fig. 2(a)].

An ideal region to study fronts into an unstable state is $\mu > 0$. In this region of parameter space, there are fronts between the planar unstable u_p and stable reoriented state u_+. Figure 4 shows the front propagation for $\mu > 0$. In order to study the effects of nonvariational terms, we consider a front solution initially with $b = c = 0$ and at a given time ($t = 20$) we activate the nonvariational effects ($b = 0$ and $c = -30$). In the variational regime, the minimal front speed v_{min} is determined by the linear terms, *marginal criterion* [1], which has the explicit expression $v_{min} = 2\sqrt{\mu}$. Indeed, if the values of the nonlinear parameters are changed, the front speed does not change. From Fig. 4, we infer that when the nonvariational terms are included the profile of the front is modified. The front solution exhibited a readjust of the spatial profile where the front suffers a back propagation, and after this readjust, the front solution acquires a form with which it spreads with the marginal speed. Figure 4 depicts the front profiles without and with the influence of non-variational terms. Unexpectedly, although the front profile is markedly modified, the front speed remains constant.

To analyze how the front speed is modified as a function of the non-variational terms, we have numerically measured the front speed as a function of $b = c = L$. This is consistent with

Optics EXPRESS

the functional dependence of the parameters as a function of the free propagation length L. Figure 3(b) summarizes the front speed as a function of the free propagation length L. We observe that for free negative propagation lengths the front speed is constant and as it increases the numerical precision it tends to the front speed predicted by the marginal criterion [see Fig. 3(b)]. It is well-known that numerical discretization effects modify this speed [12]. For free positive propagation lengths, we observed that the speed of the front grows linearly with L. Hence, we observe that the front speed presents a transition between a plateau and a growing regime, which is consistent with experimental observations [cf. Figs. 2(b) and 3(b)]. Indeed, the system exhibits a transition between fronts where its speed is determined by the marginal criterion (pulled front [1]) to fronts where the nonlinear terms determine the speed, nonlinear criterion (pushed front [1]). A pulled-pushed transition of fronts, with a speed transition diagram similar to that shown in Fig. 3(b), is well-known in a cubic reaction-diffusion model when the nonlinear terms are modified [16]. To figure out how the front speed is modified by the presence of the nonvariational terms a perturbative analysis can be performed.

4. Analytical and numerical analysis of the front speed

Due to the transition between pulled-pushed fronts occurs at free propagation length $L = 0$, we can consider the nonlinear diffusion and advection terms as perturbatives ($b, c \ll 1$). Let us consider $u_f(x - v_0 t)$ as the front solution for the unperturbed problem of Eq. (1) with $b = c = 0$, where $v_0 \geqslant 2\sqrt{\mu}$ is the front speed. To calculate the front speed for the perturbed problem, we consider the following ansatz,

$$u(x,t) = u_f\left(z \equiv x - v_0 t - \dot{P}(t)\right) + w(x - v_0 t - p(t)), \tag{3}$$

where z is the coordinate in co-moving system, $\dot{P}$ and w account for the correction of the front speed and the profile function, respectively. Moreover, $\dot{P}$ and w are of order of $b \sim c \sim \epsilon$, where $\epsilon \ll 1$ is a small control parameter. Introducing the ansatz (3) in Eq. (1) and leaving only the

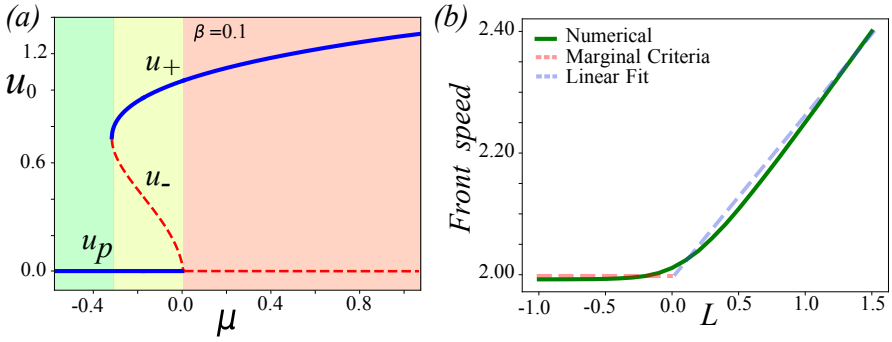

Fig. 3. Characterization of bifurcation diagram and front speed of model Eq. (1). (a) Bifurcation diagram of Eq. (1). Equilibrium amplitude u_o as a function of the parameter μ for fixed β. The continuous and dashed curves account for stable and unstable equilibrium, respectively. These curves were obtained by solving the algebraic equation $0 = \mu u_0 + \beta u_0^2 + u_0^3 - u_0^5$; u_p, u_-, and u_p account for the upper, middle, and lower equilibrium branch, respectively. The system exhibits three regions, two monostable and one bistable. (b) Front speed as a function of free propagation length L. The continuous curve shows the front speed of model Eq. (1) obtained numerically with $\mu = 1.0$, $\beta = 0.1$, and $b = c = L$. The dashed horizontal curve accounts for the minimal front speed using the marginal criterion $v_{min} = 2\sqrt{\mu}$.

Optics EXPRESS

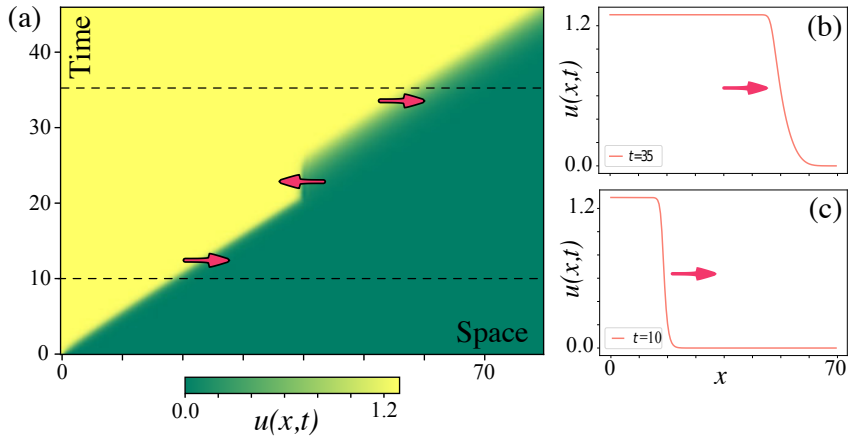

Fig. 4. Front propagation into an unstable state of model Eq. (1). (a) Spatiotemporal evolution of amplitud of critical model $u(x,t)$ of model Eq. (1) by $\mu = 1.0$, $\beta = 0.1$, and $b = 0$. Temporal evolution of the front propagation after ($c = 0, t < 20$) and before ($c = -30$, $t \geqslant 20$) consider the nonvariational advection term. The arrows show the direction of front propagation in the respective periods. Front profiles at $t = 35$ (b) and $t = 10$ (c), respectively.

terms up to ϵ order, after straightforward calculations, we get the linear equation

$$\mathcal{L}w = -\dot{p}(t)\partial_z u_f - b u_f \partial_{zz} u_f - c(\partial_z u_f)^2, \tag{4}$$

where the linear operator has the form $\mathcal{L} \equiv [\mu + 2\beta u_f + 3u_f^2 - 5u_f^4 + v\partial_z + \partial_{zz} + b(u_f\partial_{zz} + \partial_{zz}u_f) + 2c\partial_z u_f \partial_z]$. To solve this linear equation, we use the Fredholm alternative or solvability condition [17] and obtain

$$\dot{p}(t) = v_{nv} \equiv -b\frac{\langle\phi|\, u_f\partial_{zz}u_f\rangle}{\langle\phi|\,\partial_z u_f\rangle} - c\frac{\langle\phi|\,(\partial_z u_f)^2\rangle}{\langle\phi|\,\partial_z u_f\rangle}, \tag{5}$$

where the symbol $\langle f|\, g\rangle \equiv \int_{-\infty}^{\infty} f(z)g(z)dz$ and the function $\phi(z)$ belong to the kernel of the adjoint operator of $\mathcal{L}$, which is independent of diffraction effect. The ϕ function is only accessible numerically. As a matter of fact, the correction of the front speed of nonvariational origin is proportional to the free propagation length L. When $L > 0$ (L<0), the previous integrals are negative (positive) then v_{nv} is positive (negative). Hence the front speed has two contributions, one of variational origin given by the linear criterion and another nonlinear one given by the nonvariational effects, i.e.,

$$v = v_0 + v_{nv}. \tag{6}$$

Therefore, from this perturbative analysis, it is expected that the front speed increases or decreases with the free propagation length L. However, numerically only for positive diffraction, the front speed increases linearly with the free propagation length [cf. Fig. 3(b)]. Figure 5 shows how the speed and the profile of the front are modified when the free propagation length L is changed. Therefore, for $L > 0$, the system exhibits an excellent qualitative agreement with Eq. (5). Despite the above calculation, for $L < 0$, the speed of the front remains at the minimum speed in contradiction with Eq. (6). This behavior can be understood in the following way, the front modifies its asymptotic profile (cf. Figs. 4 and 5), which increases its propagation speed given by the linear criterion [18], so that it cancels the speed decrement induced by the nonvariational effects. Then, the previous perturbative analysis cannot be valid because the base

Optics EXPRESS

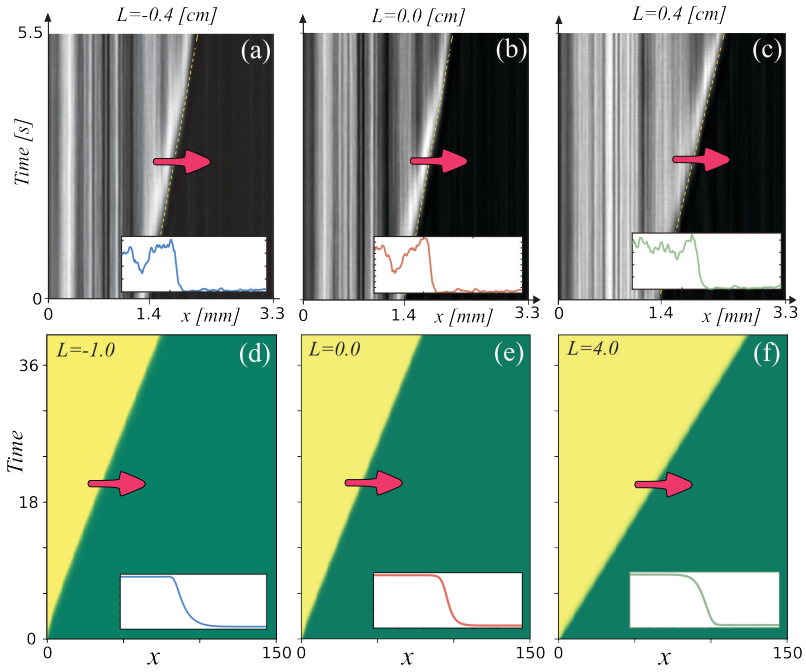

Fig. 5. Spatiotemporal propagation of front solution into an unstable state for different free propagation lengths. Top panels account for front propagation in the experiment by $L = -0.4$ cm (a), $L = 0.0$ cm (b), and $L = 0.4$ cm (c), respectively. Bottom panels stand for the front propagation of model Eq. (1) by $\mu = 1.0$, $\beta = 0.1$, and free propagation length $L = -1.0$ (d), $L = 0$ (e), and $L = 4.0$ (f). The insets account for the front profile at a given instant experimentally and numerically, respectively.

solution is modified and it is not a small correction. This mechanism explains the origin of the pull-pushed transition of fronts, when the disturbance tries to decrease the fronts speed, it adapts their shape to maintain the minimum speed. Also, when the disturbance increases the speed of propagation, the system responds by increasing the speed. Therefore, the system exhibits a pull-pushed transition of fronts at zero free propagation length in the optical feedback loop, $L = 0$, when the disturbance begins to increase the minimum speed. Spatiotemporal diagrams are an adequate tool to characterize this type of transitions. When the parameters are modified, if the speed remains unchanged, pulled fronts will not produce any noticeable change in the spatiotemporal diagram, however when fronts are pushed, the spatiotemporal diagram presents a change in the front position slope (cf. Fig. 5).

5. Conclusions and remarks

Based on a liquid crystal light valve experiment with optical feedback, we have investigated a mechanism of speed control in interfaces connecting a stable with an unstable state based on varying the free propagation length, showing a supercritical transition from a plateau speed to an increasing speed regime, *pulled-pushed front transition*. Experimental and theoretically, we have characterized this supercritical transition, which result shows quite fair agreement.

The possibility of having different molecular domains with varying effective refractive indices, being able to manipulate the speed between these domains, allows the opportunity of having switches between electronic and optical elements. The presented results open the possibility of

Optics EXPRESS

novel photonic devices in such direction.

Funding

Comisión Nacional de Investigación Científica y Tecnológica (2015-21151618, 2017-21171672); Fondo Nacional de Desarrollo Científico y Tecnológico (1180903).

Acknowledgments

A. J. Álvarez-Socorro, C. Castillo, M. G. Clerc and G. González-Cortés gratefully acknowledge the financial support from the Millennium Institute for Research in Optics (MIRO).

References

1. W. van Saarloos, "Front propagation into unstable states," Phys. Reports **386**(2), 29–222 (2003).
2. R. A. Fisher, "The wave of advance of advantageous genes," Ann. Eugen. **7**, 353–369 (1937).
3. A. N. Kolmogorov, I. G. Petrovskii, and N. S. Piskunov, "A study of the diffusion equation with increase in the amount of substance, and its application to a biological problem," Bull. Mosc. Univ. Math. Mech. **1**(6), 1–26 (1937). Reprinted in: V. M. Tikhomirov (ed.), *Selected Works of A. N. Kolmogorov, vol. 1* (Kluwer, 1991). Also in: O. A. Oleinik, *I. G. Petrowsky Selected Works, Part II* (Gordon and Breach, 1996).
4. M. G. Clerc, S. Residori, and C. S Riera, "First-order Fréedericksz transition in the presence of light-driven feedback in nematic liquid crystals," Phys. Rev. E **63**, 060701 (2001).
5. S. Residori, A. Petrossian, T. Nagaya, C. S. Riera, and M. G. Clerc, "Fronts and localized structures in a liquid crystal-light-valve with optical feedback," Phys. D: Nonlinear Phenom. **199**, 149–165 (2004).
6. S. Residori, "Patterns, fronts and structures in a liquid crystal-Light-Valve with optical feedback," Phys. Reports **416**, 201–272 (2005).
7. M. G. Clerc, A. Petrossian, and S. Residori, "Bouncing localized structures in a liquid crystal light-valve experiment," Phys. Rev. E **71**, 015205 (2005).
8. M. G. Clerc, T. Nagaya, A. Petrossian, S. Residori, and C. S. Riera, "First-order Frédericksz transition and front propagation in a liquid crystal light valve with feedback," Euro Phys. J. D **28**(3), 435–445 (2004).
9. F. Haudin, R. G. Elias, R. G. Rojas, U. Bortolozzo, M. G. Clerc, and S. Residori, "Driven Front Propagation in 1D Spatially Periodic Media," Phys. Rev. Lett. **103**, 128003 (2009).
10. F. Haudin, R. G. Elias, R. G. Rojas, U. Bortolozzo, M. G. Clerc, and S. Residori, "Front dynamics and pinning-depinning phenomenon in spatially periodic media," Phys. Rev. E **81**, 056203 (2010).
11. A. J. Álvarez-Socorro, M. G. Clerc, G. González-Cortés, and M. Wilson, "Nonvariational mechanism of front propagation: Theory and experiments," Phys. Rev. E **95**, 010202 (2017).
12. K. Alfaro-Bittner, M. G. Clerc, M. García-Nustes, and R. G. Rojas, "π-kink propagation in the damped Frenkel-Kontorova model," Europhys. Lett. **119**(4), 40003 (2018).
13. I. Prigogine and G. Nicolis, *Self-Organization in Non-Equilibrium Systems,* (John Wiley & Sons Inc., 1997).
14. H. Haken, *Advanced synergetics: Instability hierarchies of self-organizing systems and devices,* (Springer Verlag, 1983).
15. M. G. Clerc, G. González-Cortés, V. Odent, and M. Wilson, "Optical textures: characterizing spatiotemporal chaos," Opt. Express **24**(14), 15478–15485 (2016).
16. K. P. Hadeler and F. Rothe, "Travelling fronts in nonlinear diffusion equations," J. Math. Biol. **2**(3), 251–263 (1975).
17. E. I. Fredholm, "Sur une classe d'equations fonctionnelles," Acta Math. **27**, 365-390 (1903).
18. D. Mollison, "Spatial contact models for ecological and epidemic spread," J. R. Statist. Soc. B **39**, 283-326 (1977).

Chapter 3

Novariational Effects in Normal Fronts

3.1 Introduction

As was mentioned in chapter 1, the dynamics of macroscopic systems are described typically by a small number of variables as a consequence of coarse-grained and averaging approaches reaching nonvariational or non gradient systems. Instead of chapter 2, here we will consider the nonvariational effect in fronts connecting two stable states, bistable fronts. Thus, we will investigate the dynamics of front solutions corresponding to

$$\partial_t u = -\frac{\delta V(u)}{\delta u} + \varepsilon F_{NV} = F_V + \varepsilon F_{NV} \tag{3.1}$$

where $F_V(u)$ correspond to a bistable potential and F_{NV} correspond to the nonvariational part of the energy functional [81] and ε is a control parameter of the nonvariational effects. For $\varepsilon = 0$, we have a variational bistable system whose dynamics is characterized by relaxation to reach equilibrium, following the minimization of the energy functional associated. Moreover, as was explained in chapter 1, in a front connecting two stable states, the energetically favorable states will invade the less favorable.

In this chapter, we will try to answer the following question, *what are the mechanism for front propagation in nonvariational systems?*. We address the above question by considering two generic bistable systems. The first one is given by

$$\partial_t u = -\alpha u + \beta u^2 - u^3 + \partial_{xx} u + \varepsilon F_{NV}, \tag{3.2}$$

that can be deduced for $\varepsilon = 0$ from the Landau-De Gennes theory for liquid crystals [82], and the second one, for $\varepsilon = 0$ known as the spatially-extended pitchfork normal form or bistable model, given by

$$\partial_t u = \eta + \mu u - u^3 + \partial_{xx} u + \varepsilon F_{NV}, \tag{3.3}$$

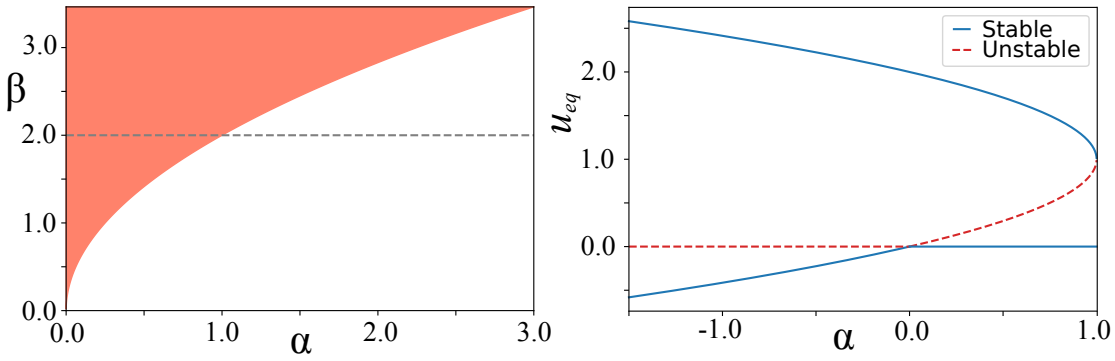

Figure 3.1: Bifurcation diagrams for Landau DeGennes equation.

This equation has been appear in a wide range of contexts, ranging from population dynamics to liquid crystals [79, 80]. The nonvariational part F_{NV} is a mix of nonlinear diffusion and nonlinear advection, and is given by

$$F_{NV} = bu\partial_{xx}u + c(\partial_x u)^2, \tag{3.4}$$

The weight coefficients b and c enable us to control the nonvariational effects in the dynamical behavior of the system. In the following section, we will characterize the front solutions for the Eq. (3.2), their speed, and the relationships between Eqs. (3.2) and (3.3).

3.2 Landau-De Gennes System

To characterize the homogeneous steady states of the system, we start finding it by solving

$$-\alpha u + \beta u^2 - u^3 = 0, \tag{3.5}$$

whose roots are given by

$$u_0 = 0, u_\pm = \frac{\beta \pm \sqrt{\beta^2 - 4\alpha}}{2}, \tag{3.6}$$

in the liquid crystal theory, the states u_0 and u_+ correspond to the isotropic and nematic phases, respectively. Note that the three solutions coexist only for $\beta^2 - 4\alpha > 0$. Calculating the derivative of the scalar field and evaluating in the equilibrium we obtain for $u_0 = 0$,

$$\frac{\partial F}{\partial u}\Big|_{u=u_0} = -\alpha + 2\beta u - 3u^2\Big|_{u=u_0} = -\alpha, \tag{3.7}$$

i.e., u_0 is stable for $\alpha > 0$ and unstable for $\alpha < 0$. For $u_\pm = \frac{\beta \pm \sqrt{\beta^2 - 4\alpha}}{2}$ we obtain that

$$\frac{\partial F}{\partial u}\Big|_{u=u_\pm} = -\alpha + 2\beta u - 3u^2\Big|_{u=u_\pm} = -\frac{\beta^2 \mp \beta\sqrt{\beta^2 - 4\alpha}}{2} + 2\alpha, \tag{3.8}$$

Notice that there exist a region where u_- is unstable, characterized by the inequality

$$-\frac{\beta^2 + \beta\sqrt{\beta^2 - 4\alpha}}{2} + 2\alpha > 0, \tag{3.9}$$

Such region is characterized in figure 3.1 and correspond to the region defined by the inequalities $\alpha > 0; \beta = 0$ that describes a straight line in the $\alpha\beta$-parameter space and $\alpha > 0; \beta > 2\sqrt{\alpha}$.

3.2.1 Analytical Solution and Front Speed Calculation

To obtain the analytical solutions corresponding to the interface connecting the coexisting stable states of Eq. (3.2) for $\varepsilon = 0$, we look for a traveling solution of the form $u := u(x - vt)$, where v is the propagation speed. Putting the system in the co-moving frame $z = x - vt$, Eq. (3.2) takes the Newton-like form

$$\partial_{zz}u + v\partial_z u - \alpha u + \beta u^2 - u^3 = 0, \tag{3.10}$$

We can assume that $\alpha \geq 0$, accounting for the region where both $u_0 = 0$ and u_+ are both stable. and inspired in the tanh-method [83, 84], we considering a parameter-dependent solution of first order in tanh, connecting the states 0 and $A = u_+$ [85]

$$u(z) = \frac{A}{2}(\tanh(Bz) + 1), \tag{3.11}$$

substituting the proposed solution (3.11) in Eq. 3.10 we obtain:

$$\begin{aligned} -AB^2\tanh(Bz)(1 - \tanh^2(Bz)) + \frac{vAB(1 - \tanh^2(Bz))}{2} - \frac{\alpha A(1 + \tanh(Bz))}{2} \\ + \frac{\beta A^2}{4} + \frac{A^2\tanh(Bz)\beta}{2} + \frac{A^2\beta\tanh^2(Bz)}{4} - \frac{A^3}{8} - \frac{3A^3\tanh(Bz)}{8} \\ - \frac{3A^3\tanh^2(Bz)}{8} - \frac{A^3\tanh^3(Bz)}{8} = 0, \end{aligned} \tag{3.12}$$

and factorizing in $\tanh(Bz)$ we get

$$
\begin{aligned}
&(AB^2 - \frac{A^3}{8})\tanh^3(Bz) \\
&+(-\frac{1}{2}vAB + \frac{1}{4}\beta A^2 - \frac{3}{8}A^3)\tanh^2(Bz) \\
&+(-AB^2 - \frac{1}{2}\alpha A + \frac{1}{2}\beta A^2 - \frac{3}{8}A^3)\tanh(Bz) \\
&+\frac{vAB}{2} - \frac{\alpha A}{2} + \frac{\beta A^2}{4} - \frac{A^3}{8} = 0.
\end{aligned} \tag{3.13}
$$

This drive us to the following system of equations

$$
\begin{cases}
AB^2 - \frac{A^3}{8} &= 0 \\
-\frac{1}{2}vAB + \frac{1}{4}\beta A^2 - \frac{3}{8}A^3 &= 0 \\
-AB^2 - \frac{1}{2}\alpha A + \frac{1}{2}\beta A^2 - \frac{3}{8}A^3 &= 0 \\
+\frac{vAB}{2} - \frac{\alpha A}{2} + \frac{\beta A^2}{4} - \frac{A^3}{8} &= 0,
\end{cases} \tag{3.14}
$$

From the first equation we get $B = \sqrt{2}/4A$ and substituting on the third one we get

$$
\alpha - \beta A + A^2 = 0, \tag{3.15}
$$

whose solutions are

$$
A = \frac{\beta \pm \sqrt{\beta^2 - 4\alpha)}}{2} = u_{\pm}. \tag{3.16}
$$

Note that for solutions connecting $u_0 = 0$ and $u = u_+$ corresponding to the isotropic and nematic phases respectively in the Landau–De Gennes model, we get from the second equation of the system (3.14) an analytical expression for the speed of this front, given by

$$
-(\beta\sqrt{2\beta^2 - 8\alpha} + (\beta^2 - 2\alpha)\sqrt{(2)})v + (3\alpha - \beta^2)\sqrt{\beta^2 - 4\alpha} - \beta^3 + 5\alpha\beta = 0, \tag{3.17}
$$

and solving for v we obtain,

$$
v = \frac{(\beta - 3\sqrt{\beta^2 - 4\alpha})\sqrt{2}}{4}. \tag{3.18}
$$

Figure 3.2 show the front speed for $\beta = 2$.

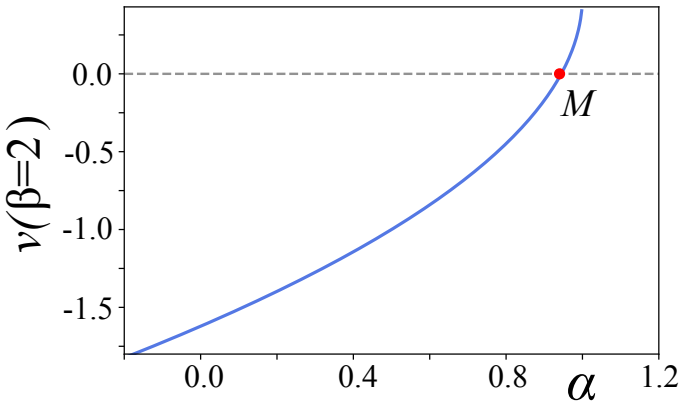

Figure 3.2: Front speed calculated from Eq. (3.18) for $\beta = 2$. The letter M corresponds to the Maxwell point where both equilibrium are energetically equivalent.

3.2.2 Nonvariational contribution to the speed

To calculate nonvariational contribution to the front speed, we consider the ansatz $u = u_0 + w$ where w is an small error function, with $w \ll \partial_t w \sim b \sim c \ll 1$. Putting the system in the co-mobile frame $z = x - (v_0 + v_{nv})t$, substituting in the equation 3.2, and keeping the terms up to order w, from the left side we get

$$\partial_t u_0 = -v_0 \partial_z u_0 - v_{nv} \partial_z u_0, \tag{3.19}$$

and from the right side

$$\begin{aligned} \partial_t u_0 \quad = \quad & (-\alpha u_0 + \beta u_0^2 - u_0^3 + \partial_{zz} u_0) \\ & + (-\alpha + 2\beta u_0 - 3u_0^2 + \partial_z z) w \\ & + b u_0 \partial_{zz} u_0 + c(\partial_z u_0)^2. \end{aligned} \tag{3.20}$$

Note that the first two terms in the right side of Eqs. (3.19) and (3.20) are canceled, because they satisfy the variational equation. Letting $\mathcal{L} = [-\alpha + 2\beta u_0 - 3u_0^2 + \partial_z z]$, we obtain the following simplified equation

$$\mathcal{L}\,|w\rangle = -v_{NV} \partial_z u_0 - b u_0 \partial_{zz} u_0 - c(\partial_z u_0)^2, \tag{3.21}$$

and applying solvability condition or Fredholm alternative, i.e., bracketing the above equation with $\langle\phi| \in \mathrm{Ker}\mathcal{L}$, we get

$$V_{NV} = \frac{-b\,\langle\phi|\, u_0 \partial_{zz} u_0\rangle - c\,\langle\phi|\,(\partial_z u_0)^2\rangle}{\langle\phi|\,\partial_z u_0\rangle}, \tag{3.22}$$

Then, the front contribution to the speed is proportional to the nonvariational terms. It is nothewortly that both terms generates speeds with oposite direction, vanishing particularly when $b = c = 0$ and for $b = 2c$.

3.2.3 Swift-Hohenberg from Landau De-Gennes

Another archetypal equation from pattern formation is the Swift-Hohenberg equation. In this section we will explore a connection between two models (3.3) and (3.2). Thus, given the Eq. (3.2), consider the variable change $u = u_0 + w$. From the Landau-De Gennes Equation (3.2) we get

$$\partial_t w = -w^3 + (\beta - 3u_0)w^2 + (2\beta u_0 - 3u_0^2 - \alpha)w + \beta u_0 - u_0^3 - \alpha u_0, \tag{3.23}$$

Assigning $u \to w$ in the Swift-Hohenberg equation, and comparing it with Eq. (3.2.3) we get

$$\begin{cases} \eta &= \beta u_0 - u_0^3 - \alpha u_0 \\ \mu &= 2\beta u_0 - 3u_0^2 - \alpha \\ 0 &= \beta - 3u_0, \end{cases} \tag{3.24}$$

obtaining $u_0 = \beta/3$ and from the fist two equations of the system (3.25) we obtain the following relations

$$\begin{cases} \eta &= \dfrac{2}{27}\beta^3 - \dfrac{1}{3}\alpha\beta \\ \\ \mu &= \dfrac{\beta^2}{3} - \alpha, \end{cases} \tag{3.25}$$

reaching in this way to the Swift-Hohenberg equation.

Note that, although both equation (3.3) and (3.2) appears to be equivalent, they are not from the physical point of view. A simple way to illustrate this point is observing that for the Swift-Hohenberg equation, moving the η parameter outside of the stable region eliminates any of the stable states (nematic or isotropic depending of the direction where η is varied). Nevertheless, in the model (3.11) only the nematic phase can disappear.

3.3 2D Fronts

Fronts occur commonly in nature, at least in two-dimensional systems. Some examples are the fire propagation in a forest, spreading of a virus, growth of a population, magnetization domains in a magnetic media, or the orientation domains in a LCLV. Thus, we are interested in nonvariational effects in fronts in dimensions larger than one and how nonvariational effects interact with 2D properties like the front's curvature.

To study these effects, we will consider the Nonvariational Turing-Swift-Hohenberg equation given by

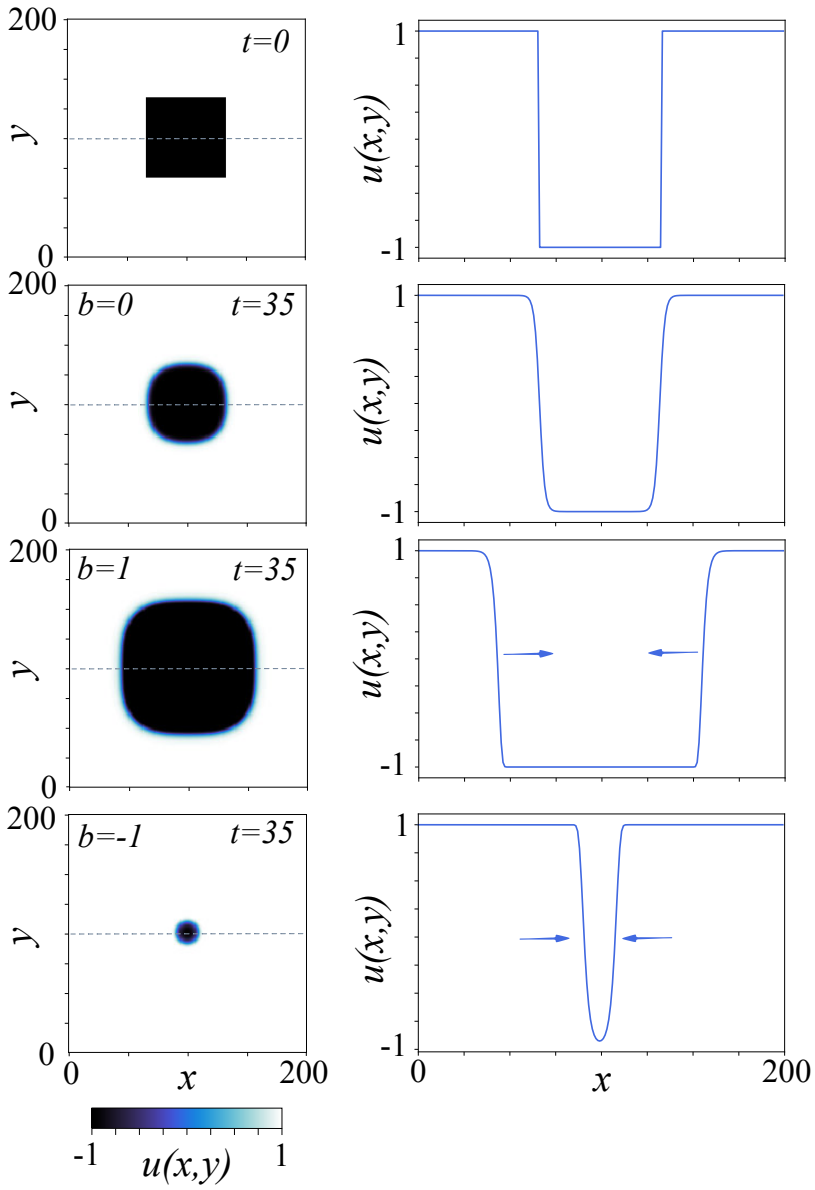

Figure 3.3: Curvature and nonvariational effects in 2D fronts.

$$\partial_t u = \eta + \mu u - u^3 + \nabla^2 u + bu\nabla^2 u + c(\boldsymbol{\nabla} u)^2 \tag{3.26}$$

Inspired in the numerical results, shown in the top panels of Fig. 3.3, we the simplified scenario of a circular front $u = u(r - vt)$ for the model given by Eq. 3.26, where $\{r, \theta\}$ are the radial and angular coordinates respectively. Taking into account that we can write in polar coordinates the laplacian and gradient operators,

$$\nabla^2 u = \partial_{rr} u + \frac{1}{r}\partial_r u + \frac{1}{r^2}\partial_{\theta\theta} u \tag{3.27}$$

and,

$$(\nabla u)^2 = (\partial_r u)^2 + \frac{1}{r^2}(\partial_\theta u)^2 \tag{3.28}$$

we can study the front propagation speed towards a radial axis, where all the derivatives in θ vanishes. Then, the equation 3.26 takes the simple 1D form

$$\partial_t u = \eta + \mu u - u^3 + \partial_{rr} u + \frac{1}{r}\partial_r u + bu\Big(\partial_{rr} u + \frac{1}{r}\Big) + c(\partial_r u)^2 \tag{3.29}$$

furthermore, it can be simplified more considering $r = R_0 + x$, where R_0 is the initial radius and x the position of the front. If R_0 is sufficiently larger, we can approximate $1/(R_0 + x) \approx 1/R_0$, obtaining in this way

$$\partial_t u = \eta + \mu u - u^3 + \partial_{xx} u + bu\partial_{xx} u + c(\partial_x u)^2 + \frac{1 + bu}{R_o}\partial_x u \tag{3.30}$$

Note that this equation is similar to the Eq. 3.3, nevertheless it comes with two advective terms, a linear and a nonlinear one. In order to calculate the speed, we follow the same strategy done in section 3.2.2. Putting the system in the co-moving frame, we obtain the following relation to the contributions to the front speed:

$$-v_{NV}\partial_z u_0 = \Big[\mu - 3u_0^2 + \partial_{zz} u_0 + \frac{\partial_z}{R_0}\Big] w + bu_0\partial_{zz} u_0 + c(\partial_z u_0)^2 + \frac{\partial_z u_0}{R_0} + \frac{bu_0\partial_z u_0}{R_0} \tag{3.31}$$

Letting $\mathcal{L} = [\mu - 3u_0^2 + \partial_{zz} u_0 + \partial_z/R_0]$, using the bracket notation $w(z = x - vt) := |w\rangle$ and rewriting the above equation, we get

$$\mathcal{L}\,|w\rangle = -v_{NV}\partial_z u_0 - bu_0\partial_{zz} u_0 - c(\partial_z u_0)^2 - \frac{\partial_z u_0}{R_0} - \frac{bu_0\partial_z u_0}{R_0} \tag{3.32}$$

and applying solvability condition or Fredholm alternative, i.e., bracketing the above equation with $\langle\phi| \in \mathrm{Ker}\mathcal{L}$, we get

$$V_{NV} = -\frac{(b\,\langle\phi|\,u_0\partial_{zz}u_0\rangle + c\,\langle\phi|\,(\partial_z u_0)^2\rangle + 1/R_0\,\langle\phi|\,\partial_z u_0\rangle + b/R_0\,\langle\phi|\,u_0\partial_z u_0\rangle)}{\langle\phi|\,\partial_z u_0\rangle} \tag{3.33}$$

obtaining in this way, a pure nonvariational contribution (similar to the 1D contribution), a contribution from the curvature (given by the thrid derivative term), and another contribution that is a mixed term that comes from the curvature and the nonvariational terms.

3.4 Outline

- Normal fronts are extremely common in physical systems.
- In addition, the generality of the spatially-extended pitchfork normal form suggests that this strategy of control of front propagation can be applied in several contexts, ranging from liquid crystals up to opinion dynamics in social media.
- We are also interested in understanding how nonvariational effects are affected by discreteness and heterogeneity in the spatial coupling.
- These results could be of particular interest in designing optical and magnetical storage devices and computational processors.
- In the LCLV experiment mentioned in the above chapter, close to a bistability point, we could apply the theory to predict and control the molecular re-orientation front propagation direction and speed using a nonvariational perish.
- In high dimensions, we exhibit several contributions to the normal front speed, namely, the difference of energy, the curvature effect (also known as Gibbs-Thompson effect), the nonvariational effect, and a mixed term depending on both curvature and nonvariational terms.

PHYSICAL REVIEW E **95**, 010202(R) (2017)

Nonvariational mechanism of front propagation: Theory and experiments

A. J. Alvarez-Socorro,[1] M. G. Clerc,[1] G. González-Cortés,[1] and M. Wilson[1,2]
[1]*Departamento de Física, FCFM, Universidad de Chile, Casilla 487-3, Santiago, Chile*
[2]*CONACYT–CICESE, Carretera Ensenada-Tijuana 3918, Zona Playitas, CP 22860, Ensenada, México*
(Received 13 June 2016; revised manuscript received 14 December 2016; published 17 January 2017)

Multistable systems exhibit a rich front dynamics between equilibria. In one-dimensional scalar gradient systems, the spread of the fronts is proportional to the energy difference between equilibria. Fronts spreading proportionally to the energetic difference between equilibria is a characteristic of one-dimensional scalar gradient systems. Based on a simple nonvariational bistable model, we show analytically and numerically that the direction and speed of front propagation is led by nonvariational dynamics. We provide experimental evidence of nonvariational front propagation between different molecular orientations in a quasi-one-dimensional liquid-crystal light valve subjected to optical feedback. Free diffraction length allows us to control the variational or nonvariational nature of this system. Numerical simulations of the phenomenological model have quite good agreement with experimental observations.

DOI: 10.1103/PhysRevE.95.010202

The coexistence between different equilibria is a characteristic property of nonequilibrium systems [1–3]. Inhomogeneous initial conditions caused by, e.g., inherent fluctuations of macroscopic systems, generate spatial domains which are separated by domain walls. These interfaces are known as front interfaces, domain walls, or wave fronts [3,4]. Interfaces between these metastable states appear in the form of propagating fronts and give rise to rich spatiotemporal dynamics [5]. Front dynamics has been observed in several contexts, such as walls separating magnetic domains, liquid-crystal phases, fluidized granular states, chemical reactions, and solidification and combustion processes, to mention a few. Indeed, front solutions are robust phenomena ranging from chemistry and biology to physics. Moreover, these propagative fronts can be regarded as particle-type solutions, i.e., they can be characterized by a set of continuous parameters such as position, core width, and so forth. Front propagation depends on the nature of the states that are being connected. For example, in the case of a front connecting a stable and an unstable state, its speed is not unique but is determined by the initial conditions [6]. This scenario changes for a front connecting two stable uniform states. For variational or gradient systems, the most stable state invades the other one, in order to minimize its nonequilibrium energy or Lyapunov functional [7]. Likewise, there is only one point in the parameter space for which the front is motionless, the Maxwell's point.

Due to a time-scale separation of the microscopic variables, the dynamics of macroscopic systems is described by a small number of variables (coarse-graining process), which generally satisfy nonvariational or nongradient equations [2–4]. In this framework, walls connecting two equivalent vectorial fields through spontaneous symmetry breaking can spread according to a given chirality of the vector field [8]. This mechanism, the nonvariational Ising-Bloch transition, is well known [9]. A deeper understanding of front propagation in macroscopic systems out of equilibrium will open the possibilities for applications in nonequilibrium crystal growth, operation of nonequilibrium magnetic and optical memories, control of nonequilibrium chemical reactions, to mention a few.

The aim of this Rapid Communication is to show that front solutions in scalar field models generically propagate based on two mechanisms: (i) the energy difference between states, and (ii) nonvariational effects. Considering a simple nonvariational bistable model, we show analytically and numerically that front propagation is led by nonvariational dynamics. A quasi-one-dimensional liquid-crystal light valve (LCLV) experiment with optical feedback allows us to evidence nonvariational front propagation between different molecular orientations. Free diffraction lengths allow us to control the variational or nonvariational nature of this optical system. A phenomenological model for small free diffraction lengths is derived. Numerical simulations of this model have quite good agreement with experimental observations.

Simple bistable model. Let us consider a bistable model

$$\begin{aligned}\partial_t u &= \eta + \mu u - u^3 + \partial_{xx} u + \epsilon[c(\partial_x u)^2 + bu\partial_{xx} u] \\ &= -\frac{\delta F}{\delta u} + \epsilon F_{NV},\end{aligned} \tag{1}$$

where the scalar field $u(x,t)$ is an order parameter that accounts for an imperfect pitchfork bifurcation [4], μ is a bifurcation parameter, η stands for the asymmetry between the equilibria, ϵ is an small parameter, $\epsilon \ll 1$, that controls the nonvariational force $F_{NM} \equiv c(\partial_x u)^2 + bu\partial_{xx} u$, $\{c,b\}$ account for, respectively, nonlinear convective and diffusive terms, and the functional

$$F \equiv \int dx \left[V(u) + \frac{(\partial_x u)^2}{2} \right], \tag{2}$$

where $V(u) \equiv -\eta u - \mu u^2/2 + u^4/4$ is a potential. Notice the above model is invariant under spatial reflection symmetry ($x \to -x$). Moreover, model (1) is variational when $b = 2c$.

For $\epsilon = 0$, the above model (1) becomes a variational one. This model has two stable equilibria for η small and positive μ, $u = \pm\sqrt{\mu} + O(\eta)$, represented by $\{\mathcal{A},\mathcal{B}\}$. Figure 1 depicts the potential $V(u)$ for different values of η. A nontrivial solution of this variational model is front waves, $u_F(x - vt) \approx \pm\sqrt{\mu}\tanh[\sqrt{\mu/2}(x - vt)] + O(\eta)$, that connect these two equilibria [7]. The middle and lower panels of Fig. 1 show the profiles of the front solutions and their respective spatiotemporal evolutions. Notice that fronts propagate at a constant speed. The location and the region of the space where

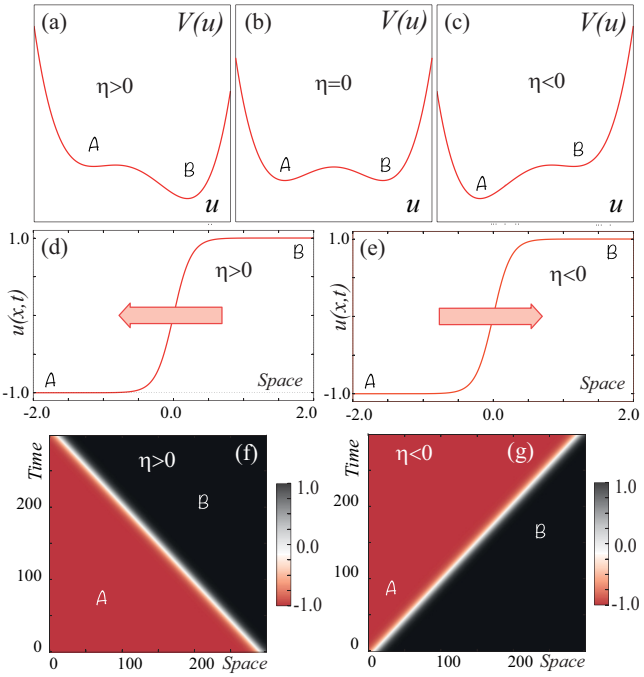

FIG. 1. Front propagation in the bistable variational model Eq. (1) with $\epsilon = 0$. The upper panels represent the potential $V(u)$ for different values of η, (a) $\eta = 0.2$, (b) $\eta = 0$, and (c) $\eta = -0.2$, with $\mu = 1.0$. The middle and lower panels illustrate the front profiles and their respective spatiotemporal evolutions for (d), (f) $\mu = 1.0$, $\eta = 0.3$, and (e), (g) $\eta = -0.3$.

the front has a greater variation is known as the front position and core, respectively. In the pioneering work of Pomeau [7], it was shown that the front speed v is ($\eta \ll 1$)

$$v = v_V \equiv \frac{V(\mathcal{A}) - V(\mathcal{B})}{\int_{-\infty}^{\infty}(\partial_x u_F)^2 dx} \approx \frac{3\sqrt{2}}{2\mu}\eta. \tag{3}$$

Hence, the front speed is proportional to the energy difference between the equilibria and the front core shape (denominator). Indeed, the most energetically favorable state invades the least favorable one (cf. Fig. 1). Likewise, when both states have the same energy, $\eta = 0$, the front is motionless, which corresponds to Maxwell's point. Therefore, for variational systems the mechanism of front propagation is the energy difference between the connected equilibria.

In the case where nonvariational terms are considered, $\epsilon \neq 0$, the above scenario changes drastically. To figure out these changes, we consider model Eq. (1) at Maxwell's point and the nonvariational terms as perturbative, $\epsilon \ll 1$. Then, in this limit we can use the following ansatz for the front solution, $u(x,t) = u_F(x - vt) + w(x - vt, v)$, where w is a small adjustment function, which is of order of ϵ. Using this ansatz in Eq. (1), linearizing in w, and imposing solvability conditions, we get

$$v_{NV} \equiv \epsilon \frac{c\int_{-\infty}^{+\infty}(\partial_x u_F)^3 dx + b\int_{-\infty}^{+\infty} u_F \partial_x u_F \partial_{xx} u_F dx}{\int_{-\infty}^{+\infty}(\partial_x u_F)^2 dx}. \tag{4}$$

Then, the front speed is proportional to the nonvariational terms. Notice that a similar method to obtain the speed of

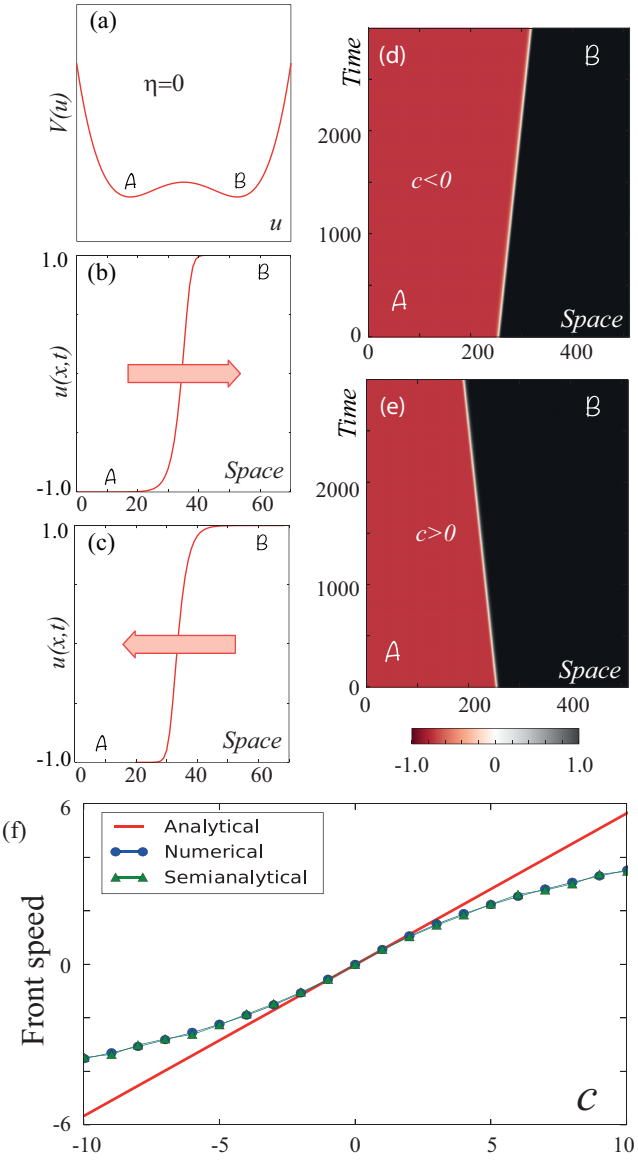

FIG. 2. Nonvariational front propagation model Eq. (1) at Maxwell's point ($\eta = 0, \epsilon = 1$, and $\mu = 1$). (a) Potential $V(u)$. Front profiles at a given instant for (b) positive $c = 3$, (c) negative $c = -3$, and $b = 0$. (d) and (e) represent the spatiotemporal evolutions of front solutions with positive and negative parameters c respectively and $b = 0$. (f) Dimensionless front speed as a function of parameter c. Points account for the numerical front speed obtained from Eq. (5) with $b = 0$, $\eta = 0$, and $\epsilon = 1$, the solid straight line is obtained from the analytical formula $v_{NV} \approx (2c - b)\epsilon\mu\sqrt{2}/5$, and the curve is obtained using formula (4) with a numerical front profile u_F.

the propagative front was used to characterize the Ising-Bloch transition [9].

From the above formula, we can conclude that the mechanism generating the spread of this front is only the front shape. Namely, the front core shape [$\partial_x u_F \sim O(1)$] determines the propagation speed and not the energy difference between equilibria. The above expression can be approximated by $v_{NV} \approx (2c - b)\epsilon\mu\sqrt{2}/5$. Figure 2 illustrates the nonvariational front propagation observed from the model (1) for

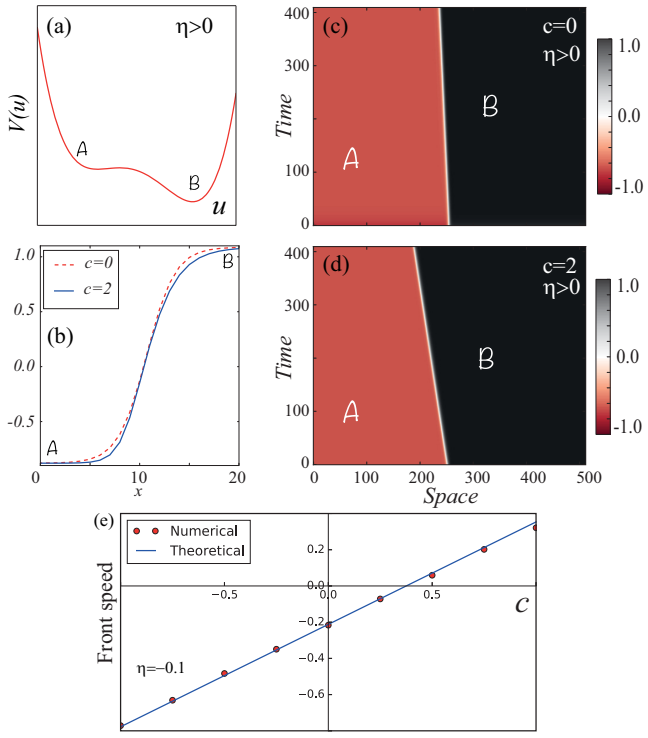

FIG. 3. Front propagation model Eq. (1) with $\eta = 0.3$ and $\mu = 1$. (a) Potential $V(u)$. (b) Front profiles for zero (dashed line) and positive (solid line) c and $b = 0$. (c) and (d) represent the spatiotemporal evolutions of the front solution with zero and positive parameter c. (e) Dimensionless front speed as a function of parameter c. Points account for the numerical front speed and continuous curve $v = v_V + v_{NV}$.

different values of parameter c. For small c, the system exhibits quite good agreement with the above approximation. For large c, we can use formula (4) with u_F obtained numerically. This semianalytical approach has quite fair agreement (cf. Fig. 2). Notice that nonlinear convection and diffusion are opposite effects for front speed. The front becomes motionless when the system is variational ($b = 2c$).

When considering the general case of asymmetry between equilibria ($\eta \neq 0$) and the presence of nonvariational terms, the front speed is determined by the two mechanisms discussed above, i.e., the front speed is $v = v_V + v_{NV}$. Figure 3 depicts the front propagation in the generic case. A comparison between numerical simulations and theoretical results shows quite good agreement (cf. Fig. 3). Note that there is always a point in the parameter space where the front is motionless ($v_V = -v_{NV}$), but which does not correspond to equal energy between states.

Liquid-crystal light valve with optical feedback. A simple physical system that exhibits nonvariational behaviors and multistability is a LCLV with optical feedback [10–13]. This setup contains a LCLV inserted in an optical feedback loop (see Fig. 4). The LCLV is composed of a nematic liquid-crystal film sandwiched in between a glass and a photoconductive plate over which a dielectric mirror is deposited (see Ref. [11] and references therein). The feedback loop is closed by an optical fiber bundle (FB) and is designed in such a way that diffraction and polarization interferences are simultaneously present. The optical free propagation length is given by L.

The liquid-crystal film under consideration is planarly aligned (nematic director $\vec{n}$ parallel to the walls), with a thickness $d = 15$ μm. The liquid crystal filling the LCLV is a nematic LC-654, produced by NIOPIK. It is a mixture of cyanobiphenyls, with a positive dielectric anisotropy $\Delta\varepsilon = \varepsilon_\parallel - \varepsilon_\perp = 10.7$ and a large optical birefringence $\Delta n = n_\parallel - n_\perp = 0.2$, where $\varepsilon_\parallel$ and $\varepsilon_\perp$ are the dielectric permittivities $\parallel$ and $\perp$ to $\vec{n}$, respectively, and $n_\parallel$ and are $n_\perp$ are the extraordinary ($\parallel$ to $\vec{n}$) and ordinary ($\perp$ to $\vec{n}$) refractive indices [14]. Transparent electrodes over the glass plates allow for the application of an electrical voltage V_0 across the nematic layer. The photoconductor behaves as a variable resistance, which decreases for increasing illumination. The light which has passed through the liquid-crystal layer and has been reflected by the dielectric mirror experiences a phase shift which depends on the liquid-crystal molecular orientation and, at its turn, modulates the effective voltage that is locally applied to the liquid-crystal sample. Over a critical voltage, the molecules tend to orient along the direction of the applied electric field,

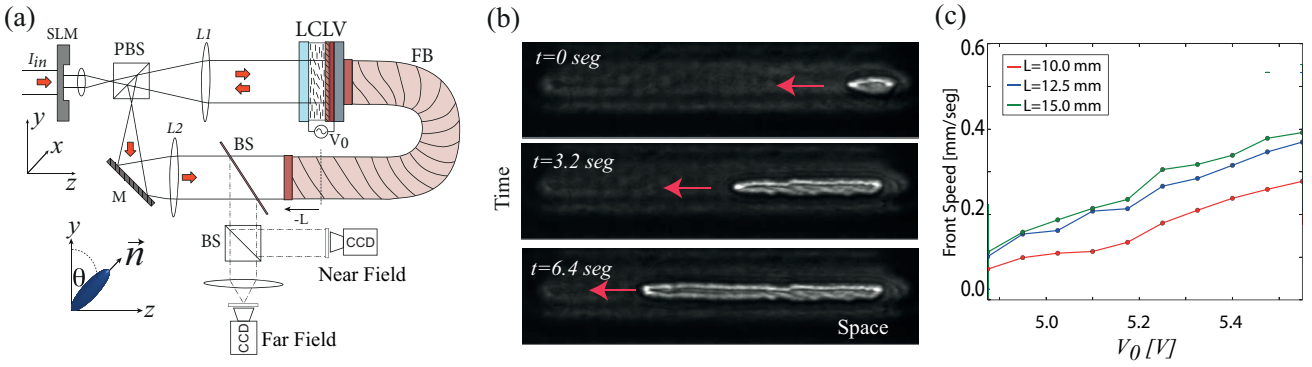

FIG. 4. Nonvariational front propagation in a LCLV with optical feedback. (a) Schematic representation of the experimental setup. $\{L1, L2\}$ stands for two lenses with a focal distance $f = 25$ cm, M is a mirror, FB is an optical fiber bundle, PBS is a polarizing beam splitter cube, BS represents a beam splitter, and SLM is a spatial light modulator driven by a computer. V_0 external voltage applied across the LCLV. (b) Temporal sequence of snapshots of front propagation from top to bottom. (c) Front speeds as a function of voltage V_0 for different free propagation lengths L.

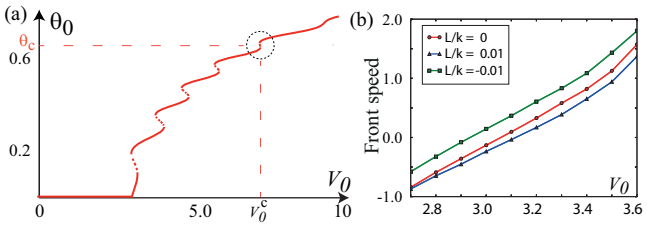

FIG. 5. Front propagation of the numerical simulation of the phenomenological model of LCLV with optical feedback Eq. (5). (a) Bifurcation diagram of molecular average orientations θ_0 as a function of voltage V_0. V_0^c accounts for a critical value of voltage for which the system exhibits nascent bistability at $\theta_0 = \theta_c$. (b) Front speeds as functions of voltage V_0 for different free propagation lengths.

which changes local and dynamically following the spatial distribution of illumination present in the photoconductor wall of the cell. When liquid-crystal molecules reorient, due to their birefringent nature, they induce a refractive index change. Thus, the LCLV acts as a manageable Kerr medium, causing a phase variation $\phi = \beta\cos^2\theta \equiv 2kd\,\Delta n\cos^2\theta$ in the reflected beam proportional to the intensity of the incoming beam I_w on the photoconductive side, where θ is the longitudinal average of the molecular reorientation. Here, $k = 2\pi/\lambda$ is the optical wave number. The LCLV is illuminated by an expanded He-Ne laser beam, $\lambda = 633$ nm, with a 1 cm transverse diameter and power $I_{in} = 6.5\ \mathrm{mW/cm^2}$, linearly polarized along the vertical y axis. A spatial light modulator (SLM, controlled through an external computer) was placed in the input beam in order to carry out one-dimensional experiments. The system dynamics is controlled by adjusting the external voltage V_0 and free propagation length L.

Theoretical description of the LCLV. The light intensity I_w reaching the photoconductor is given by $I_w(\theta,L) = I_{in}|e^{-i\frac{L}{2k}\partial_{xx}}(1+e^{-i\beta\cos^2\theta})|^2/2$ [11], where x is the transverse direction of the liquid-crystal layer. As long as I_{in} is sufficiently small ($I_{in} \sim 1\ \mathrm{mW/cm^2}$), the effective voltage V_{eff} applied to the liquid-crystal layer can be expressed as $V_{\mathrm{eff}} = \Gamma V_0 + \alpha I_w$, where $0 < \Gamma < 1$ is a transfer factor that depends on the electrical impedances of the photoconductor, dielectric mirror, and the liquid crystal, while α is a phenomenological dimensional parameter that describes the linear response of the photoconductor [11].

The dynamics of the average director tilt $\theta(x,t)$ is described by a nonlocal relaxation equation of the form [10]

$$\tau\partial_t\theta = l^2\partial_{xx}\theta - \theta + \frac{\pi}{2}\left(1 - \sqrt{\frac{\Gamma V_{\mathrm{FT}}}{\Gamma V_0 + \alpha I_w(\theta,L)}}\right), \quad (5)$$

with $V_{\mathrm{FT}} \approx 3.2\ \mathrm{V_{rms}}$ the threshold for the Fréedericksz transition, $\tau = 30$ ms the liquid-crystal relaxation time, and $l = 30\ \mu$m the electric coherence length.

Let us consider the zero free propagation length, $L = 0$, $I_w(\theta, L=0) = I_{in}\{1+\cos(\beta\cos^2\theta)\}/2$. In this limit, Eq. (5) is a gradient model. To derive a simple description of the above model, we study its dynamics around the emergence of bistability, i.e., when the system becomes multivalued or exhibits nascent bistability [15]. Figure 5(a) depicts nascent bistability. We express the expression for equilibria $\theta(x,t) = \theta_0$ as follows, $V_0(\theta_0) = V_{\mathrm{FT}}/\Gamma(1 - 2\pi^{-1}\theta_0)^2 - \alpha\, I_{in}[1+\cos(\beta\cos^2\theta_0)]/2\Gamma$, and from this relation we determine the values of the parameters for the emergence of bistability. Indeed, in the parameter space, the above expression generates a folded surface from which one can geometrically infer the points of nascent bistability [cf. Fig. 5(a)]. In fact, θ_0 becomes multivalued when the function $V_0(\theta_0, I_{in})$ has a saddle point at $\theta_0 = \theta_c$. Around the saddle point $V_0(\theta_c)$ creates two new extreme points that determine the width of the bistability region. To find the saddle points of $V_0(\theta_c, I_{in})$, we have to impose the conditions $dV_0/d\theta_c = 0$, $d^2V_0/d^2\theta_c = 0$, and, after straightforward algebraic calculations, we obtain the relations $I_{in} = \pi^2 V_{\mathrm{FT}}/\alpha\beta(\pi/2-\theta_c)^3\sin(2\theta_c)\sin(\beta\cos^2\theta_c)$, and $(\theta_c - \pi/2)[2\csc 2\theta_c + \beta\sin 2\theta_c\cot(\beta\cos^2\theta_c)] = 3$. The first expression gives the critical value of I_{in} for which V_0 becomes multivalued. The second expression is an algebraic equation that depends only on the parameter β and determines all the points of nascent bistability. Notice that only half of them have physical significance because the other half correspond to negative values of the intensity. By taking into account the constraint that the intensity must be positive and considering that the cotangent function is π periodic, we have that the actual number of points of nascent bistability is equal to the next smallest integer of $\beta/2\pi$. For the values considered in our experiment, β is about 54, then one expects to find eight points of nascent bistability in the entire (V_0, I_{in}) parameter space, a prediction that is confirmed by the experiment [10].

The dynamics around a nascent bistability point can be described by a scalar field $u(x,t)$ governed by a cubic nonlinearity. Hence, close to this point, $I_{in} \equiv I_{in}^c$, $V_0 \equiv V_0^c$, and we can consider

$$\theta(x,t) \approx \theta_c + u(x,t)/u_0, \quad (6)$$

where $u_0^2 \equiv 2\beta\cos 2\theta_c\cot(\beta\cos^2\theta_c) + (4+\beta^2\sin 2\theta_c)/3 - 2/(\pi/2-\theta_c)^2$ is a normalization constant.

Considering the above ansatz in Eq. (5) with a zero free propagation length $L = 0$, and developing in a Taylor series by keeping the cubic terms, after straightforward algebraic calculations, we can reduce the full LCLV model to a simple bistable model,

$$\tau\partial_t u = \eta + \mu u - u^3 + l^2\partial_{xx}u, \quad (7)$$

where $\eta \equiv \alpha[1-\cos(\beta\cos^2\theta_c)](\pi/2-\theta_c)^3[I_{in} - I_c + \alpha[1-\cos(\beta\cos^2\theta_c)(V_0 - V_c)]/2]/\pi^2 V_{\mathrm{FT}}$, and $\mu \equiv 12\Gamma\{(\pi/2-\theta_c)^2(V_0 - V_c) + [\pi^2 V_{\mathrm{FT}}/12 - (\pi/2-\theta_c)^2](I_{in} - I_c)/I_c\}/\pi^2 V_{\mathrm{FT}}$.

For a small free propagation length ($L \sim \epsilon \ll 1$), the light intensity I_w reached in the photoconductor can be approximated by a local model characterized by

$$\begin{aligned} I_w(\theta,L) \approx\ & I_{in}\{1+\cos(\beta\cos^2\theta) \\ & + L[1+\cos(\beta\cos^2\theta)\partial_{xx}\sin(\beta\cos^2\theta)]/k \\ & - L\sin(\beta\cos^2\theta)\partial_{xx}\cos(\beta\cos^2\theta)/k\}/2. \end{aligned}$$

Introducing this expression in Eq. (5), using ansatz (6), developing in a Taylor series by keeping the cubic terms in u, considering that the order parameter is a slow variable in space ($\partial_{xx}u \ll \partial_x u \ll 1$), renormalizing space, and after

straightforward calculations, we obtain Eq. (1), with

$$b = c \equiv -\frac{\pi\alpha\beta\cos(2\theta_c)I_c\left(\frac{V_{\mathrm{FT}}}{2V_c+\alpha I_c[1+\cos(\beta\cos^2\theta_c)]}\right)^{3/2}}{\sqrt{2}lu_0V_{\mathrm{FT}}}.$$

Hence, close to nascent bistability, model Eq. (5) can be approximated by a simple nonvariational model Eq. (1), which describes the complex dynamics observed around this critical point.

Numerical simulations of model (5) in the region of bistability for a small free propagation length show that the system exhibits front solutions. The front speed is affected when the free propagation length is changed. Therefore, these fronts present a propagation mechanism of a nonvariational nature.

Experimental nonvariational front propagation. Using the SLM, we have conducted quasi-one-dimensional experiments in a LCLV with optical feedback. As voltage V_0 is varied as a control parameter, we identify the bistable region, where two different molecular orientation states coexist. In this bistability region, the SLM is not only used to create a one-dimensional channel, but also to create localized perturbations, which allow us to observe the emergence of fronts between two different molecular orientations. Hence, the light observed in the near field has different intensities, which are associated with the molecular orientations. Figure 4(b) shows a temporal sequence of snapshots of front propagation. By recording the interface evolution over the channel with a CCD camera, we have measured the front speed, which is plotted in Fig. 4(c) as a function of V_0 for different values of free propagation length L. For small L, experimental imperfections are relevant. We consider nonsmall L. Note that as the free propagation length increases, the front speed increases, which is consistent with the theoretical prediction. Therefore, the mechanism that generates the spread of these fronts is the energy difference and front core shape (nonvariational effect).

In summary, we have characterized a mechanism of nonvariational front propagation in one-dimensional scalar fields, where the process responsible for generating the spread of this front is the front shape and not the energy difference between equilibria. In higher dimensions we expect that the propagation is only corrected by curvature effects, e.g., the Gibbs-Thomson effect [3].

Acknowledgments. M.G.C. and M.W. acknowledge funding from the FONDECYT Projects No. 1150507 and No. 3140387. A.J.A.-S. acknowledges financial support from Becas Conicyt 2015, Contract No. 21151618.

[1] P. Glansdorff and I. Prigogine, *Thermodynamic Theory of Structures: Stability and Fluctuations* (Wiley, New York, 1971).

[2] G. Nicolis and I. Prigogine, *Self-Organization in Nonequilibrium Systems* (Wiley, New York, 1977).

[3] L. M. Pismen, *Patterns and Interfaces in Dissipative Dynamics* (Springer, Berlin, 2006).

[4] M. Cross and H. Greenside, *Pattern Formation and Dynamics in Nonequilibrium Systems* (Cambridge University Press, New York, 2009).

[5] J. S. Langer, Instabilities and pattern formation in crystal growth, Rev. Mod. Phys. **52**, 1 (1980).

[6] W. van Saarloos, Front propagation into unstable states, Phys. Rep. **386**, 29 (2003).

[7] Y. Pomeau, Front motion, metastability and subcritical bifurcations in hydrodynamics, Physica D **23**, 3 (1986).

[8] P. Coullet, J. Lega, B. Houchmanzadeh, and J. Lajzerowicz, Breaking Chirality in Nonequilibrium Systems, Phys. Rev. Lett. **65**, 1352 (1990).

[9] M. G. Clerc, S. Coulibaly, and D. Laroze, Nonvariational Ising-Bloch transition in parametrically driven systems, Int. J. Bifurcation Chaos Appl. Sci. Eng. **19**, 2717 (2009); D. Michaelis, U. Peschel, F. Lederer, D. V Skryabin, and W. J. Firth, Universal criterion and amplitude equation for a nonequilibrium Ising-Bloch transition, Phys. Rev. E **63**, 066602 (2001).

[10] M. G. Clerc, A. Petrossian, and S. Residori, Bouncing localized structures in a liquid-crystal light-valve experiment, Phys. Rev. E **71**, 015205 (2005).

[11] S. Residori, Patterns, fronts and structures in a liquid-crystal-light-valve with optical feedback, Phys. Rep. **416**, 201 (2005).

[12] M. G. Clerc, T. Nagaya, A. Petrossian, S. Residori, and C. S. Riera, First-order Fréedericksz transition and front propagation in a liquid crystal light valve with feedback, Eur. Phys. J. D **28**, 435 (2004).

[13] F. Haudin, R. G. Elias, R. G. Rojas, U. Bortolozzo, M. G. Clerc, and S. Residori, Driven Front Propagation in 1D Spatially Periodic Media, Phys. Rev. Lett. **103**, 128003 (2009); Front dynamics and pinning-depinning phenomenon in spatially periodic media, Phys. Rev. E **81**, 056203 (2010).

[14] P. G. de Gennes and J. Prost, *The Physics of Liquid Crystals* (Oxford University Press, New York, 1995).

[15] M. Tlidi, P. Mandel, and R. Lefever, Localized Structures and Localized Patterns in Optical Bistability, Phys. Rev. Lett. **73**, 640 (1994).

Chapter 4

Nonvariational Effects in Localized Structures

4.1 Introduction

In the previous chapters, the effects of the inclusion of non-variational terms in the dynamics of normal and FKPP fronts were explored, understanding such non-variational terms as typical in the formation of evolution laws macroscopic systems. This chapter will study their impact on localized structures dynamics and their role in their propagation. Indeed, an important challenge in studying localized dissipative structures is to understand the mechanisms that allow or drive propagation and how to control such propagation. For this reason, our focus is on understanding how non-variational effects can make a localized structure go from motionless to propagative. Since its inception, the motion of localized structures has been the subject of intense research. The seminal work of Scott Russell on propagating solitons in a water channel [86], is maybe the first attempts to understand how and why these solitons propagate at almost constant speeds and maintaining their shape for long period of time. While his work was mainly descriptive, he laid the groundwork for further study of solitons. Now, there are a variety of mechanisms of propagation of localized structures reported. However, all are based on the same principle, breaking the symmetry of the localized structure. In other words, asymmetry is the cause of propagation in localized structures. Perhaps the most intuitive way to do this is by entering drift terms or phase gradients [87]. Another similar nature approach places asymmetry in terms of coupling or feedback, thus having off-axis couplings [88] or translational couplings in space [89]. Finally, and perhaps the closest propagation mechanism to our work would be symmetry breaking via the introduction of space or time delay terms [90, 91, 92, 93, 94], which are also non-variational. However, in our work, we identified a simple propagation mechanism, in which the breaking of the symmetry of the localized structure occurs spontaneously, thus giving rise to a transition from motionless to propagative. In order to understand this transition in a simple system, we consider the non-variational Turing-Swift-Hohenberg equation, explored in the previous chapters, and given by:

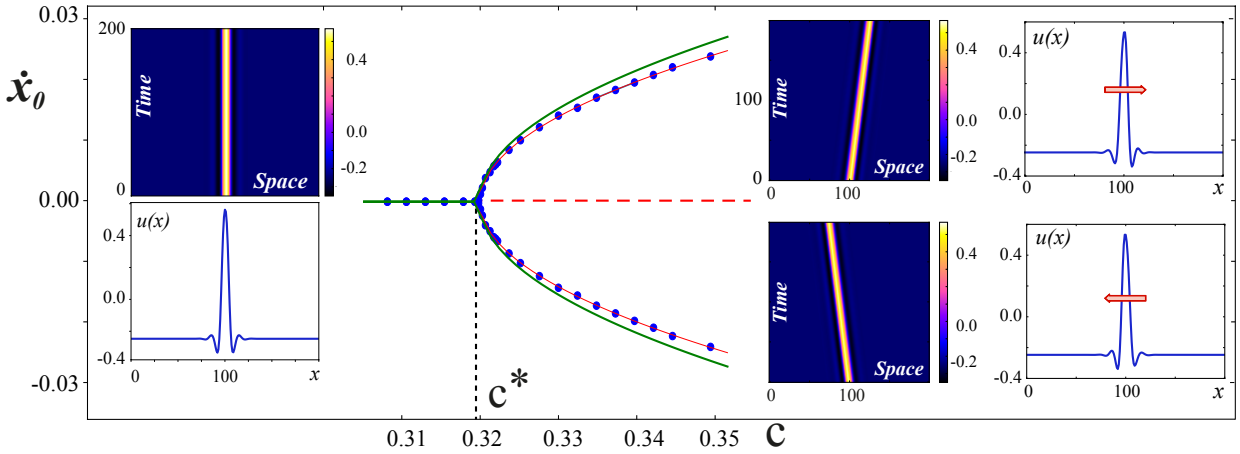

Figure 4.1: Speed of localized structure $v = \dot{x}_0$ as a function of the parameter c. At the transition point $c \equiv c^* \approx 0.319$. Dots indicate localized structures speed obtained from numerical simulations of Eq. (4.1). Green curves is associated with the analytical results developed in our paper and red curves are associated with the fit of the numerical values given by : $v = \dot{x}_0 = 0.1467\sqrt{c - 0.319}$ Parameters are $\mu = \eta = -0.02$, $\nu = 1$, and $b = -0.9$. Left insets account for the profile and the spatiotemporal evolution of a motionless localized structure. Right top (bottom) insets account for the profile and the spatiotemporal evolution of a right (left) moving localized structure.

$$\partial_t u = \eta + \mu u - u^3 - \partial_{xx} u - \partial_{xxxx} u + 2bu\partial_{xx} u + c(\partial_x u)^2, \tag{4.1}$$

Note that the equation is variational for $b = c$ in this way. The next section illustrates how the localized structures for equation (4.1) propagate, along with the region's details in the parameter space in which they appear.

4.2 Propagation of localized states driven by nonvariational effects

Through a numerical study of the nonvariational effects in a generalization of Turing-Swift-Hohenberg equation, we found that these can generate a spontaneous symmetry break and induce movement in localized structures. A spectral method was used for spatial integration and a Runge-Kutta of order 4 for temporal integration, however central derivatives were also used, and in all cases, the results were equivalent.

In particular, leaving $b = -0.9$ fixed by varying the parameter c we could see the transition from motionless to traveling. In the figure 4.1 such a transition is shown, where we take $c < c^*$ (in the motionless zone) and $c > c^*$ in the propagative zone, where $c^* \approx 0.319$ is the bifurcation point. The bifurcation diagram of these localized structures was also characterized. In the figure 4.1, you can see a Pitchfork type bifurcation for all the fixed parameters, leaving only c to vary. The paper can be found an extended version of this bifurcation diagram, allowing the parameter b variation. Collisions By studying the interaction of these localized structures, we seek to see their behavior in the face of collisions. In this case, when

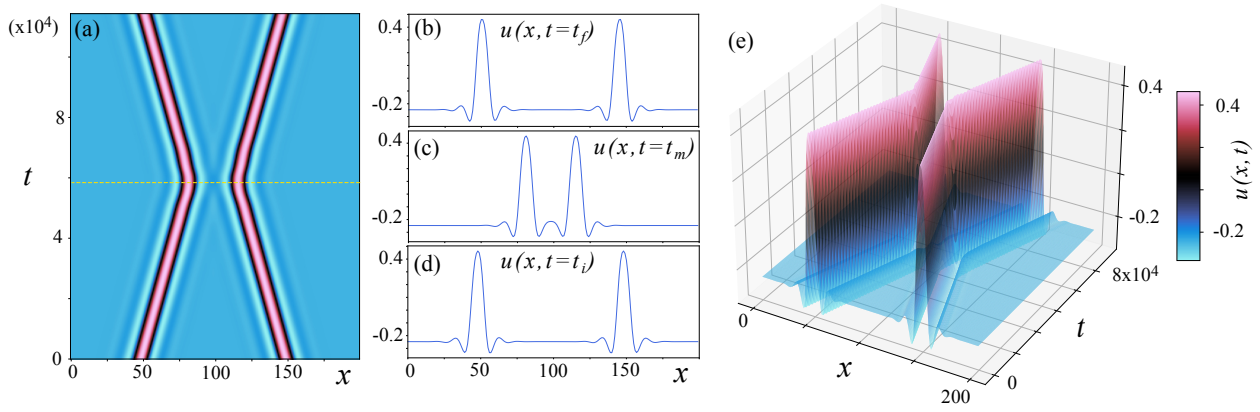

Figure 4.2: Elastic collision of LS. Panel (a) shows the collision between two localized states in the spatiotemporal diagram. Panels (b), (c) and (c) shows the profile of the solution in three time instants corresponding to the initial time $t = 0$, the collision time $t \approx 6 \times 10^4$ and the final state $t = 10^5$ respectively. Panel (e) show a representation in 3D of the spatiotemporal diagram.

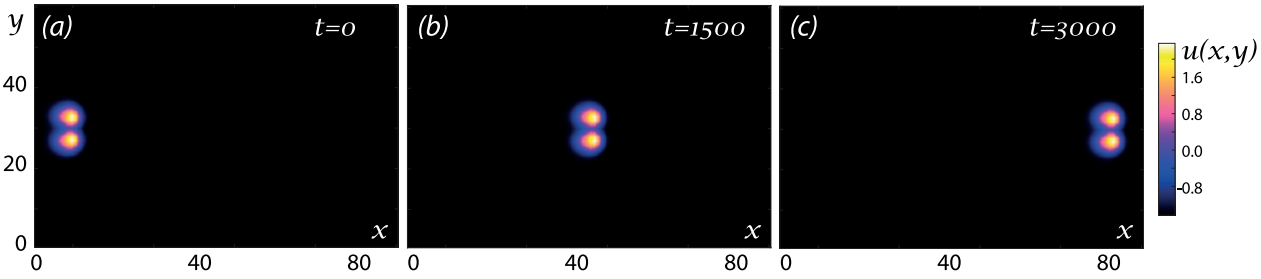

Figure 4.3: Bounded localized states, called catamaran structure, propagating on space. Parameters are $\eta = -2$, $\nu = -1$, $\mu = -0.092$, $b = -2.8$, and $c = 3.2$.

two of these collided, we saw that their interaction is elastic type, as can be seen in figure 4.2. i.e., the interaction between the localized structures presented here appears to be repulsive. Although a more in-depth analysis of the interaction between non-variationally forced dissipative localized structures is necessary, outside the scope of our research on propagation mechanisms will be addressed later.

4.3 Catamaran states: a 2D generalization

When trying to generalize the results obtained previously to systems of greater dimension, we searched for these solutions in the 2D generalization of this system:

$$\partial_t u = \eta + \mu u - u^3 - \nabla^2 u - \nabla^4 u + 2bu\nabla^2 u + c(\nabla u)^2, \tag{4.2}$$

However, we could not find an analogue of a peak that is propagative for the two-dimensional system. In other words, the solution of a peak is unstable in the propagative region. However, we find that the bound states of two peaks can break symmetry and prop-

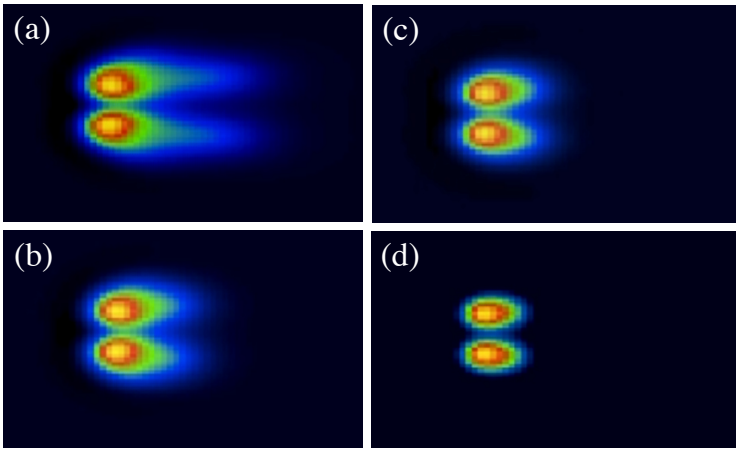

Figure 4.4: Catamaran structures obtained when parameter η is varying in the region where catamaran structures exist. In panel (a) correspond to $\eta = 0.5$ and present a more asymmetric shape, and exhibit a long tail compared with figures in panels (b), (c), and (c) that corresponds to $\eta = -1, -2$ and -5 respectively.

agate. We call them catamarans due to their particular structure made up of two peak structures and their ability to move through space. For fixed parameters, the speed of these can be controlled via the terms that weigh the non-variational contributions. However, by varying the eta parameter, we find that it is also possible to change its shape, thus displaying an exciting variety of this type of localized structures. Some of these are shown in figure 4.4.

4.4 Experimental Catamarans.

This type of structure was not sought in the setup composed of the liquid crystal light valve with optical retro-injection studied in the above chapters because the non-variational parameters in such experiment are not free, instead there are linked to the free propagation length, and the region in which they appear are initially inaccessible for the experiment. However, after our theoretical investigation, a series of experimental works were published showing localized catamaran-like structures in nematics. The setup is composed of a sandwich-type nematic liquid crystal layer with a ground state director vector parallel to the plates that encapsulate the liquid crystal so that solitons (which can be described as deformation waves of the local director vector) are induced by an electric field of alternating current applied on the plate on which there are transparent electrodes. More details about the experiment and the setup parameters can be seen in [1, 2]. Other examples of propagative linked localized structures have been reported by Purwins et al. However, this type of states dynamics is of the rotating type or forming aligned trains, rather than catamarans.

4.5 Outline

- We show a very simple and generic model of a scalar field system exhibiting a parity breaking transition of dissipative localized structures driven by nonvariational terms.
- The weights in nonvariational terms enable us to control the speed of these localized

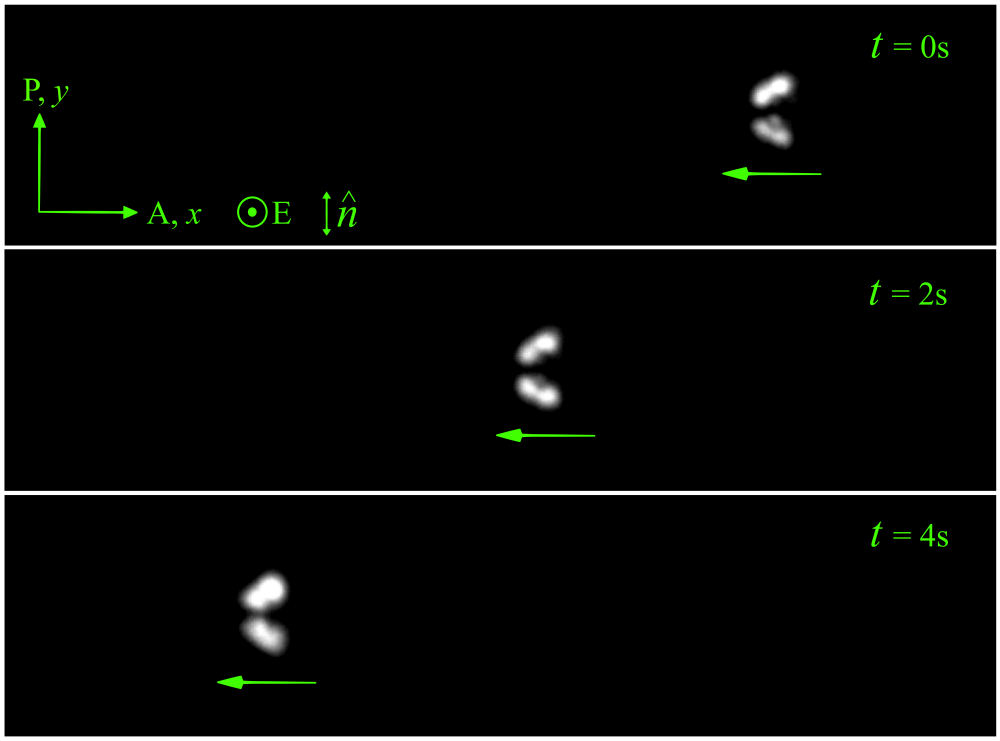

Figure 4.5: Localized structures exhibited in the liquid crystal based setup reported in [1, 2] . The bright and dark domains corresponds to the nematic and isotropic phases respectively.

structures.

- These kinds of solutions suffer a drift bifurcation (transition from motionless to traveling LS) following a supercritical Pitchfork bifurcation, analyzed in detail in our published paper.
- We deduce semi-analytically the Pitchfork normal form for the speed.
- We explore the 2D extension of the model and show that there are propagative localized structures, but they are paired instead of single spots.
- Due to the nonvariational TSH-equation genericity, we expect to observe this kind of propagative bounded localized states in more examples of nature.

The possibility of controlling the propagation of this type of structure and its relationship with the dynamics of liquid crystals, optical devices, and in general, with the dynamics of interfaces allows the creation of a bridge to investigate their applications in the labeled delivery of information in photonic devices information storage and processing as well as the delivery of micro-scale cargoes. Additionally, in the course of this research, a wide variety of patterns with exciting dynamics were found, some of them explored in-depth, e.g., the traveling and wandering chaotics (detailed in the next chapters), and others that are in development at the time of writing this chapter and are part of future postdoctoral research.

Spontaneous motion of localized structures induced by parity symmetry breaking transition

A. J. Alvarez-Socorro,[1] M. G. Clerc,[1] and M. Tlidi[2]
[1]*Departamento de Física and Millennium Institute for Research in Optics, FCFM, Universidad de Chile, Casilla 487-3, Santiago, Chile*
[2]*Département de Physique, Université Libre de Bruxelles (U.L.B.), CP 231, Campus Plaine, Bruxelles 1050, Belgium*

(Received 15 December 2017; accepted 7 May 2018; published online 29 May 2018)

We consider a paradigmatic nonvariational scalar Swift-Hohenberg equation that describes short wavenumber or large wavelength pattern forming systems. This work unveils evidence of the transition from stable stationary to moving localized structures in one spatial dimension as a result of a parity breaking instability. This behavior is attributed to the nonvariational character of the model. We show that the nature of this transition is supercritical. We characterize analytically and numerically this bifurcation scenario from which emerges asymmetric moving localized structures. A generalization for two-dimensional settings is discussed. *Published by AIP Publishing.*
https://doi.org/10.1063/1.5019734

The formation of localized structures (LSs) often called cavity solitons or dissipative solitons is a universal feature of the self-organized non-equilibrium systems and is of common occurrence in many fields of nonlinear science ranging from biology, chemistry, to physics. The important issue of our analysis is to reveal the transition from a stationary to moving localized structures that may occur in practical systems. We show that an internal parity symmetry breaking bifurcation allows localized structures to move in an arbitrary direction. We illustrate this bifurcation scenario in the paradigmatic nonvariational Swift-Hohenberg equation that has been derived for many far from equilibrium systems. These results are obtained in the particular limit of nascent bistability and large wavelength or small wavenumber pattern forming regime. Therefore, the present analysis could be applied to more realistic models. Understanding the dynamics of localized structures may allow for the manipulation and the control of light in advanced optical devices.

I. INTRODUCTION

Localized structures (LS's) have been theoretically predicted and experimentally observed in many fields of nonlinear science, such as laser physics, hydrodynamics, fluidized granular matter, gas discharge system, and biology.[1–10] These solutions correspond to a portion of the pattern surrounded by regions in the homogeneous steady state. However, localized structures are not necessarily stationary. They can move or exhibit a self-pulsation as a result of *external* symmetry breaking instability induced by a phase gradient,[11] off-axis feedback,[12] resonator detuning,[13] and space-delayed feedback.[14] This motion has also been reported using a selective[15,16] or a regular time-delay feedbacks.[17]

We identify an internal symmetry breaking instability that causes a spontaneous transition from stationary to moving localized structures in nonvariational systems. In contrast, variational systems, i.e., dynamical systems characterized by a functional, an internal symmetry breaking instability causes the emergence of motionless asymmetric localized states.[19,20] To investigate this nonvariational transition, we consider a generic nonvariational scalar Swift-Hohenberg equation. This is a well-known paradigm in the study of spatial periodic and localized patterns. It has been derived for that purpose in liquid crystal light valves with optical feedback,[21,22] in vertical cavity surface emitting lasers,[23] and in other fields of nonlinear science.[24] Generically, it applies to systems that undergo a Turing-Prigogine instability, close to a second-order critical point marking the onset of a hysteresis loop. This equation reads

$$\partial_t u = \eta + \mu u - u^3 - \nu\nabla^2 u - \nabla^4 u + 2bu\nabla^2 u + c(\nabla u)^2. \tag{1}$$

The real order parameter $u = u(x, y, t)$ is an excess field variable measuring the deviation from criticality. Depending on the context in which Eq. (1) is derived, the physical meaning of the field variable u can be the electric field, biomass, molecular average orientation, or chemical concentration. The control parameter η measures the input field amplitude, the aridity parameter, or the chemical concentration. The parameter μ is the cooperativity, and ν is the diffusion coefficient. The Laplace operator $\nabla^2 \equiv \partial_{xx} + \partial_{yy}$ acts on the plane (x, y). The parameters b and c measure the strength of nonvariational effects. The terms proportional to c and b, respectively, account for the nonlinear advection and nonlinear diffusion, which in optical systems can be generated by the free propagation of feedback light.[21,22]

For $b = c$, Eq. (1) is variational,[24] i.e., the model reads $\partial_t u = -\delta F(u)/\delta u$, with $F(u)$ being the free energy or the Lyapunov functional. In this case, any perturbation compatible with boundary conditions evolves toward either a homogeneous or inhomogeneous (periodic or localized) stationary states corresponding to a local or global minimum of $F(u)$.

Therefore, complex dynamics such as time oscillations, chaos, and spatiotemporal chaos are not allowed in the limit $b = c$. In particular, in this regime, stationary localized structures and localized patterns have been predicted.[25] An example of a stationary LS in one-dimension is shown in the left panel of Fig. 1. The obtained localized structure has a maximum value of field $u(x, t)$ located at the position x_0. The stationary LS has been studied for Eq. (1) in one dimensional (1D) spatial coordinate, as well their snaking bifurcation diagram.[26,27] When $b \neq c$, the model equation losses its variational structure and allows for the mobility of unstable asymmetric localized structures, *rung states*, that connect the symmetric states.[26] Indeed, the system exhibits a drift instability leading to the motion of localized structures in an arbitrary direction. However, these states are unstable states for small nonvariational coefficients.

In this paper, we characterize the transition from stable stationary to moving localized structures in non-variational real Swift-Hohenberg equation. Figure 1 illustrates stable moving localized structures. We show that there exists a threshold over which a single LS starts to move in an arbitrary direction since the system is isotropic in both spatial directions. We compute analytically and numerically the bifurcation diagram associated with this transition. In one dimensional setting, the transition is always supercritical within the range of the parameters that we explore. The threshold and the speed of LS is evaluated both numerically and analytically. In two-dimensional settings, numerical simulations of the governing equation indicate that the nature of the transition towards the formation of moving localized bounded states is not a supercritical bifurcation. It is worth to mention another type of internal mechanism that occurs in regime devoid of patterns and may lead to a similar phenomenon for fronts propagation through a non-variational Ising Bloch transition.[19,28–30] The Ising-Bloch transition has been first studied in the context of magnetic walls.[19] Soon after, it has been considered in a various out of equilibrium systems such as driven liquid crystal,[29] coupled oscillators,[30] and nonlinear optic cavity.[31] More recently, it has been shown that non-variational terms can induce propagation of fronts in quasi-one-dimensional liquid crystals based devices.[32] Experimental observation of a supercritical transition from stationary to moving localized structures has been realized in two-dimensional planar gas-discharge systems.[33]

The paper is organized as follows: the numerical characterization of the bifurcation scenarios triggered by an internal symmetry breaking instability leading to the formation of asymmetric traveling localized structures is discussed in Sec. II. At the end of this section, we perform numerical simulations in one-dimensional system Eq. (1). In Sec. III, we perform an analytical analysis of the symmetry breaking instability. Two-dimensional moving bounded localized structures are analyzed, and their bifurcation diagram is determined in Sec. IV. Finally, the conclusions are presented in Sec. V.

II. NUMERICAL CHARACTERIZATION OF PARITY BREAKING TRANSITION

We investigate the model Eq. (1) numerically in the case where $b \neq c$ in 1D with periodic boundary conditions. The results are summarized in the bifurcation diagram of Fig. 1. We fix all parameters and we vary the nonvariational parameter c. When increasing the parameter $c < c^*$, LS's are stationary. There exist a threshold $c = c^*$ at which transition from stationary to moving LS's takes place. This transition is supercritical. For $c > c^*$, stationary LS becomes unstable, and the system undergoes a bifurcation towards the formation of moving localized structures. The direction in which LS propagates depends on the initial condition used. Indeed, there is no preferred direction since the system is isotropic. The spatial profiles of the stationary and the moving localized states are shown in Fig. 2. The shadow regions allow emphasizing the symmetric (stationary) and asymmetric (moving) solutions concerning the localized structure position. We clearly see from this figure that stationary LS is

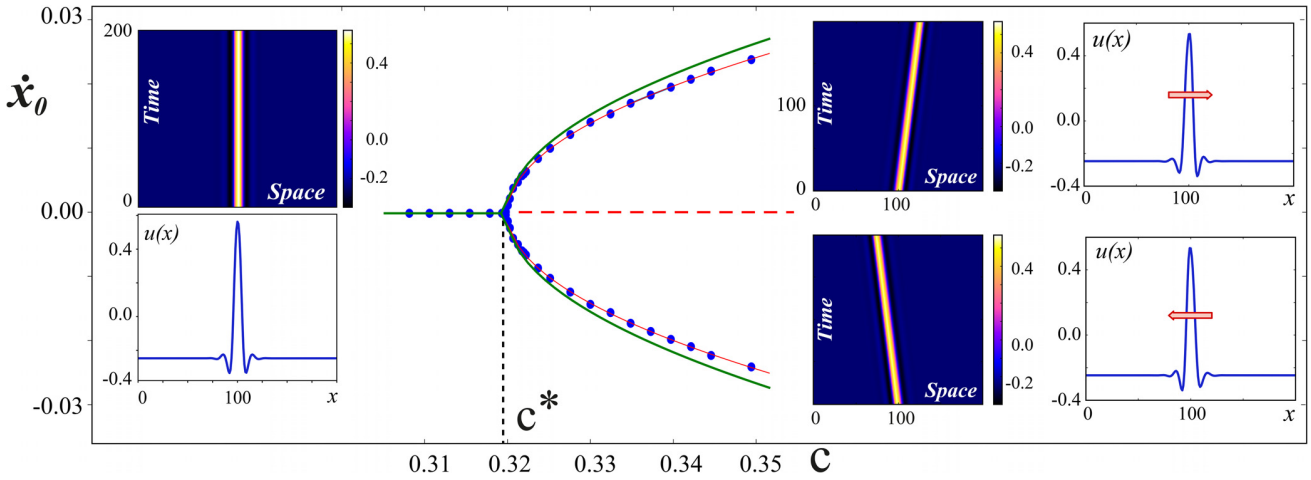

FIG. 1. The speed of localized structure $v = \dot{x}_0$ as a function of the parameter c. At the transition point, $c \equiv c^* \approx 0.319$. Dots indicate localized structures speed obtained from numerical simulations of Eq. (1). Green curves are associated with the analytical results depicted in Sec. III and red curves are associated with the fit of the numerical values given by: $v = \dot{x}_0 = 0.1467\sqrt{c - 0.319}$. Parameters are $\mu = \eta = -0.02$, $\nu = 1$, and $b = -0.9$. Left insets account for the profile and the spatiotemporal evolution of a motionless localized structure. Right top (bottom) insets account for the profile and the spatiotemporal evolution of a right (left) moving localized structure.

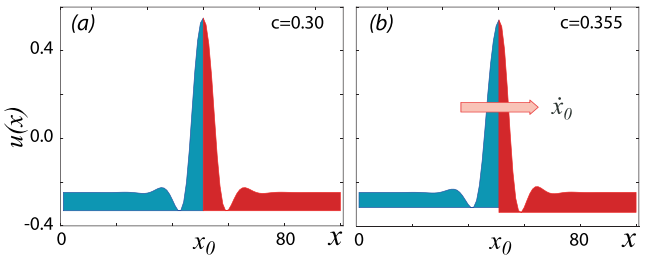

FIG. 2. Profile of localized structures obtained from numerical simulations of Eq. (1). Parameters are $\mu=\eta=-0.02$, $\nu=1$, and $b=-0.9$. (a) Stationary and (b) moving localized structure.

symmetric concerning its maximum. This can be explained by the fact that a spontaneous spatial parity breaking symmetry accompanies the transition from stationary to moving localized structures. In fact, if the parity with respect to its position $\int_{x_0-L}^{x_0+L} u(x,t)dx$ is positive (negative), it moves to the right (left).

We have measured the speed of moving LS solutions of Eq. (1) numerically, by varying both c and b parameters. The results are summarized in Fig. 3. There are three different dynamical regimes. When increasing both parameters b and c, the stationary localized structures are stable in the range delimited by the curve Γ_1. These structures exhibit a spontaneous motion leading to the formation of moving LSs solutions in the range of parameters delimited by the curves Γ_1 and Γ_2. By exploring the parameter space (b, c), we see clearly from Fig. 3 that the bifurcation towards the formation of moving LSs remains supercritical.

After the numerical characterization, we perform an analytical analysis of the transition towards moving LS. For this purpose, let us consider the linear dynamics around

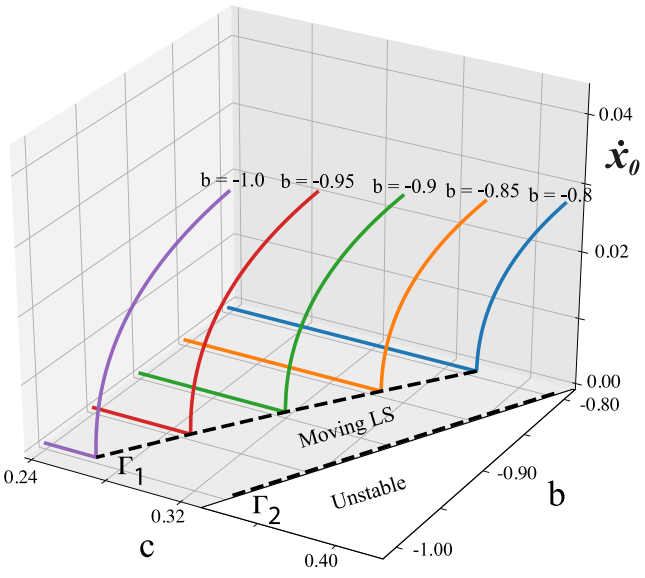

FIG. 3. The speed $v=\dot{x}_0$ as a function of the nonvariational parameters c and b obtained by numerical simulations of Eq. (1). Parameters are $\mu=\eta=-0.02$, and $\nu=1$; for each curve, different fixed values of the parameter b are considered, which are indicated in the upper part of the respective curve. The two segmented curves (Γ_1, Γ_2) limit the region where moving localized structures are observed. The line Γ_1 marks the transition from stationary to moving localized structures.

stationary LS; $u_{ls}(x-x_0)$ located at $x=x_0$. The linear operator reads

$$\mathcal{L}\varphi \equiv \left[\mu - 3u_{ls}^2 - \nu\partial_{xx} - \partial_{xxxx} + 2bu_{ls}\partial_{xx}\right]\varphi + 2c(\partial_x u_{ls})\partial_x\varphi + 2b(\partial_{xx}u_{ls})\varphi. \quad (2)$$

Note that the operator $\mathcal{L}$ is not self-adjoint ($\mathcal{L}\neq\mathcal{L}^\dagger$). Due to the lack of analytical solutions of LS for Eq. (1), we compute numerically the spectrum and eigenvectors associated with $\mathcal{L}$, $\mathcal{L}^2$, and $\mathcal{L}^\dagger$. The spectrum of $\mathcal{L}$ always has an eigenvalue at the origin of the complex plane (the Goldstone mode) as shown in Fig. 4(a). The corresponding eigenfunction denoted by $|\chi_0\rangle \equiv \partial_z u_{ls}(x-x_0)$ is depicted in Fig. 4(a-i). When approaching the parity breaking transition threshold, another mode collides with the Goldstone mode as shown in Fig. 4(a). The corresponding eigenfunction of this mode is depicted in Fig. 4(a-ii). Note, however, that the profiles of both eigenfunctions are almost the same. At the threshold, these eigenfunctions are identical. This degenerate bifurcation has been reported in the Swift-Hohenberg equation with delayed feedback.[17,18] The spectrum of $\mathcal{L}^2$ operator is obtained by using the Jordan matrix decomposition as shown in Fig. 4(b). There are two eigenfunctions $|\chi_0\rangle$ and $|\chi_1\rangle = u_{as}(x-x_0)$, which satisfy

$$\begin{aligned}\mathcal{L}|\chi_1\rangle &= |\chi_0\rangle,\\ \mathcal{L}^2|\chi_1\rangle &= 0.\end{aligned} \quad (3)$$

The profiles of $|\chi_0\rangle$ and $|\chi_1\rangle$ are plotted in Figs. 4(b-i) and 4(b-ii), respectively. From this figure, we can see that for $|\chi_0\rangle$ mode, the integral $\int_{x_0-L}^{x_0+L}|\chi_0\rangle dx = 0$, while for $|\chi_1\rangle$ mode, the integral $\int_{x_0-L}^{x_0+L}|\chi_1\rangle dx \neq 0$. This indicate that the profile of $|\chi_1\rangle$ is asymmetric. This asymmetric mode has been reported in Refs. 19, 20, 26, 30, and 33. The eigenvalues and the critical eigenfunctions associated with the adjoint operator $\mathcal{L}^\dagger$ are depicted in Fig. 4(c).

Introducing the canonical inner product

$$\langle g|f\rangle = \int_{-\infty}^{\infty} f(x)g(x)dx \quad (4)$$

numerically, we have verified that critical modes are orthogonal $\langle\chi_0|\chi_1\rangle = 0$.

III. ANALYTICAL DESCRIPTION OF PARITY SYMMETRY BREAKING TRANSITION

To provide an analytical understanding of the parity symmetry breaking bifurcation, we focus our analysis on the one-dimensional setting. To do that, we explore the space-time dynamics in the vicinity of the critical point associated with the transition from stationary to moving LS at $c=c^*$ by defining a small parameter ϵ which measures the distance from that critical point as $c=c^*+\epsilon^2 c_0$. Our objective is to determine a slow time and slow space amplitude equations. We expand the variable $u(x,t)$ as

$$u(x,t) = u_{ls}(x-x_0(\epsilon t)) + \epsilon A'(\epsilon^2 t)u_{as}(x-x_0(\epsilon t)) + w(x,x_0,A'), \quad (5)$$

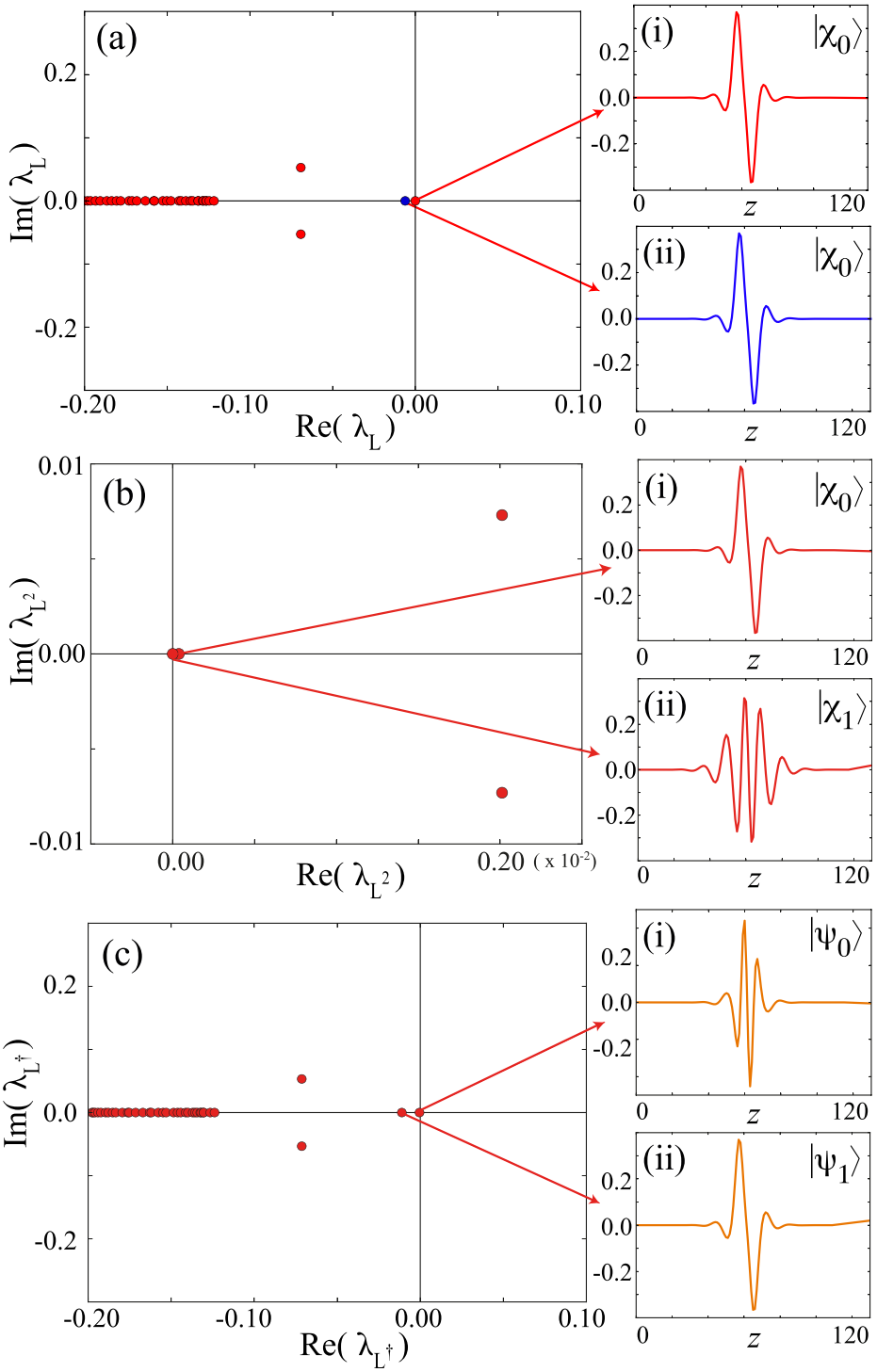

FIG. 4. Spectrum of linear operators. Real and imaginary parts of the eigenvalues associated with the linear operators (a) $\mathcal{L}$, (b) $\mathcal{L}^2$, and (c) $\mathcal{L}^\dagger$. Parameters are $\mu=-0.02$, $\nu=1.0$, $b=-0.9$, and $c=0.318$. Inset figures are the real part of the eigenfunction $|\chi_0\rangle$, $|\chi_1\rangle$, $|\psi_0\rangle$, and $|\psi_1\rangle$ for the Goldstone and the asymmetric mode associated with the zero eigenvalue, respectively.

where $u_{ls}(x-x_0(\epsilon t))$ is the stationary localized structure, and x_0 stands for the position of the localized structure. We assume that this position evolves on the slow time scale ϵt. The function $u_{as}(x-x_0(\epsilon t)) \equiv |\chi_1\rangle$ is the generalized eigenfunction corresponding to the asymmetric mode. The amplitude A' is assumed to evolve on a much slower tine scale $\epsilon^2 t$, and $w(x,x_0,A')$ is a small nonlinear correction function that follows the scaling $w \ll \epsilon A' \ll 1$. By replacing the above ansatz (5) in the corresponding one-dimensional model of Eq. (1) and linearized in w, after straightforward calculations we obtain

$$\begin{aligned}-\mathcal{L}|w\rangle =& \epsilon\dot{x}_0|\chi_0\rangle - \epsilon^3\dot{A}'|\chi_1\rangle + \ell\epsilon A'|\chi_1\rangle \\ &+c_0\left[\partial_z u_{ls}|\chi_0\rangle + \epsilon^2 A'^2\partial_z u_{as}\partial_z|\chi_1\rangle + 2\epsilon A'\partial_z u_{as}|\chi_0\rangle\right] \\ &-\epsilon^3 A'^3 u_{as}^2|\chi_1\rangle - 3\epsilon^2 A'^2 u_{as}u_{ls}|\chi_1\rangle + c^*\epsilon^2 A'^2\partial_z u_{as}\partial_z|\chi_1\rangle \\ &+2b(\epsilon A')^2 u_{as}\partial_{zz}|\chi_1\rangle, \end{aligned} \tag{6}$$

where we have introduced the notation $\dot{x}_0 = \partial_t x_0$, $\dot{A}' = \partial_t A'$, $z \equiv x - x_0(t)$ that corresponds to the coordinate in the co-moving reference frame with speed $\dot{x}_0$, and $|w\rangle \equiv w(x,x_0,A',\epsilon)$.

At order ϵ, the solvability condition[34] reads

$$\dot{x}_0 = -A'. \tag{7}$$

To determine the equation of the amplitude A' of the asymmetric mode, we apply on Eq. (6) the linear operator $\mathcal{L}$ and we obtain

$$\begin{aligned}-\mathcal{L}^2|w\rangle = &-\epsilon^3 \dot{A}'\mathcal{L}|\chi_1\rangle + c_0\mathcal{L}\partial_z u_{ls}|\chi_0\rangle + c(\epsilon A')^2\mathcal{L}\partial_z u_{as}\partial_z|\chi_1\rangle \\ &+ 2\Delta c\epsilon A'\mathcal{L}\partial_z u_{as}|\chi_0\rangle - (\epsilon A')^3\mathcal{L}u_{as}^2|\chi_1\rangle \\ &+ c^*(\epsilon A')^2\mathcal{L}\partial_z u_{as}\partial_z|\chi_1\rangle + 2b(\epsilon A')^2\mathcal{L}u_{as}\partial_{zz}|\chi_1\rangle \\ &- 3(\epsilon A')^2\mathcal{L}u_{as}u_{ls}|\chi_1\rangle.\end{aligned}$$

The application of the solvability condition at the next order leads to

$$\dot{A}' = \frac{2c_0\langle\psi_1|\mathcal{L}\partial_z u_{as}|\chi_0\rangle}{\langle\psi_1|\chi_0\rangle}A' - \frac{\langle\psi_1|\mathcal{L}u_{as}^2|\chi_1\rangle}{\langle\psi_1|\chi_0\rangle}A'^3. \tag{8}$$

To simplify further Eqs. (7) and (8), we propose the following scaling and change of parameters:

$$A \equiv \frac{\langle\psi_1|\mathcal{L}u_{as}^2|\chi_1\rangle}{\langle\psi_1|\chi_0\rangle}A', \quad \tau \equiv \frac{\langle\psi_1|\chi_0\rangle}{\langle\psi_1|\mathcal{L}u_{as}^2|\chi_1\rangle}t, \tag{9}$$

$$\sigma \equiv 2c_0\frac{\langle\psi_1|\mathcal{L}\partial_z u_{as}|\chi_0\rangle\langle\psi_1|\mathcal{L}u_{as}^2|\chi_1\rangle}{\langle\psi_1|\chi_0\rangle^2},$$

we get the dynamics for the critical modes

$$\dot{A}(\tau) = \sigma A - A^3, \tag{10}$$

$$\dot{x}_0(\tau) = -A. \tag{11}$$

The parameter $\sigma \propto (c - c^*)$ measures the distance from the critical point associated with the parity symmetry breaking transition. The stationary speed of amplitude Eqs. (10) and (11) is $v = \pm\sqrt{\sigma} \propto (c - c^*)^{1/2}$. This implies that the asymmetric mode undergoes at the onset of the instability a drift-pitchfork bifurcation,[35,36] as result of parity breaking symmetry.[19,20,26,30,33] This bifurcation scenario is in perfect agreement with the results of direct numerical simulations of Eq. (1) presented in Sec. II [see the bifurcation diagram of Fig. 1]. Note that the interaction between symmetric stationary LSS has been investigated in the variational Swift-Hohenberg equation by Aranson *et al.*[36]

IV. BOUNDED MOVING LOCALIZED STATES IN TWO SPATIAL DIMENSIONS

Most of the experimental observations of localized structures have been realized in two-dimensional systems,[4,5] in which stationary localized structures are observed. Experimentally, it has been reported a supercritical transition from stationary to moving localized structures in a planar gas-discharge system.[33]

An example of two-dimensional moving localized states obtained by numerical simulations of Eq. (1) is depicted in Fig. 5(a). In this figure, a time sequence of two-dimensional moving bounded states obtained for periodic boundary conditions is shown. The two spots are bounded together in the course of the motion. The nonvariational effects render this localized moving spots asymmetric. There is no preferred direction for this motion since the system is isotropic in the xy plane. We characterize this motion by computing the speed ($\dot{x}_0$) as a function of the nonvariational parameter c. The result is shown in Fig. 5(b). The existence domain of this moving structures occurs in the range of $c_1 < c < c_2$. For $c < c_1$, the system undergoes a well documented curvature instability that affects the circular shape of LS and in the course of time leads to a self-replication phenomena.[37] This behaviour is illustrated in Fig. 6(a). However, for $c > c_2$, bounded localized structures become unstable and we observe in this regime transition to homogeneous steady state as shown in Fig. 6(b).

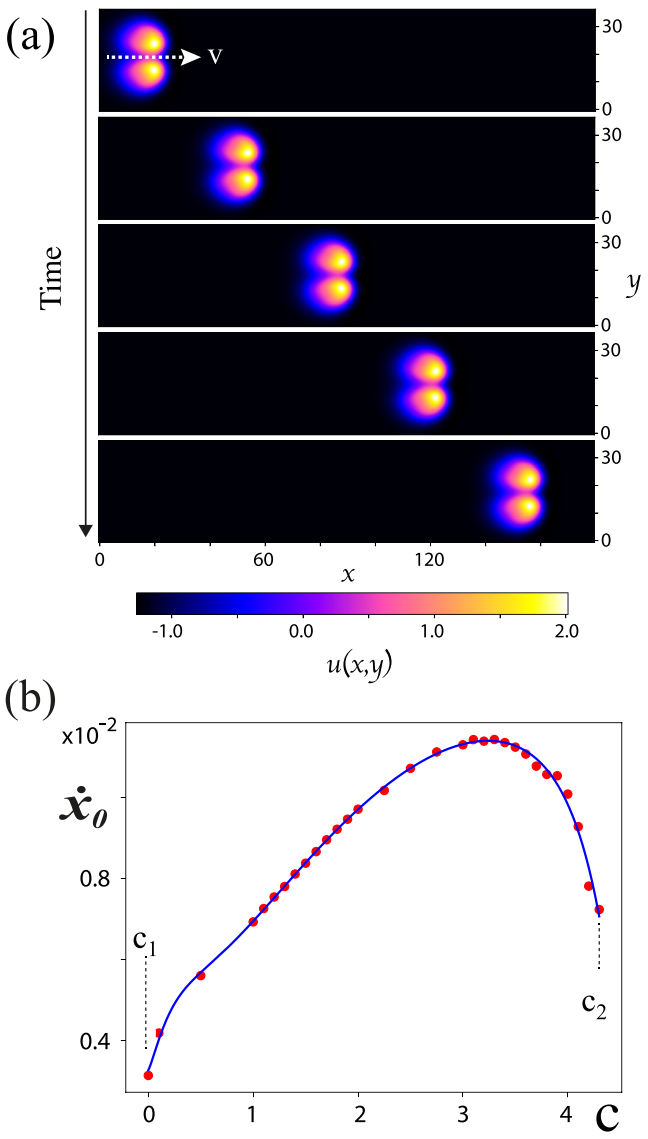

FIG. 5. Moving bounded localized structures obtained from numerical simulations of Eq. (1). (a) Temporal sequence of the moving bounded LSs in (x, y) plane obtained at $t_1 = 0$, $t_2 = 1500$, $t_3 = 3000$, $t_4 = 4500$, and $t_5 = 6000$ time steps. Parameters are $\eta = -2$, $\nu = -1$, $\mu = -0.092$, $b = -2.8$, and $c = 3.2$. (b) The speed of bounded moving LSs as a function of the parameter c. Other parameters are the same as in (a). The red dots indicate localized structures speed obtained from numerical simulations of Eq. (1) and the blue curve shows an interpolation obtained from these dots.

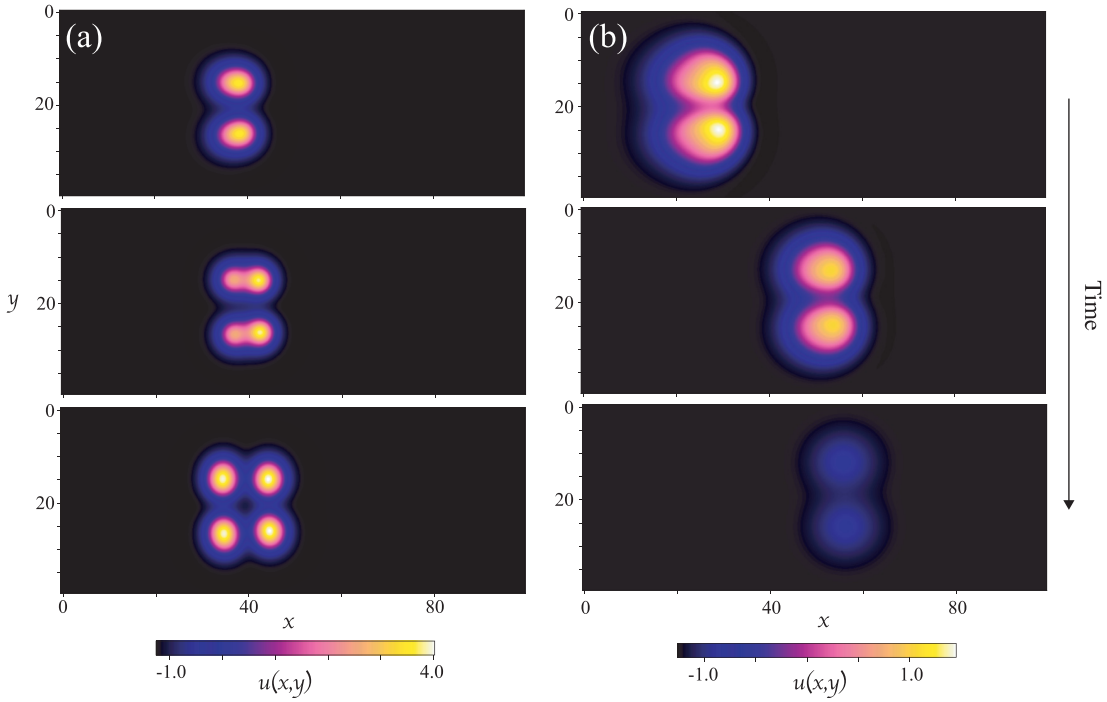

FIG. 6. Temporal sequence of destabilization of bounded localized structures via (a) a self-replication or (b) a transition towards stationary homogeneous steady states. Parameters are the same as in Fig. 5 except for c, (a) $c = -0.2$ and (b) $c = 4.5$.

V. CONCLUSION

We have considered the paradigmatic real nonvariational Swift-Hohenberg equation with cubic nonlinearity. We have investigated the transition from stable stationary to moving localized structures. We have shown that the spontaneous motion of localized structures induced by parity symmetry transition and nonvariational effects is supercritical and occurs in wide range of the system parameter values. In one dimensional setting, the analytical and the numerical bifurcation diagrams have been established. We have derived a normal form equation to describe the amplitude and the speed of moving localized structures. We have estimated the threshold as well as the speed of moving asymmetric localized structures. A similar scenario has been established for cubic-quintic Swift-Hohenberg equation with only the nonvariational nonlinear advective term.[38] In this paper, a drift pitchfork bifurcation of localized states has been discussed where the resulting traveling states are linearly stable. However, in two-dimensional systems, we have shown through numerical simulations that the transition towards bounded moving localized state is rather subcritical. We have shown that there exist a finite range of parameters where bounded LS is stable. Out of this parameter range, the 2D bounded localized state self-replicates or exhibits transition towards a stationary homogeneous steady state.

Our results are valid in the double limits of a critical point associated with nascent bistability and close to short wavenumber or large wavelength pattern forming regime. However, given the universality of model (1), we expect that the transition considered here should be observed in various far from equilibrium systems.

ACKNOWLEDGMENTS

M.G.C. and M.T. acknowledge the support of CONICYT Project No. REDES-150046. M.T. received support from the Fonds National de la Recherche Scientifique (Belgium). M.G.C. thanks FONDECYT Project No. 1150507 and Millennium Institute for Research in Optics. A.J.A.-S. thanks financial support from Becas Conicyt 2015, Contract No. 21151618.

[1]P. Glansdorff and I. Prigogine, *Thermodynamic Theory of Structures, Stability and Fluctuations* (Wiley, New York, 1971).
[2]M. C. Cross and P. C. Hohenberg, "Pattern formation outside of equilibrium," Rev. Mod. Phys. **65**, 851 (1993).
[3]*Dissipative Solitons: From Optics to Biology and Medicine*, Lecture Notes in Physics Vol. 751, edited by N. Akhmediev and A. Ankiewicz (Springer, Heidelberg, 2008).
[4]H. G. Purwins, H. U. Bodeker, and S. Amiranashvili, "Dissipative solitons," Adv. Phys. **59**, 485 (2010).
[5]O. Descalzi, M. G. Clerc, S. Residori, and G. Assanto, *Localized States in Physics: Solitons and Patterns* (Springer, 2011).
[6]H. Leblond and D. Mihalache, Phys. Rep. **523**, 61 (2013).
[7]M. Tlidi, K. Staliunas, K. Panajotov, A. G. Vladimiorv, and M. Clerc, Philos. Trans. R. Soc., A **372**, 20140101 (2014).
[8]L. Lugiato, F. Prati, and M. Brambilla, *Nonlinear Optical Systems* (Cambridge University Press, 2015).
[9]*Nonlinear Dynamics: Materials, Theory and Experiments*, Springer Proceedings in Physics Vol. 173, edited by M. Tlidi and M. G. Clerc (Springer, 2016).
[10]M. E. Cates, D. Marenduzzo, I. Pagonabarraga, and J. Tailleur, Proc. Natl. Acad. Sci. U. S. A. **107**, 11715 (2010).
[11]D. Turaev, M. Radziunas, and A. G. Vladimirov, Phys. Rev. E **77**, 065201(R) (2008).
[12]R. Zambrini and F. Papoff, Phys. Rev. Lett. **99**, 063907 (2007).
[13]K. Staliunas and V. J. Sanchez-Morcillo, Phys. Rev. A **57**, 1454 (1998).
[14]F. Haudin, R. G. Rojas, U. Bortolozzo, M. G. Clerc, and S. Residori, Phys. Rev. Lett. **106**, 063901 (2011).

[15]P. V. Paulau, D. Gomila, T. Ackemann, N. A. Loiko, and W. J. Firth, Phys. Rev. E **78**, 016212 (2008).
[16]A. J. Scroggie, W. J. Firth, and G.-L. Oppo, Phys. Rev. A **80**, 013829 (2009).
[17]M. Tlidi, A. G. Vladimirov, D. Pieroux, and D. Turaev, Phys. Rev. Lett. **103**, 103904 (2009).
[18]S. V. Gurevich and R. Friedrich, Phys. Rev. Lett. **110**, 014101 (2013).
[19]P. Coullet, J. Lega, B. Houchmanzadeh, and J. Lajzerowicz, Phys. Rev. Lett. **65**, 1352 (1990).
[20]J. Burke and E. Knobloch, Chaos **17**, 037102 (2007).
[21]M. G. Clerc, A. Petrossian, and S. Residori, Phys. Rev. E **71**, 015205(R) (2005).
[22]C. Durniak, M. Taki, M. Tlidi, P. L. Ramazza, U. Bortolozzo, and G. Kozyreff, Phys. Rev. E **72**, 026607 (2005).
[23]G. Kozyreff, S. J. Chapman, and M. Tlidi, Phys. Rev. E **68**, 015201(R) (2003).
[24]G. Kozyreff and M. Tlidi, Chaos **17**, 037103 (2007).
[25]M. Tlidi, P. Mandel, and R. Lefever, Phys. Rev. Lett. **73**, 640 (1994).
[26]J. Burke and J. H. Dawes, SIAM J. Appl. Dyn. Syst. **11**, 261 (2012).
[27]M. Tlidi, E. Averlant, A. Vladimirov, and K. Panajotov, Phys. Rev. A **86**, 033822 (2012).
[28]D. Michaelis, U. Peschel, F. Lederer, D. Skryabin, and W. J. Firth, Phys. Rev. E **63**, 066602 (2001).
[29]J. M. Gilli, M. Morabito, and T. Frisch, J. Phys. II France **4**, 319–331 (1994).
[30]M. G. Clerc, S. Coulibaly, and D. Laroze, Int. J. Bifurcation Chaos Appl. Sci. Eng. **19**, 2717 (2009).
[31]A. Esteban-Martín, V. B. Taranenko, J. García, G. J. de Valcárcel, and E. R. Eugenio, Phys. Rev. Lett. **94**, 223903 (2005).
[32]A. J. Alvarez-Socorro, M. G. Clerc, M. Gonzelez-Cortes, and M. Wilson, Phys. Rev. E **95**, 010202 (2017).
[33]H. U. Bödeker, M. C. Röttger, A. W. Liehr, T. D. Frank, R. Friedrich, and H. G. Purwins, Phys. Rev. E **67**, 056220 (2003).
[34]I. Fredholm, Acta Math. **27**, 365 (1903).
[35]S. Wiggins, *Introduction to Applied Nonlinear Dynamical Systems and Chaos* (Springer-Verlag, New York, 1990).
[36]I. S. Aranson, K. A. Gorshkov, A. S. Lomov, and M. I. Rabinovich, Phys. D **43**, 435 (1990).
[37]I. Bordeu *et al.*, Sci. Rep. **6**, 33703 (2016).
[38]S. M. Houghton and E. Knobloch, Phys. Rev. E **84**, 016204 (2011).

Chapter 5

Traveling Chimeras

5.1 Introduction

As was mentioned in chapter 1, chimera states have been an intensive research object in the last 20 years. Despite this, there is still much to discover about these intriguing states. For example, until recently, all chimeras studies focused on recognizing these states in spatially discrete systems. There are only a few works on traveling chimera states in spatially discrete systems [95, 96, 97, 98, 99, 100, 101, 102]. In the scenario of continuous media, we report the first traveling chimera state to the best of our knowledge. Any external cause does not drive its spatial propagation, i.e., no drift terms force its propagation. Instead, such propagation is driven by the system itself due to a spontaneous symmetry breaking. The formation of such kind of intriguing states creates a bridge between totally coherent and complex spatiotemporal behaviors. More formally, a traveling chimera state can be understood as chimera patterns whose domains constituting it exhibit a motion, i.e., considering the incoherent domain, its position travels along with the media, independently if the media is discrete or continuous.

It is noteworthy than in almost all papers about traveling chimeras, these states propagates in a discrete media with a complex coupling topology. In contrast, we investigate this phenomenon from the dissipative localized structure's point of view. In this case, we consider a continuous media, where the coupling is described by spatial derivatives, namely diffusion and advective terms. Besides, we show that this phenomenon in a generic equation from pattern formation theory, namely, the nonvariational Turing-Swift-Hohenberg, presented in the above chapters. Due to the equation's generic nature, we expect to see such states in a wide range of natural and technological systems, particularly in liquid crystal dynamics. This model describes the dynamics of a liquid crystal light valve with optical feedback.

On the other hand, traveling and motionless chimera states are of interest due to its possible connections with the opinion dynamics in social systems [103, 104, 105], population dynamics [106], as well as in out equilibrium chemical reactions[107] and electro-chemical oscillators [108].

In the combustion process, the interface phase dynamics between burned and unburned states can be considered a traveling localized state. Depending on the reactive used and

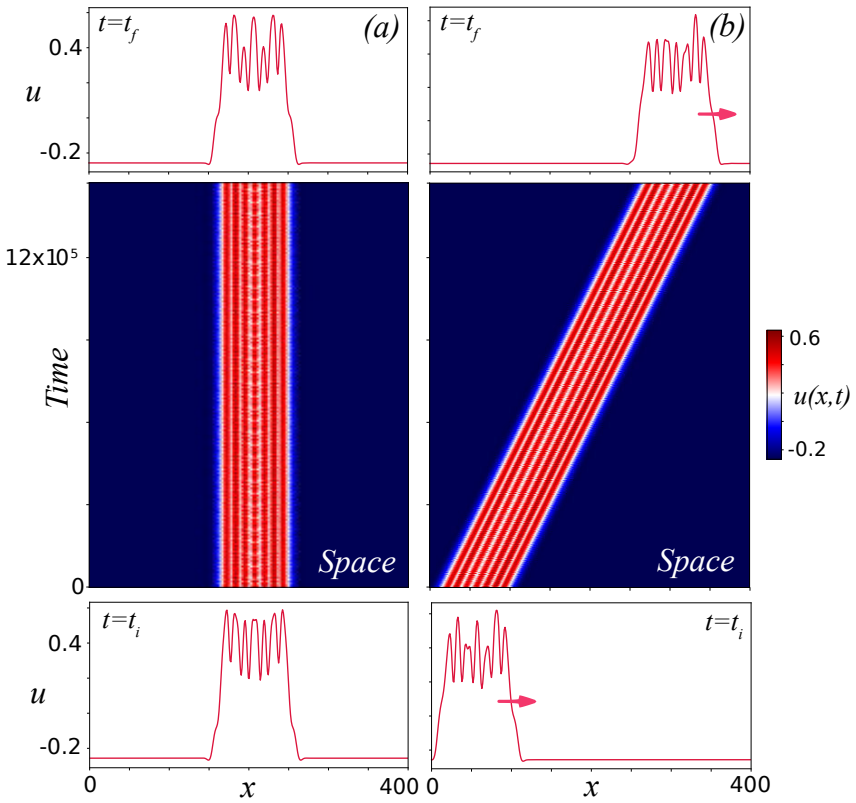

Figure 5.1: Coexisting motionless and traveling chimera states. Spatiotemporal diagrams for motionless (a) and traveling (b) chimera states for parameter values $\eta = -0.04$, $\mu = -0.09$, $\nu = 1$, $b = -1.5$, and $c = 10$. The top and bottom panels accounts for the profiles of the chimera state at the initial $u(x, t = t_{\mathrm{i}} = 0)$ and final $u(x, t = t_f = 15 \times 10^5)$ instant of the spatiotemporal diagram.

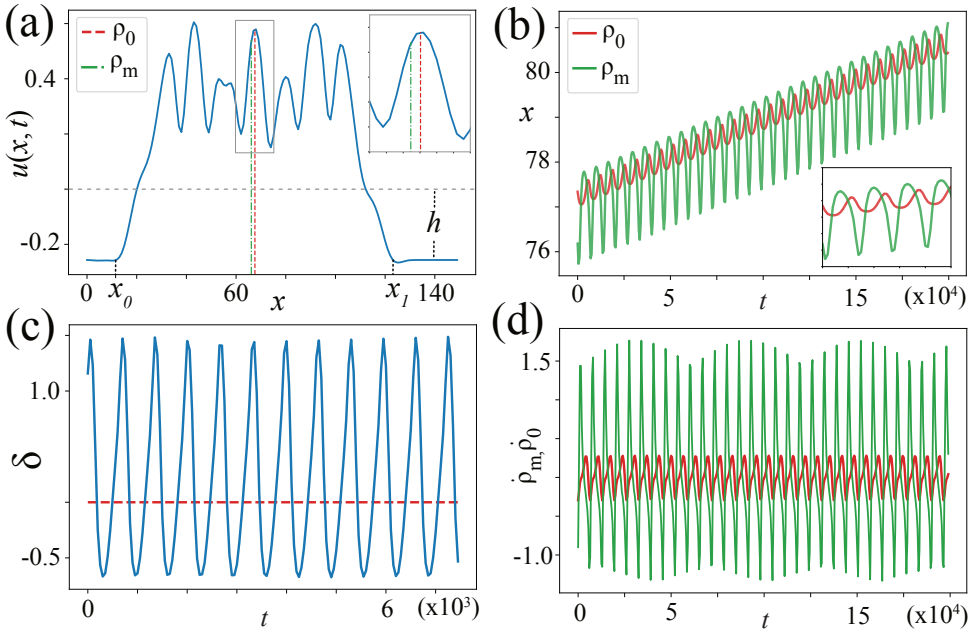

Figure 5.2: Propagation characterization of a chimera state for Eq. (5.1) with $\eta = -0.04$, $\mu = -0.09$, $\nu = 1$, $b = -1.5$, and $c = 10$. (a) Profile of a propagative chimera-like at a given time. Its centroid ρ_0 and median ρ_m are indicated by the red and green dashed vertical line, respectively and h accounts for the background value of the chimera state. (b) Temporal evolution of the centroid and median. (c) Temporal evolution of the disparity of the localized structure. The dashed curve accounts for the horizontal axis. (d) Temporal derivative of the centroid (green) and median (red).

the material heterogeneity, the dynamics could be highly complex, as almost all can see at burning gunpowder or in some fireworks [109].

5.2 Traveling chimera states in the nonvariational Turing-Swift-Hohenberg equation

To illustrate the phenomenon of traveling chimera states, we will explore the dynamics of the generalized Turing-Swift-Hohenberg equation, presented in the above chapter and given by

$$\partial_t u = \eta + \mu u - u^3 - \nu \partial_{xx} u - \partial_{xxxx} u + b u \partial_{xx} u + c(\partial_x u)^2. \tag{5.1}$$

For the reader's ease, we recall that the first three terms account for an imperfect pitchfork normal form, μ is a bifurcation parameter, and η stands for the asymmetry between the equilibria. The second and fourth derivatives account for diffusion and hyper-diffusion process. The terms weighted by b and c accounts for the nonlinear diffusion and nonlinear advection and are responsible for the nonvariational dynamics. In the nonvariational regime, Eq. (5.1) exhibit different kinds of traveling chimera states. In Fig. 5.1 is shown a typical traveling chimera state. Note that chimera states can coexist with motionless chimeras.

To unveil such dynamical solutions and statistical properties, we realize an in-depth numerical exploration and define some metrics to track its position and capture its asymmetry.

5.3 Position, speed, and asymmetry of chimeras

To characterize the propagation speed of the traveling chimeras, we need first define its position. In this scenario, we explore two possibilities, namely, the centroid of the localized solution defined by

$$\rho_0(t) \equiv \frac{\int_{-L/2}^{L/2} x(u(x,t)-h)\mathrm{d}x}{\int_{-L/2}^{L/2}(u(x,t)-h)\mathrm{d}x}, \tag{5.2}$$

and a second one inspired in the most more straightforward geometric definition of position, given by the median of the localized structure, defined by

$$\rho_m(t) \equiv \frac{x_0(t)+x_1(t)}{2}, \tag{5.3}$$

Both Eqs. (5.2) and (5.3) enable us to track the localized state throughout the space. These solutions enable us to define a mean speed, taking as speed the slope of the linear fit of the curve described by the position vs. time. The position and speed of a chimera state of $N = 7$ peaks is shown in figure 5.2. To reveal the mechanism behind the propagation of these localized structures, we propose quantifying its disparity by

$$\delta(t) \equiv \rho_0(t) - \rho_m(t). \tag{5.4}$$

Obtaining that for motionless chimera states, the averaged disparity $\langle\delta(t)\rangle \approx 0$. For traveling chimeras, this value reaches a well-determined value that is positive or negative, depending on the direction of propagation of the localized structure. A plot for the temporal evolution and mean values of the asymmetry for both motionless and traveling states is shown in figure 5.1.

5.4 Traveling chimeras and bounded solutions

We let vary the parameters of the model in order to look for other traveling chimera states. In particular, we found chimera states of different sizes or peaks, as shown in figure 5.3.

It enabled us to explore its coexistence, interaction, and bounded states formation. To clarify these points, we consider numerically several scenarios, e.g., taking

1. two coexisting traveling chimeras of different sizes propagating in the same direction,
2. two counter-propagative chimeras of the same size, and
3. two counter-propagative chimeras with different sizes.

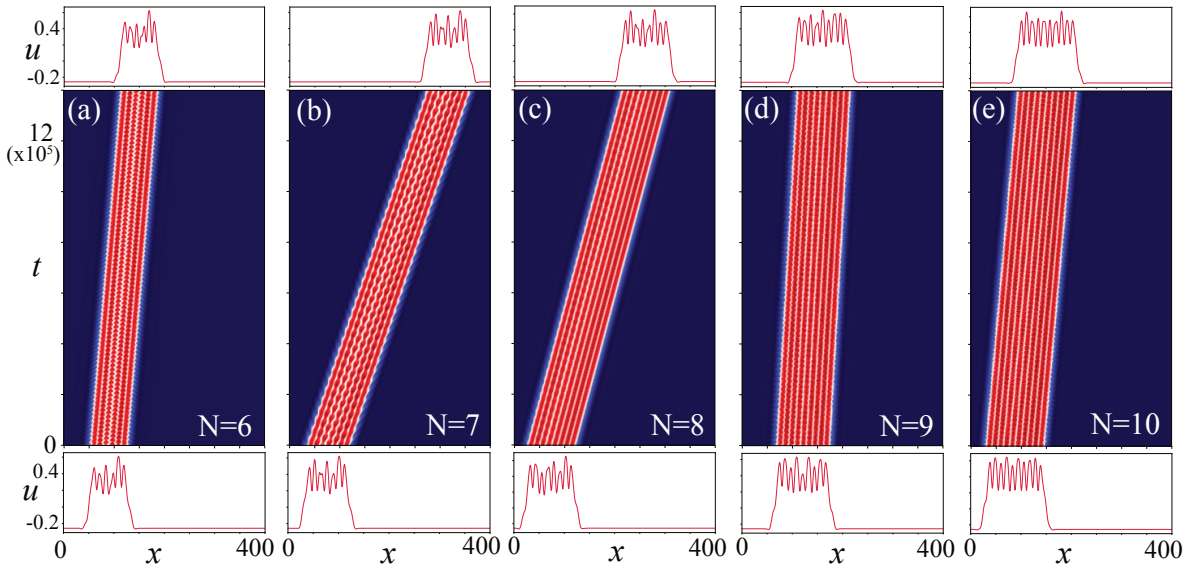

Figure 5.3: Spatiotemporal diagrams for chimera states of $N = 6, 7, 8, 9, 10$ peaks.

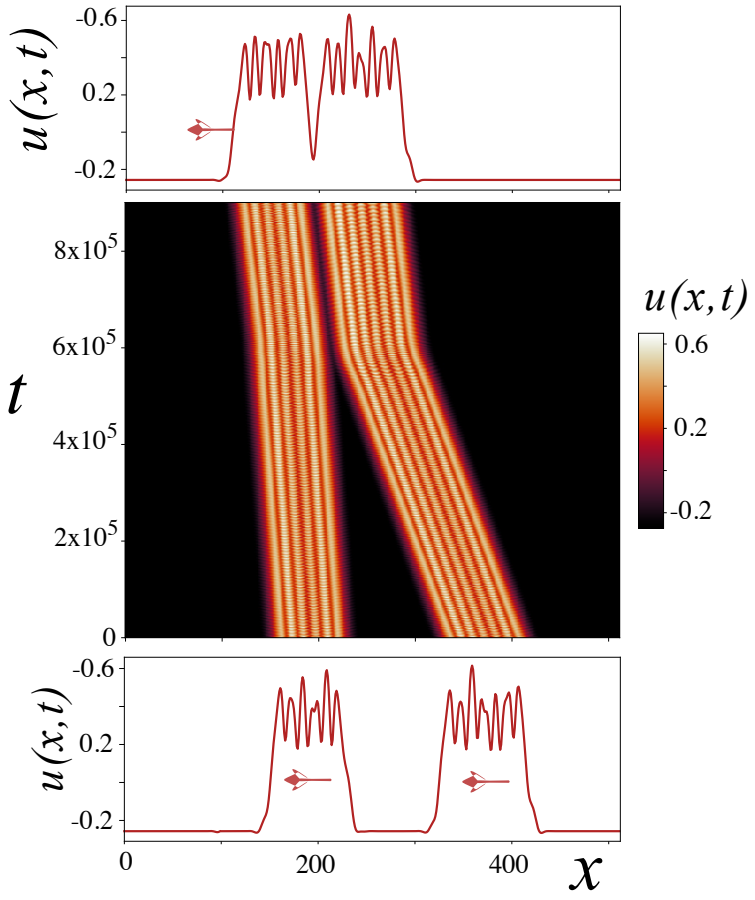

Figure 5.4: Two traveling chimera states propagating in the same direction, forming a train-like bounded state.

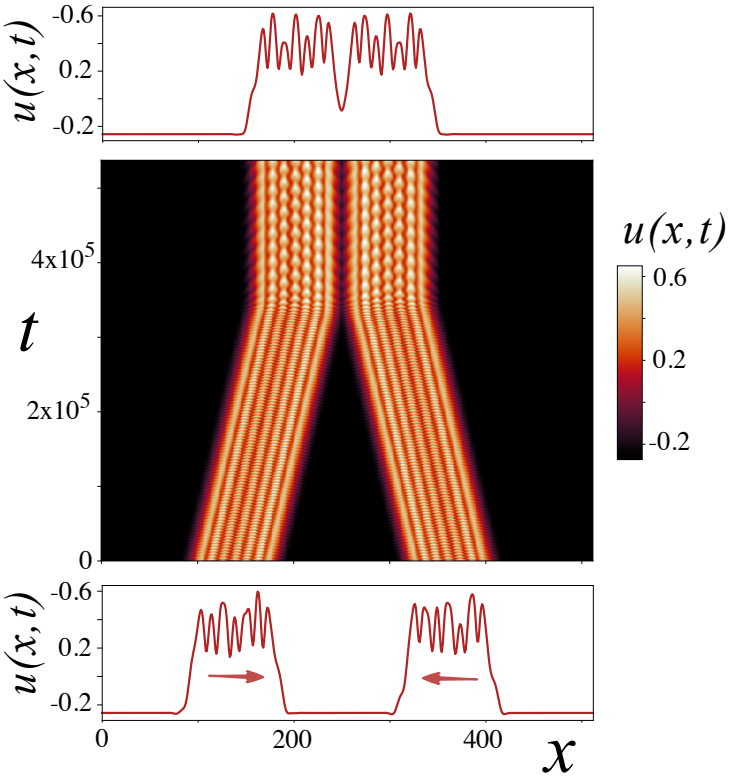

Figure 5.5: Plastic collision of two counterpropagative chimera states of equal sizes.

In the first scenario of two coexisting chimeras of different sizes and propagating in the same direction, we obtain that the faster reach to the slower and interact forming a new bounded state (train-like) as is depicted in Fig. 5.4, whose speed is slightly faster than the speed of the slower chimera.

As a second numerical test, to explore the interaction of equal size counter-propagative chimera to see the effect of such collision. In this case, we observe a plastic collision as is expected of a soft-matter macroscopic "particle", as we can see in Fig. 5.5. It is noteworthy that, for the one-peak localized states studied in the above chapter, the collision of two particles was elastic, and the plasticity in the scenario of chimera states could be a consequence of the interplay between the intrinsic dynamics and the interaction of the localized states.

Finally, we explore the scenario of counter-propagative chimera states with different sizes. In this case, after the collision, the particle with more "mass" drag the smaller one, as is represented in the spatiotemporal diagram showed in Fig. 5.6.

5.5 Dark traveling chimeras

From the optical point of view, dark solitons can be understood as dark spots in an optical illuminated medium [110, 111], contrasting to the bright solitons. From the nonlinear physics point of view, both can be represented by solitary-wave solutions (or dissipative solitons) where its envelope is positive or negative concerning the background state, whose shape does not change the co-moving frame. Although it has mainly been described in fiber optics dy-

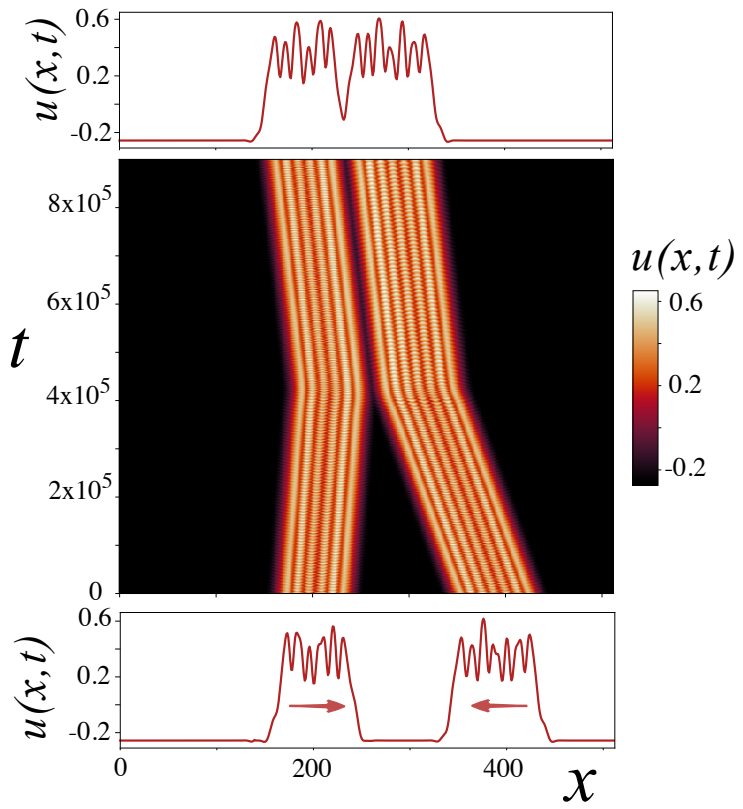

Figure 5.6: Collision of two counterpropagative chimera states of different sizes.

namics [111, 112], but there appears in liquid crystals [113, 114], photovoltaic photorefractive materials [115] to mention a few. In a more general framework, dark solitons can be seen as holes in the order parameter (typically a density) in the spatially extended system under study. In this scenario, if we identify the above-studied chimera state as a bright soliton, we can define an equivalent to a dark chimera, where the hole represents the incoherent zone. In figure 5.7 we can see this kind of solution for the nonvariational Turing-Swift-Hohenberg equation.

It is noteworthy that, in the context of the Turing-Swift-Hohenberg equation, dark chimeras exist due to the symmetry properties of the equations. It could be obtained from bright traveling chimeras by performing the following variable changes $\eta \to -\eta$, $b \to -b$ and $c \to -c$ and taking $u(x,0) = -u(x,0)$ as the initial condition.

5.6 Outline

- The emergence of these intriguing states brings a natural bridge between coherence and incoherence behavior in natural systems.
- The generalization of chimera states in higher dimensions remains under research.
- We are interested in the design of experiments where such kinds of states appear. The nonvariational terms could be accessible as a physical knob, similar to the diffraction in the fronts observed in the liquid crystal light valve experiment.

- Due to the emergence of the Turing-Swift-Hohenberg in disciplines like ecology, chemistry, and social dynamics, we expect to see these states in such systems. A possible direction for further work is to explain the mechanism behind the appearance of such dissipative structures in such disciplines and their consequences.

Commun Nonlinear Sci Numer Simulat 94 (2021) 105559

Contents lists available at ScienceDirect

Commun Nonlinear Sci Numer Simulat

journal homepage: www.elsevier.com/locate/cnsns

Research paper

Traveling chimera states in continuous media

A.J. Alvarez-Socorro [a,b,*], M.G. Clerc [a], N. Verschueren [c]

[a] Departamento de Física and Millennium Institute for Research in Optics, Facultad de Ciencias Físicas y Matemáticas, Universidad de Chile, Casilla Santiago, 487-3, Chile
[b] Laboratorio de Investigación, Desarrollo e Innovación, Zenta Group, Andrés Bello 2687, Las Condes, Santiago, Chile
[c] College of Engineering, Mathematics and Physical Sciences, University of Exeter, Exeter, United Kingdom

ARTICLE INFO

Article history:
Received 4 February 2020
Revised 23 September 2020
Accepted 2 October 2020
Available online 6 October 2020

Keywords:
Localized structures
Chimeras
Nonvariational effects
Traveling states

ABSTRACT

Coupled oscillators exhibit intriguing dynamical states characterized by the coexistence of coherent and incoherent domains known as chimera states. Similar behaviors have been observed in coupled systems and continuous media. Here we investigate the transition from motionless to traveling chimera states in continuous media. Based on a prototype model for pattern formation, we observe coexistence between motionless and traveling chimera states. The spatial disparity of chimera states allows us to reveal the motion mechanism. The propagation of chimera states is described by their median and centroidal point. The mobility of these states depends on the size of the incoherent domain. The bifurcation diagram of traveling chimeras is elucidated.

1. Introduction

In recent years the so-called chimera states, defined as dynamical behaviors having coexistence of coherent and incoherent domains, have attracted the attention of the scientific community [1–22]. Since the seminal work of Kuramoto and Battogtokh [2], the universal phenomenon of chimeras states has been intensively studied. Most of these studies focus on discrete systems of coupled oscillators and only recently the dynamical richness of chimera solutions in continuous models has been explored [23,24,26,27]. In continuous media, the chimera states can be understood as localized spatiotemporal complex patterns resulting from a symmetry breaking. These localized structures can be of spatiotemporal chaotic, chaotic, or quasi-periodic nature. Experimentally, these states were reported in a liquid crystal light valve with optical feedback (termed *Chaoticons* [23,24]) and in fluids (identified as localized turbulence [28]). A requirement for observing chimera states in continuous media is the coexistence between a chaotic spatiotemporal or quasi-periodic pattern and a homogeneous state. The origin by which the domains are blocked is because the pattern in the interfaces induces a barrier, *pinning effect* [23,24,29]. As a result of this mechanism, one expects to find a family of localized solutions organized through a snaking type bifurcation diagram [30]. The discrete counterpart of the snaking type bifurcation diagram for chimera states has also been reported [15–18].

Experimentally, chimera states have been observed in discrete coupled systems in the following contexts: chemical oscillators [4], neurodynamics [19], liquid crystals [5], optoelectronic delayed feedback setup [20], laser diode coupled to a nonlinear saturable absorber [21], and laser diode subjected to a coherent polarization [22], among others. Chimera solutions

* Corresponding author at: Departamento de Física and Millennium Institute for Research in Optics, Facultad de Ciencias Físicas y Matemáticas, Universidad de Chile, Casilla 487-3, Santiago, Chile.
E-mail address: alejandro.alvarez@ing.uchile.cl (A.J. Alvarez-Socorro).

https://doi.org/10.1016/j.cnsns.2020.105559
1007-5704/

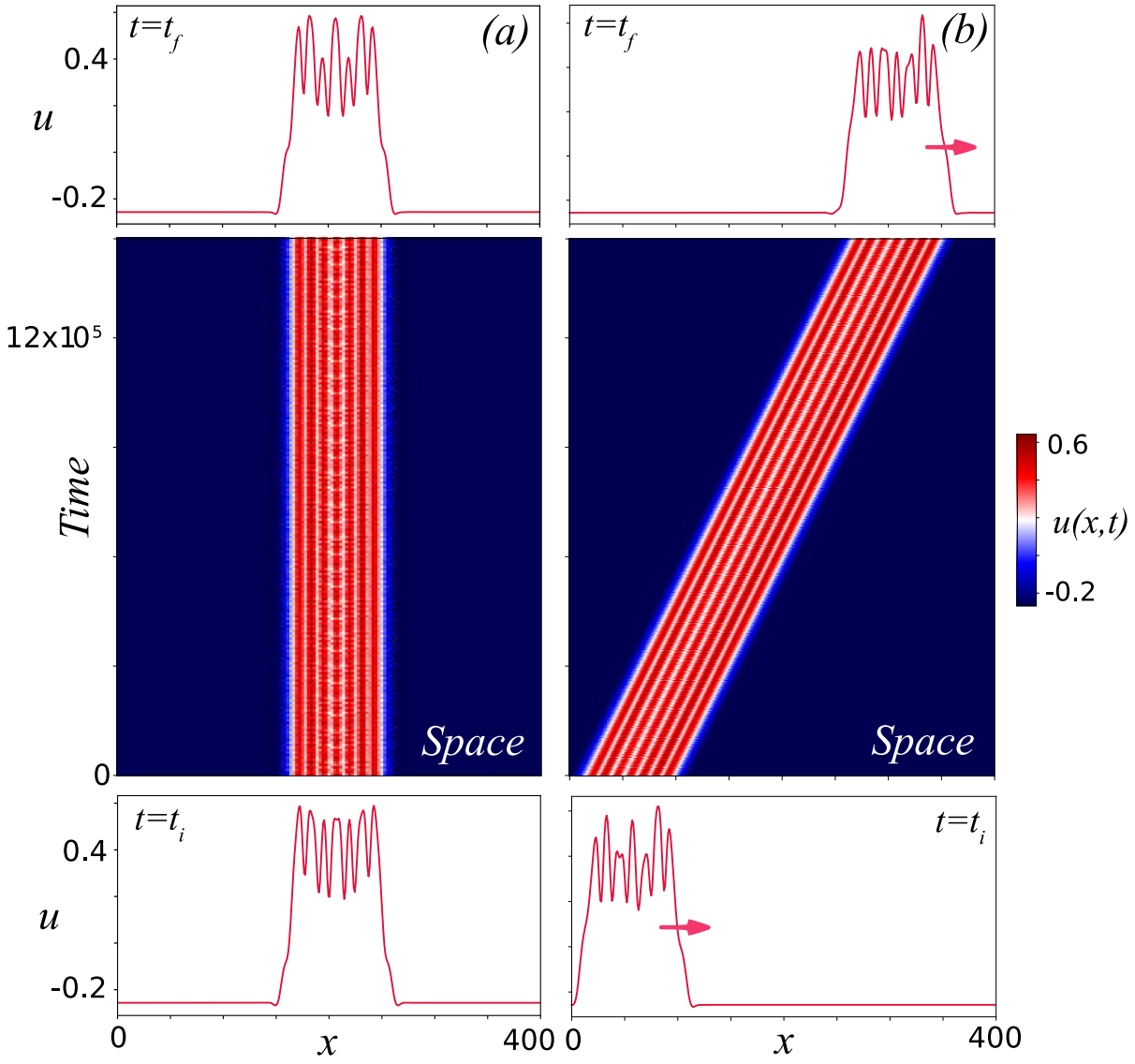

Fig. 1. (color online) Coexisting motionless and traveling chimera states. Spatiotemporal diagram of motionless (a) and traveling chimera state (b) for Eq. (1) when $\eta = -0.04$, $\mu = -0.09$, $\nu = 1$, $b = -1.5$, and $c = 10$. The top and bottom panels account for the profiles of the chimera state at the initial $u(x, t = t_i = 0)$ and final $u(x, t = t_f = 15 \times 10^5)$ instant of the spatiotemporal diagram.

can be interpreted as particle-type solutions; that is, these solutions can be characterized by a set of continuous parameters such as the position and width. They can be motionless [3], propagative [31–33], or wandering [34] in their position or centroid. The localized structures can move as a result of external symmetry-breaking instability induced by a phase gradient [35], off-axis feedback [36], resonator detuning [37], and space-delayed feedback [38]. Likewise, internal symmetry-breaking instability can induce propagative localized states [39,40]. Indeed, when a parameter is modified in continuous media, localized solutions become asymmetric and propagate due to non-variational effects. The dynamics of localized states can be described by the median and centroid. The median is defined as the middle point of the incoherent (spatiotemporal) domain. Meanwhile, the centroid is the point defined by the profile weighted average of the localized state. In general, for asymmetric solutions, both quantities do not coincide. The difference between these quantities accounts for the disparity.

In this manuscript, we aim to investigate traveling chimera states in continuous media. Fig. 1 illustrates, for the same parameters, a motionless and traveling chimera state. Using a prototype model for pattern formation, the non-variational Turing-Swift-Hohenberg equation, we unveil the transition of chimera states from motionless to propagative. Since this transition is subcritical, depending on the initial conditions the system would exhibit coexistence between chimera states of different sizes and speeds. Indeed, a family of propagative chimera states and their respective bifurcation diagram is presented. The motion mechanism of chimera states can be characterized using their spatial disparity. Notice that in spite of their spatiotemporal chaotic nature, traveling chimera states propagate with a well-defined oscillatory speed.

The rest of the article is organized as follows. In Section 2, the mathematical model for pattern formation used throughout the paper as well as their chimera solutions are introduced. Section 3 presents a characterization of chimera solutions in

terms of the temporal evolution of their centroid, median, and disparity. Section 4 is devoted to the study of the propagation of chimera states as a function of their width. Concluding remarks are presented in Section 5.

2. The non-variational Turing-Swift-Hohenberg equation

A prototype model in pattern formation is the Swift-Hohenbeg equation [41]. This model, originally deduced to describe the pattern formation on Rayleigh-Bénard convection [41], is an isotropic real order parameter nonlinear equation with reflection symmetry.

A recent paper [42], has shown that Alan Turing derived essentially the same equation in a completely different context. In his unpublished draft notes entitled "'Outline of the development of the Daisy", Turing anticipates pattern formation based on the interaction of Fourier modes, proposing the equation and organizing the stability of symmetric pattern solutions through symmetry. As a recognition to both origins of the equation and to emphasize its robustness, from here on we will refer to this model as *the Turing-Swift-Hohenbeg equation*.

A generalization of this equation, including reflection symmetry breaking terms, describes the dynamics of a system in the vicinity of a spatial symmetry breaking instability and close to a second-order critical point marking the onset of a hysteresis loop. This critical point is denominated as the *Lifshitz point* [43]. Due to the universality of this bifurcation, this generalized model has been deduced in several contexts such as chemistry [44], plant ecology [45,46] and nonlinear optics [47].

This model exhibits extended patterns as well as localized structures as equilibrium solutions. However, due to its variational nature, these structures do not have permanent dynamics. In this manuscript, we will consider a non-variational generalization. For a one dimensional spatially extended systems, the model is given by Residori et al. [48], Clerc et al. [49],

$$\partial_t u = \eta + \mu u - u^3 - \nu \partial_{xx} u - \partial_{xxxx} u + 2bu\partial_{xx} u + c(\partial_x u)^2, \tag{1}$$

where $u = u(x,t)$ is a real scalar field, function of the spatial coordinate x and time t. The interpretation of u depends on the physical context where the model has been derived. For instance, it could correspond to the electric field, deviation of molecular orientations, phytomass density, or chemical concentration [48–50]. Regarding the parameters, μ is the bifurcation parameter responsible for the bistability of the homogeneous equilibria. The parameter η is also a bifurcation parameter, breaking the reflection symmetry of the scalar field ($u \to -u$) and therefore accounts for the asymmetry between homogeneous states. The term proportional to ν account of the diffusion ($\nu < 0$) or anti-diffusion process ($\nu > 0$). The symbols ∂_{xx} and ∂_{xxxx} stand for the Laplacian and bilaplacian, respectively. The bilaplacian term accounts for a hyper-diffusion process. Terms proportional to b and c, account for nonlinear diffusion and advection, respectively. Notice that when $\eta = b = c = 0$, one recovers the Turing-Swift-Hohenbeg equation.

2.1. Chimera states in continuous media

For a certain region of parameters, model Eq. (1) exhibits coexistence between a chaotic spatiotemporal pattern and a uniform state [23]. In Ref. [51] a detailed study of the chaotic spatiotemporal pattern is reported. As stated before, the coexistence of these behaviors is a prerequisite for observing spatiotemporal chaotic localized states, chaoticons or chimera states in continuous media. A numerical investigation on this parameters region shows that depending on the initial conditions, localized structures of stationary [47], oscillatory [49], and chaotic [23] nature can be observed. Moreover, the width of these localized structures seems to quantify the complexity of their behavior. A wider localized structure allows the existence of a higher number of spatial modes and therefore the number of positive Lyapunov exponents increases [23].

The conducted numerical study considers simulations of model Eq. (1) with periodic boundary conditions. Integration was implemented using a fourth-order explicit Runge-Kutta scheme for the time with a fixed time-step size and a finite differences scheme in space with a centered stencil of 7 grid points. $dx = 0.6$ and grid size $L = 400$. The results presented in this manuscript consider, for the sake of reproducibility, the fixed numerical parameters $(dt, dx, L) = (0.01, 0.6, 400)$. We have numerically confirmed that these results hold for different values of the numerical parameters. Likewise, for simplicity, we have only varied the non-variational parameter c to study chimera states. However, the reported findings are also observed for different values of the other parameters.

Fig. 1 shows a motionless (left panel) and traveling (right panel) chimera-type states observed for the same parameters and different initial conditions. A well-defined speed for the traveling chimera can be observed in the spatiotemporal diagram [cf. Fig. 1(b)]. The motionless (traveling) chimera is characterized on average by being symmetric (asymmetric).

To obtain chimera states, we use as initial conditions asymmetric Gaussians with different widths and heights sustained by the steady homogeneous state. Symmetric and asymmetric Gaussians initial conditions were used for Fig. 1. Chimera states in continuous media can be understood as stable equilibrium points of the interaction of fronts that separate the coherent and incoherent domains [23,24]. They can be considered as attractors and consequently any localized initial condition with size and amplitude similar to a chimera state will converge to it. Consequently, any localized initial condition with size and amplitude similar to a chimera state will converge to it.

To figure out the complexity of motionless and traveling chimera states for the same parameters, we have computed the instantaneous and average power spectrum of each state, $a[u] \equiv |\int_{-L/2}^{L/2} e^{ikx} u(x,t)|^2 dx$ and $\langle a[u] \rangle \equiv \int_0^T a[u(t,k)]dt/T$, respec-

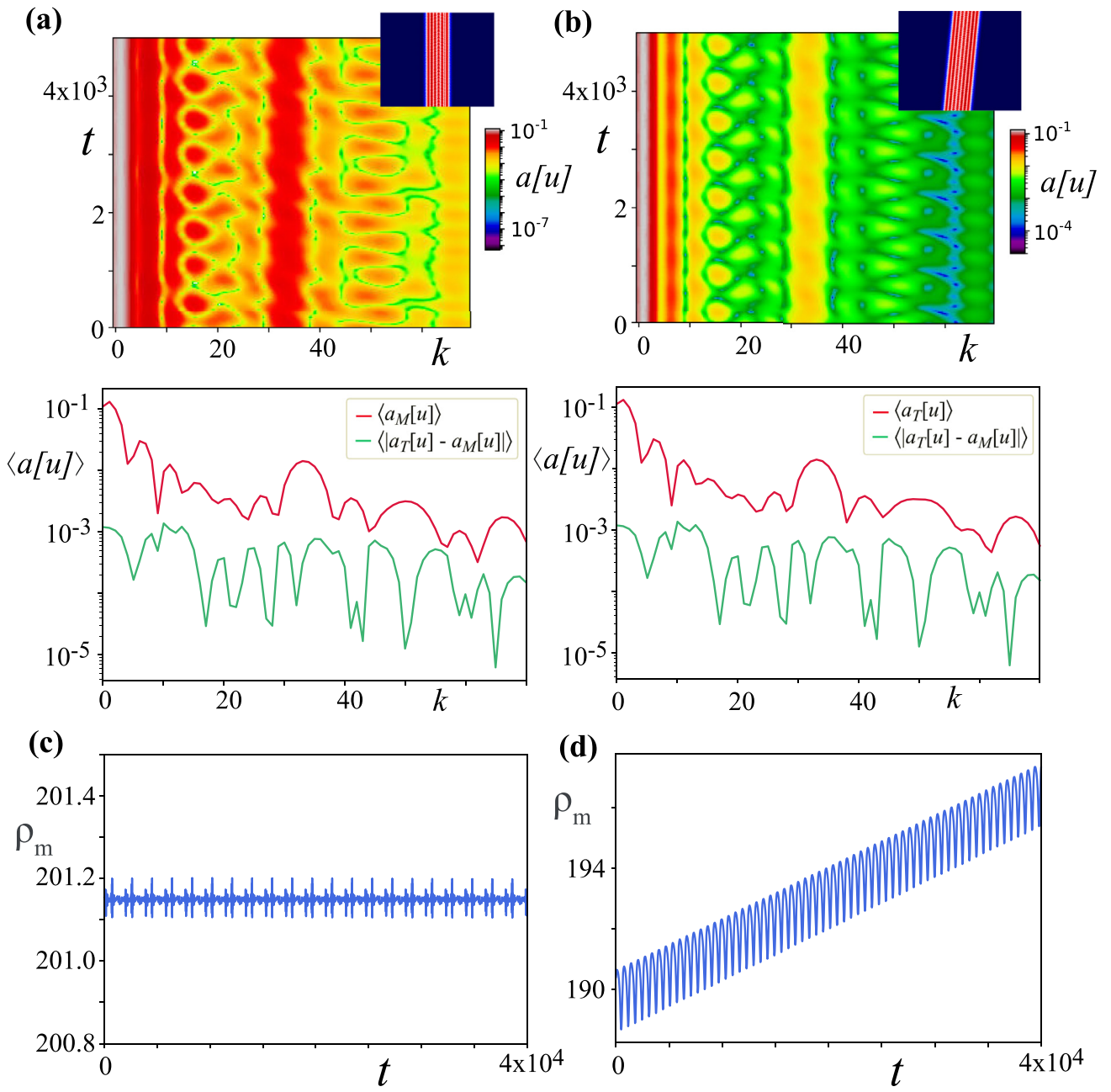

Fig. 2. (color online) Motionless versus traveling chimera state. Power spectra of motionless (a) and traveling chimera state (b). The top and bottom panels account for the instantaneous $a[u]$ and average $\langle a[u]\rangle$ power spectrum. Insets in top panels stand for spatiotemporal evolution of the motionless and traveling chimera states, respectively. Median evolution of motionless (c) and traveling (d) chimera states.

tively. Fig. 2 depicts the power spectra of motionless and traveling chimera state and the evolution of their median. These spectra reveal the complex spatiotemporal nature of both states. Although the spectra of traveling and motionless chimera share many features, the extra complexity exhibited by the motionless one allows a distinction via the power spectrum (see bottom panels of Fig. 2a and b).

3. Propagation characterization of chimera state

To shed light on the collective dynamics of chimera-like states, let us consider as a order parameter, the centroid of the localized structure,

$$\rho_0(t) \equiv \frac{\int_{-L/2}^{L/2} x(u(x,t)-h)dx}{\int_{-L/2}^{L/2}(u(x,t)-h)dx}, \tag{2}$$

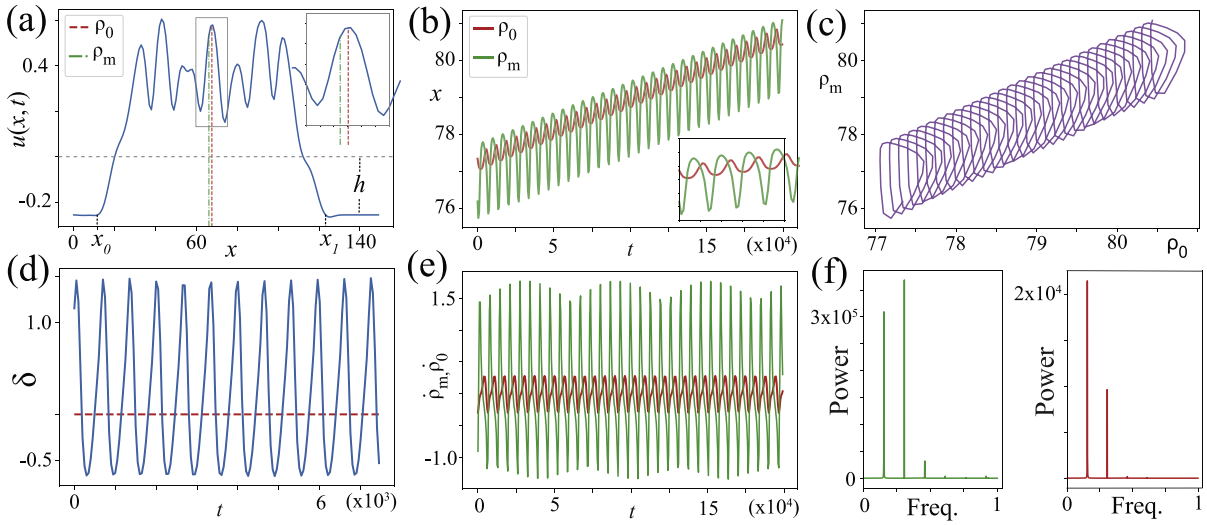

Fig. 3. (color online) Propagation characterization of a chimera state for Eq. (1) with $\eta = -0.04$, $\mu = -0.09$, $\nu = 1$, $b = -1.5$, and $c = 10$. (a) Profile of a propagative chimera-like at a given time. Its centroid ρ_0 and median ρ_m are indicated by the red and green dashed vertical line, respectively and h accounts for the background value of the chimera state. (b) Temporal evolution of the centroid and median. (c) Dynamics in the phase portrait build-up by the median and centroid variable. (d) Temporal evolution of the disparity of the localized structure. The dashed curve accounts for the horizontal axis. (e) Temporal derivative of the centroid (green) and median (red). (f) Power spectra of the derivatives of centroid and median, respectively.

where L is the system size and h is a constant which corresponds to the background of the chimera state (see Fig. 3a) and statisfy $\eta + \mu h - h^3 = 0$. The median of the localized structure is defined by

$$\rho_m(t) \equiv \frac{x_0(t) + x_1(t)}{2}, \tag{3}$$

where x_0 and x_1 are, respectively, the left and right extreme points of the incoherence region (see Fig. 3a). Note that $u(x_0, t) = u(x_1, t) = -h$. Fig. 3b shows the temporal evolution of the median (green) and centroid (red) of the chimera state. Both trajectories are oscillating and propagating. The average speed is numerically computed by taking the coefficient of the linear regression fitting for the centroidal trajectory. Fig. 3c depicts the dynamics of the centroid versus the dynamics of the median. Both quantities are oscillating out of phase in the comoving frame. That is, they describe a helicoidal trajectory (a closed cycle in the comoving frame).

To understand the mechanism behind the propagation of chimera states in continuous media, let us introduce the disparity parameter $\delta(t)$ (or asymmetry) of the localized structure, defined by

$$\delta(t) \equiv \rho_0(t) - \rho_m(t). \tag{4}$$

This quantity measures the asymmetry of the localized solution and a preferential propagation direction will be reflected in the dynamics of $\delta(t)$. For instance, Fig. 3(d) depicts the behavior of the disparity. Although this quantity oscillates, the average value is positive and consequently the centroid is shifted towards a direction determined by the initial conditions. Fig. 3(e) provides a speed profile of the localized structure by considering the temporal derivatives of the centroid and median. Power spectra of $\dot{\rho}_m(t)$ and $\dot{\rho}_0(t)$ have been included in panel (*f*), from which we can infer that the dynamic of the centroid and median are anharmonic and they can be represented in good approximation into the dominant Fourier modes.

4. Family of traveling localized structures

To study the family of chimera states and their organization, it will be useful to introduce the following terminology a N-chimera state corresponds to a chimera with N peaks.

So far a 7-chimera has been considered. Depending on the initial conditions, given by a slightly asymmetrical Gaussian with several widths were considered. More precisely, we consider widths of the order of 1,2,3,... wavelength of the chaotic spatiotemporal pattern, which allows observing $N = 6, 7, 8, 9, 10,$ and 11-chimera states. Furthermore, coexistence between distinct propagative chimera states was also observed. Interestingly, the smallest traveling chimera state found in the parameter region considered is a 6-chimera (see Fig. 4a). Fig. 4 shows the spatiotemporal evolution of different traveling chimera states using the same conventions as Fig. 1. Note that the complexity exhibited by the chimeras seems to increase with their width. As stated before, this can be regarded as a consequence of an increase in the number of positive Lyapunov exponents [23].

For equal parameters, chimera states of larger size propagate faster (have greater mobility). The origin of this is because the engine of propagation is the asymmetry of the localized solution and consequently the larger the localized state, the more asymmetrical modes are involved in the internal dynamics of the chimera solution.

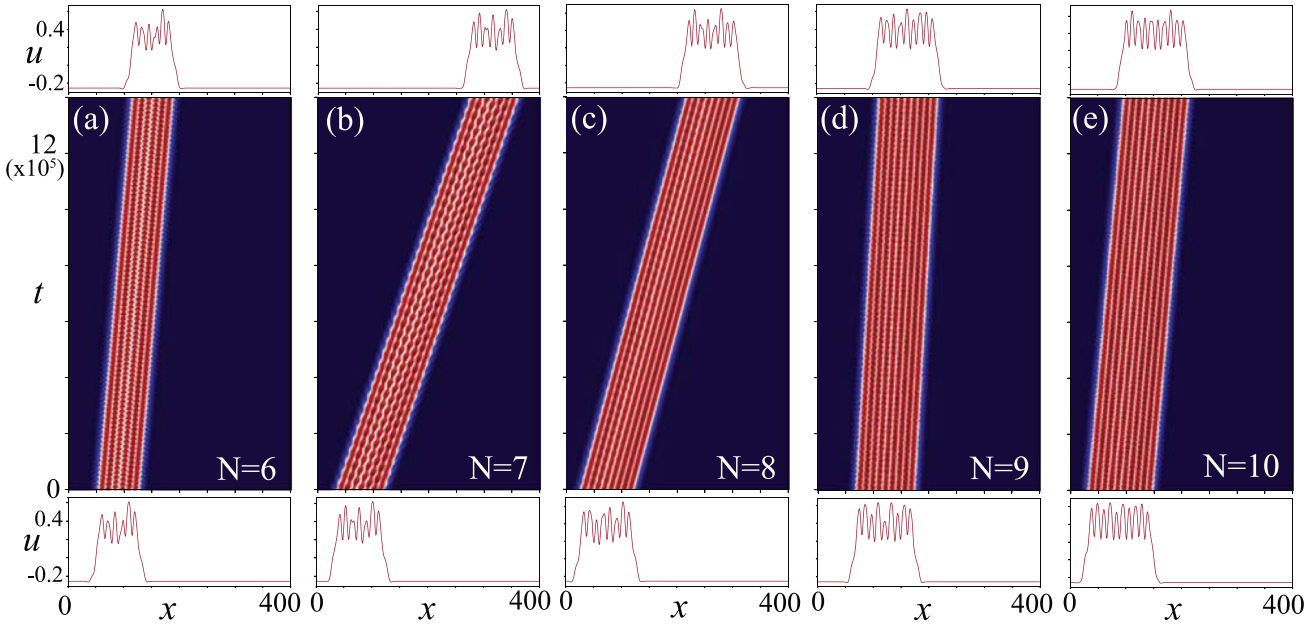

Fig. 4. (color online) Spatiotemporal diagrams for diverse traveling chimera states for N-chimera of model Eq. (1), for $\eta = -0.04$, $\mu = -0.09$, $\nu = 1$, $b = -1.5$. (a) $N = 6$ at $c = 10.3$, (b) $N = 7$ at $c = 10$, (c) $N = 8$ at $c = 9.7$, (d) $N = 9$ at $c = 9.5$ and (e) $N = 10$ at $c = 9.3$. At the top and bottom of each spatiotemporal diagram is shown the initial ($t = 0$) and final ($t = 14 \times 10^5$) profile state.

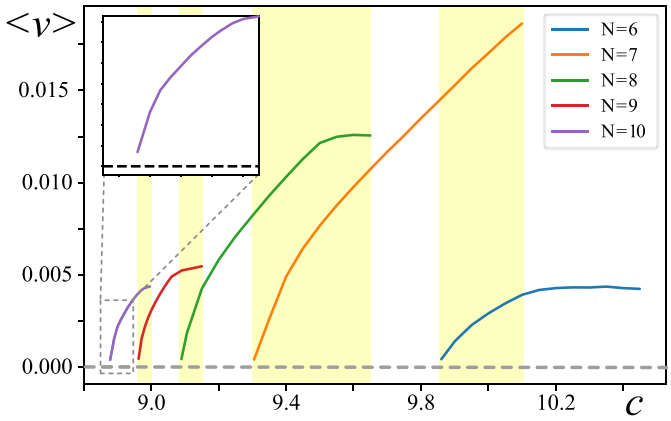

Fig. 5. (color online) Average speed $\langle v \rangle$ and coexistence of traveling chimera states of model Eq. (1) as a function of advection c parameter, for $\eta = -0.04$, $\mu = -0.09$, $\nu = 1$, and $b = -1.5$. Painted regions (beige) account for the region of coexistence of two traveling chimera states. The curves of different colors account for localized propagative structures of different peaks. The inset presents more detail of the first branch $N = 10$.

To explore the dynamics of a localized solution of a given size, we consider an asymmetric initial condition with a similar size and let the system evolves. Once the solution is stationary, i.e., it maintains its area fluctuating around a value. Then, we determine the centroid and its average speed. By measuring the slope of a linear fit over position with respect to time the average speed is determined. Later, the c parameter is increased or decreased by ± 0.01. To check the persistence of the solution is verified that there are no significant changes in the area and speed. The above process is systematically repeated for different chimeras. Fig. 5 summarizes the speed of chimera states as a function of the non-variational advection parameter c. Beige panels highlight the regions where coexistence of traveling chimera states is observed. Notice that we have only found regions of a single or coexistence of at most two traveling chimera states. When the value of c is increased, chimeras propagate faster. Observe that traveling chimera states always emerge with a finite no null speed (see Fig. 5).

Due to the asymmetry generated by the oscillations of the peaks, we conjecture that chimeras smaller than a critical size will not be able to achieve a preferential direction of propagation. Nevertheless, they could still develop an erratic or wandering dynamical behavior within a bounded region of the order of one wavelength. On the other hand, in chimera states of large sizes the centroid is closer to the geometric center on average and therefore the average disparity will tend to zero. Hence, large structures will not propagate. In the parameter regime considered, the largest structure observed was a 11-chimera. Therefore, traveling chimera solutions will only be observed in a range of sizes.

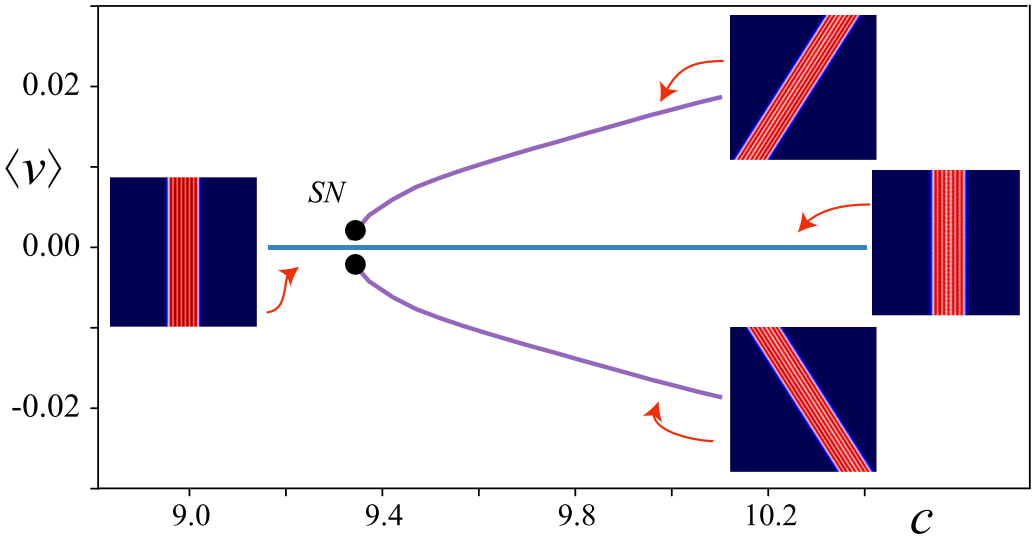

Fig. 6. (color online)(a) Speed of 7-chimera states as a function of nonlinear advection parameter c of model Eq. (1) for $\eta = -0.04$, $\mu = -0.09$, $\nu = 1$, and $b = -1.5$. The inserts correspond to the respective chimera states. Circles account for the saddle-node bifurcations.

5. Bifurcations

In the previous section, we observed that the advection parameter c in model Eq. (1) seems to control the speed of chimera states. In this section, we consider the transition of a 7-chimera from static to traveling when c is varied.

Fig. 6 shows the speed of the 7-chimera state as a function of c. This chart was obtained using a similar method employed for Fig. 5. However, asymmetric and complimentary initial conditions were used to obtain a chimera and its counterpropagating one. The complimentary initial condition is obtained by inverting the spatial coordinate sense. From the numerical simulations we infer that the propagative chimera states emerge from a saddle-node bifurcation. This instability is represented by full circles denoted by SN in Fig. 6. Due to the lack of a continuation method for unstable chaotic solutions, we can not complete the bifurcation diagram. By increasing the value of parameter c, we observe that the propagative chimera becomes unstable. Depending on the initial conditions, this propagative localized states can engender the uniform state, smaller localized structures, or motionless chimera. Therefore, the basin of attraction of these equilibria are of complex nature, probably with fractal structures. Studies of these basins of attraction are in progress.

6. Conclusions

We have shown a novel class of chimera traveling solutions in spatially extended continuous systems, using the non-variational Turing-Swift-Hohenberg type Eq. (1), as a prototype model. Since this is a model of broad interest in pattern formation and relevant in a wide variety of systems [50], we expect to observe these solutions in several natural and technological systems.

We have investigated the properties of chimera states by defining and studying the temporal evolution of the centroid and median of localized structures. These quantities suggested the consideration of the disparity to measure the asymmetry of chimeras in time. The disparity provided a description for the mechanism responsible for the propagation of chimera states. In particular, it provides a plausible argument for the existence of traveling chimera state in an interval of sizes (6–11 in our case). Moreover, using this dynamical quantities a bifurcation diagram of stable propagative chimera solutions has been presented. To obtain a complete bifurcation diagram, a continuation method is required. However, there are not continuation methods for unstable chaotic solutions yet. This is a major problem in modern bifurcation theory.

Recently, the chimera state phenomenon has been extended to 2 and 3 spatial dimensions [25,26,32,52–55]. We expect that the phenomenon studied in the present paper can be observed in more dimensions, work in this direction is in progress.

Declaration of Competing Interest

The authors declare that they have no known competing financial interests or personal relationships that could have appeared to influence the work reported in this paper.

CRediT authorship contribution statement

A.J. Alvarez-Socorro: Conceptualization, Investigation, Validation, Software, Writing - original draft, Writing - review & editing. **M.G. Clerc:** Supervision, Project administration, Conceptualization, Investigation, Validation, Methodology, Writing - review & editing. **N. Verschueren:** Writing - review & editing, Validation.

Acknowledgments

MGC thanks for the financial support of FONDECYT projects 1180903. This work was funded by ANID–Millennium Science Initiative Program–ICN17_012. AJAS thanks financial support from Becas Conicyt 2015, Contract no. 21151618.

References

[1] Kaneko K. Clustering, coding, switching, hierarchical ordering, and control in a network of chaotic elements. Phys D 1990;41:137–72.
[2] Kuramoto Y, Battogtokh D. Coexistence of coherence and incoherence in nonlocally coupled phase oscillators. Nonlinear Phenom Complex Syst 2002;5:380–5.
[3] Abrams DM, Strogatz SH. Chimera states for coupled oscillators. Phys Rev Lett 2004;93:174102.
[4] Tinsley MR, Nkomo S, Showalter K. Chimera and phase-cluster states in populations of coupled chemical oscillators. Nat Phys 2012;8:662–5.
[5] Hagerstrom AM, Murphy TE, Roy R, Hövel P, Omelchenko I, Schöll E. Experimental observation of chimeras in coupled-map lattices. Nat Phys 2012;8:658–61.
[6] Omel'chenko OE. Coherence-incoherence patterns in a ring of non-locally coupled phase oscillators. Nonlinearity 2013;26:2469–98.
[7] Martens EA, Thutupalli S, Fourriere A, Hallatschek O. Chimera states in mechanical oscillator networks. Proc Natl Acad Sci 2013;110:10563.
[8] Kapitaniak T, Kuzma P, Wojewoda J, Czolczynski K, Maistrenko Y. Imperfect chimera states for coupled pendula. Sci Rep 2014;4:6379.
[9] Gambuzza LV, Buscarino A, Chessari S, Fortuna L, Meucci R, Frasca M. Experimental investigation of chimera states with quiescent and synchronous domains in coupled electronic oscillators. Phys Rev E 2014;90:032905.
[10] Larger L, Penkovsky B, Maistrenko Y. Virtual chimera states for delayed-feedback systems. Phys Rev Lett 2013;111:054103.
[11] Wickramasinghe M, Kiss IZ. Spatially organized dynamical states in chemical oscillator networks: synchronization, dynamical differentiation, and chimera patterns. PLoS One 2013;8:e80586x.
[12] Schmidt L, Schönleber K, Krischer K, Garcia-Morales V. Coexistence of synchrony and incoherence in oscillatory media under nonlinear global coupling. Chaos 2014;24:013102.
[13] Wickramasinghe M, Kiss IZ. Spatially organized partial synchronization through the chimera mechanism in a network of electrochemical reactions. Phys Chem Chem Phys 2014;16:18360.
[14] Rosin DP, Rontani D, Haynes ND, Schöll E, Gauthier DJ. Transient scaling and resurgence of chimera states in networks of boolean phase oscillators. Phys Rev E 2014;90:030902(R).
[15] Clerc MG, Coulibaly S, Ferre MA, Garcia-Nustes MA, Rojas RG. Chimera-type states induced by local coupling. Phys Rev E 2016;93:052204.
[16] Hizanidis J, Lazarides N, Tsironis GP. Robust chimera states in SQUID metamaterials with local interactions. Phys Rev E 2016;94:032219.
[17] Clerc M, Ferré MA, Coulibaly S, Rojas RG, Tlidi M. Chimera-like states in an array of coupled-waveguide resonators. Opt Lett 2017;42:2906–9.
[18] Clerc MG, Coulibaly S, Ferré MA, Rojas RG. Chimera states in a duffing oscillators chain coupled to nearest neighbors. Chaos 2018;28:083126.
[19] Compte A, Brunel N, Rakic GPS, Wang XJ. Synaptic mechanisms and network dynamics underlying spatial working memory in a cortical network model. Cerebral Cortex 2000;10:910–23.
[20] Larger L, Penkovsky B, Maistrenko Y. Laser chimeras as a paradigm for multistable patterns in complex systems. Nat Commun 2015;6:7752.
[21] Viktorov EA, Habruseva T, Hegarty SP, Huyet G, Kelleher B. Coherence and incoherence in an optical comb. Phys Rev Lett 2014;112:224101.
[22] Uy CH, Weicker L, Rontani D, Sciamanna M. Optical chimera in light polarization. APL Photon 2019;4:056104.
[23] Verschueren N, Bortolozzo U, Clerc MG, Residori S. Spatiotemporal chaotic localized state in liquid crystal light valve experiments with optical feedback. Phys Rev Lett 2013;110:104101.
[24] Verschueren N, Bortolozzo U, Clerc MG, Residori S. Chaoticon: localized pattern with permanent dynamics. Philos Trans R Soc A 2014;372:20140011.
[25] Schmidt L, Krischer K. Chimeras in globally coupled oscillatory systems: From ensembles of oscillators to spatially continuous media. Chaos 2015;25:064401.
[26] Nicolaou ZG, Riecke H, Motter AE. Chimera states in continuous media: Existence and distinctness. Phys Rev Lett 2017;119:244101.
[27] Alvarez-Socorro AJ, Clerc MG, Ferré M. Wandering walk of chimera-like states in continuous media. Manuscript submitted for publication 2020.
[28] Bohr T, Jensen MH, Paladin G, Vulpiani A. Dynamical systems approach to turbulence. Cambridge University Press; 2005.
[29] Pomeau Y. Front motion, metastability and subcritical bifurcations in hydrodynamics. Phys D 1986;23:3–11.
[30] Coullet P, Riera C, Tresser C. Stable static localized structures in one dimension. Phys Rev Lett 2000;84:3069.
[31] Dudkowski D, Czolczyński K, Kapitaniak T. Traveling chimera states for coupled pendula. Nonlinear Dyn 2019;95:1859–66.
[32] Omelchenko OE. Traveling chimera states. J Phys A 2019;52:104001.
[33] Xie J, Knobloch E, Kao HC. Multicluster and traveling chimera states in nonlocal phase-coupled oscillators. Phys Rev E 2014;90:022919.
[34] Omelchenko O, Wolfrum M, Maistrenko YL. Chimera states as chaotic spatiotemporal patterns. Phys Rev E 2010;81:065201(R).
[35] Turaev D, Radziunas M, Vladimirov AG. Chaotic soliton walk in periodically modulated media. Phys Rev E 2008;77:065201(R).
[36] Zambrini R, Papoff F. Signal amplification and control in optical cavities with off-axis feedback. Phys Rev Lett 2007;99:063907.
[37] Staliunas K, Sanchez-Morcillo VJ. Spatial-localized structures in degenerate optical parametric oscillators. Phys Rev A 1998;57:1454–7.
[38] Haudin F, Rojas RG, Bortolozzo U, Clerc MG, Residori S. Vortex emission accompanies the advection of optical localized structures. Phys Rev Lett 2011;106:063901.
[39] Alvarez-Socorro AJ, Clerc MG, Tlidi M. Spontaneous motion of localized structures induced by parity symmetry breaking transition. Chaos 2018;28:053119.
[40] Alvarez-Socorro AJ, Clerc M, González-Cortés G, Wilson M. Nonvariational mechanism of front propagation: Theory and experiments. Phys Rev E 2017;95:010202.
[41] Swift J, Hohenberg PC. Hydrodynamic fluctuations at the convective instability. Phys Rev A 1977;15:319–28.
[42] Dawes JH. After 1952: the later development of Alan Turing's ideas on the mathematics of pattern formation. Hist Math 2016;43:49–64.
[43] Hornreich RM, Luban M. Critical behavior at the onset of k-space instability on the λ line. Phys Rev Lett 1975;35:1678–82. R. M. Hornreich, J. Magn. Magn. Mater. 1980; 15, 387.
[44] Hilali MF, Dewel G, Borckmans P. Subharmonic and strong resonances through coupling with a zero mode. Phys Lett A 1996;217:263–8.
[45] Tlidi M, Lefever R, Vladimirov A. On vegetation clustering, localized bare soil spots and fairy circles. Lect Notes Phys 2008;751:381–402.
[46] Lefever R, Barbier N, Couteron P, Lejeune O. Deeply gapped vegetation patterns: on crown/root allometry, criticality and desertification. J Theor Biol 2009;261:194–209.
[47] Tlidi M, Mandel P, Lefever R. Localized structures and localized patterns in optical bistability. Phys Rev Lett 1994;73:640–3.
[48] Residori S, Petrossian A, Nagaya T, Clerc MG. Localized structures and their dynamics in a liquid crystal light valve with optical feedback. J Opt B 2004;6:S169.
[49] Clerc MG, Petrossian A, Residori S. Bouncing localized structures in a liquid-crystal light-valve experiment. Phys Rev E 2005;71:015205(R).
[50] Kozyreff G, Tlidi M. Nonvariational real Swift-Hohenberg equation for biological, chemical, and optical systems. Chaos 2007;17:037103.
[51] Clerc MG, Verschueren N. Quasiperiodicity route to spatiotemporal chaos in one-dimensional pattern-forming systems. Phys Rev E 2013;88:052916.
[52] Maistrenko Y, Sudakov O, Osiv O, Maistrenko V. Chimera states in three dimensions. New J Phys 2015;17.
[53] Laing CR. Chimeras in two-dimensional domains: heterogeneity and the continuum limit. SIAM J Appl Dyn Syst 2017;16:974.
[54] Omelchenko OE, Knobloch E. Chimerapedia: coherence–incoherence patterns in one, two and three dimensions. New J Phys 2019;21:093034.
[55] Clerc MG, Coulibaly S, Ferre N, Tlidi M. Two-dimensional optical chimera states in an array of coupled waveguide resonators. Chaos 2020;30:043107.

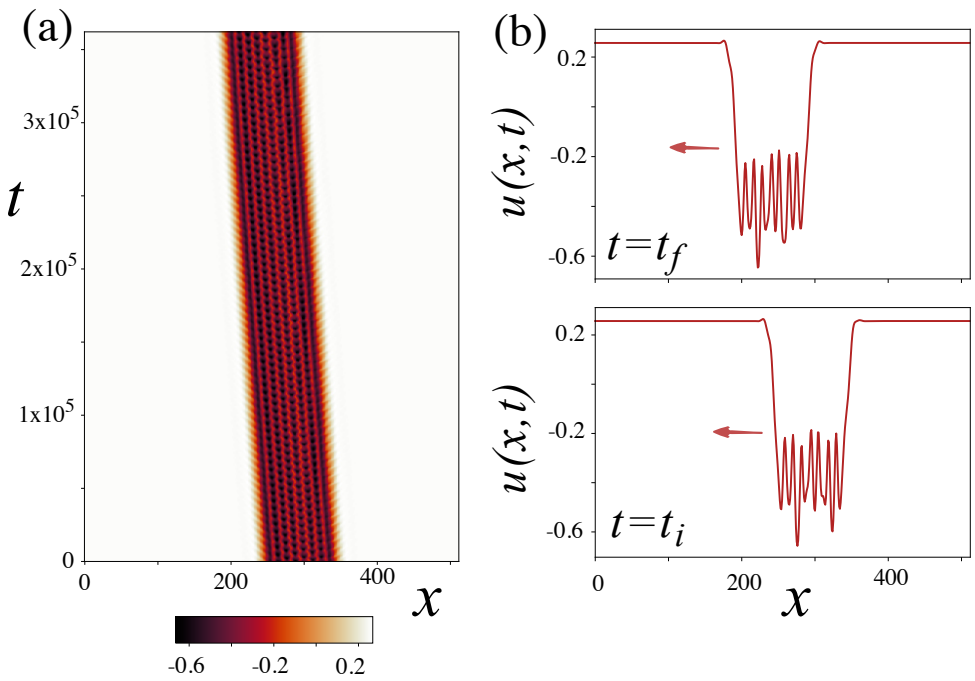

Figure 5.7: Dark chimera of $N = 8$ holes, obtained for the parameters $\eta = 0.04$, $\mu = -0.09$, $b = 1.5$ and $c = -9.7$

Chapter 6

Wandering Chimeras

6.1 Introduction

As was seen in the previous chapter, chimeras, as an example of localized dissipative structures, not only exhibit a fascinating display of coexistence between coherent and incoherent behavioral domains, but these domains can also propagate in space. How they spread is related to a break of symmetry that induces a disparity in the localized structure, and therefore yields a movement in a preferential direction [116] . However, this is not the only type of spread that these intriguing states are capable of displaying. This chapter shows another kind of propagation, which we call wandering walking (to differentiate it from random walking). These chimera state exhibits erratic behavior, resembling a random walk, but governed by simple deterministic equations. As in the previous chapter, these chimeras appears in the non-variational Turing-Swift-Hohenberg solutions, and therefore they live in a continuous medium.

The wandering motion of chimera states has been reported in the literature. For example, in [117] is shown chimera states whose incoherent domain propagates erratically through space for a system of nonlocal coupled Kuramoto-like oscillators. In this case, these chimera states share two of the main Brownian motion properties, i.e., a self-correlation function for the displacements decaying to zero and a Gaussian shape distribution for its displacements. Another work in this direction is given by [118] where are studied chimera states where the wandering motion comes from the coherent domain. A discrete set of coupled oscillators defines the system. Its dynamics exhibit a decaying self-correlation function and Gaussian shape distribution for its displacements and therefore is modeled by Gaussian white noise.

On the other hand, the chimera states reported in the present chapter live in continuous media. Instead of the works mentioned above, the associated self-correlation function for its displacements does not decay to zero, evidencing memory effects and highlighting its deterministic nature.

Another kind of dissipative structures presenting this kind of wandering behavior of deterministic nature is the so-called explosive solitons [119, 120, 121], mainly studied for the cubic-quintic Ginzburg Landau equation [122]. Nevertheless, in this case, explosive solitons

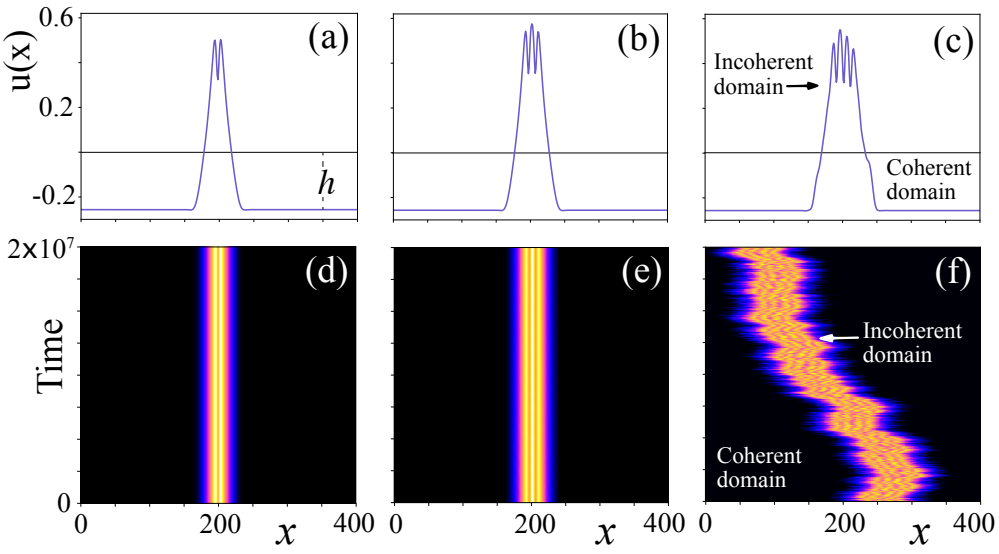

Figure 6.1: Single localized structures of the non-variational Swift-Hohenberg Eq. (6.1) by $\eta = -0.04$, $\mu = -0.09$, $\nu = 1$, $b = -2$, $c = 24$, $\mathrm{d}x = 0.4$ and $\mathrm{d}t = 0.001$. (a) Profile and (d) spatiotemporal evolution of the motionless localized structure with two bumps. h is the distance of the homogeneous state to zero. (b) Profile and (e) spatiotemporal evolution of the motionless localized structure with three bumps. The position or centroid of the localized structure is maintained at a fixed location. Besides, the heights of the bumps oscillate with a fixed amplitude and frequency. (c) Profile and (f) spatiotemporal evolution of the wandering complex localized solution. This state has four bumps. Each of them exhibits complex aperiodic oscillations, while the localized structure changes its position erratically. Here the coherent domain has a constant dynamics, whereas the incoherent domain has complex dynamical behavior.

are transient dissipative solutions whose propagation is driven by the spatiotemporal chaotic fluctuations of the media, and there is not a persistent coherent domain. Therefore are not chimera states. Another interesting point to highlight is that the displacements of this kind of localized dissipative structure have a self-correlation function decaying to zero. A similar phenomenon is reported in [123], nevertheless, it will be explained in chapter 8 where is studied more in-depth the effects of spatiotemporal chaotic fluctuations on dissipative localized states.

6.2 Wandering Chimeras

Exploring numerically the nonvariational effects on localized structures in the non-variational Turing-Swift-Hohenberg equation 6.1,

$$\partial_t u = \eta + \mu u - u^3 - \nu \partial_{xx} u - \partial_{xxxx} u + bu\partial_{xx} u + c(\partial_x u)^2. \tag{6.1}$$

we could evidence the existence of a particular type of chimera-type solution, propagating in space in a random-like way, as shown in figure 6.1. These kind of solution was founded for the parameters values $\eta = -0.04$, $\mu = -0.09$, $\nu = 1$, $b = -2$, $c = 24$, $\mathrm{d}x = 0.4$ and

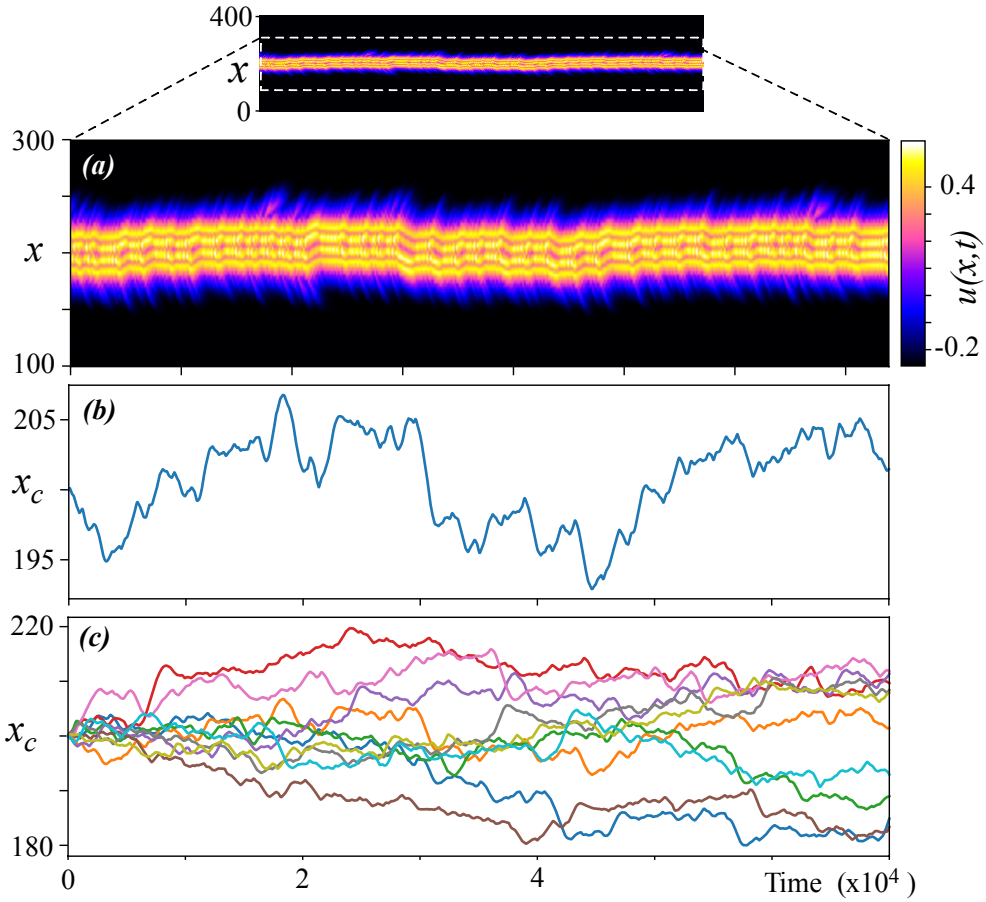

Figure 6.2: Wandering walk of chimera states of the non-variational Swift-Hohenberg Eq. (6.1) by $\eta = -0.04$, $\mu = -0.09$, $\nu = 1$, $b = -2$, $c = 24$, $\mathrm{d}x = 0.4$ and $\mathrm{d}t = 0.001$. (a) Excerpts of Spatiotemporal diagram of a wandering chimera state. (b) Temporal evolution of the centroid $x_c(t)$ of the chimera state, calculated using formula (6.2), of the respective spatiotemporal evolution presented in panel (a). (c) Several trajectories of the centroid of chimera state calculated for different slightly initial conditions.

$\mathrm{d}t = 0.001$. Nevertheless, the solution is generic and exist in a wide domain in the parameter space.

Although this type of behavior has indeed been reported for dissipative structures presenting stochastic forcing, in our work, all evolution laws are uniquely deterministic. Thus, we are in the presence of perhaps the simplest example of a chimera state with erratic propagation and the first example of these in a continuous medium.

When trying to characterize its behavior, we use, analogously to the strategy presented in the previous chapter, the centroid concept, given by the equation 6.2.

$$x_c(t) \equiv \frac{\int_{-L/2}^{L/2} x(u(x,t) - h)\mathrm{d}x}{\int_{-L/2}^{L/2} (u(x,t) - h)\mathrm{d}x}. \tag{6.2}$$

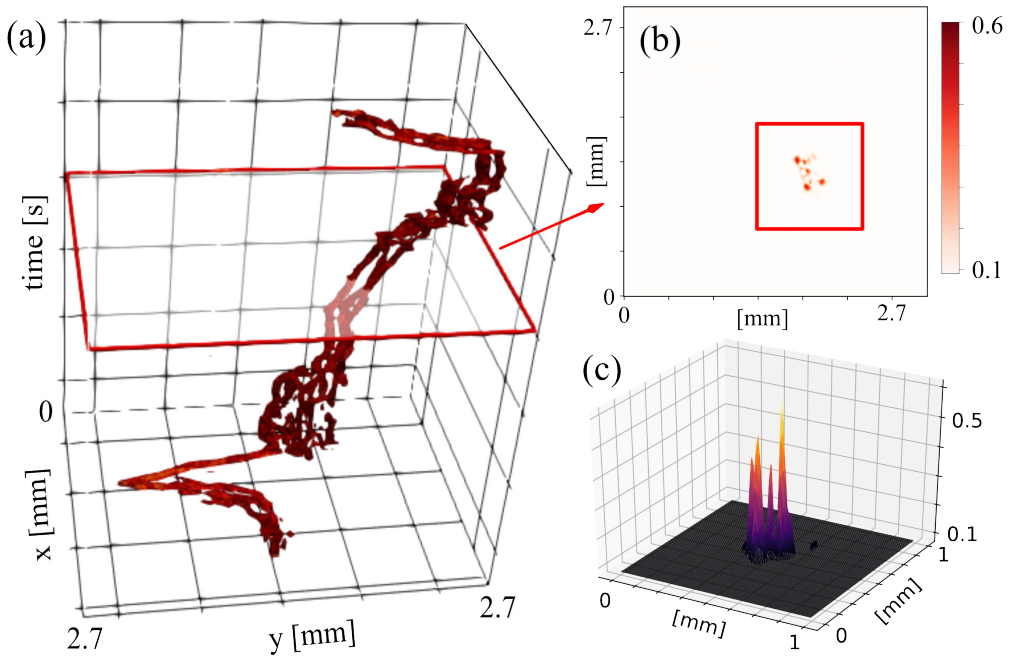

Figure 6.3: Wandering chimera state pinned by symmetric walls.

Figure 6.2 show the dynamics of the centroid for a wandering chimera.

Additionally, we study the fluctuations in its displacements defined by $\delta x_c(t+\mathrm{d}t) - x_c(t)$, allowing us to characterize its behavior statistically. The distribution of the displacements was fit to a truncated Gaussian distribution. Unlike random walks, we were able to show that the behavior of the self-correlation function $R(T) = \langle \Delta x_c(t) \Delta x_c(t+\tau) \rangle$ does not decay to zero for values of τ large as in the case of random walkers. Instead, it kept fluctuating between 0.4 and -0.4, thus evidencing not only its deterministic nature but also its memory effects. Finally, we evidence its complexity by studying its power spectral density and the Lyapunov spectrum, observing, in this case, the appearance of 5 non-zero Lyapunov exponents, highlighting low-dimensional chaotic dynamics.

6.3 Wandering localized structures in physical experiments

This type of localized structures with erratic behavior has been evidenced in various physical systems. In particular, in the liquid crystal light valve setup, it was possible to observe the emergence of an erratic walk of a spot, captured via the measurement of light intensity measured by a CCD. This localized structure and its dynamics can be seen in figure 6.3.

Another experimental example of dissipative localized structure with wandering motion appears in the gas-discharge systems studied in [124], where current filaments between parallel plates emerge when an externally applied voltage is applied. More details about the phenomena and experiments could be consulted in [124] and references therein.

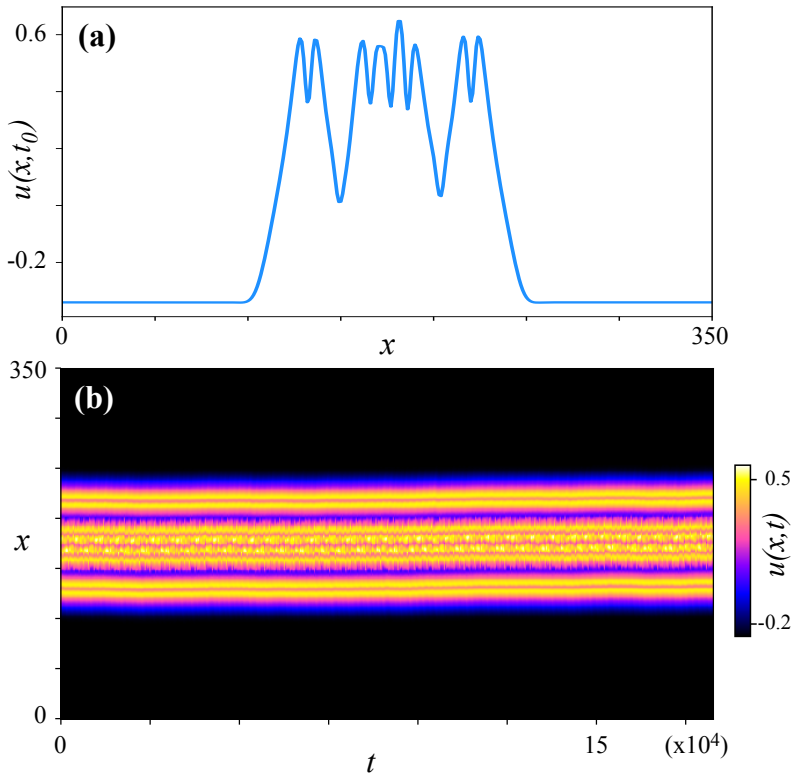

Figure 6.4: Wandering chimera state pinned by symmetric walls.

6.4 Control of wandering motion: pinning and chaotical engines

Given the complexity of the spatial propagation of wandering chimeras, we try to answer whether it is possible to control their behavior, either by confining their dynamics and achieving the pinning of the localized structure or controlling its motion through the generation of a preferential direction of propagation. We note that this localized structure coexists with other fundamental localized structures (without permanent dynamics) to answer this question. One given by a localized structure of 3 peaks and another given by a localized structure of 2 peaks, as shown in figure 6.1.

So the interaction of the wandering chaoticon with different types of arrangements of these structures was explored numerically. The first thing we found is that by confining the wandering chaotic between identical walls, defined by these fundamental and motionless localized structures, it was possible to confine it and thus prevent its propagation throughout space, as shown in figure 6.4.

Additionally, we consider the case of asymmetric walls, i.e., considering a structure with three peaks on one side and another with two peaks on the other side. With this, we find that the localized structure defined by the bound state began to have a preferential propagation direction, in which the wandering chaoticon became the motor of this bound state. Figure 6.5 shows the dynamics of this type of state resulting from the mixture of the different coexisting localized structures.

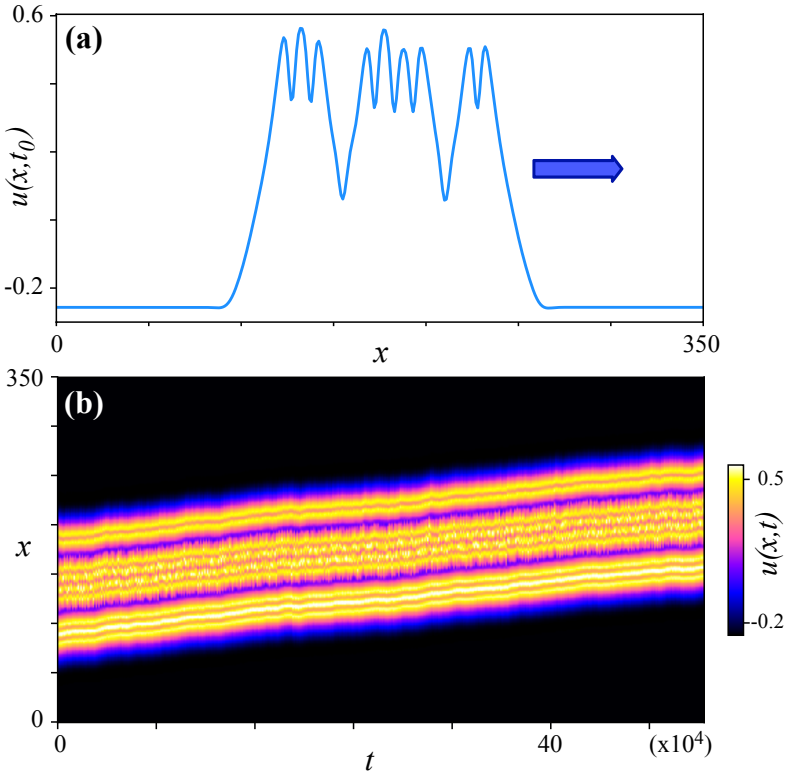

Figure 6.5: Control of propagation direction of a wandering chimera states locating by the formation of a bounded state with two different coexisting localized states without permanent dynamics

6.5 Outline

- We show the emergence of wandering chimera states in continuous media.
- We show evidence of these wandering chimera states in the LCLV experiment. Nevertheless, such states need to be explored with more detail from the experimental point of view.
- Its propagation was characterized by the statistical and nonlinear dynamics point of view, characterizing its displacement statistics and dynamical complexity.
- We built the geometry of the displacement dynamics attractor and was shown its geometrical complexity.
- The leading Lyapunov exponents were calculated, obtaining that its chaotic dynamics is of low-dimensional type.
- Due to the genericity of the non-variational Turing-Swift-Hohenberg equation, we expect the observation of these kinds of states in a wide variety of natural and technological systems.
- Some control strategies were offered to achieve spatial pinning or propagation with a preferential direction of motion, enabling its potential use in designing electro-optical devices for storage and computing as well as micro energy generators.

Chaos, Solitons and Fractals 140 (2020) 110169

Contents lists available at ScienceDirect

Chaos, Solitons and Fractals

Nonlinear Science, and Nonequilibrium and Complex Phenomena

journal homepage: www.elsevier.com/locate/chaos

Wandering walk of chimera states in a continuous medium

A.J. Alvarez-Socorro [a,b,*], M.G. Clerc [a], M.A. Ferré [a]

[a] Departamento de Física and Millennium Institute for Research in Optics, Facultad de Ciencias Físicas y Matemáticas, Universidad de Chile, Santiago, Chile
[b] Laboratorio de Investigacin, Desarrollo e Innovación, Zenta Group, Andrés Bello 2687, Las Condes, Santiago, Chile

ARTICLE INFO

Article history:
Received 16 July 2020
Accepted 27 July 2020

Keywords:
Localized structures
Chimeras
Nonvariational effects
Wandering walks
Spatiotemporal chaos

ABSTRACT

The coexistence of coherent and incoherent domains in discrete coupled oscillators, *chimera state*, has been attracted the attention of the scientific community. Here we investigate the macroscopic dynamics of the continuous counterpart of this phenomenon. Based on a prototype model of pattern formation, we study a family of localized states. These localized solutions can be characterized by their sizes, and positions, and Yorke-Kaplan dimension. Chimera states in continuous media correspond to chaotic localized states. As a function of parameters and their size, the position of these chimera states can be bounded or unbounded. This allows us to classify these solutions as wandering or confined walk. The wandering walk is characterized by a chaotic motion with a truncated Gaussian distribution in its displacement as well as memory effects.

Localized structures are a characteristic feature of the self-organized non-equilibrium systems [1–3]. These structures, described as particle-like solutions, are characterized by continuous order parameters like the position, width, and amplitude [4]. Notwithstanding, localized structures corresponds to extended solutions. They have been observed in numerous fields, ranging from physics, chemistry to biology [4–6]. The localized structures are the dissipative counterpart of the solitons in conservative systems. In one-dimensional systems, they can be interpreted as spatial trajectories that connect one steady state with itself. Indeed, they are homoclinic orbits of the spatial co-moving system [7]. Localized structures are not necessarily motionless. As a result of symmetry breaking instabilities, they can exhibit motion or self-pulsation [8–14]. Recently, it has been shown that parity symmetry breaking induces spontaneous motion of localized structures [15]. A unified description of localized structures and their dynamic behavior can be achieved by the nonvariational Swift-Hohenberg equation [16–19]. This model accounts for a scalar field that does not follow minimization principles. The nonvariational Swift-Hohenberg equation has been derived in several contexts [19]. Moreover, this equation is used to puts light on the existence, stability properties, and dynamical evolution of complex spatiotemporal localized structures called *chaoticons* [20]. This intriguing phenomenon is observed in a liquid crystal light valve experiment with optical feedback. Furthermore, numerically chaoticons are obtained in nonlocal nonlinear Schrödinger equation [22], Ginzburg-Landau equation [21] and a reaction-diffusion model [23]. Indeed, these states show a coexistence between coherence (stationary) and incoherence (spatiotemporal chaotic) domains. Hence, chaoticons are the continuous counterpart of chimera states [24], namely, chaoticons correspond to chimera-like solutions. Originally, chimera states were observed in nonlocally coupled phase oscillators [25]. These intrigued states correspond to breaking symmetry solution without bistability. Extension of chimera states in bistable systems was proposed in several coupled systems [26–29], which was usually denominated chimera-like states. Depending on the initial condition, these states have different size and exhibit a family of solutions with the coexistence of coherent and incoherent domains.

Since then, chimera states have been investigated in more general frameworks [30–35]. Initially, even though the existence of chimera states was attributed to the nonlocal nature of the coupling [24]. Subsequently, chimera states have been observed in systems that are coupled globally [36–38], and locally [26–28,39,40,21]. In all these studies, domains remain motionless. However, under special conditions, chimera states are traveling solutions. This is observed under symmetric [41,42] and asymmetric schemes of coupling [29,43–45]. Even, chimera states show an erratic motion with stochastic nature in a finite number of coupled oscillators [42,46]. This fact is reflected by the loss of memory of the chimera position, which is counterintuitive for a deterministic system. Henceforth in this manuscript, we will use the term

* Corresponding author.
E-mail address: alejandro.alvarez@ing.uchile.cl (A.J. Alvarez-Socorro).

https://doi.org/10.1016/j.chaos.2020.110169
0960-0779/

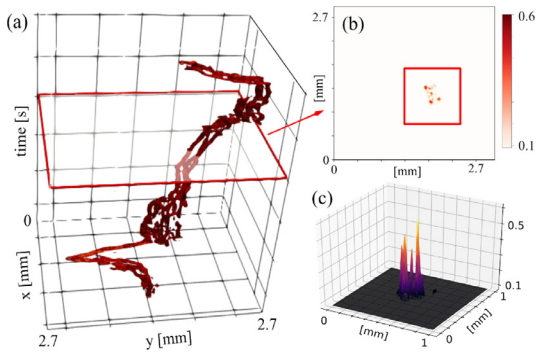

Fig. 1. (color online) Experimental observation of an erratic walk of a localized spot in a liquid crystal light valve with optical feedback. (a) Experimental spatiotemporal evolution of a localized spot. (b) Instantaneous snapshot of the localized state. (c) A plot of the light intensity at a given time (Courtesy of Nicolas Verschueren).

chimera to refer a complex spatiotemporal localized state in continuous media.

Unexpectedly, in a liquid crystal light valve experiment with optical feedback, an erratic walk dynamics of chaoticons is observed (see Fig. 1). This complex walk accounts for an erratic motion of the position of the complex localized structure. This dynamic is of deterministic nature. Theoretically, the chaoticon was described by the non-variational Swift-Hohenberg equation [20]. However, the reported dynamics of chaoticons of this model are characterized by erratic localized fluctuations in a bounded region of the order of one wavelength of the spatiotemporal chaotic state [20], at variance to the experimental observations characterized by an unbounded erratic walk. The mechanism that produces these states and their dynamics is an open problem.

In this paper, we investigate the erratic walk of chimera states in continuous media. Based on a prototype model of localized structures—the non-variational Swift-Hohenberg equation—we numerically observe and analyze wandering walks of localized structures. To characterize this wandering motion, we use tools of the dynamical systems and statistics theory. Finally, in comparison to the random dynamics of chimera states in coupled oscillators [46], the motion of the wandering walk of chimera-like state shows memory effects. Namely, the self-correlation of the position of this localized state does not become zero.

An archetypal model that shows patterns, fronts, localized structures, and chimera-like states in continuous media is the non-variational Swift-Hohenberg equation [19,20,47,48]. It describes the dynamics near a Lifshitz critical point [2] that accounts for the confluence of a spatial instability and a nascent of bistability through the scalar order parameter $u(x, t)$,

$$\partial_t u = \eta + \mu u - u^3 - \nu \partial_{xx} u - \partial_{xxxx} u + c(\partial_x u)^2 + 2bu\partial_{xx} u, \qquad (1)$$

where x and t stand for the spatial and temporal coordinates, respectively. μ is the bifurcation parameter ($\mu \ll 1$), η accounts for the asymmetry between homogeneous states, c, ν, and b are, respectively, the nonlinear advection, the linear and the nonlinear diffusion coefficients. The term proportional to the four spatial derivative accounts for the hyperdiffusion. Higher-order terms in Eq. (1) are ruled out by scaling analysis, since $u \sim \mu^{1/2}$, $\eta \sim \mu^{3/2}$, $\nu \sim \mu^{1/2}$, $\partial_t \sim \mu$, $\partial_x \sim \mu^{1/4}$, and $c \sim b \sim O(1)$.

When $b = c = \eta = 0$, Eq. (1) corresponds to the well-known Swift-Hohenberg model [2,49]. The minimization of free energy characterizes the dynamics of Eq. (1). Hence, the Swift-Hohenberg equation shown only stationary solutions as equilibria. Indeed, this dynamics is of variational nature. However, in the case that $b \neq c$, model Eq. (1) losses its variational structure, allowing the existence of solutions that show permanent dynamics, such as propagative fronts [50], moving and oscillatory localized structures

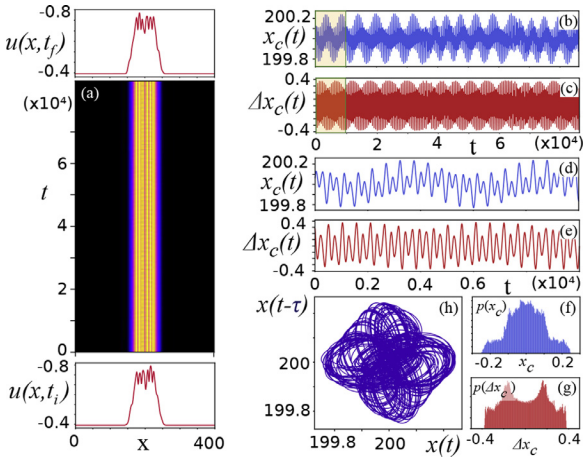

Fig. 2. (color online) Confined chimera states observed in the Swift-Hohenberg Eq. (1) by $\eta = -0.09$, $\mu = -0.04$, $\nu = 1$, $b = -2$, $c = 21$, $dx = 0.6$ and $dt = 0.01$. (a) Spatiotemporal evolution of a confined chimera state of 6 bumps. Temporal evolution of the centroid (b) and displacement (c) of the chimera state. Panels (d) and (e) show, respectively, an excerpt of the centroid and displacement for the first 10^4 time steps. (f) and (g) are the statistical distribution for centroid and displacements of chimera state, respectively. (h) Phase portrait reconstruction in 2D space of chimera state centroid.

[15,48,51], and chimera-like states [20]. Fig. 2(a) displays a typical chimera state of model Eq. (1). This dynamic behavior is characterized by presenting localized spatiotemporal chaos, which is surrounded by homogeneous states on its flanks. It is noteworthy to note that despite its spatiotemporal complexity, the evolution of the chimera state position is localized in space, that is, the localized state is confined. To characterize the dynamics of the chimera state, let us introduce its position or centroid as

$$x_c(t) = \frac{\int_{-L}^{L} x\hat{u}(x,t)dx}{\int_{-L}^{L} \hat{u}(x,t)dx}, \qquad (2)$$

where $\hat{u}(x,t) \equiv u(x,t) + h$ and h is the distance of the homogeneous state to zero. Moreover, we consider displacements of chimera state Δx_c, taking the difference of its position between two successive time steps.

Fig. 2 shows the temporal evolution of the centroid and displacements of the chimera state. These dynamics reveal a rich and complex evolution. Note that the dynamics of the centroid is bounded by one wavelength. Hence, the chimera state remains around a given position. The statistical characterization of the centroid and displacements dynamics are shown in Fig. 2(f) and (g), respectively. In both cases, the distributions are bounded, reflecting the fact that the spatiotemporal chaotic localized structure is pinned. The richness and complexity of such kind chaotic localized structures have been studied previously in Verschueren et al. [20]. The reconstruction of the attractor for the centroid of chimera state—following the classical Fraser and Swinney method [53]—obtaining by unfolding in a 2D space is shown in Fig. 2(h). Unexpectedly, when changing parameters, the position of the chimera exhibits complex behaviors, which causes the chimera to move distances greater than the characteristic wavelength of the spatiotemporal chaotic state (cf. right panels in Fig. 3).

To the best of our knowledge, the complex and unbounded dynamical behavior of the position of chimera states has not been reported in continuous media. To investigate such localized structures dynamics, we have conducted a numerical analysis of model Eq. (1) in the nonvariational regime. For the sake of simplicity, periodic boundary conditions have been considered, however, similar dynamic behaviors are observed with other boundary conditions. Fourth-order Runge-Kutta in time and finite differences in space

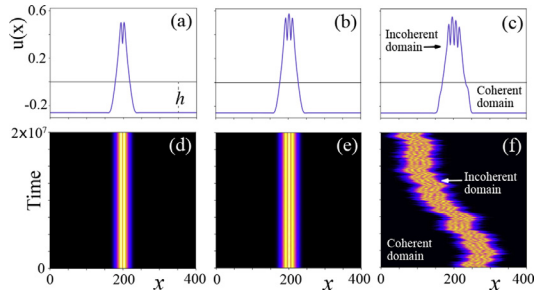

Fig. 3. (color online) Single localized structures of the non-variational Swift-Hohenberg Eq. (1) by $\eta = -0.04$, $\mu = -0.09$, $\nu = 1$, $b = -2$, $c = 24$, $dx = 0.4$ and $dt = 0.001$. (a) Profile and (d) spatiotemporal evolution of the motionless localized structure with two bumps. h is the distance of the homogeneous state to zero. (b) Profile and (e) spatiotemporal evolution of the motionless localized structure with three bumps. The position or centroid of the localized structure is maintained at a fixed location. Besides, the heights of the bumps oscillate with a fixed amplitude and frequency. (c) Profile and (f) spatiotemporal evolution of the wandering complex localized solution. This state has four bumps. Each of them exhibits complex aperiodic oscillations, while the localized structure changes its position erratically. Here the coherent domain has a constant dynamics, whereas the incoherent domain has complex dynamical behavior.

are the numerical methods used to integrate model Eq. (1). In all simulations, the space is discretized in 400 points with $dx = 0.4$, and the time step size is $dt = 0.001$. Fig. 3 shows typical localized solutions exhibited by the model Eq. (1). The system shows only these three types of single localized states in a given region of parameters. These localized solutions as a function of their width are characterized by being stationary, oscillatory, or chaotic, respectively. Other localized states are a composition of these simple solutions. The top panels in Fig. 3 show profiles of each localized structure at a given time, and the bottom panels display the respective spatiotemporal evolution of localized states. Solutions that have two and three bumps correspond to stationary states, depicted in Fig. 3(d) and (e). However, a complex spatiotemporal evolution is shown by the localized structure that exhibits four bumps, see Fig. 3(f). In the former case, the system shows coexistence between coherent and incoherent domains. Indeed, this state corresponds to a chimera state, but instead of the chimera state shown in Fig. 2, it exhibits a wandering walk in its position, which is characterized by move several times the characteristic wavelength of the chaotic domain. Hence, the incoherence domain presents wandering movements which resemble a random walk [52].

Fig. 4 illustrates the temporal evolution of the four-bumps chimera solution and its respective centroid $x_c(t)$. To figure out the sensitivity of the initial conditions on the motion of this chimera state the position $x_c(t)$ is calculated for slightly different initial conditions [see Fig. 4(c)]. From this figure, one can infer that the position of the chimera solution presents complex dynamics as a function of the initial conditions. Likewise, to reveal the nature of the movements, we compute its displacements, taking the difference of its position between two successive time steps. Hence, the displacements are defined by $\Delta x(t) \equiv x_c(t) - x_c(t-\tau)$. Fig. 5 shows the temporal evolution of the displacement $\Delta x(t)$ and its respective histogram which has a bell shape. Building the associated distribution of displacements, we found that a Gaussian distribution well describes it. Consider a fitting distribution function of the form

$$f(\Delta x) = \frac{1}{\beta\sqrt{2\pi}} e^{-\frac{(\Delta x-\mu)^2}{2\beta}}, \tag{3}$$

where μ corresponds to the mean value of the displacements ($\mu \equiv \langle \Delta x \rangle$, where the symbol $\langle \cdot \rangle$ accounts for the average on the values of the displacements). β accounts for the standard deviation. The probability density distribution, and the Gaussian func-

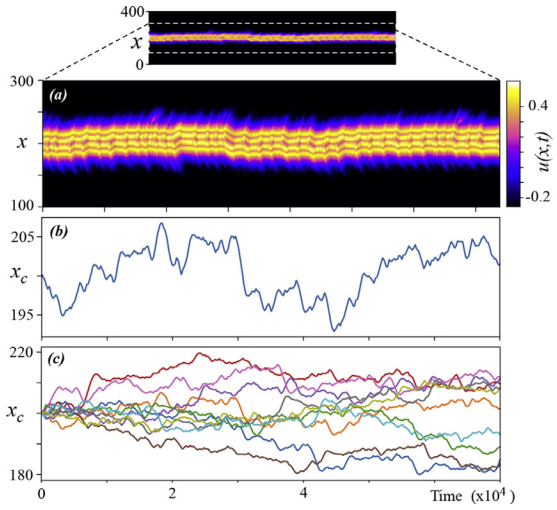

Fig. 4. (color online) Wandering walk of chimera states of the non-variational Swift-Hohenberg Eq. (1) by $\eta = -0.04$, $\mu = -0.09$, $\nu = 1$, $b = -2$, $c = 24$, $dx = 0.4$ and $dt = 0.001$. (a) Excerpts of Spatiotemporal diagram of a wandering chimera state. (b) Temporal evolution of the centroid $x_c(t)$ of the chimera state, calculated using formula (2), of the respective spatiotemporal evolution presented in panel (a). (c) Several trajectories of the centroid of chimera state calculated for different slightly initial conditions.

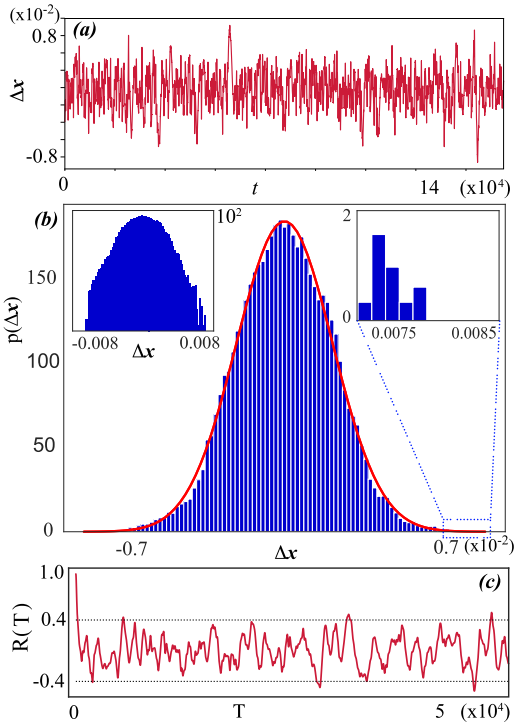

Fig. 5. (color online) Statistical characterization of displacements of the position of the chimera solution $\Delta x(t)$ for Eq. (1) with $\eta = -0.04$, $\mu = -0.09$, $\nu = 1$, $b = -2$, $c = 24$, $dx = 0.4$ and $dt = 0.001$. (a) Longtime evolution of the displacements $\Delta x(t)$. (b) The probability distribution of displacements, which shows a Gaussian-like distribution. The continuous curve (red) accounts for a Gaussian adjustment function, formula (3), with $\mu \approx 0$ and $\beta \approx 2.158 \times 10^{-3}$. The left inset shows the probability distribution of displacements in the log-log scale. This illustrates that the distribution corresponds to a truncated Gaussian. The right inset shows amplification of the tails of the distribution. (c) Self-correlation function $R(T)$ based on Pearson's coefficient. The fact that this function does not decay to zero highlight the memory effects of the wandering motion of chimera states. (For interpretation of the references to color in this figure legend, the reader is referred to the web version of this article.)

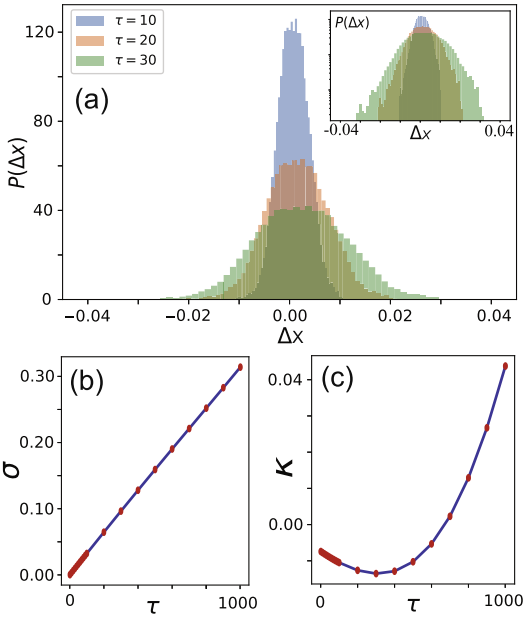

Fig. 6. (color online) Temporal characterization of statistical measures of wandering chimera states for model Eq. (1) by $\eta = -0.04$, $\mu = -0.09$, $\nu = 1$, $b = -2$, $c = 24$, $dx = 0.4$ and $dt = 0.001$. (a) Displacement distributions for different waiting times $\tau = 10$, 20, and 30, respectively. Temporal evolution of the standard deviation (b), and the excess kurtosis (c).

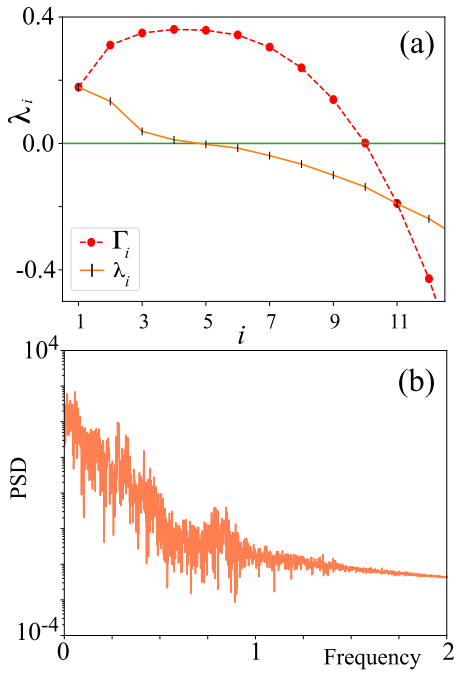

Fig. 7. (color online) Dynamic characterization of the wandering chimera state of the non-variational Swift-Hohenberg Eq. (1) by $\eta = -0.04$, $\mu = -0.09$, $\nu = 1$, $b = -2$, $c = 24$, $dx = 0.4$ and $dt = 0.001$. (a) Lyapunov characteristic exponents of the wandering chimera solution and the partial sums of the Lyapunov exponents $\Gamma_i = \sum_{k=1}^{i} \lambda_k$. (b) Power spectrum of displacements time series.

tion (3) are compared in Fig. 5(b). The probability distribution of displacements of chimera-like states resembles to the probability distribution of displacements of a Brownian motion. The rhythms of the displacements of a Brownian particle are completely determined by a random process (Wiener process [52]). However, unlike a Brownian motion, the self-correlation function $R(T) = \langle \Delta x(t)\Delta x(t+T)\rangle$ does not decrease despite the increasing of T, highlighting the memory effects of this motion. Moreover, the self-correlation shows an oscillatory behavior between a considerable maxima and minima values [see Fig. 5(c)]. Observe that $R(T)$ was measured using the Pearson correlation coefficient. Besides, we have plotted the distribution of displacement in the log-log scale, see insets in Fig. 5(b). This chart reveals that the displacement distribution corresponds to a truncated Gaussian distribution. This type of distribution is a consequence of the central limit theorem for a finite number of elements [54–56]. To check out this result, we have conducted different numerical simulations with very long periods and of different sizes and the distribution obtained is the same.

To characterize the statistical evolution of the displacement Δx in a given waiting time τ, we have monitored the evolution of the displacement distribution, the standard deviation σ, and the excess kurtosis κ. Fig. 6 summarizes this statistical analysis. Note that σ and κ show a linear and parabolic waiting time dependence, respectively. Similar dynamical behavior of σ was reported in phase coupled oscillators [46]. This type of dynamical statistical behavior is not peculiar of Brownian motion.

In brief, the position of the chimera-like state shows a wandering motion with a truncated Gaussian distribution of its displacement and memory effects.

To shed light on the dynamic nature of the wandering walk of chimera-like states, we will use tools from the theory of dynamic systems such as the power spectrum and Lyapunov exponents. These type of tools allows us to characterize the dynamics of modes and establish if the dynamics are of chaotic nature. When the largest Lyapunov exponent $\lambda_{\max}$ is negative, the system has a stationary equilibrium, for instance, homogeneous or pattern states. On the contrary, when it is positive, the system under study exhibits chaotic dynamics. Indeed, the Lyapunov spectrum characterizes the exponential sensibility to the initial conditions [57]. The analytical study of the Lyapunov spectrum is a titanic endeavor and in practice inaccessible. The numerical derivation of the exponents is a standard strategy. Indeed, it is necessary to spatially discretize the model Eq. (1). Hence, model (1) is approximated to a set of coupled ordinary differential equations, *discretized system*. From these equations, one can determine the discretized Jacobian at the chaotic solution, which characterizes the linear evolution of the state under study. To determine the Lyapunov exponents, we follow the linear evolution of an orthonormal deviation vectors basis of the discretized system. At every temporal evolution step, the deviation vectors are replaced by a new set of orthonormal vectors. From these orthonormalization procedures, Lyapunov exponents are estimated (see Ref. [58] for more details). We have calculated numerically the leading Lyapunov exponents of the chimera solution. Fig. 7 shows the positive Lyapunov spectrum of the chimera solution. From this spectrum, it is inferred that the strange attractor has at least 4 unstable directions. Note that few exponents are positive, which highlight a low-dimensional chaotic dynamics. In addition, one can determine the dimension of the strange attractor that characterizes the dynamics of the position of the chimera-like solution, using the Yorke-Kaplan conjecture [59]. The Yorke-Kaplan dimension is defined as $D_{YK} = n + \sum_{i=1}^{n} \lambda_i/|\lambda_{n+1}|$, where n is the largest integer such that $\lambda_1 + +\lambda_n > 0$. Fig. 7(a) shows the partial sum of the Lyapunov exponents $\Gamma_i = \sum_{k=1}^{i} \lambda_k$. From this chart, we found that $n = 10$. Then, the dimension is $D_{YK} \approx 10.005$. Besides, Fig. 7(b) displays the power spectrum of the temporal evolution of the displacements. The complex evolution of the wandering chimera state is revealed in a large number of frequency that is involved in the dynamics, which is typical of chaotic behaviors.

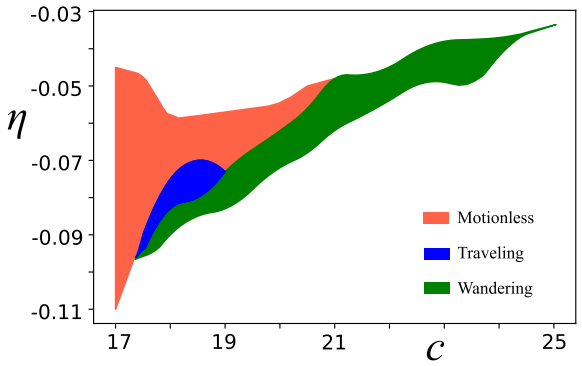

Fig. 8. (color online) Phase diagram of chimera states in parameter-space $\eta - c$ and for $\mu = -0.09$, $\nu = 1$, $b = -2$, $dx = 0.6$ and $dt = 0.01$. The green, blue and light red area account for the region where wandering, traveling, and motionless chimeras states are observed. The motionless and traveling chimera states are characterized by bounded and traveling centroid. (For interpretation of the references to color in this figure legend, the reader is referred to the web version of this article.)

Therefore, from the previous analysis, we infer that the wandering walk of the chimera-like solution is of a chaotic nature.

The wandering chimera-like states are observed in a wide range of parameters, which is a manifestation of the robust nature of these localized states. Fig. 8 shows the phase diagram of chimeras with wandering walks in $\eta - c$ parameters space. Hence, chimeras with wandering walks are observed in a wide region of the parameter space. It is important to note that these chimeras with wandering walks can coexist with motionless localized structures and confined chimeras.

In conclusion, we have shown that wandering dynamics of the position of chimera solutions in continuous spatially extended systems. These intriguing states are observed in the nonvariational Swift-Hohenberg equation, which is a prototype model of pattern formation. We have investigated the statistical and dynamical properties of wandering chimera states. The wandering walk of these solutions shows a truncated Gaussian distribution in its displacements. This property and the sensitivity to the initial conditions resemble a sort of Brownian motion. However, the wandering walk of the chimera states exhibits memory effects that are characterized by the self-correlation function. Besides, we have shown that the evolution of the position of wandering chimera-like state corresponds to chaotic behavior. To support this statement, the leading Lyapunov exponents were calculated.

Due to the generic character of the nonvariational Swift-Hohenberg equation, we expect the observation of wandering chimera-like states in a wide range of systems. In addition, we can take advantage of these wandering chimera-like states as Brownian motors [60] to induce propagation or control of coexisting localized structures. Finally, this work provides insights into novel ways of light beam generation with coexisting coherent and incoherent domains. The incoherent domain remains in a wandering motion. We expect that such kind of light beam will have significant and far-reaching ramifications in the development of novel and practical technological applications. Work in this direction is in progress.

Declaration of Competing Interest

The authors declare that they have no known competing financial interests or personal relationships that could have appeared to influence the work reported in this paper.

Acknowledgments

This work was supported by CONICYT under grant CONICYT-USA PII20150011. MGC and MAF also thank the Millennium Institute for Research in Optics (MIRO) FONDECYT Project no. 1180903 for financial support. AJA-S thanks financial support from Becas Conicyt 2015, Contract No 21151618.

References

[1] Prigogine I. Self-Organization in Non Equilibrium SystemsSelf-Organization in non equilibrium systems. New York: J. Wiley & Sons; 1977.
[2] Cross MC, Hohenberg PC. Pattern formation outside of equilibrium. Rev Mod Phys 1993;65:851.
[3] Pismen LM. Patterns and Interfaces in Dissipative DynamicsPatterns and interfaces in dissipative dynamics. Berlin, Heidelberg: Springer Series in Synergetics Springer; 2006.
[4] Descalzi O, Clerc M, Residori S, Assanto G. Localized States in Physics: Solitons and Patterns. New York: Springer; 2010.
[5] Purwins HG, Bödeker HU, Amiranashvili S. Dissipative solitons. Adv Phys 2010;59:485.
[6] edited by solitons Dissipative. From Optics to Biology and Medicine. Lecture Notes in Physics, 751 Springer, Heidelberg; 2008. edited by.
[7] Coullet P. Localized patterns and fronts in non equilibrium systems. Int J Bifurcation Chaos Appl Sci Eng 2002;12:2445.
[8] Turaev D, Radziunas M, Vladimirov AG. Chaotic soliton walk in periodically modulated media. Phys Rev E 2008;77:065201 R.
[9] Zambrini R, Papoff F. Signal Amplification and Control in Optical Cavities with Off-Axis Feedback. Phys Rev Lett 2007;99:063907.
[10] Staliunas K, Sanchez-Morcillo VJ. Spatial-localized structures in degenerate optical parametric oscillators. Phys Rev A 1998;57:1454.
[11] Haudin F, Rojas RG, Bortolozzo U, Clerc MG, Residori S. Vortex Emission Accompanies the Advection of Optical Localized Structures. Phys Rev Lett 2011;106:063901.
[12] Paulau PV, Gomila D, Ackemann T, Loiko NA, Firth WJ. Self-localized structures in vertical-cavity surface-emitting lasers with external feedback. Phys Rev E 2008;78:016212.
[13] Scroggie AJ, Firth WJ, Oppo GL. Cavity-soliton laser with frequency-selective feedback. Phys Rev A 2009;80:013829.
[14] Tlidi M, Vladimirov AG, Pieroux D, Turaev D. Spontaneous Motion of Cavity Solitons Induced by a Delayed Feedback. Phys Rev Lett 2009;103:103904.
[15] Alvarez-Socorro AJ, Clerc MG, Tlidi M. Spontaneous motion of localized structures induced by parity symmetry breaking transition. Chaos 2018;28:053119.
[16] Clerc MG, Petrossian A, Residori S. Bouncing localized structures in a liquid-crystal light-valve experiment. Phys Rev E 2005;71:015205 R.
[17] Durniak C, Taki M, Tlidi M, Ramazza PL, Bortolozzo U, Kozyreff G. Modulated optical structures over a modulationally stable medium. Phys Rev E 2005;72:026607.
[18] Kozyreff G, Chapman SJ, Tlidi M. Interaction of two modulational instabilities in a semiconductor resonator. Phys Rev E 2003;68:015201 R.
[19] Kozyreff G, Tlidi M. Nonvariational real Swift-Hohenberg equation for biological, chemical, and optical systems. Chaos 2007;17:037103.
[20] Verschueren N, Bortolozzo U, Clerc MG, Residori S. Spatiotemporal Chaotic Localized State in Liquid Crystal Light Valve Experiments with Optical Feedback. Phys Rev Lett 2013;110:104101.
[21] Nicolaou ZG, Riecke H, Motter AE. Chimera States in Continuous Media: Existence and Distinctness. Phys Rev Lett 2017;119:244101.
[22] Zhong L, Li Y, Chen Y, Hong W, Hu W, Guo Q. Chaoticons described by nonlocal nonlinear Schrödinger equation. Sci Rep 2017;7:41438.
[23] Verschueren N, Bortolozzo U, Clerc MG, Chaoticon Residori S. localized pattern with permanent dynamics. Phil Trans R Soc A 2014;372:20140011.
[24] Abrams DM, Strogatz SH. Chimera States for Coupled Oscillators. Phys Rev Lett 2004;93(17):174102.
[25] Kuramoto Y, Battogtokh D. Coexistence of Coherence and Incoherence in Nonlocally Coupled Phase Oscillators. Nonlinear Phenom Complex Syst (Minsk, Belarus) 2002;5:380.
[26] Clerc MG, Coulibaly S, Ferré MA, García-Ñustes MA, Rojas RG. Chimera-type states induced by local coupling. Phys Rev E 2016;93:052204.
[27] Clerc MG, Ferré MA, Coulibaly S, Rojas RG, Tlidi M. Chimera-like states in an array of coupled-waveguide resonators. Opt Lett 2017;42:2906–9.
[28] Clerc MG, Ferré MA, Coulibaly S, Rojas RG. Chimera states in a Duffing oscillators chain coupled to nearest neighbors. Chaos 2018;28:083126.
[29] Nicolaou ZG, Eroglu D, Motter AE. Multifaceted Dynamics of Janus Oscillator Networks. Phys Rev X 2019;9:011017.
[30] Bastidas VM, Omelchenko I, Zakharova A, Scholl E, Brandes T. Quantum signatures of chimera states. Phys Rev E 2015;92:062924.
[31] Lazarides N, Neofotistos G, Tsironis GP. Chimeras in SQUID metamaterials. Phys Rev B 2015;91:054303.
[32] Santos MS, Szezech JD, Borges FS, Iarosz KC, Caldas IL, Batista AM, et al. Chimera-like states in a neuronal network model of the cat brain. Chaos Solitons Fractals 2017:101.
[33] Larger L, Penkovsky B, Maistrenko Y. Virtual Chimera States for Delayed-Feedback Systems. Phys Rev Lett 2013;111:054103.
[34] Bera BK, Ghosh D. Chimera states in purely local delay-coupled oscillators. Phys Rev E 2016;93:052223.
[35] Gonzalez-Avella JC, Cosenza MG, Miguel MS. Localized coherence in two interacting populations of social agents. Phys A 2014;399:24.
[36] Sethia GC, Sen A. Chimera States: The Existence Criteria Revisited. Phys Rev Lett 2014;112:144101.

[37] Yeldesbay A, Pikovsky A, Rosenblum M. Chimeralike States in an Ensemble of Globally Coupled Oscillators. Phys Rev Lett 2014;112:144103.
[38] Hens CR, Mishra A, Roy PK, Sen A, Dana SK. Chimera states in a population of identical oscillators under planar cross-coupling. Pramana 2015;84:229–35.
[39] Laing CR. Chimeras in networks with purely local coupling. Phys Rev E 2015;92:050904 R.
[40] Hizanidis J, Lazarides N, Tsironis GP. Robust chimera states in SQUID metamaterials with local interactions. Phys Rev E 2016;94:032219.
[41] Sethia GC, Sen A, Johnston GL. Amplitude-mediated chimera states. Phys Rev E 2013;88:042917.
[42] Xie J, Knobloch E, Kao HC. Multicluster and traveling chimera states in nonlocal phase-coupled oscillators. Phys Rev E 2014;90:022919.
[43] Bera BK, Ghosh D, Banerjee T. Imperfect traveling chimera states induced by local synaptic gradient coupling. Phys Rev E 2016;94:012215.
[44] Hizanidis J, Panagakou E, Omelchenko I, Schöll E, Hövel P, Provata A. Chimera states in population dynamics: Networks with fragmented and hierarchical connectivities. Phys Rev E 2015;92:012915.
[45] Omel'chenko OEJ. Traveling chimera states. Phys A: Math Theor. J. Phys A 2019;52.
[46] Omel'chenko OE, Wolfrum M, Maistrenko YL. Chimera states as chaotic spatiotemporal patterns. Phys Rev E 2010;81:065201 R.
[47] Residori S, Petrossian A, Nagaya T, Clerc MG. Localized Structures and their Dynamics in a Liquid-Crystal-Light-Valve with Optical Feedback. JJ. Opt. B: Quantum Semiclass. Opt. 2004;6:S169.
[48] Burke J, Dawes JH. Localized states in an extended Swift–Hohenberg equation. SIAM J Appl Dyn Syst 2012;11:261.
[49] Swift J, Hohenberg PC. Hydrodynamic fluctuations at the convective instability. Phys Rev A 1977;15:319.
[50] Alvarez-Socorro AJ, Clerc MG, González-Cortés G, Wilson M. Nonvariational mechanism of front propagation: Theory and experiments. Phys Rev E 2017;95:010202 R.
[51] Houghton SM, Knobloch E. Swift-Hohenberg equation with broken cubic-quintic nonlinearity. Phys Rev E 2011;84:016204.
[52] Rudnick J, Gaspari G. Elements of the random walk. New York: Cambridge University Press; 2004.
[53] Fraser AM, Swinney HL. Independent coordinates for strange attractors from mutual information. Phys Rev A 1986;33:1134–40.
[54] Kaneko K. Globally coupled chaos violates the law of large numbers but not the central-limit theorem. Phys Rev Lett 1990;65:1391.
[55] Pikovsky AS, Kurths J. Do globally coupled maps really violate the law of large numbers? Phys Rev Lett 1994;72:1644.
[56] González JA, Moreno AJ, Guerrero LE. Non-invertible transformations and spatiotemporal randomness. Int J Bifurc Chaos Appl Sci Eng 2007:16.
[57] Pikovsky A, Politi A. Lyapunov exponents: a tool to explore complex dynamics. Cambridge University; 2016.
[58] Skokos CH. Dynamics of small solar system bodies and exoplanets. Springer; 2010. p. 63–135.
[59] Ott E. Chaos in dynamical systems. 2nd ed. Cambridge University; 2002.
[60] CVd Broeck, Kawai R, Meurs P. Microscopic analysis of a thermal Brownian motor. Phys Rev Lett 2004;93:090601.

Chapter 7

Effect of Deterministic Fluctuations in Fronts Dynamics

7.1 Introduction

The effect of fluctuations in the dynamics of macroscopic systems, particularly in the dynamics of fronts or interphases, is a topic of interest in a wide range of the scientific areas. Its study enables a better description and understanding of the interaction between the environmental dynamics and the system under consideration. Typically, such external or environmental fluctuations have been modeled by stochastic processes or noise, and the noise-induced transitions are itself a topic of intensive research in nonlinear sciences [125, 126]. The nature of its role in the dynamics of a system has been illustrated in several theoretical models, and experimental setups [127].

Almost all literature has been focused on stochastic fluctuations. Meanwhile, deterministic fluctuations have only been explored in simple scenarios like periodic and quasi-periodic fluctuations. On the other hand, dynamics of high complexity and deterministic nature like chaos and spatio-temporal chaos have been less explored, and to the best knowledge of the authors, the first work in this direction is the subject of this chapter. In our research, we were obtaining a novel approach to understand how deterministic fluctuations can induce transitions that differ from noise-induced transitions.

In this chapter, we unveil the effects of deterministic fluctuation in the front dynamics and compare it with the effect of random white noise as stochastic fluctuations counterpart. In particular, we found that fronts may remain pinned under deterministic fluctuations compared to the stochastic analogous. This is because chaotic dynamics exhibit forbidden transitions that limit fluctuations that can occur in time. The pinning-depinning transition is illustrated for archetypical equations coming from pattern formation theory, and it is deduced a law for the front position in the form of a parametrically driven oscillator with a chaotical forcing frequency. This research a relevant step to understanding how chaos and spatiotemporal chaos can induce transitions in out-of-equilibrium systems.

7.2 Deterministic versus stochastic fluctuations

To compare random and deterministic fluctuations, it is necessary to define some concepts coming from stochastic dynamics and probability theory. Thus, consider an experiment in which the sample space composed of all the possible outcome events is denoted by Ω. A real function X defined on the space Ω is called a random variable. In simple words, a random variable assigns a real number $X(\omega)$ to each possible outcome $\omega \in \Omega$. Random variables could be discrete or continuous, depending on if they take values into a discrete set or a continuous one. Thus, we say that a random variable has a discrete distribution if there exists a non-negative function such that for any $\omega \in \Omega$, the probability of occurrence of such event ω is given by

$$f(x) = P(X = \omega). \tag{7.1}$$

Therefore, for any indexed subset of $A = \{\omega_1, \ldots, \omega_{\mathrm{i}}, \ldots\} \subset \Omega$ we have that

$$P(X(\omega) \in A) = \sum_{\omega_{\mathrm{i}} \in A} f(\omega_{\mathrm{i}}). \tag{7.2}$$

On the other hand, a random variable has a continuous distribution, meaning that the random variable has a nonnegative function such that, for any interval $\mathcal{I}$

$$P(X \in \mathcal{I}) = \int_{\mathcal{I}} f(x)\mathrm{d}x. \tag{7.3}$$

A particular kind of random variable are the Gaussian distributed random variables, where the probability density function takes the form

$$f(x) = \frac{1}{2\sqrt{2\pi}} \mathrm{e}^{\frac{-(x-\mu)^2}{2\sigma^2}}, \tag{7.4}$$

where μ is the mean value of the random variable and σ its standar deviation.

Therefore, we can define a continuous-time random process as a time-indexed random process for which the index variable takes a continuous set of values, typically associated with time. A white noise process is a random process where the random Gaussian variables are temporally uncorrelated, have zero mean and finite variance. Thus $X(t)$ is a white noise like random process if

1. $\langle X(t) \rangle = 0$
2. $\langle X(t_1)X(t_2) \rangle = 0$, for $t_1 \neq t_2$
3. $\langle X(t)^2 \rangle < \infty$

The effect of this kind of fluctuations in the dynamics of fronts has been deeply explored in [125, 126, 128], exhibiting as the main result the pinning zone destruction phenomena.

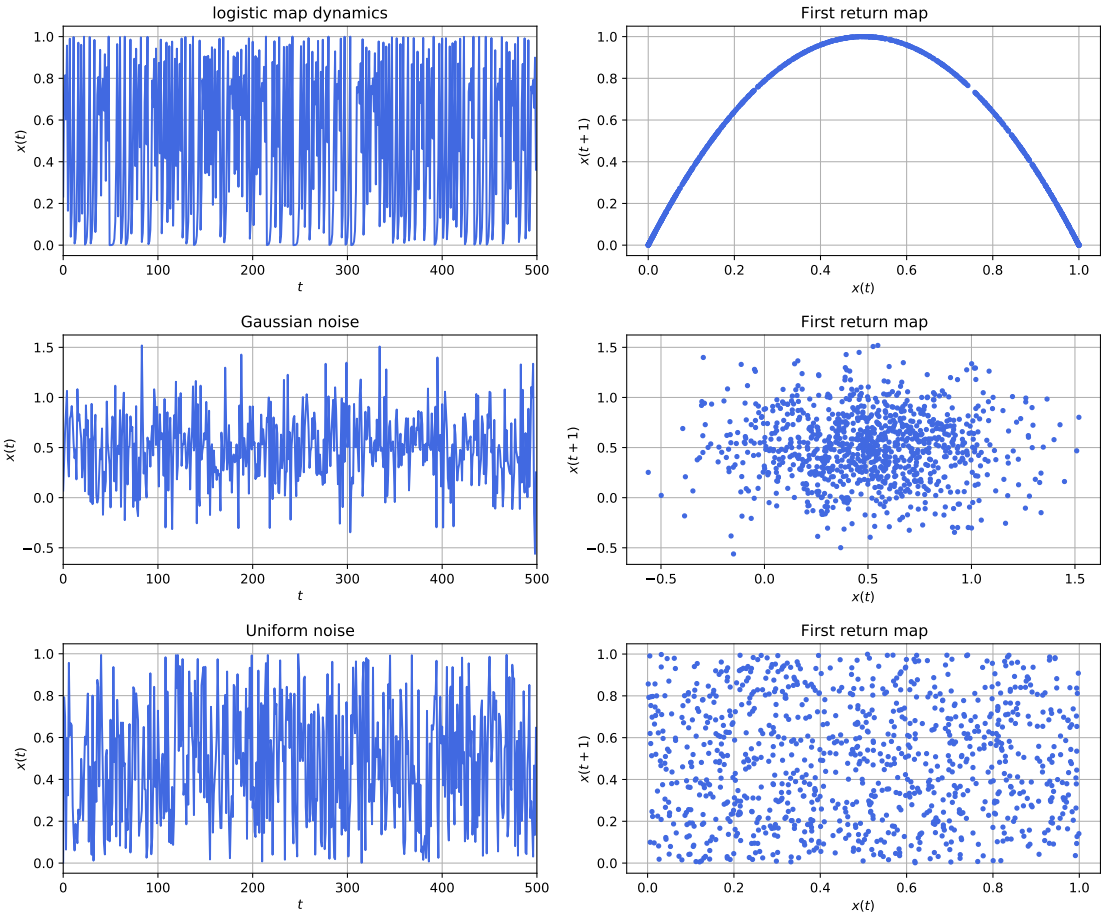

Figure 7.1: Geometrical differences between chaos and noise. Figures (a) (c) and (e) shows the first 500 iterations of the logistic map, a Gaussian noise $N(\mu = 0.5, \sigma \approx 0.35354)$, and a uniform noise $U[0, 1]$. Figures (b), (d) and (f) represent the first return map for the dynamics of logistic map, $N(\mu = 0.5, \sigma \approx 0.35354)$ and $U[0, 1]$ respectively.

On the other hand, we are interested in comparing these results with the effects that the system exhibits under deterministic spatiotemporal chaotic fluctuations. Both are complex and random-like. Nevertheless, in the addressed scenarios, some properties enable us to differentiate the chaos of noise easily.

7.2.1 Dynamical and statistical differences

Meanwhile, for a random process and any sub-interval with where the density function is non-zero, it is possible to get values in such subinterval at any time instant. In other words, it is possible to get (almost) the same value for each time step (or time interval for continuous-time processes). In deterministic chaotical systems, it is impossible because in the time-evolution of the system, starting in the attractor basin, it draws all the attractor for a sufficiently larger time. It is referred to as forbidden transitions and is described as transitions graphs [129] that could be obtained numerically in a similar way that invariant measures are calculated theoretically by a symbolic dynamics approach.

Another point of difference is found when the self-correlation is measured. For random white noise, the Pearson self-correlation goes to zero for $t > t_0$ quickly. Nevertheless, it is not the case for continuous chaotic systems, where memory is preserved, unveiling its deterministic origin. Nevertheless, scenarios where a chaotic system can exhibit a Pearson self-correlation function that vanishes quickly, e.g., the logistic map. Moreover, such maps have been used as part of algorithms for the generation of pseudo-random numbers [130]. Nevertheless, the hidden self-correlations could be captured with more sophisticated measures like mutual information, and partition cross-entropy [131, 132, 133]. Finally, a third interesting point that differentiates randomness from chaos is that chaotical orbits typically generate fractal structures. There exist patterns that appear behind the complexity. Random fluctuations do not generate patterns, as shown in the first return maps plotted in figure 7.1. Now, we can compare the effect of chaotic fluctuations versus stochastic ones.

7.3 The Nagumo–Kuramoto–Sivashinsky system

In this section, we will illustrate the effect of chaotic spatiotemporal fluctuations on a propagating interface between a homogeneous state and a complex spatiotemporal one, considering following set of equations.

$$\begin{cases} \partial_t u = u(\alpha - u)(u - 1) + \partial_{xx} u + \beta u cos(kx) + \gamma u \partial_x \psi & \text{(7.5a)} \\ \partial_t \psi = -\mu \partial_{xx} \psi - (\partial_x \psi)^2 - \partial_{xxxx} \psi & \text{(7.5b)} \end{cases}$$

where $u(x,t)$ is a scalar field. Equation (7.5a) can be understood as a bistable system with Nagumo type nonlinearity, with spatial diffusion and periodic spatial forcing (with wavelength $\lambda = 2\pi/k$) and chaotic spatial forcing weighed by the parameter γ.

The unforced Eq. (7.5a), $\beta = \gamma = 0$, corresponds to the well-known Nagumo model [134]. This model has two stable homogeneous states $u = 1$ and $u = 0$ that may be connected by a front. Such fronts propagate with a speed that depends on the value of the parameter α ($0 < \alpha < 1$) and only remains motionless for $\alpha = 1/2$. This particular value of α is called the Maxwell point [40]. Moreover, α describe the relative stability between the two competing states: for $\alpha < 1/2$ (resp. $\alpha > 1/2$), the state $u = 1$ (resp. $u = 0$) takes over the system. When the spatial forcing is taken into account ($\beta \neq 0$, $\gamma = 0$), the state equivalent to $u = 1$ is replaced by a periodic state with imprinted wavelength $2\pi/k$ [135, 136], meanwhile the state $u = 0$ remains as solution. Therefore, in this parameter regime, it is possible to found fronts connecting the periodic pattern and the homogeneous state, a situation that is conducive to front pinning [38]: the presence of spatial heterogeneity generates an energy barrier that must be overcome before the front can move. Consequently, the front speed vanishes over a relatively large interval of parameters, the so-called *pinning range*. Figure 7.3 shows the bifurcation diagram for the speed in terms of the parameter α, exhibiting for the spatial forcing intensity $\beta = 0.085$ the associated pinning range.

The second equation corresponds to the famous Kuramoto-Sivashinsky equation [137, 138, 28, 139, 140], which is perhaps the simplest system that presents spatiotemporal chaos. Given the spatial forcing, it is known that the dynamics of the front for equation (7.5b) exhibits

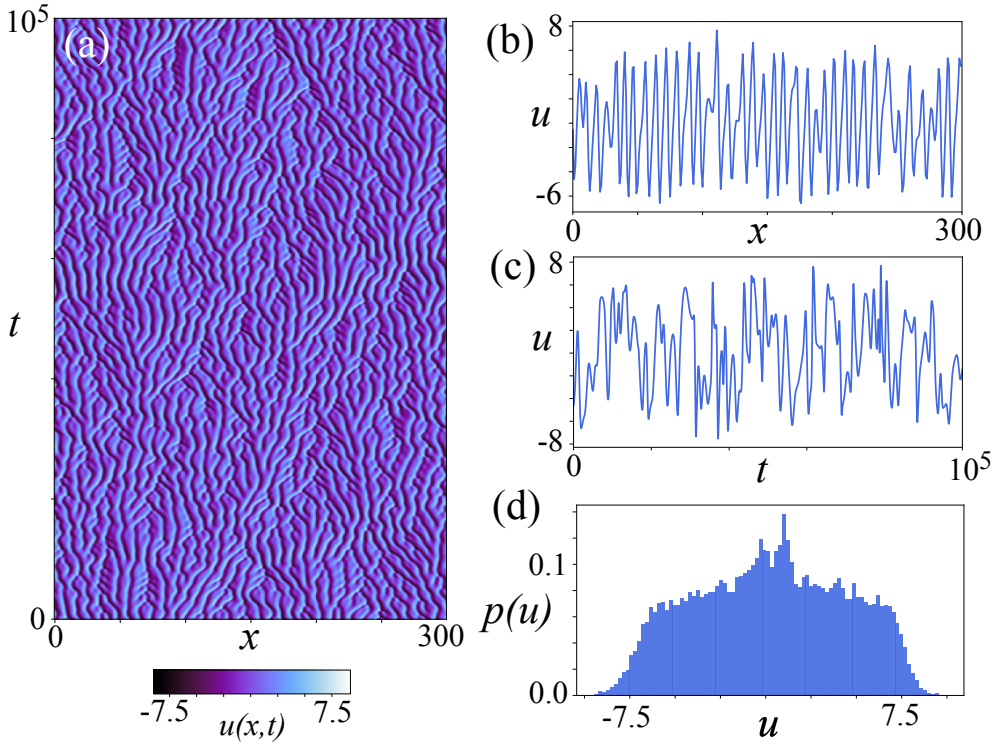

Figure 7.2: KS properties

pinning whenever the energy difference between the states connecting the front is not capable of overcoming the potential barrier generated by the periodic forcing.

The plot shows that the pinning-depinning transition corresponds to a supercritical bifurcation that takes place at $\alpha_c = \alpha_{\pm}$. These critical points correspond to SNIPER (Saddle-Node In a PERiodic orbit) bifurcations as found in related depinning problems [141]. Indeed, the average front speed, $\langle V \rangle$, grows as the square root of the distance from the critical point, $\langle V \rangle \sim \sqrt{|\alpha - \alpha_{\pm}|}$.

In the following section we will explore how deterministic fluctuations, corresponding to $\gamma \neq 0$ affect this bifurcation diagram.

7.4 The effect of spatiotemporal chaos in the front propagation: a chaos-induced transition

To understand the effect of spatiotemporal chaotic fluctuations in front dynamics, we take the system described by the equations (7.5a - 7.5b) and realize several numerical simulations, integrating using finite differences for spatial discretization and a fourth-order Runge-Kutta method for the time evolution. Neumann boundary conditions were imposed on both the Nagumo-Kuramoto and the Kuramoto-Sivashinsky equations. The domain length was fixed at $L = 300$ with a space discretization interval $\mathrm{d}x = 0.6$ and time step $\mathrm{d}t = 0.01$ for the time evolution.

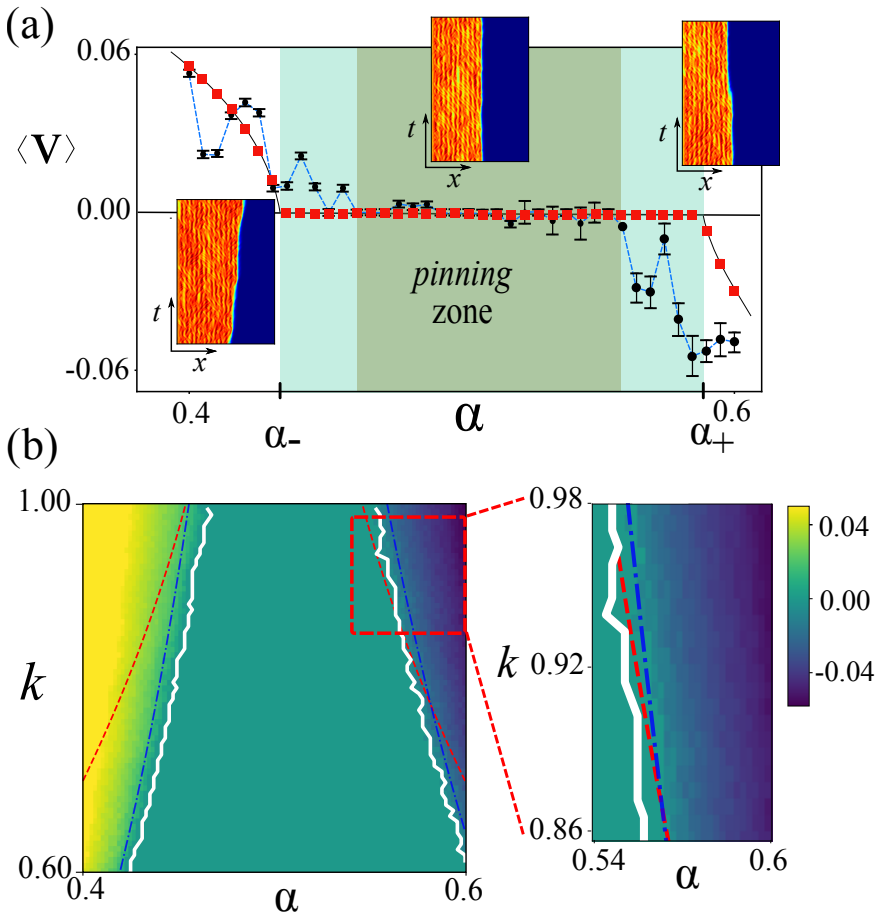

Figure 7.3: Pinning-depinning transition of spatiotemporally chaotic patterns embedded in a stable homogeneous state. (a) Average front speed $\langle V \rangle$ as a function of α. The squares ($\square$) and filled circles ($\bullet$) represent the average speed of the front obtained from numerical simulations of Eqs. (7.5a)–(7.5b) with $\beta = 0.085$, $k = 0.7$, and, respectively, $\gamma = 0$ and $\gamma = 0.055$. The vertical bars show the standard deviation of the front speed. The pinning region for $\beta \neq 0$ and $\gamma = 0$ is shown using light shading. This region shrinks as a result of spatiotemporally chaotic forcing, $\gamma \neq 0$ (dark shaded region). The insets show the spatiotemporal dynamics of the fronts in different parameter regimes. (b) Pinning region in the (α, k) parameter space. The white curve represents the boundary of the pinning region of the spatiotemporally forced system (7.5a)–(7.5b) with $\beta = 0.085$, $\gamma = 0.055$ computed numerically.

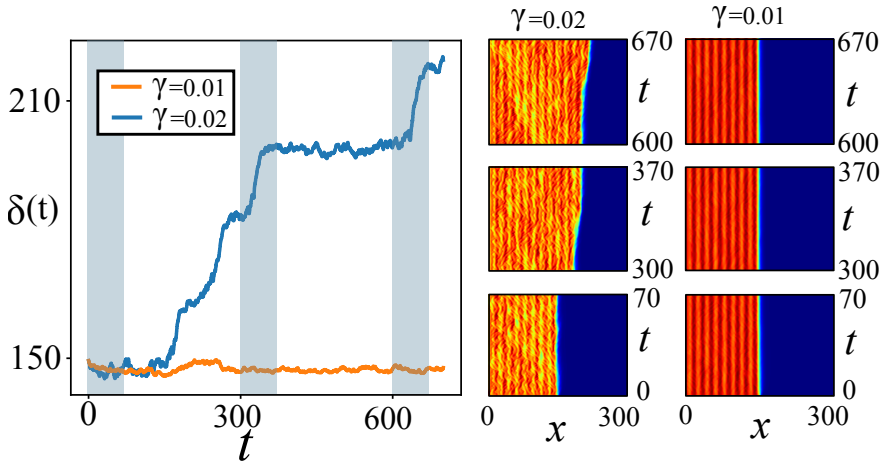

Figure 7.4: Position of the front core, calculated using the centroid formula on the derivative of the profile.

When $\gamma \neq 0$ the pattern state around $u = 1$ becomes spatiotemporally chaotic, obtaining that main result is not a pinning zone destruction effect. Moreover, there exists a range of γ values where the pinning zone exists, and for γ sufficiently larger, the spatiotemporal chaotic pattern always invades the homogeneous state. Besides, we evidence a shrinking effect of the pinning zone, obtaining that the extreme points defining the pinning zone $\alpha_-, alpha_+$ depends on γ. This shrink effect is shown in Fig. 7.3.

These differences between the effect of random and deterministic fluctuations put into the light a deeper question, how we can understand the emergence of noise from deterministic systems and how it is possible to model a limit from deterministic fluctuations to noise fluctuations in the same sense that a thermodynamic limit. The following sections try to approach these questions.

7.5 Emergence of noise from chaos

The differences between chaos and noise have been examined mainly by the design of metrics and indicators that enable us to distinguish both regimes in a certain quantifier space. Nevertheless, the origin of noise and its relationship to deterministic dynamics has been less explored. Does this drive us to questions like, is the randomness in nature a consequence of a collective of chaotical entities? It motivates us to verify if it is possible to find the noise ingredients (from a probability theory point of view) in deterministic dynamical systems. To give an approach to a possible answer, we consider a system composed of several components and built dynamical macroscopic variables like the average to measure. We found that the size of the system (number of constituent elements) and the coupling weakness between the elements are the two main ingredients to satisfy the probability criteria for randomness, decreasing the self-correlation when the system's size increases and the coupling are almost zero.

Randomness is typically understood as a memory-less behavior in which there is no possibility of predicting an event outcome (at least with precision). Nevertheless, we have

information about the random event distribution and predict where it is most probable to find an event. Also, in a random macroscopic process, it is impossible to predict the outcome when we perform the same experiment at a particular time. The main reason is that it is impossible to prepare a system with the same initial state for all its elements that constitute it when the number of elements is sufficiently larger. This property is related, in fact, with one of the main ingredients of chaos, called sensibility to initial conditions, and accounts for the experimental predictability in chaotic systems. A simple small change in the initial conditions can drive the system to final states far between them. Another interesting feature to consider is the so-called invariant measure (equivalent to the probability density function of a random variable), enabling us to access more rich dynamical and geometrical details of deterministic systems to compare with noise. Typically such invariant measures are nontrivial functions, and the dynamics itself of the system could be embedded into higher dimensional spaces where the orbits unfold, unveiling rich geometrical structures (fractals).

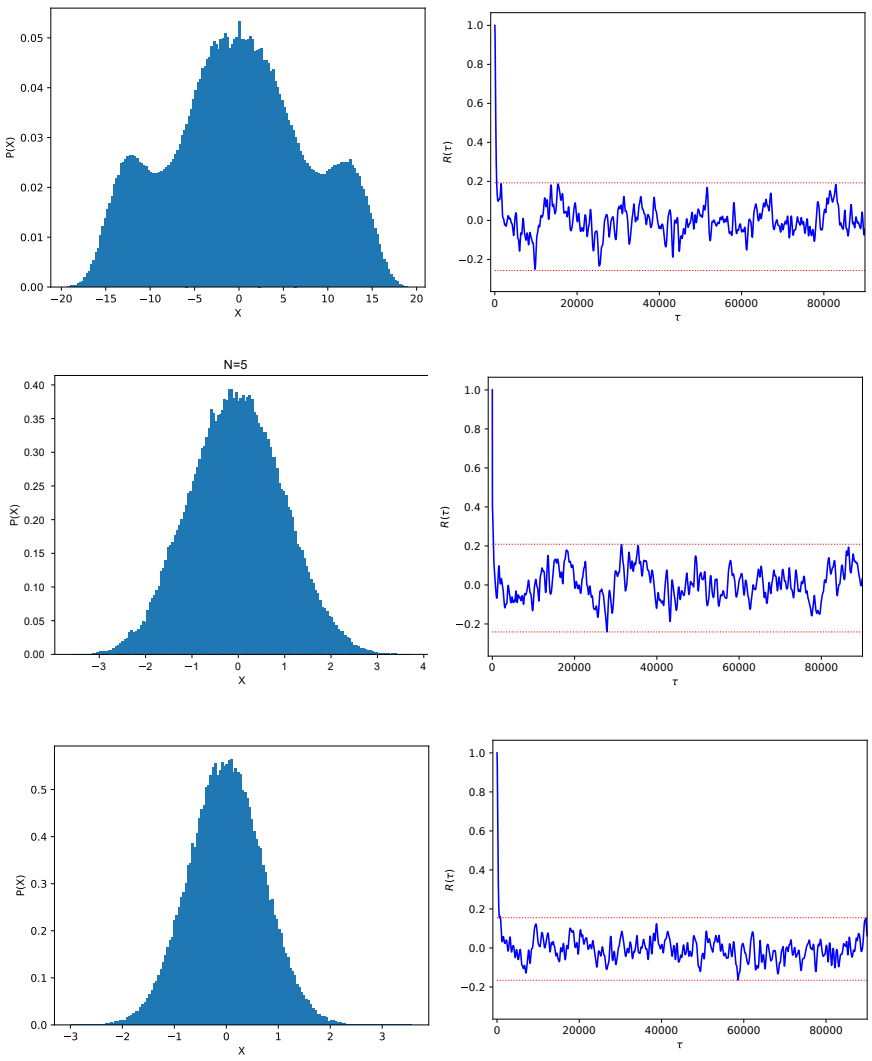

Figure 7.5: Dynamics of the macroscopic variable given by the equation (7.6). The increasing of N drives a Gaussian shape distribution of the variable and the loss of memory evidenced by the shrink in the variability range of the self-correlation function.

7.5.1 Noise from Lorenz equation

To illustrate the differences of deterministic fluctuations and noise, as well as how a deterministic system acquires random properties, we will consider two scenarios; the first one is a set of N independent copies of a Lorenz system with N large and the average of the X component as the macroscopic variable to measure in the whole system. As was mention in chapter 1, the Lorenz model is given by

$$\begin{aligned} \dot{X} &= \sigma(Y - X), \\ \dot{Y} &= X(\rho - Z) - Y, \\ \dot{Z} &= XY - \beta Z, \end{aligned}$$

and the parameters are fixed at $\beta = 8/3$, $\sigma = 10$ and $\rho = 28$ used by Lorenz to study the chaotic behavior of this system [142]. Note that $X(t)$ has a symmetric distribution about $X = 0$ and a correlation function that does not decay, as shown in the first two plots in Fig. 7.5. To study how can emerge randomness from chaos consider N independent copies of this system. Keeping with the X_{i} coordinate of each system and normalizing it conveniently, we building the macroscopic variable (coarse graining variable)

$$\bar{X}(t) = \frac{1}{\langle\sigma\rangle\sqrt{n}} \sum_{k=1}^{N} X_{\mathrm{i}}(t) \tag{7.6}$$

In figure 7.5 we can see the associated distribution and self-correlation function for $N = 1, 5$ and 200. Note that the distribution calculated taking the Lyapunov normalization term converges clearly to a normal distribution $N(0, 1)$ and the region where the self-correlation varies is decreasing in terms of N as expected.

7.5.2 Logistic Chaos

Another interesting example to examine is the logistic map, as a time discrete example of chaotic system, analized in detail in chapter 1 and given by

$$x^{t+1} = f(x^t) = \mu x^t (1 - x^t). \tag{7.7}$$

This is one of the simplest and paradigmatical systems exhibiting chaotical behavior. For our purposes, we put the parameter $\mu = 4$ at the fully developed chaotic region, where the interval $[0, 1]$ corresponds to the invariant set (basin of attraction) of the map. We build the approximated invariant measure for it, using the standard method of binning the phase space and realize a normalized histogram, obtaining the Fig. 7.6.

This map achieve easily a Gaussian-like distribution with few number of elements, namely, $N = 5$. Nevertheless, the self-correlation function vanishes almost instantaneously, and to evidence the loss of memory, we plot how this map loss one of the signatures of chaos fractal geometrical patterns in the first-return embedding space. Note that, in this case it is needed $N = 100$ to loss all the patterns, as was shown in Fig. 7.6.

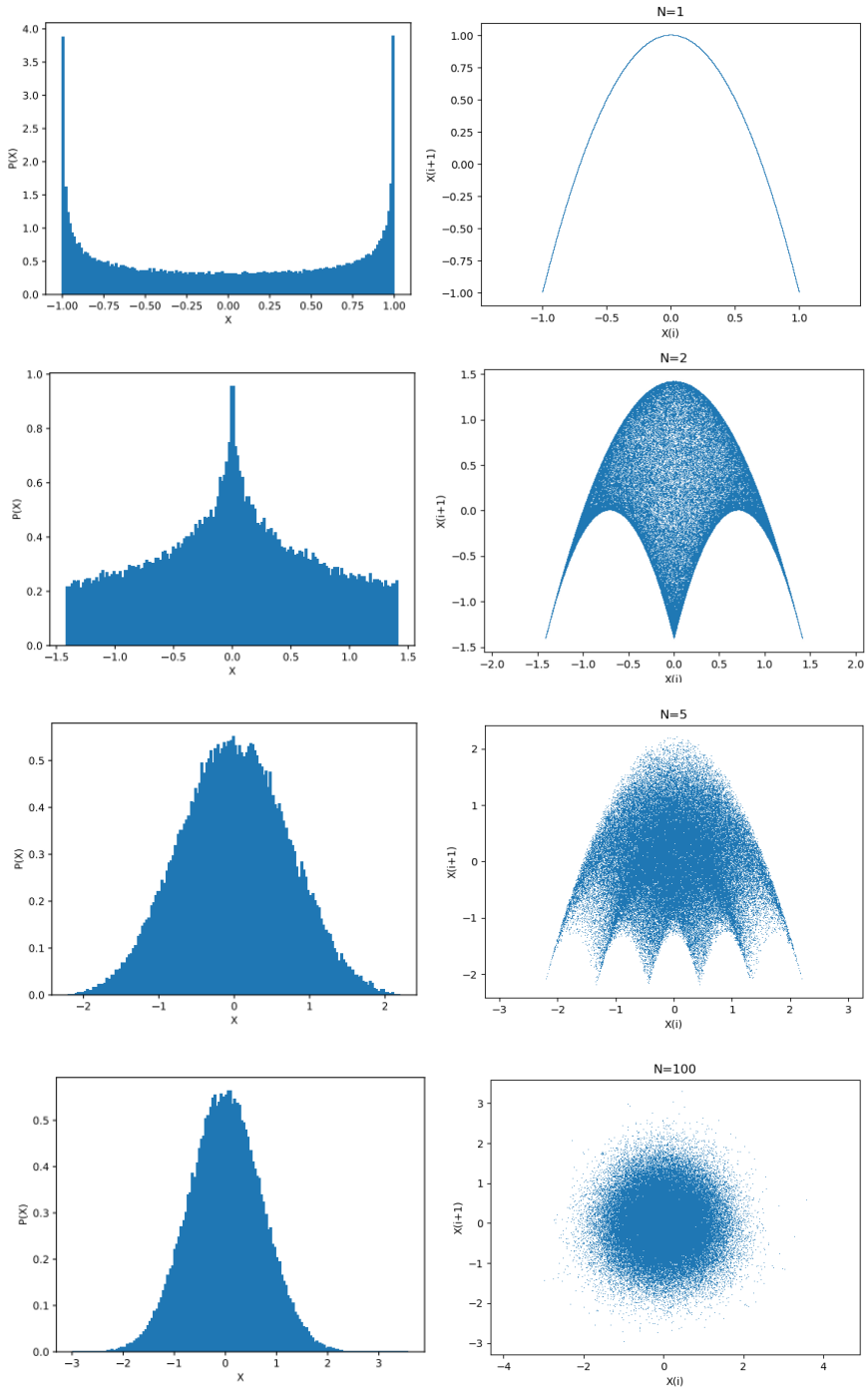

Figure 7.6: Dynamics of the macroscopic variable given by the equation (7.6) for the logistic map. The increasing of N drive to a Gaussian shape distribution of the variable, nevertheless in this scenario, the self-correlation vanishes faster than the case of Lorenz system. Thus, we evidence the memory loss by showing the first return map.

A more interesting chagenge us to se if a macroscopic variable comming from a sum of chaotical entities can satisfy one of the more fascinating results of the random variables and in general of the probability theory, the celebrated central limit theorem [143, 144]. In the following section, we will explore this question from a numerical perspective.

7.6 Obtaining a Central Limit Theorem

There exist a lot of variants from the central limit theorem (CLT) that mainly depends on the shape of the distributions of the corresponding random variables. The classical CLT due to Lindeberg–Lévy stablish that for a sequence $\{X_1, X_2, \dots\}$ of independent and identically distributed (i.i.d.) random variables with $\langle X_{\rm i}\rangle = \mu$ and $Var[X_{\rm i}] = \sigma^2 < \infty$, defining $S_n = \sum_{k=1}^{n} X_{\rm i}$ we have that $\sqrt{n}S_n - \mu$ converge in distribution to a normal $N(0, \sigma^2)$. Nevertheless, in general the invariant measure of a chaotical system is not i.i.d. Thefore, we will use the following generalization of the CLT due to Lyapunov.

Lyapunov's CLT. Suppose $\{X_1, X_2, \dots\}$ is a sequence of independent random variables, each with finite expected value $\mu_{\rm i}$ and variance $\sigma_{\rm i}^2$. Defining $s_n^2 = \sum_{\rm i=1}^{n} \sigma_{\rm i}^2$, if for some $\delta > 0$, Lyapunov's condition

$$\lim_{n\to\infty} \frac{1}{s_n^{2+\delta}} \sum_{\rm i=1}^{n} \left\langle \left[|X_{\rm i} - \mu_{\rm i}|^{2+\delta} \right] \right\rangle = 0$$

is satisfied, then a sum converges in distribution to a standard normal random variable, as n goes to infinity, i.e.,

$$\frac{1}{s_n} \sum_{\rm i=1}^{n} (X_{\rm i} - \mu_{\rm i}) \xrightarrow{\rm d} N(0, 1). \tag{7.8}$$

In practice, it is usually easiest to check Lyapunov's condition for $\delta = 1$.

Thus, we consider a macroscopic variable as a sum of several chaotical entities proposed in the Eq. 7.8. In this scenario, we can observe how the macroscopic variable converge in distribution to a Gaussian, as Lyapunov's CLT aims. In fact, in Fig. 7.6 we can see how this convergence is achieved as the number of uncoupled copies N increases. To reach a good convergence in distribution, we only need a value of $N = 5$. Thus, it is possible to conjecture that there exists a central limit theorem for chaotic systems that satisfy the same hypothesis as the central limit theorem of Lyapunov. The relationships between chaos and the central limit theorem have been boarded in [145, 146, 147] from a theoretical point of view. Nevertheless, a demonstration of a central limit theorem for chaotic systems remains open. We currently realize future research in this direction.

7.7 Outline

- This work opens the possibility to explore how complex deterministic fluctuations can affect the interface dynamics and propose an interesting question, it is always external fluctuations be modeled by stochastic processes?
- These complex deterministic fluctuations could correspond to a system coupled with a small reservoir bath, defined with a small number of particles, whose dynamics could be modeled by an n-body problem which have chaotical solutions typically.

- Our research creates a bridge to exploring deterministic fluctuation modify pre-existing phase transitions or even induce new ones. In this sense, a complete study of chaos-induced transition is missing and creates an interesting area to explore.
- Some physical processes such as phase separation in binary mixtures or alloys (with a certain degree of isolation) could enable some possible applications to understand the propagation of interfaces.
- Besides, using SLM as a device to introduce spatio-temporal chaos in devices like liquid crystal light valves with optical feedback could enable us to explore the effect of chaos in such devices experimentally.
- Finally, an approach to understand how randomness can emerge from deterministic systems is elucidated.

Front depinning by deterministic and stochastic fluctuations: A comparison

A. J. Alvarez-Socorro,[1] Marcel G. Clerc,[1] M. A. Ferré,[1] and Edgar Knobloch[2]
[1]*Departamento de Física and Millennium Institute for Research in Optics, Facultad de Ciencias Físicas y Matemáticas, Universidad de Chile, Casilla 487-3, Santiago, Chile*
[2]*Department of Physics, University of California at Berkeley, Berkeley, California 94720, USA*

(Received 21 March 2019; published 27 June 2019)

Driven dissipative many-body systems are described by differential equations for macroscopic variables which include fluctuations that account for ignored microscopic variables. Here, we investigate the effect of deterministic fluctuations, drawn from a system in a state of phase turbulence, on front dynamics. We show that despite these fluctuations a front may remain pinned, in contrast to fronts in systems with Gaussian white noise fluctuations, and explore the pinning-depinning transition. In the deterministic case, this transition is found to be robust but its location in parameter space is complex, generating a fractal-like structure. We describe this transition by deriving an equation for the front position, which takes the form of an overdamped system with a ratchet potential and chaotic forcing; this equation can, in turn, be transformed into a linear parametrically driven oscillator with a chaotically oscillating frequency. The resulting description provides an unambiguous characterization of the pinning-depinning transition in parameter space. A similar calculation for noise-driven front propagation shows that the pinning-depinning transition is washed out.

DOI: 10.1103/PhysRevE.99.062226

I. INTRODUCTION

Nonequilibrium systems, i.e., driven dissipative systems, frequently exhibit rich and complex interface dynamics as one state displaces another or defects nucleate, drift, and annihilate [1–4]. This defect evolution is usually dominated by interface, wall, or front dynamics depending on the physical context under study. These nonlinear waves do not obey the superposition principle, and each interface has a well-defined profile that depends on the parameter values of the system. The concept of front propagation originally emerged in the context of population dynamics [5], gene propagation [6] as well as flame propagation [7], and has since attracted growing interest in chemistry, biology, physics, and mathematics [1–3,8].

In physics, fronts play a central role in a large variety of situations, ranging from reaction-diffusion models and solidification processes to pattern-forming systems arising in fluid dynamics (see, e.g., [1,3,9] and references therein). From the point of view of dynamical systems theory a one-dimensional front of constant form corresponds to a heteroclinic orbit connecting two spatially extended homogeneous states [10]. The propagation speed of the front depends on the type and stability of the states connected by the front. One of the most studied types of front is that connecting a stable spatially homogeneous state with an unstable one, the so-called FKPP or pulled front [2,11]. The speed of such a front is not, in general, unique and depends on the initial condition [11]. Another well-known type of front, a bistable or pushed front, connects two stable homogeneous states [4]. Such fronts are found inside a bistability region between two homogeneous states and are characterized by a single speed that is determined by the free energy difference between the two states whenever the system is variational. In this case the state with the lower energy displaces that with higher energy [4] and the front speed only vanishes at the Maxwell point, at which both states have the same energy [1].

The previous scenario changes when the front connects a homogeneous state to a spatially periodic or patterned state. As first pointed out by Pomeau [4], the presence of spatial heterogeneity is expected to generate an energy barrier or pinning potential that has to be overcome before the front can propagate, i.e., front propagation only occurs when the energy difference between the two states exceeds a nonzero minimum value. In the vicinity of the Maxwell point the energy difference is too small for propagation and the front remains motionless or pinned. When the energy difference is large enough and the front depins, it moves in a stick-slip manner, with a mean speed that increases as the square root of the distance from the parameter value for depinning. The existence of a pinning range has been discussed in a number of physical contexts, and in particular in the context of the generalized Swift-Hohenberg model [12] and the crystallization kinetics of cellular patterns (see the textbook [1] and references therein). Experimentally, an observation of the pinning-depinning transition in a spatially periodic optical medium was reported in [13]. However, the inclusion of inherent incoherent fluctuations (i.e., noise) drastically changes the pinning-depinning transition [14,15]. Noise-induced escape over the confining potential barrier [16] allows the system to escape permanent pinning and ultimately always results in front propagation. Likewise, one can consider fronts that connect a state with coherent intrinsic spatiotemporal fluctuations (chaos, spatiotemporal chaos, turbulence, etc.) with a nonfluctuating homogeneous state. This type of front is fundamental to the understanding of flame propagation in combustion [17–19], emergence of turbulence in pipe flow [20], turbulence propagation [21], and the propagation of spatiotemporal chaos in an optical fiber cavity [22,23]. However,

in these systems no pinning-depinning transition is observed. In contrast, phase-coupled oscillators with a nonlocal coupling exhibit states with partial synchrony called chimera states. These states can be considered to be bound states of a pair of synchronization fronts bounding a coherent state, embedded in a background incoherent state [24–28]. Despite the fluctuations in the background these fronts do not depin and the length of the interval of coherence fluctuates about a well-defined mean determined by the parameters of the problem.

Incoherent fluctuations, such as those arising from thermal effects, are usually described by a random variable having equal intensity at different frequencies (white noise), i.e., a constant power spectrum density [29]. Thus, fluctuations of any size are allowed, with the restriction that large fluctuations are unlikely. In contrast, deterministic (chaotic) fluctuations have a power spectrum dominated in general by certain incommensurate frequencies [30]. Moreover, since the strange attractor responsible for the chaos is typically bounded, the associated deterministic fluctuations have a maximum size. This difference between the accessible deterministic and stochastic fluctuations has a major impact on the dynamics of fronts.

The basic question is whether coherent spatiotemporal fluctuations always trigger a depinning transition in systems exhibiting pinned fronts between two distinct states, in other words whether deterministic fluctuations behave like additive noise [16]. We show here that in the presence of coherent spatiotemporal fluctuations fronts between a spatiotemporally chaotic pattern and a homogeneous state may indeed remain pinned, albeit in a narrower parameter range. We also show, using a bistable model that exhibits a pinning-depinning transition driven by phase turbulence, that this transition is robust but that the pinning-depinning boundary becomes complex, generating a fractal-like structure in parameter space. We describe the pinning-depinning transition using an effective equation for the front position which takes the form of an equation for an overdamped system with a ratchet potential and chaotic forcing determined by the instantaneous location of the front. These fluctuations are bounded and may be insufficient to trigger a depinning transition. Using a series of transformations we convert this problem into a linear parametrically driven oscillator with a chaotically oscillating frequency. The resulting description allows us to characterize the pinning-depinning transition unambiguously, by identifying the unbounded (bounded) solutions of the oscillator problem with pinned (depinned) solutions of the front problem, and hence allows us to compute the boundary between the two, i.e., the location in parameter space of the pinning-depinning transition. A similar calculation for a noise-driven system leads to the same ratchet potential but driven by additive white noise. In this case the front always eventually depins.

II. MODEL

To investigate the propagation of an interface between homogeneous and complex spatiotemporal states, we consider the following model:

$$\partial_t u = u(\alpha - u)(u - 1) + \partial_{xx} u + \beta u \cos(kx) + \gamma u \partial_x \psi, \quad (1)$$

where $u(x,t)$ is a scalar field. The first term on the right-hand side describes a bistable system and corresponds to the Nagumo nonlinearity in the context of population dynamics [8]. The second term accounts for diffusion. The third term represents spatial forcing with amplitude β and wavelength $\lambda = 2\pi/k$ which gives rise to a pattern state. Finally, the last term represents multiplicative spatiotemporally chaotic forcing, with the auxiliary scalar field ψ taken to satisfy the Kuramoto-Sivashinsky equation

$$\partial_t \psi = -\mu \partial_{xx} \psi - (\partial_x \psi)^2 - \partial_{xxxx} \psi. \quad (2)$$

Equation (2) describes the propagation of nonlinear waves of chemical concentration in the Belousov-Zhabotinskii reaction [32–34] and the propagation of flame fronts [35,36], and is perhaps the simplest model that exhibits spatiotemporal chaos [37]. In this context, $\psi(x,t)$ determines the position of an interface between two distinct states. In this paper we use this equation to provide spatiotemporal forcing of Eq. (1) via the zero-mean coupling term $\partial_x \psi$. Note that the field $u(x,t)$ does not feed back on $\psi(x,t)$. Thus, the spatiotemporal forcing is *prescribed*. A model similar to Eqs. (1) and (2) was originally introduced to understand the existence of localized but spatiotemporally chaotic solutions [31].

The unforced Eq. (1), $\beta = \gamma = 0$, corresponds to the well-known Nagumo model [8,38]. This model has two stable homogeneous states $u = 1$ and $u = 0$ that may be connected by a front. Such fronts are typically nonstationary and so propagate with a speed that depends on the value of the parameter α ($0 < \alpha < 1$). Thus α measures the relative stability of the two competing states: for $\alpha < 1/2$ (respectively, $\alpha > 1/2$), the state $u = 1$ (respectively, $u = 0$) takes over the system. There is only one value of α, $\alpha \equiv \alpha_M = 1/2$, at which the interface is motionless. This particular value of α is called the Maxwell point [1]. When the spatial forcing is taken into account ($\beta \neq 0$, $\gamma = 0$), the above scenario changes. Although the state $u = 0$ persists unchanged, the state $u = 1$ is replaced by a periodic state with imprinted wavelength $2\pi/k$, cf. [13,39,40]. Hence, in this parameter regime, the system possesses fronts between a periodic solution and a homogeneous state, a situation that is conducive to front pinning [4]: the presence of spatial heterogeneity generates an energy barrier that must be overcome before the front can move. Consequently, the front speed vanishes over a relatively large interval of parameters, the so-called *pinning range*. Figure 1(a) shows a typical pinning range as a green shaded area. Square symbols (■) represent the numerically determined average front speed. The plot shows that the pinning-depinning transition corresponds to a supercritical bifurcation that takes place at $\alpha_c = \alpha_\pm$. These critical points correspond to SNIPER (Saddle-Node In a PERiodic orbit) bifurcations as found in related depinning problems [41]. Indeed, the average front speed, $\langle V \rangle$, grows as the square root of the distance from the critical point, $\langle V \rangle \sim \sqrt{|\alpha - \alpha_\pm|}$. Far from this critical point, the average front speed grows linearly [42]. The resulting bifurcation diagram was verified experimentally in a spatially forced liquid crystal light valve experiment [13,39].

When $\gamma \neq 0$ the pattern state around $u = 1$ becomes spatiotemporally chaotic and as a result the pinning range shrinks [Fig. 1(a)]. The pinning interval that remains decreases as the forcing wave number k increases [Fig. 1(b)], and vanishes in a

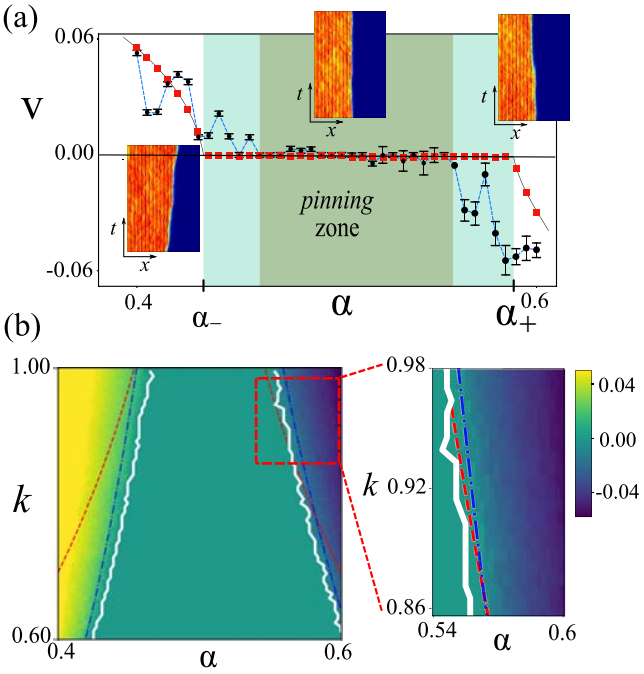

FIG. 1. Pinning-depinning transition of spatiotemporally chaotic patterns embedded in a stable homogeneous state. (a) Average front speed $\langle V \rangle$ as a function of α. The filled squares (■) and circles (●) represent the average speed of the front obtained from numerical simulations of Eqs. (1) and (2) with $\beta = 0.085$, $k = 0.7$, and, respectively, $\gamma = 0$ and $\gamma = 0.055$. The vertical bars show the standard deviation of the front speed. The pinning region for $\beta \neq 0$ and $\gamma = 0$ is shown using light shading. This region shrinks as a result of spatiotemporally chaotic forcing, $\gamma \neq 0$ (dark shaded region). The insets show the spatiotemporal dynamics of the fronts in different parameter regimes. (b) Pinning region in the (α, k) parameter space. The white curve represents the boundary of the pinning region of the spatiotemporally forced model (1) and (2) with $\beta = 0.085$, $\gamma = 0.055$ computed numerically. For comparison we also show the location of the theoretically predicted pinning-depinning transition $\alpha_\pm = \alpha_M \pm \sqrt{\beta k A(k)/2}$ with $\alpha_M = 1/2$ and $A(k)$ determined from formula (10) (red dashed line) and from numerical integration of the interface equation (8) (blue dashed-dotted line). Both procedures are valid for $\gamma \ll 1$ only. The quality of the theoretical predictions can be ascertained from the enlargement shown in the lower right panel.

cusp at $(\alpha, k) = (1/2, \infty)$ as $k \to \infty$ (not shown). Figure 2(a) shows a typical spatiotemporal evolution of the chaotic pattern state. This state may be characterized by means of Lyapunov exponents, which provide information about the solution sensitivity to exponentially close initial conditions [43]. From a dynamical systems point of view, if the largest Lyapunov exponent is positive, the system is chaotic, but not necessarily spatiotemporally chaotic. To distinguish between these two types of complex dynamical behavior, it is necessary to compute the Lyapunov spectrum, i.e., the set of Lyapunov exponents [43,44]. Spatiotemporal chaos has a Lyapunov spectrum with a continuous set of positive values. In this case, the number of positive exponents in the Lyapunov spectrum depends on the length L of the domain. In contrast, chaos in a low-dimensional system possesses a Lyapunov spectrum with a discrete set of positive exponents whose number is

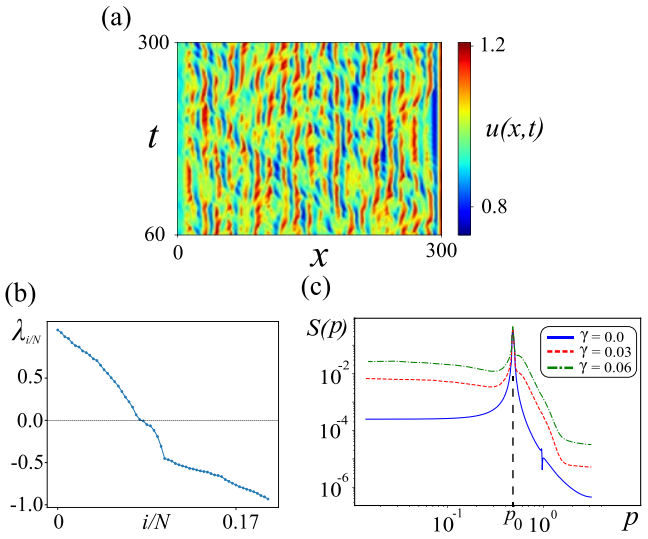

FIG. 2. Spatiotemporally chaotic pattern state of the Kuramoto-Sivashinsky-Nagumo model, Eqs. (1) and (2), when $\alpha = 0.38$, $\beta = 0.085$, $\gamma = 0.03$, and $k = 0.6$. (a) Space-time diagram. (b) The corresponding Lyapunov spectrum. (c) Power spectra $S(p)$ of the pattern state $u(x,t)$ for three different values of the forcing amplitude γ averaged over $T = 10^6$ snapshots. The forcing wave number k is denoted by p_0.

independent of L. Figure 2(b) shows the Lyapunov spectrum of the spatiotemporally chaotic pattern state in Fig. 2(a), computed from Eqs. (1) and (2) using the strategy proposed in [45,46]. Here, N counts the number of points into which the system has been discretized and i is an integer that indexes the Lyapunov exponents. The figure shows that this state is indeed spatiotemporally chaotic. All the numerical simulations were conducted using finite differences for spatial discretization and a fourth-order Runge-Kutta method for the time evolution. Neumann boundary conditions were imposed on both the Nagumo-Kuramoto and the Kuramoto-Sivashinsky equations. The domain length was fixed at $L = 300$ with a space discretization interval $dx = 0.6$ and time step $dt = 0.01$ for the time evolution.

With the aim of understanding the mode dynamics of the state shown in Fig. 2(a), we introduce the time-averaged power spectrum [37]

$$S(p) = \frac{1}{T}\int_0^T \left| \int_0^L u(x,t) e^{ipx} dx \right|^2 dt, \tag{3}$$

where L is the system size and T is a large time interval. The resulting spectra, computed from Eqs. (1) and (2) for several different values of the forcing amplitude γ, are shown in Fig. 2(c) and confirm the broad-band nature of the mode-mode interactions involved in the spatiotemporally chaotic state despite the dominance of the forcing wave number $p_0 = k$ and its harmonics.

From Fig. 1 and the related results in Fig. 2 we infer that the model (1) and (2) exhibits coexistence between a spatiotemporally chaotic pattern $u(x,t)$ and the homogeneous state $u = 0$. Under these conditions one expects to find front solutions between these states. The insets in Fig. 1(a)

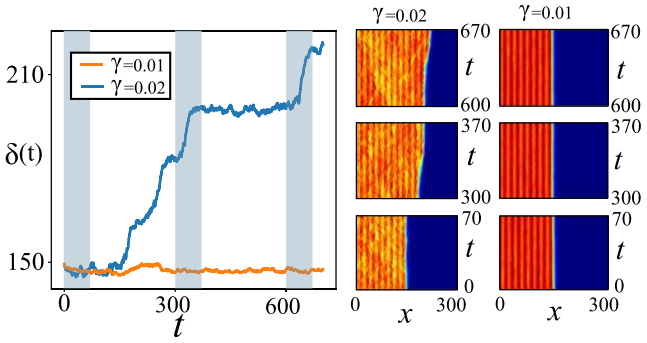

FIG. 3. Temporal evolution of the front position $x = \delta(t)$ in the model (1) and (2) in the pinning and depinning regimes when $\alpha = 0.45$, $\beta = 0.085$, $k = 0.9$, and $\gamma = 0.01$ (pinned front, right panel) and $\gamma = 0.02$ (unpinned front, middle panel).

depict typical front solutions of this type and their temporal evolution for different values of the parameter α. The filled circles (•) in Fig. 1(a) represent the average front speed computed numerically and these show that for $k = 0.7$ and $\gamma = 0.055$ the pinning-depinning transition not only persists but also acquires complex dependence on the forcing wave number k.

To characterize the dynamics of the front in greater detail, we monitored its position $x = \delta(t)$ defined by the condition

$$\delta(t) \equiv \frac{\int_{-L/2}^{L/2} x\partial_x u(x,t)\,dx}{\int_{-L/2}^{L/2} \partial_x u(x,t)\,dx}, \tag{4}$$

where L is the system size. Thus $\delta(t)$ corresponds to a value of the field $u(x,t)$ between the two equilibria. In particular, in the unperturbed problem $u(x=\delta) = 1/2$, a value exactly halfway between the two equilibria. Figure 3 illustrates the temporal evolution of the front position in the pinning and depinning regimes, respectively. As a result of chaotic forcing the pinning-depinning boundary becomes complex, generating a fractal-like structure [see Fig. 1(b), white curve]. Complex fluctuations around a given location characterize the front position inside of the pinning region (see Fig. 3, dark orange curve). Outside of the pinning region, the front position exhibits stick-slip dynamics with complicated oscillations around a fixed position alternating with jumps to a new position. This process repeats, with jumps of order of the wavelength $2\pi/k$ and always in the same direction (see Fig. 3, dark blue curve). The complexity of the front motion can be quantified in terms of the largest Lyapunov exponent which characterizes the behavior of the sudden jumps in the front position $\delta(t)$ as parameters are varied in the spatiotemporally chaotic regime [43]. Figure 4 shows the largest Lyapunov exponent, $\lambda_{\rm LLE}$, of this motion, computed from 200 slightly different initial conditions, as a function of the parameter α. The exponent $\lambda_{\rm LLE}$ tends to increase with increasing α but cannot be used to infer the location of the pinning region. In other words, the chaotic behavior inside and outside of the pinning region exhibits similar characteristics, and $\lambda_{\rm LLE}$ is not a good indicator of the pinning-depinning transition.

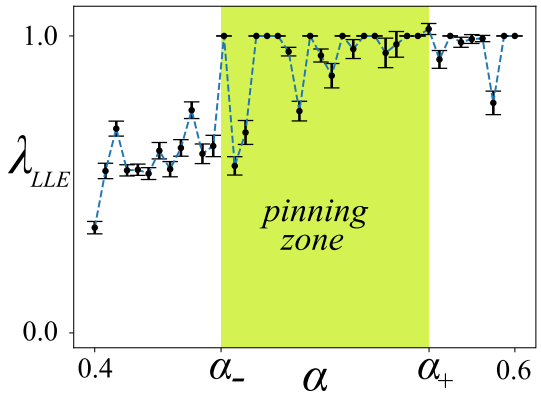

FIG. 4. Largest Lyapunov exponent $\lambda_{\rm LLE}$ of the front position as a function of α for $k = 0.7$, $\gamma = 0.055$, and $\beta = 0.085$. The shaded region shows the pinning region.

III. ANALYTICAL CHARACTERIZATION OF INTERFACE DYNAMICS

In this section, we explain the pinning-depinning transition in terms of the front position $\delta(t)$. An equation describing the dynamics of δ is deduced using perturbation methods. Similar approaches have been used to explain the existence of both stationary [42] and time-dependent [31] localized structures.

The unforced model, Eqs. (1) and (2) with $\beta = \gamma = 0$, has an exact stationary front solution at the Maxwell point $\alpha_M = 1/2$ connecting the two homogeneous states $u = 0$ and $u = 1$:

$$u_F(x,\delta) = \frac{1}{2} + \frac{1}{2}\tanh\left(\frac{\sqrt{2}}{4}(x-\delta)\right). \tag{5}$$

To understand the effect of spatial ($\beta \neq 0$) and spatiotemporally chaotic ($\gamma \neq 0$) forcing, we suppose that both β and γ are small and that the system is close to the Maxwell point, i.e., $\gamma \sim \beta \ll 1$ and $\tilde{\alpha} \equiv \alpha_M - \alpha$, with $\tilde{\alpha} \sim \gamma \sim \beta$. Let us consider the following ansatz:

$$u(x,t) = u_F(x - \delta(t)) + \mathrm{W}(x,t), \tag{6}$$

where the front position $\delta(t)$ is promoted to a temporal function representing the dynamics of the interface. The remainder term $\mathrm{W}(x,t)$ is assumed to be small, of the order of β, γ, and $\tilde{\alpha}$. Introducing the above ansatz in Eq. (1) together with the definition of the comoving coordinate $z \equiv x - \delta(t)$, and linearizing in W, we obtain

$$\begin{aligned} -\hat{\mathscr{L}}\mathrm{W} = {} & \partial_z u_F \dot{\delta} - \tilde{\alpha} u_F(u_F - 1) + \beta u_F \cos(kz + k\delta) \\ & + \gamma u_F \partial_z \psi(z+\delta, t), \end{aligned} \tag{7}$$

where the linear operator $\hat{\mathscr{L}} \equiv 3u_F - 3u_F^2 - 1/2 + \partial_{zz}$. To solve the above linear equation, we introduce the inner product $\langle f|g\rangle = \int_{-\infty}^{\infty} f^*(z)g(z)dz$. Using this inner product, it is easy to show that $\hat{\mathscr{L}}$ is self-adjoint, $\hat{\mathscr{L}} = \hat{\mathscr{L}}^\dagger$. Note that $\partial_z u_F$ is an element of the kernel of $\hat{\mathscr{L}}^\dagger$. Applying the solvability condition, equivalently the Fredholm alternative [47], one obtains, after straightforward calculations,

$$\dot{\delta} = -\frac{\partial U}{\partial \delta} - 6\sqrt{2}\gamma \mathrm{B}(t). \tag{8}$$

The first term is the gradient of an effective time-independent potential given by

$$U(\delta) \equiv \sqrt{2}\tilde{\alpha}\delta + \beta A \sin(k\delta + \phi), \tag{9}$$

where

$$A \equiv 6\pi\sqrt{1+2k^2}\,\mathrm{csch}(\sqrt{2}\pi k), \tag{10}$$

$$\phi \equiv \arctan(\sqrt{2}k). \tag{11}$$

The potential $U(\delta)$ in Eq. (9) is called a washboard potential or equivalently a *generalized Peierls-Nabarro potential* because of its use in describing the dynamics of dislocations in crystals [48–50]. However, it also describes the motion of charged particles in a periodic crystal in the presence of an electric field, and arises in other spatially forced physical systems as well. In particular, the potential has been used to explain the existence of localized spatiotemporally chaotic solutions in both continuous [31] and discrete media [27,51].

The second term on the right-hand side of Eq. (8) corresponds to additive time-dependent forcing with amplitude

$$\mathrm{B}(t) \equiv \int_{-\infty}^{\infty} u_F(z)\partial_z u_F(z)\partial_z \psi(z+\delta, t)\, dz. \tag{12}$$

Although this chaotic forcing appears to depend on the front position δ this fact does not change the statistical properties of $\mathrm{B}(t)$ which remain on average homogeneous.

Equation (8) describes an overdamped system with a ratchet potential and chaotic forcing. When the potential barrier between equilibria is sufficiently large the front position fluctuates around an equilibrium position and we call the front pinned. On increasing the forcing amplitude γ above a critical value, the front position begins to explore nearby equilibria in order to minimize energy, leading to a pinning-depinning transition, i.e., to the onset of front propagation. Thus front propagation corresponds to a *chaotic ratchet motor*.

In the absence of spatiotemporally chaotic forcing, $\gamma = 0$, an analytical expression for the pinning-depinning transition can be deduced from the stationary solution of Eq. (8). The width of the pinning region is determined by the condition $A^2(k) = 2\tilde{\alpha}^2(k)k^2/\beta^2$. Figure 1(b) shows the smooth dependence of the resulting pinning-depinning transition $\alpha_{\pm}(k)$ on the wave number k (dashed red line).

When spatiotemporally chaotic forcing is included, $\gamma \neq 0$, the pinning-depinning boundary $\alpha_{\pm}(k)$ is fundamentally altered, and now takes on a fractal structure. In Fig. 1(b) this boundary is indicated by the white curve. To understand the complex dynamics exhibited by the fronts near this boundary and the complex structure of the boundary in parameter space, one must first characterize the spatiotemporally chaotic forcing given by Eq. (12). Figure 5 shows the temporal evolution of the function $\mathrm{B}(t)$ obtained from the Kuramoto-Sivashinsky model (2) with $\mu = 3.0$. The statistical characterization of the spatiotemporally chaotic forcing and its probability density function can be determined from Eq. (2), and is shown in Fig. 5(b). Note that the histogram of the values acquired by the function $\mathrm{B}(t)$ is similar to a Gaussian distribution [the fit in Fig. 5(b) has standard deviation 0.2355] although the distribution has compact support (see the zoom of the histogram tail). This is a consequence of the fact that the function $\partial_z u_F(z)$ in the integrand in Eq. (12) cuts off

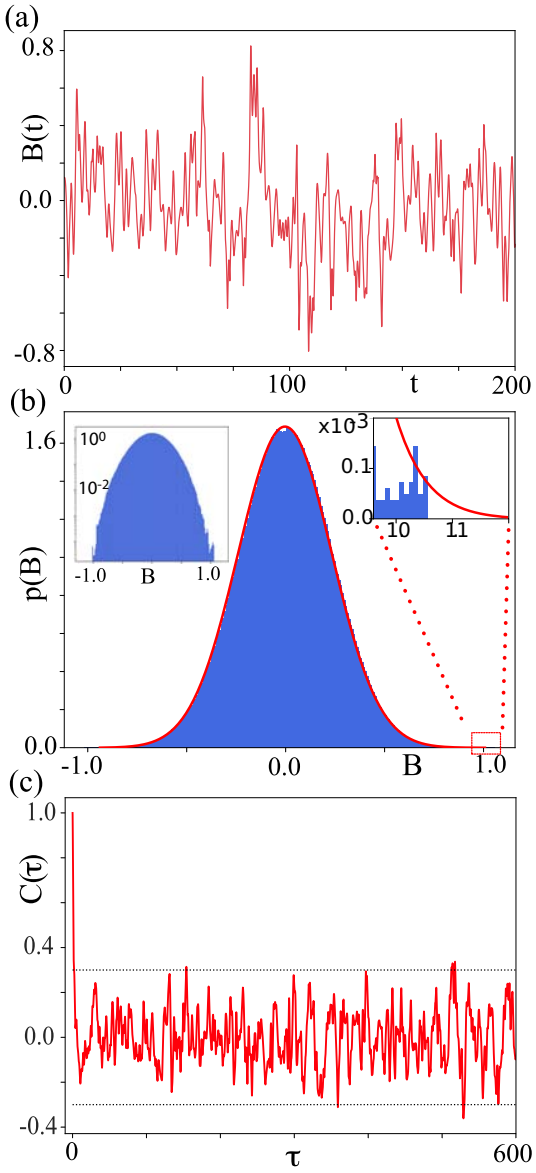

FIG. 5. Statistical characterization of the spatiotemporally chaotic forcing term $\mathrm{B}(t)$ in Eq. (12). (a) Typical temporal evolution of $\mathrm{B}(t)$ obtained from the Kuramoto-Sivashinsky forcing (2) with $\mu = 3.0$ and domain length $L = 300$, computed with a discretization interval $dx = 0.6$ and time step $dt = 0.01$. (b) Probability density function of $\mathrm{B}(t)$ in terms of a histogram (blue columns). The red curve represents a Gaussian fit. The left inset displays the probability density function of $\mathrm{B}(t)$ in a semi-log plot, while the right inset shows the tail of the histogram, suitably magnified, showing the truncation of the distribution. (c) Correlation function $C(\tau) \equiv \langle B(t)B(t+\tau)\rangle$, where the symbol $\langle\cdot\rangle$ denotes an average over the time t.

the contributions from the spatiotemporally chaotic process $\partial_z\psi(z,t)$ at large $|z|$, implying that $\mathrm{B}(t)$ does not behave as an infinite sum of independent identically distributed random variables. Consequently, $\mathrm{B}(t)$ is not a Gaussian white noise, a fact confirmed by the correlation function $C(\tau)$ shown in Fig. 5(c). This correlation function does not decay to zero as $\tau \to \infty$, in contrast to a genuine stochastic process.

In the following we explore the consequences of the above finding.

IV. PINNING-DEPINNING TRANSITION AS A PARAMETRIC RESONANCE

The pinning-depinning transition of a front can be understood as a parametric resonance [52]. To see this we transform Eq. (8) into a linear parametric oscillator equation using a series of nonlinear changes of the dependent variable $\delta(t)$. The effective frequency of the resulting oscillator problem fluctuates chaotically as a result of the spatiotemporally chaotic forcing. In order to identify the threshold for the transition in these circumstances we need to perform long integrations and impose stringent convergence criteria as first done in Ref. [53].

We begin by writing $x(t) \equiv \tan[k\delta(t)/2]$. Equation (8) then becomes an inhomogeneous Riccati equation,

$$\dot{x} = a + 2\,\Omega\, x + b\, x^2, \tag{13}$$

where

$$\begin{aligned} a(t,\tilde{\alpha},\gamma,\beta,k) &\equiv -\frac{k}{\sqrt{2}}\tilde{\alpha} - 3\sqrt{2}k\gamma B(t) - \frac{3k}{2\sqrt{2}}\beta A\cos\phi, \\ b(t,\tilde{\alpha},\gamma,\beta,k) &\equiv -\frac{k}{\sqrt{2}}\tilde{\alpha} - 3\sqrt{2}k\gamma B(t) + \frac{3k}{2\sqrt{2}}\beta A\cos\phi, \\ \Omega(t,\beta,k) &\equiv \frac{3k}{2\sqrt{2}}\beta A\sin\phi. \end{aligned} \tag{14}$$

Next, using the Riccati transformation $x = -\dot{y}/[b(t)y]$, we find that the auxiliary variable $y(t)$ satisfies a damped second-order linear ordinary differential equation,

$$\ddot{y} - \left(2\,\Omega + \frac{\dot{b}}{b}\right)\dot{y} + a\,b\,y = 0, \tag{15}$$

which can in turn be transformed into an undamped Hill equation using the change of variable $y(t) = z(t)\exp[\xi(t)]$, where $\xi \equiv \int(2\Omega + \dot{b}/b)dt/2$:

$$\ddot{z} + \left\{\frac{\ddot{b}}{2b} - \frac{\dot{b}^2}{2b^2} - \frac{1}{4}\left(2\Omega + \frac{\dot{b}}{b}\right)^2 + ab\right\}z = 0. \tag{16}$$

This linear equation represents a parametrically driven oscillator with a frequency that fluctuates chaotically. Note that this frequency diverges at $b = 0$. Figure 6 shows that while b can indeed pass through zero, it does so infrequently. Moreover, since the term in braces, hereafter referred to as ω^2, is then large and negative the solution $z = 0$ is then strongly unstable and hence far from the pinning-depinning transition which remains unaffected.

In the following we study the boundedness of solutions of Eq. (16) as a function of the parameters, employing the strict convergence criteria developed for the stability of the $z = 0$ solution for quasiperiodic frequencies [53]. Specifically, we evolve the equation up to a maximum of 10^7 time steps. To define the notion of convergence, we introduce the radius $R(t) \equiv \sqrt{z(t)^2 + \dot{z}(t)^2}$ representing the instantaneous amplitude of the solution in phase space. A solution $z(t)$ will be called unbounded (bounded) if it exceeds (fails to exceed) $R_{\min} = 10^{-1}$ during an integration time of $0 \leqslant t \leqslant 10^7$. Unbounded trajectories $z(t)$ correspond to pinning in the original problem. In Fig. 7 the shaded (unshaded) region obtained in this manner corresponds to pinned (depinned) fronts.

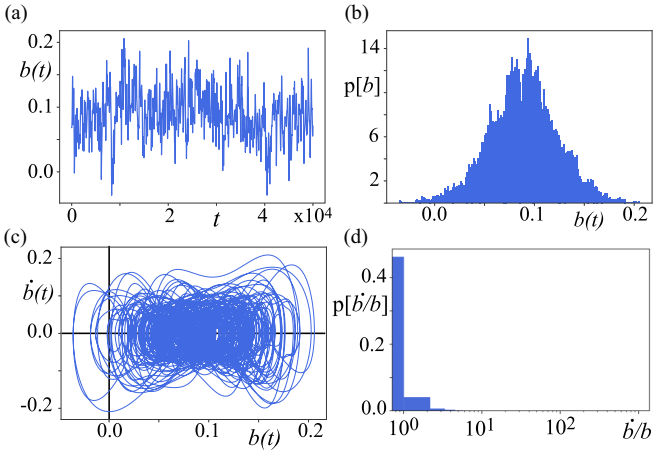

FIG. 6. Statistical characterization of the auxiliary function $b(t)$ defined in Eq. (14b). (a) Temporal evolution and (b) histogram of $b(t)$. (c) Reconstruction of the dynamics in $(b, \dot{b})$ space. (d) Probability density function of $\dot{b}/b$ in terms of a histogram.

A. Hill equation with chaotic frequency

To gain insight into the dynamics of the front position in the presence of chaotic forcing, we consider an overdamped pendulum, described by an angle θ and subject to the effect of a chaotic torque,

$$\dot{\theta} = -\sin\theta + r(t), \tag{17}$$

where $r(t) = r_0 + \xi X(t)$, r_0 and ξ are control parameters, and $X(t)$ is a zero-mean component of the Lorenz model [54], satisfying

$$\dot{X} = \sigma(Y - X), \quad \dot{Y} = X(\rho - Z) - Y, \quad \dot{Z} = XY - \beta Z. \tag{18}$$

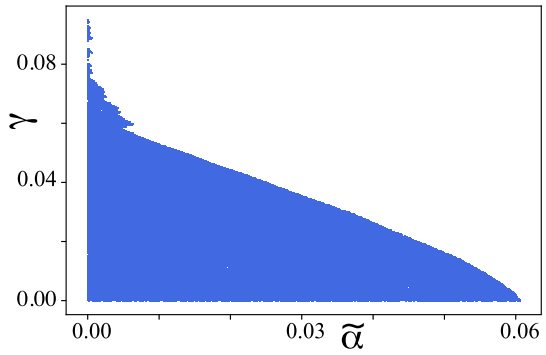

FIG. 7. Region with unbounded solutions (blue, pinned fronts) of the the Hill equation (16) shown in the $(\tilde{\alpha}, \gamma)$ parameter space, where $\tilde{\alpha} = \alpha_M - \alpha$. The equation has a chaotic frequency arising from B(t). Outside this region the solutions are bounded (depinned fronts). Parameters are $\beta = 0.085$ and $k = 0.7$.

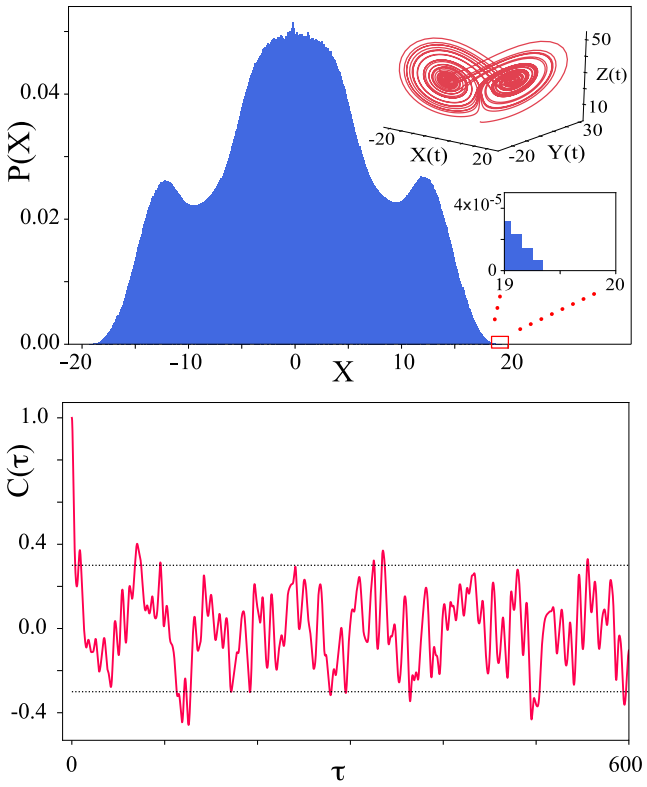

FIG. 8. Statistical characterization of the chaotic forcing function $X(t)$ showing the probability density distribution of $X(t)$ in the Lorenz model with $\beta = 8/3$, $\sigma = 10$, and $\rho = 28$. The top inset shows the corresponding strange attractor. The bottom inset shows a zoom of the tail of the probability distribution. (b) Correlation function $C(\tau) \equiv \langle X(t)X(t+\tau)\rangle$.

We employ the traditional parameter values $\beta = 8/3, \sigma = 10$, and $\rho = 28$ used by Lorenz to study the chaotic behavior of this system [54]. Note that $X(t)$ has a symmetric distribution about $X = 0$ and that its correlation function does not decay as shown in Fig. 8. These properties mimic the behavior of the effective forcing $B(t)$ in Eq. (12), cf. Fig. 5. Moreover, the forced overdamped pendulum, Eq. (17), resembles Eq. (8) for the front position $\delta(t)$ in the sense that for $\xi = 0$ and $r_0 \leqslant 1$ ($r_0 > 1$) the trajectories of the pendulum in phase space are bounded (unbounded). However, when $\xi \neq 0$ and chaotic forcing is present the characterization of the stability of a trajectory in phase space becomes a nontrivial problem.

Using variable changes similar to those used to transform Eq. (8) into Eq. (16), that is, using $h \equiv \tan(\theta/2)$, $h = -2\dot{y}/[r(t)y]$, $y(t) = z(t)\exp[\xi(t)]$, where $\xi(t)$ is now given by $\xi = -\int(1 - \dot{r}/r)dt/2$, we can cast Eq. (17) into a Hill equation as well:

$$\ddot{z} + \left\{\frac{\ddot{r}}{2r} - \frac{\dot{r}^2}{2r^2} - \frac{1}{4}\left(1 - \frac{\dot{r}}{r}\right)^2 + \left(\frac{r}{2}\right)^2\right\} z = 0. \quad (19)$$

When the term in braces, i.e., the square of the instantaneous frequency ω^2, is a periodic function of time, it is well known that this equation has both bounded and unbounded solutions depending on the oscillation frequency [55,56]. This situation persists when the oscillation frequency is quasiperiodic but the boundary between bounded and unbounded solutions becomes a complex function of the parameters whose complete characterization remains an open problem [53]. In the present case $r(t)$ also occasionally passes through zero, but as in Eq. (16), this does not affect the pinning-depinning transition.

To study the boundedness of solutions of Eq. (19) as a function of the parameters, we employ the same strategy as in the previous section. Figure 9 depicts a sample trajectory

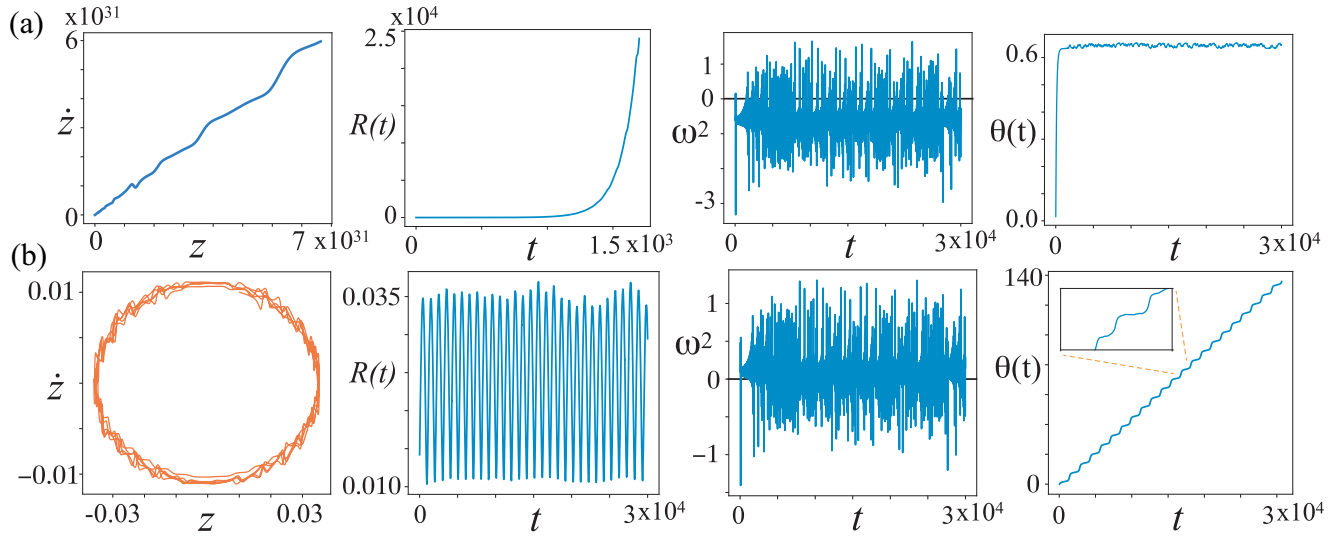

FIG. 9. Temporal evolution of the Hill equation (19) with Lorenz forcing computed for (a) $\xi = 0.001$, $r_0 = 0.6$ [$z(t)$ unbounded, $\theta(t)$ pinned] and (b) $\xi = 0.001$, $r_0 = 1.1$ [$z(t)$ bounded, $\theta(t)$ depinned]. The panels from left to right show the trajectory in the $(z, \dot{z})$ phase space, the temporal evolution of $R(t)$, the effective squared frequency ω^2 in the Hill equation, and the angle $\theta(t)$ reconstructed from the temporal evolution of $z(t)$ in the region of (a) pinning and (b) depinning.

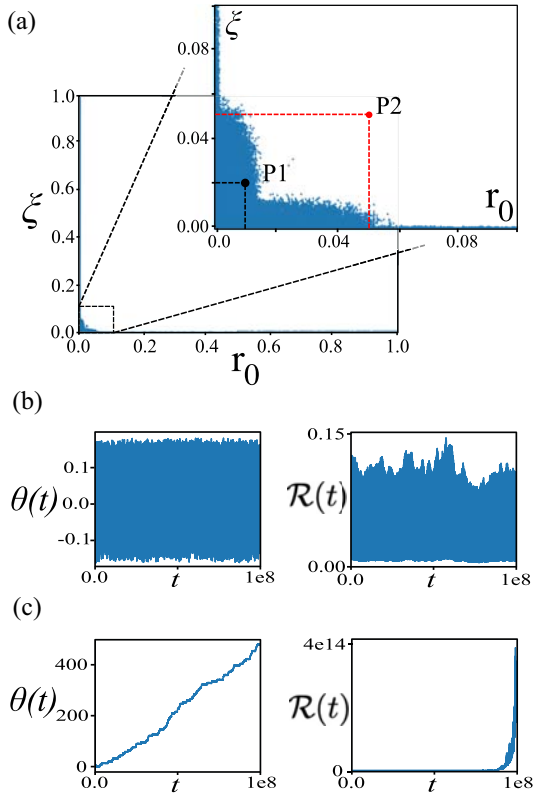

FIG. 10. (a) Parameter space of the Hill equation (19) with Lorenz forcing. Shaded (unshaded) regions correspond to pinned (depinned) fronts as determined by the condition $R(t) > 10^{-6}$ [$R(t) < 10^{-6}$] in time $0 \leqslant t \leqslant 10^7$ analogous to that used in Eq. (16), starting from an initial condition with $R(0) = 10^{-9}$. (b), (c) Temporal evolution of $\theta(t)$ and the analogous quantity $\mathcal{R}(t) \equiv \sqrt{\theta(t)^2 + \dot{\theta}(t)^2}$ as obtained from Eq. (17) in the region of (b) pinning and (c) depinning, corresponding, respectively, to locations P_1 and P_2 in parameter space (a).

in the $(z, \dot{z})$ phase space, the temporal evolution of the radius $R(t) \equiv \sqrt{z(t)^2 + \dot{z}(t)^2}$, the coefficient $\omega^2(t)$ in the Hill equation (19), and the reconstructed variable $\theta(t)$ corresponding to (a) pinning, and (b) depinning. Observe that in (a) ω^2 is on average negative while in (b) it is positive.

Using this type of analysis, one can explore the parameter space of the problem and map out in detail the boundary between pinning and depinning within Eq. (17). Figure 10 summarizes this analysis in the (r_0, ξ) plane: blue points represent trajectories that diverge. The boundary between the trajectories that have and have not diverged is evidently complex, and remains to be characterized in detail. The figure also shows the evolution of $\theta(t)$ and the quantity $\mathcal{R}(t) \equiv \sqrt{\theta(t)^2 + \dot{\theta}(t)^2}$ obtained numerically from Eq. (17) in the region of (b) pinning and (c) depinning, respectively.

V. MULTIPLICATIVE NOISE INDUCES FRONT PROPAGATION

The first description of macroscopic matter is usually done using a small number of coarse-grained or macroscopic fields,

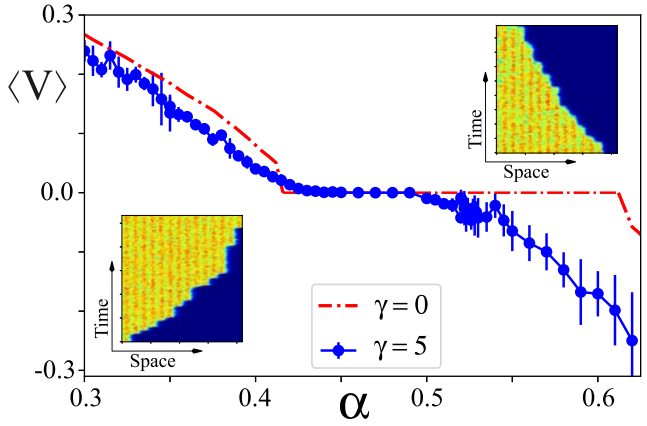

FIG. 11. Average speed of a front connecting homogeneous and pattern states as function of α for the stochastic model, Eq. (20), with $\beta = 0.085$ and $k = 0.7$. The red dot-dashed curve and the blue curve with filled circles show the deterministic and stochastic evolution of the front between a homogeneous and a periodic state, respectively. The insets show sample spatiotemporal evolution of the front before (lower left) and after (upper right) the Maxwell point when $\gamma = 5$.

whose evolution is described by deterministic differential equations. This reduction is a consequence of temporal scale separation, which allows a description in terms of the slowly varying macroscopic variables. An improved description includes fluctuations due to the elimination of a large number of fast variables whose effect can be modeled by including suitable inherent stochastic terms (or noise) in the differential equations. The stochastic term can be classified into two types: additive (multiplicative) noise that does not depend (depends) on the variable under study. Additive noise induces propagation of a static front connecting a stable homogeneous equilibrium and a pattern state [14,15]. The effect of multiplicative noise on fronts that connect a pair of homogeneous states has also been studied (see the textbook [57] and reference therein). In particular, the dynamic evolution of a system with fronts connecting an absorbing state (a state without fluctuations) and a fluctuating one has been discussed, and the emergence of spatiotemporal intermittency established [58].

In this section we compare the pinning-depinning results obtained with deterministic spatiotemporally chaotic forcing [Eqs. (1) and (2)] with the corresponding results obtained with explicitly stochastic forcing. In both cases the forcing is multiplicative. For this purpose we consider the following stochastic model:

$$\partial_t u = u(\alpha - u)(u - 1) + \partial_{xx} u + \beta u \cos(kx) + \gamma u \zeta(x, t), \tag{20}$$

where $\zeta(x, t)$ is a Gaussian white noise with zero mean value, $\langle \zeta(x, t) \rangle = 0$, and correlation $\langle \zeta(x, t) \zeta(x', t') \rangle = \delta(x - x')\delta(t - t')$. Here, the coefficient γ represents the noise strength, as in Eqs. (1) and (2), and the symbol $\langle \cdot \rangle$ indicates averaging over the realizations of the noise.

Since the noise in Eq. (20) is multiplicative and proportional to u, the state $u = 0$ is an absorbing state. In contrast,

the state $u = 1$ is an equilibrium state that exhibits persistent fluctuations. The front position $x = \delta(t)$ between these states exhibits random motion. Figure 11 shows the average front speed in the model. As a result of inherent fluctuations, one observes that the pinning region disappears and the front is only (statistically) stationary at a single point of the parameter space, the Maxwell point. The location of this point in turn depends on the intensity level γ of the noise. The disappearance of the pinning region in the present case is notable and is due to the fact that some realization of the stochastic process always overcomes the nucleation barrier introduced by the periodic forcing [15], a phenomenon known as a noise-induced transition [16].

To characterize this behavior one can use the same strategy as in Sec. III, and write down an equation for the front position $x = \delta(t)$. Using the ansatz (6) in Eq. (20), linearizing in W, and applying the appropriate solvability condition, one obtains

$$\dot{\delta} = -\frac{\partial U}{\partial \delta} + \Gamma\xi(t), \tag{21}$$

where the potential $U(\delta)$ is defined in expression (9), and

$$\xi(t) \equiv -\frac{3\gamma}{2\sqrt{\Gamma}} \int \zeta(z+\delta, t) u_F \partial_z u_F \, dz, \tag{22}$$

$$\Gamma \equiv \left(\frac{3\gamma}{2}\right)^2 \int [u_F(z)\partial_z u_F(z)]^2 \, dz = \frac{27\gamma^2}{40\sqrt{2}}. \tag{23}$$

Here, Γ measures the strength of the effective noise at the level of the front. Equation (21) is a Langevin equation for the front position with a Gaussian white noise. Specifically,

$$\begin{aligned} \langle \xi(t) \rangle &\equiv \left\langle -\frac{3\gamma}{2\sqrt{\Gamma}} \int \zeta(z+\delta, t) u_F \partial_z u_F \, dz \right\rangle, \\ &= -\frac{3\gamma}{2\sqrt{\Gamma}} \int \langle \zeta(z+\delta, t) \rangle u_F \partial_z u_F \, dz, \\ &= 0 \end{aligned} \tag{24}$$

with the same procedure for the other cumulants. In particular, $\langle \xi(t)\xi(t') \rangle = \delta(t - t')$. Thus all the properties of the reduced noise $\xi(t)$ are inherited from the spatiotemporal noise $\zeta(z, t)$. Note that in contrast to $B(t)$ the noise $\xi(t)$ is not bounded, despite the presence of the cutoff represented by the term $\partial_z u_F(z)$ in the integrand in Eq. (22). This is because $\xi(t)$ depends on the noise realization, in addition to its time-dependence. This difference has profound consequences for the pinning-depinning transition.

Equation (21) describes an overdamped system with a ratchet potential and additive white noise. Owing to generic asymmetry of the potential U whenever $\alpha \neq 0$ and the lack of a global stationary state, the system continuously converts random fluctuations into directed motion of the front, i.e., the noise induces front propagation. This behavior is known as a Brownian motor [59]. Thus the main difference between chaotic and stochastic forcing is that the former exhibits a pinning-depinning transition while the latter does not.

VI. CONCLUSIONS AND REMARKS

The description of many-body systems using differential equations for macroscopic variables with fluctuating terms that account for ignored fast variables has been very successful. A classic example of this type of description is the Langevin equation associated with Brownian motion. This description assumes, explicitly or implicitly, that the fluctuations are incoherent and so can be modeled by a prescribed stochastic process. If the number of fast degrees of freedom is large this process is taken to be Gaussian white noise. In general one expects similar behavior in the presence of deterministic fluctuations arising from a chaotic or turbulent system. However, as shown here, there are important differences between these two descriptions when it comes to the dynamics of fronts. This is because the front profile provides a cutoff that determines the effective noise acting on the front. This cutoff, specified by the function $\partial_z u_F(z)$, acts like a smoothed out δ-function. Indeed, if we replace $\partial_z u_F(z)$ by $G\delta(z)$, we obtain from Eq. (12) the result $B(t) = G u_F(0)\partial_z \psi(\delta, t)$ as the noise acting at the location $x = \delta$ of the front. Since $\psi(\delta, t)$ is specified by the bounded dynamics of the Kuramoto-Sivashinsky equation (2) $B(t)$ represents bounded fluctuations which may or may not trigger a depinning transition. In contrast, in the stochastically driven system (20) a similar procedure leads to the expression $\xi(t) = G' u_F(0)\zeta(\delta, t)$. Since $\zeta(t)$ is a Gaussian white noise by assumption, we see that so is $\xi(t)$. However, the stochastic description allows rare but arbitrarily large fluctuations at any one location and this fact ultimately triggers a depinning transition—all that one has to do is wait long enough. This is not so in the deterministic case. We believe that it is this distinction between the effective noise at the front location that is ultimately responsible for the survival of pinning in the deterministic case and its disappearance in the stochastic case. This distinction may play a significant role in the evolution of macroscopic quantities in other circumstances as well, as in Ref. [60].

The dynamics of fronts is well known to be highly sensitive to details of the system just ahead of the front, as in the example studied by Brunet and Derrida [61,62] where departures from the continuum description were found to have an important effect on the speed of an invasion front. In this paper we have obtained a similar result and showed that deterministic spatiotemporal fluctuations can trigger a pinning-depinning transition of spatiotemporally chaotic patterns, a transition that is washed out when stochastic fluctuations are used instead. This fact represents a fundamental distinction between these two cases.

ACKNOWLEDGMENTS

The authors are very grateful to Professor Georg Gottwald for his insightful comments on the topic of this paper. This work was supported by CONICYT under Grant No. CONICYT-USA PII20150011. M.G.C. and M.A.F. also thank the Millennium Institute for Research in Optics (MIRO) for financial support. A.J.A.-S. gratefully acknowledges financial support from Becas Conicyt 2015, Contract No. 21151618.

[1] L. M. Pismen, *Patterns and Interfaces in Dissipative Dynamics* (Springer Science & Business Media, Berlin, 2006).

[2] P. Collet and J. P. Eckmann, *Instabilities and Fronts in Extended Systems* (Princeton University Press, Princeton, NJ, 1990).

[3] M. C. Cross and P. C. Hohenberg, Pattern formation outside of equilibrium, Rev. Mod. Phys. **65**, 851 (1993).

[4] Y. Pomeau, Front motion, metastability and subcritical bifurcations in hydrodynamics, Phys. D (Amsterdam) **23**, 3 (1986).

[5] R. A. Fisher, The wave of advance of advantageous genes, Ann. Eugenics **7**, 355 (1937).

[6] A. N. Kolmogorov, I. G. Petrovsky, and N. S. Piskunov, A study of the diffusion equation with increase in the amount of substance, and its application to a biological problem, Bull. Moscow Univ. Math. Mech. **1**, 1 (1937).

[7] M. Faraday, *Course of Six Lectures on the Chemical History of a Candle* (Griffin, Bohn & Co, London, 1861).

[8] J. D. Murray, *Mathematical Biology* (Springer-Verlag, Berlin, 1989).

[9] J. S. Langer, Instabilities and pattern formation in crystal growth, Rev. Mod. Phys. **52**, 1 (1980).

[10] W. van Saarloos and P. C. Hohenberg, Fronts, pulses, sources and sinks in generalized complex Ginzburg-Landau equations, Phys. D (Amsterdam) **56**, 303 (1992).

[11] W. van Saarloos, Front propagation into unstable states, Phys. Rep. **386**, 29 (2003).

[12] J. Burke, and E. Knobloch, Localized states in the generalized Swift-Hohenberg equation, Phys. Rev. E **73**, 056211 (2006).

[13] F. Haudin, R. G. Elías, R. G. Rojas, U. Bortolozzo, M. G. Clerc, and S. Residori, Driven front Propagation in 1D Spatially Periodic Media, Phys. Rev. Lett. **103**, 128003 (2009).

[14] I. S. Aranson, B. A. Malomed, L. M. Pismen, and L. S. Tsimring, Crystallization kinetics and self-induced pinning in cellular patterns, Phys. Rev. E **62**, 5(R) (2000).

[15] M. G. Clerc, C. Falcon, and E. Tirapegui, Additive Noise Induces front Propagation, Phys. Rev. Lett. **94**, 148302 (2005).

[16] W. Horsthemke and R. Lefever, *Noise-Induced Transitions* (Springer-Verlag, Berlin/Heidelberg, 2006).

[17] T. Tsuruda and T. Hirano, Growth of flame front turbulence during flame propagation across an obstacle, Combus. Sci. Tech. **51**, 323 (1987).

[18] S. S. Shy, R. H. Jang, and P. D. Ronney, Laboratory simulation of flamelet and distributed models for premixed turbulent combustion using aqueous autocatalytic reactions, Combus. Sci. Tech. **113**, 329 (1996).

[19] S. Daniele, J. Mantzaras, P. Jansohn, A. Denisov, and K. Boulouchos, Flame front/turbulence interaction for syngas fuels in the thin reaction zones regime: turbulent and stretched laminar flame speeds at elevated pressures and temperatures, J. Fluid Mech. **724**, 36 (2013).

[20] D. Barkley, Theoretical perspective on the route to turbulence in a pipe, J. Fluid Mech. **803**, P1 (2016).

[21] A. Pocheau, Scale invariance in turbulent front propagation, Phys. Rev. E **49**, 1109 (1994).

[22] M. Anderson, F. Leo, S. Coen, M. Erkintalo, and S. G. Murdoch, Observations of spatiotemporal instabilities of temporal cavity solitons, Optica **3**, 1071 (2016).

[23] Z. Liu, M. Ouali, S. Coulibaly, M. G. Clerc, M. Taki, and M. Tlidi, Characterization of spatiotemporal chaos in a Kerr optical frequency comb and in all fiber cavities, Opt. Lett. **42**, 1063 (2017).

[24] Y. Kuramoto and D. Battogtokh, Coexistence of coherence and incoherence in nonlocally coupled phase oscillators, Nonlin. Phenom. Complex. Syst. (Dordrecht, Netherlands) **5**, 380 (2002).

[25] D. M. Abrams and S. H. Strogatz, Chimera States for Coupled Oscillators, Phys. Rev. Lett. **93**, 174102 (2004).

[26] C. R. Laing, Fronts and bumps in spatially extended Kuramoto networks, Phys. D (Amsterdam) **240**, 1960 (2011).

[27] M. G. Clerc, M. A. Ferré, S. Coulibaly, R. G. Rojas, and M. Tlidi, Chimera-like states in an array of coupled-waveguide resonators, Optics Lett. **42**, 2906 (2017).

[28] M. G. Clerc, S. Coulibaly, M. A. Ferré, and R. G. Rojas, Chimera states in a Duffing oscillators chain coupled to nearest neighbors, Chaos **28**, 083126 (2018).

[29] N. G. van Kampen, *Stochastic Processes in Physics and Chemistry* (Elsevier, New York, 1992).

[30] J. P. Eckmann and D. Ruelle, Ergodic theory of chaos and strange attractors, in *The Theory of Chaotic Attractors* (Springer-Verlag, New York, 1985), pp. 273–312.

[31] N. Verschueren, U. Bortolozzo, M. G. Clerc, and S. Residori, Chaoticon: Localized pattern with permanent dynamics, Phil. Trans. R. Soc. A **372**, 20140011 (2014).

[32] Y. Kuramoto and T. Tsuzuki, On the formation of dissipative structures in reaction-diffusion systems: Reductive perturbation approach, Prog. Theor. Phys. **54**, 687 (1975).

[33] Y. Kuramoto and T. Tsuzuki, Persistent propagation of concentration waves in dissipative media far from thermal equilibrium, Prog. Theor. Phys. **55**, 356 (1976).

[34] Y. Kuramoto, Diffusion-induced chaos in reaction systems, Prog. Theor. Phys. Supplement **64**, 346 (1978).

[35] D. M. Michelson and G. I. Sivashinsky, Nonlinear analysis of hydrodynamic instability in laminar flames-I. Derivation of basic equations, Acta Astronautica **4**, 1177 (1977).

[36] D. M. Michelson and G. I. Sivashinsky, Nonlinear analysis of hydrodynamic instability in laminar flames-II. Numerical experiments, Acta Astronautica **4**, 1207 (1977).

[37] Y. Kuramoto, *Chemical Oscillations, Waves, and Turbulence* (Springer Science & Business Media, New York, 2012).

[38] M. G. Clerc, D. Escaff, and V. M. Kenkre, Patterns and localized structures in population dynamics, Phys. Rev. E **72**, 056217 (2005).

[39] F. Haudin, R. G. Elías, R. G. Rojas, U. Bortolozzo, M. G. Clerc, and S. Residori, Front dynamics and pinning-depinning phenomenon in spatially periodic media, Phys. Rev. E **81**, 056203 (2010).

[40] B. C. Ponedel and E. Knobloch, Forced snaking: Localized structures in the real Ginzburg-Landau equation with spatially periodic parametric forcing, Eur. Phys. J. Special Topics **225**, 2549 (2016).

[41] U. Thiele and E. Knobloch, Driven Drops on Heterogeneous Substrates: Onset of Sliding Motion, Phys. Rev. Lett. **97**, 204501 (2006).

[42] M. G. Clerc, R. G. Elías, and R. G. Rojas, Continuous description of lattice discreteness effects in front propagation, Phil. Trans. R. Soc. A **369**, 412 (2011).

[43] A. Pikovsky and A. Politi, *Lyapunov Exponents: A Tool to Explore Complex Dynamics* (Cambridge University Press, Cambridge, 2016).

[44] G. Nicolis, *Introduction to Nonlinear Science* (Cambridge University Press, Cambridge, 1995).

[45] F. Christianen and H. H. Rugh, Computing Lyapunov spectra with continuous Gram-Schmidt orthonormalization, Nonlinearity **10**, 1063 (1997).

[46] T. J. Bridges and S. Reich, Computing Lyapunov exponents on a Stiefel manifold, Phys. D (Amsterdam) **156**, 219 (2001).

[47] E. I. Fredholm, Sur une classe d'equations fonctionnelles, Acta Math. **27**, 365 (1903).

[48] R. Peierls, The size of a dislocation, Proc. Phys. Soc. **52**, 34 (1940).

[49] F. R. N. Nabarro, Dislocations in a simple cubic lattice, Proc. Phys. Soc. **59**, 256 (1947).

[50] F. R. N. Nabarro, *Theory of Crystal Dislocations* (Dover Publications, Inc., New York, 1947).

[51] M. G. Clerc, S. Coulibaly, M. A. Ferré, M. A. García-Ñustes, and R. G. Rojas, Chimera-type states induced by local coupling, Phys. Rev. E **93**, 052204 (2016).

[52] P. Gandhi, E. Knobloch, and C. Beaume, Dynamics of phase slips in systems with time-periodic modulation, Phys. Rev. E **92**, 062914 (2015).

[53] R. S. Zounes and R. H. Rand, Transition curves for the quasi-periodic Mathieu equation, SIAM J. Appl. Math. **58**, 1094 (1998).

[54] E. N. Lorenz, Deterministic nonperiodic flow, J. Atmos. Sci. **20**, 130 (1963).

[55] A. H. Nayfeh and D. T. Mook, *Nonlinear Oscillations* (John Wiley & Sons, New York, 2008).

[56] W. Magnus and S. Winkler, *Hill's Equation* (Dover Publications Inc., New York, 2004).

[57] J. García-Ojalvo and J. Sancho, *Noise in Spatially Extended Systems* (Springer Science & Business Media, New York, 2012).

[58] M. G. Zimmermann, R. Toral, O. Piro, and M. San Miguel, Stochastic Spatiotemporal Intermittency and Noise-Induced Transition to an Absorbing Phase, Phys. Rev. Lett. **85**, 3612 (2000).

[59] P. Reimann, Brownian motors: Noisy transport far from equilibrium, Phys. Rep. **361**, 57 (2002).

[60] C. Chatelain, P. E. Berche, and B. Berche, Second-order phase transition induced by deterministic fluctuations in aperiodic eight-state Potts models, Eur. Phys. J. B **7**, 439 (1999).

[61] E. Brunet and B. Derrida, Shift in the velocity of a front due to a cutoff, Phys. Rev. E **56**, 2597 (1997).

[62] E. Brunet and B. Derrida, Effect of microscopic noise on front propagation, J. Stat. Phys. **103**, 269 (2001).

Chapter 8

Effect of deterministic fluctuations in localized structures

8.1 Introduction

It is interesting to imagine the first thoughts of the biologist Robert Brown when looking through his microscope how a pollen particle suspended in the water seemed to come to life and move irregularly. In fact, his first impression was that he had found the most fundamental element of life, and he described the phenomenon as a "revitalization" of the pollen particle. Furthermore, to him, it seemed a sort of counterexample to the unquestioned Newton's laws that marked the golden age of determinism by describing both natural processes and mechanical/technological systems successfully. His findings were presented in a paper presented to the Royal Society entitled [148]. However, about a decade later, he had to acknowledge that he was wrong. The phenomenon could be explained due to the interaction between the water particles on the pollen particle. In this sense, the pollen particle is much larger than the water particles but small enough to show the effect of the water particles collisions. Albert Einstein in 1905 gives a complete description of the Brownian movement from fundamental physical principles [149]. Three years later, Paul Langevin in 1908, proposed a more straightforward theoretical approach, applying precisely Newton's laws to describe the dynamics of a Brownian particle [150]. In this work, he is considered a random force to explain the medium's collective effect on particle dynamics.

Nevertheless, is it always possible to describe the interaction with the medium by a random (or stochastic) fluctuation?. There are the same results when the medium is composed by a small number of particles such that the Newton equations can describe its behavior?. What are the differences between these two approaches? In this chapter, we will try to address these questions by studying a particle embedded in a spatiotemporal chaotical media and comparing it with the standard Brownian motion model where the media is random. We will compare the statistical and dynamical properties of both models and evidence a phenomenon of pinning similarly to the phenomenon exhibited for fronts reported in [151] and detail in the above chapter and contraposition with the destruction of localized states exhibited the stochastic fluctuations. In the following section we will start studying the Brownian particle

from the Langevin perspective.

8.2 Brownian motion particle

To understand the dynamics of the Brownian motion, we take a Newtonian approach. We start with Newton's second law,

$$m\frac{V(t)}{\mathrm{d}t} = F(t), \tag{8.1}$$

and

$$\frac{X(t)}{\mathrm{d}t} = V(t), \tag{8.2}$$

where m accounts for the mass of the particle, $V(t)$ accounts for its velocity, and $X(t)$ accounts for its position. The force term $F(t)$ is given by

$$F(t) = -\gamma V(t) + \frac{\beta^2}{\sqrt{\mathrm{d}t}}\xi(t), \tag{8.3}$$

where the first term at the right side of eq. 8.3 accounts for the viscous drag and the second for the interaction with the medium, modeled using a normal distributed random variable. Thus, substituting Eq. (8.3) in Eq. (8.1) we obtain

$$m\frac{V(t)}{\mathrm{d}t} = -\gamma V(t) + \frac{\beta^2}{\sqrt{\mathrm{d}t}}\xi(t), \tag{8.4}$$

and the constant parameters enable to describe the viscosity and thermal effect intensities. Note Eq. 8.4 is a differential equation for the random variable V.

A more convenient way to write Eq. (8.4), as is typically done in stochastic differential equations theory, is to express it in its differential form, given by

$$V(t+\mathrm{d}t) - V(t) = -\gamma V(t)\mathrm{d}t + \sqrt{\beta^2\mathrm{d}t}\xi(t), \tag{8.5}$$

Furthermore, the process described by the equation 8.5, together with the time integral $X(t)$ describes the Brownian motion. Perhaps the main contribution to this approach is that Langevin understood that both viscous drag and velocity fluctuations are complementary effects of the same phenomenon, e.g., the numerous collisions of the particles that make up the fluid and the Brownian particle. At this point we can integrate numerically Eq. (8.5) and obtain several realizations for the solution of this equation.

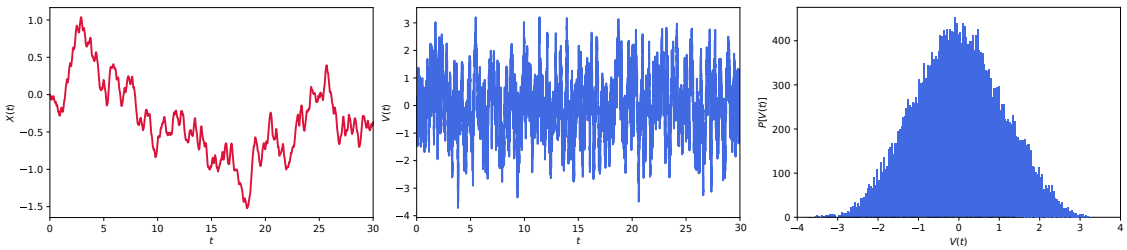

Figure 8.1: Panel (a) shows a solution of the langevin equation for $\gamma = 10$, $\beta = 5$ and $\mathrm{d}t = 0.001$. Panel (b) show the displacements given by $\Delta X = X(t + \mathrm{d}t) - X(t)$ and panel (c) show the distribution of the displacements.

A straightforward and easy approach to obtain the solutions of these equations is the following. Note that the random variables $V(\mathrm{d}t), V(2\mathrm{d}t), \ldots, V(t)$ are a linear combination of independent normal random variables, and therefore its distribution is itself normal. Thus we can write

$$V(t) = N(\langle V(t)\rangle, \sigma(V(t))), \tag{8.6}$$

transforming the problem of solving 8.4 to the problem of found expresions for the mean $\langle V(t)\rangle$ and the standard deviation $\sigma = \sigma(V(t))$, and substitute them into Eq. (8.2). We start triying to find $\langle V(t)\rangle$. Applying the mean operator in both sides of Eq. (8.5) we obtain,

$$\langle V(t + \mathrm{d}t) - V(t)\rangle \;=\; \langle -\gamma V(t)\mathrm{d}t + \sqrt{\beta^2 \mathrm{d}t}\xi(t)\rangle, \tag{8.7}$$

and therefore,

$$\langle V(t + \mathrm{d}t)\rangle - \langle V(t)\rangle \;=\; \langle -\gamma V(t)\mathrm{d}t\rangle + \sqrt{\beta^2 \mathrm{d}t}\langle \xi(t)\rangle, \tag{8.8}$$

and $\langle \xi(t)\rangle = 0$, a simple ordinary differential equation for the mean speed, given by

$$\frac{\mathrm{d}\langle V(t)\rangle}{\mathrm{d}t} = -\gamma\langle V(t)\rangle, \tag{8.9}$$

whose solutions are of the form

$$\langle V(t)\rangle = V_0 \mathrm{e}^{-\gamma t}, \tag{8.10}$$

Now, we need only the standar deviation σ. To find it, we will consider an equation for $\langle V(t)^2\rangle$. By definition

$$\mathrm{d}[V(t)^2] = V(t + \mathrm{d}t)^2 - V(t)^2, \tag{8.11}$$

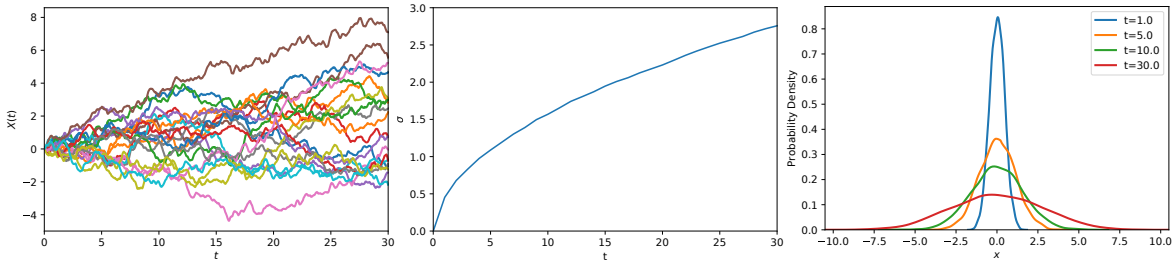

Figure 8.2: Brownian motion from Langevin equation. (a) Show the profile of difussion given by several realizations for the solutions of Langevin equation. (b) Measures of the standard deviation of the distribution of the particles along space changes on time, and (c) give us a numerical aproximation of the probability density function based on 4000 brownian particiles for times $t = 1, 10, 20, 30$.

and we can substitute Eq. (8.5) into (8.11) to obtain

$$\mathrm{d}[V(t)^2] = [(1 - \gamma \mathrm{d}t)V(t) + \sqrt{\beta^2 \mathrm{d}t}\xi(t)]^2 - V(t)^2, \tag{8.12}$$

expanding the cuadratic terms, cancelling the corresponding terms, and taking into account that $\mathrm{d}t^{3/2}$ and $\mathrm{d}t^2$ are smaller than $\mathrm{d}t$ and therefore negligible, we get

$$\mathrm{d}[V(t)^2] = -2\gamma \mathrm{d}t V(t)^2 + 2V(t)\sqrt{(\beta^2 \mathrm{d}t)}\xi(t) + \beta^2 \mathrm{d}t \xi(t)^2, \tag{8.13}$$

Taking average on noth sides of the equation, gives

$$\mathrm{d}\langle V(t)^2\rangle = -2\gamma \mathrm{d}t\langle V(t)^2\rangle + 2\langle V(t)\rangle\sqrt{(\beta^2 \mathrm{d}t)}\langle\xi(t)\rangle + \beta^2 \mathrm{d}t\langle\xi(t)^2\rangle. \tag{8.14}$$

Then, we use the fact that $V(t)$ is a linear combination of independent normal random variables and therefore

$$\langle V(t)\xi(t)\rangle = \langle V(t)\rangle\langle\xi(t)\rangle = 0, \tag{8.15}$$

and recalling that $\langle\xi(t)^2\rangle = 1$, we obtaining the following simple ordinary differential equation for the variance

$$\mathrm{d}\langle V(t)^2\rangle = -2\gamma \mathrm{d}t\langle V(t)^2\rangle + \beta^2 \mathrm{d}t, \tag{8.16}$$

or equivalently

$$\frac{\mathrm{d}}{\mathrm{d}t}\langle V(t)^2\rangle = -2\gamma\langle V(t)^2\rangle + \beta^2, \tag{8.17}$$

whose solutions can be easily calculated by taking $V(0) = v_0$, obtaining

$$\langle V(t)^2 \rangle = v_0^2 \mathrm{e}^{-2\gamma t} + \frac{\beta^2}{2\gamma}(1 - \mathrm{e}^{-2\gamma t}), \tag{8.18}$$

and therefore

$$\sigma^2(t) = \langle V(t) \rangle^2 - \langle V(t)^2 \rangle = \frac{\beta^2}{2\gamma}(1 - \mathrm{e}^{-2\gamma t}), \tag{8.19}$$

and to get the solution of the equation 8.5 we substitute (8.10) and (8.19) in Eq. (), obtaining

$$V(t) = N(\langle V(t) \rangle, \sigma^2(t)) = N(v_0 \mathrm{e}^{-\gamma t}, \frac{\beta^2}{2\gamma}(1 - \mathrm{e}^{-2\gamma t}), \tag{8.20}$$

and the probability density is easily recovered by

$$\begin{aligned} p(V(t)) &= \frac{\exp[-\frac{(V(t)-\langle V(t) \rangle)^2}{2\sigma^2}]}{\sigma\sqrt{2\pi}} \\ &= \frac{\exp\left[-\frac{(V(t)-v_0\mathrm{e}^{-\gamma t})^2}{2\frac{\beta^2}{2\gamma}(1-\mathrm{e}^{-2\gamma t})}\right]}{\sqrt{2\pi\frac{\beta^2}{2\gamma}(1 - \exp[-2\gamma t])}} \end{aligned} . \tag{8.21}$$

Note that Eqs. (8.20) and (8.21) characterize the motion and statistic of the Brownian motion particle described by the Eq. (8.5). In the following section, we will explore another kind of complex behavior particle but interacting with a spatiotemporal chaotic media.

8.3 Chaotic motion particle

In the following, we will try to explore the effect of deterministic fluctuations on the dynamics of localized structures since these allow us to give a fairly adequate description of the concept of a particle itself. Localized structures are characterized by continuous order parameters such as position, width, amplitude, and therefore these solutions can be considered a theoretical description of the particle concept from the physics perspective. For the sake of simplicity, we consider a version of the Turing-Swift–Hohenberg equation as a model in which particle-type solutions have been well studied, coupled to a chaotic space-time medium described by the Kuramoto–Sivashinsky equation, i.e.,

$$\partial_t u = \rho u - (1 + \partial_{xx})^2 u + bu^2 - u^3 + \gamma \partial_x \psi(x,t) u + \sqrt{\eta}\xi(x,t)u \tag{8.22}$$

with

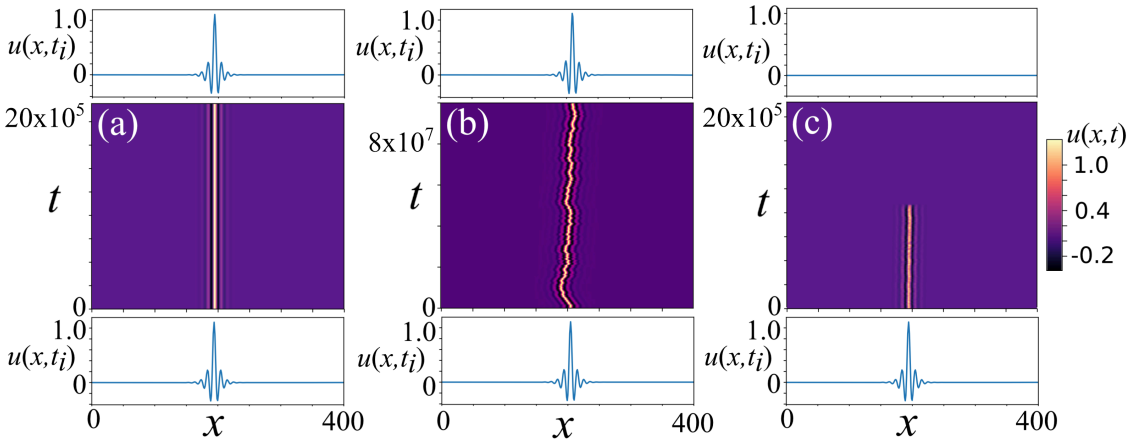

Figure 8.3: Spatiotemporal evolution of a one bump localized solution of the Swift-Hohenberg Eq. (8.22) subject to spatiotemporally chaotic forcing with given by Eq. (8.23) for parameters $\mu = 3$, $\rho = -0.27$, $b = 1.8$ and (a) $\gamma = \eta = 0$, (b) $\gamma = 0.017$ and $\eta = 0$ and (c) $\gamma = 0$, $\eta = 5$. The lower and upper panels show the solution profiles at the initial and final times, respectively. Note the much longer timescale in panel (b).

$$\partial_t \psi = -\mu \partial_{xx} \psi - (\partial_x \psi)^2 - \partial_{xxxx} \psi \tag{8.23}$$

Where the Swift-Hohenberg equation has $u \equiv 0$ as a homogeneous solution. It should also be noted that the deterministic and noisy perturbative terms, weighed by the coefficients γ and η respectively, are of the multiplicative type, so the homogeneous solution $u \equiv 0$ holds for any value that these take. For $\eta = \gamma = 0$, the system reduces to the Swift–Hohenberg equation, whose properties have been well established in [24, 152].

In order to measure the effect of deterministic fluctuations on the dynamics of localized structure-type solutions, we carried out a detailed numerical study for the system composed of the equations (8.22) and (8.23) in a region in which there are localized structures for the equation (8.22) and in which the space-time chaos of the equation (8.23) it is fully developed. Thus, setting the parameters at $\mu = 3$, $\rho = -0.27$, $b = 1.8$ and for $\gamma = 0.017$ we obtained a complex behavior, similar in appearance to that of the Brownian movement, as can be seen in figure 8.4.

8.4 Chaos-induced transitions

We it is compared the behavior of localized structures under the effect of the deterministic versus stochastic fluctuations, a first difference that highlight is that the localized structures survive to deterministic fluctuations, at difference of the case of random gaussian fluctuations. In Fig. 8.4 we explore numerically this phenomena and observe that there exist a region for the fluctuation weight parameter such that the localized structure is a persistent solution for ρ fixed and there exist a critical γ such that the solution becomes unstable, and the solution evolves to the most stable solution, that could be the homogeneous state, one of the coexisting localized pattern states or the whole pattern solution.

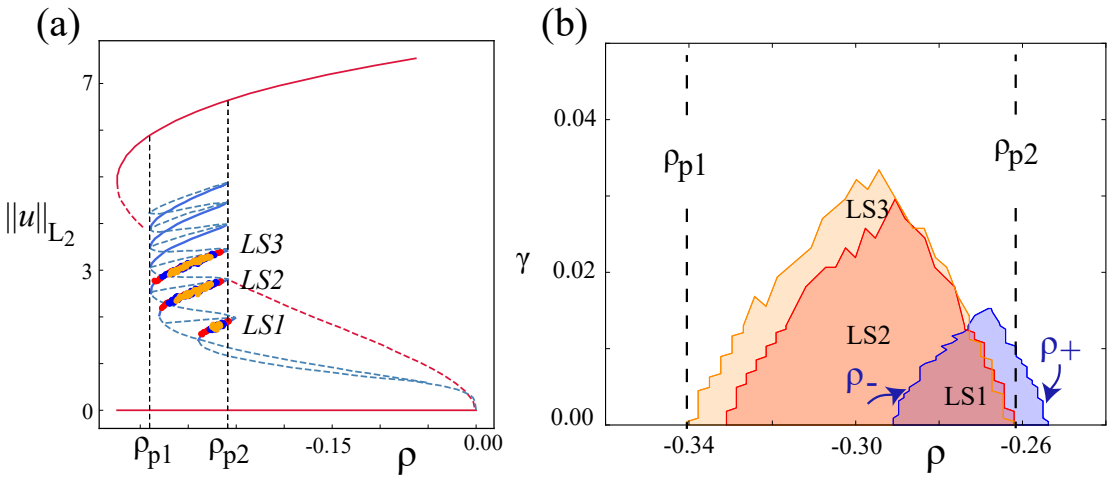

Figure 8.4: (a) Panel show the snaking diagram for the equation 8.22, and the pinning or persistence region for three values of γ and $\eta = 0$. Panel (b) shows how these solutions persist for ρ fixed and varying γ.

8.5 Outline

- This work explores the dynamical behavior of a particle-like solution exposed to a chaotic spatiotemporal medium, giving an exciting example of a chaotical particle.
- The effect of deterministic fluctuations enables a pinning zone in contraposition to the effect of randomness on localized states. This pinning zone is a consequence of the limited (or forbidden) transitions in deterministic systems.
- The pinning region shrinks as the strength of the fluctuations increase.
- Localized structures under deterministic fluctuations exhibit complex spatiotemporal dynamics, namely, a chaotic walk.
- This kind of work is of interest when the particle under study (the equivalent to the Brownian particle) is coupled to a small reservoir bath, composed of a small number of particles whose dynamics could be modeled by an n-body problem which have chaotical solutions typically.
- Brownian motion dynamics, and in general, the random motion has been used to formulate heuristically inspired blind search algorithms. In the same direction, the chaotical particle proposed here could define a novel kind of random search algorithms whose self-correlation is driven by the dynamics of the chaos model used for the fluctuations.
- Besides, it is possible to investigate these behaviors in experiments by introducing the spatio-temporal chaos using SLMs, for example, in the liquid crystal light valve experiments explained in chapters 2 and 3, enabling, in this case, a mechanism for complex propagation of light spots in liquid crystals.

Chaotic motion of localized structures

A. J. Alvarez-Socorro,[1,2] Marcel G. Clerc,[1] Michel Ferré,[1] and Edgar Knobloch[3]
[1]*Departamento de Física and Millennium Institute for Research in Optics, Facultad de Ciencias Físicas y Matemáticas, Universidad de Chile, Casilla 487-3, Santiago, Chile*
[2]*Laboratorio de Investigación, Desarrollo e Innovación, Zenta Group, Diagonal Oriente 5081, Ñuñoa, Santiago, Chile*
[3]*Department of Physics, University of California at Berkeley, Berkeley, California 94720, USA*

(Received 19 November 2019; revised manuscript received 12 January 2020; accepted 23 March 2020; published 27 April 2020)

Mobility properties of spatially localized structures arising from chaotic but deterministic forcing of the bistable Swift-Hohenberg equation are studied and compared with the corresponding results when the chaotic forcing is replaced by white noise. Short structures are shown to possess greater mobility, resulting in larger root-mean-square speeds but shorter displacements than longer structures. Averaged over realizations, the displacement of the structure is ballistic at short times but diffusive at larger times. Similar results hold in two spatial dimensions. The effects of chaotic forcing on the stability of these structures is also quantified. Shorter structures are found to be more fragile than longer ones, and their stability region can be displaced outside the pinning region for constant forcing. Outside the stability region the deterministic fluctuations lead either to the destruction of the structure or to its gradual growth.

DOI: 10.1103/PhysRevE.101.042212

I. INTRODUCTION

A fundamental problem of statistical mechanics is to describe the effect of microscopic scales on macroscopic variables. Usually this effect is modeled in terms of stochastic fluctuations, due to the large number of microscopic degrees of freedom. However, in cases where the number of degrees of freedom is restricted, the fluctuations cannot be taken as stochastic, and in this case their deterministic or chaotic character may play an important role. Here we investigate the effects of the resulting deterministic fluctuations on spatially localized structures (LSs). Such structures are a characteristic feature of self-organized nonequilibrium systems [1–3] and have been observed in numerous fields, ranging from physics and chemistry to engineering and biology. These particlelike states are characterized by continuous order parameters, such as position, width, and amplitude whose evolution may be described by macroscopic equations. The texts [4–6], together with the references cited therein, provide a helpful overview of the subject. In one spatial dimension, the profile of a stationary LS embedded in a featureless background can be interpreted in terms of a spatial trajectory that connects a homogeneous state with itself, i.e., as a homoclinic orbit of a dynamical system evolving in space [7]. In many cases the resulting states may be thought of as bound states of a pair of fronts, one connecting a homogeneous state to a pattern state, while the second connects the pattern state back to the homogeneous state. This is the case, for example, for LSs present in the region of bistability between a homogeneous state and a spatially extended pattern. Such regions typically contain a pinning or snaking interval within which one finds multiple LSs of different lengths organized in a snakes-and-ladders bifurcation diagram [8,9]. The resulting diagram captures the linear stability properties of the LSs as well as their relative (or energy) stability [10].

Localized structures are not necessarily motionless. The motion and complex dynamics of LSs can be the result of a spontaneous symmetry-breaking instability [11–18] or the result of a fluctuating background [19–21]. Despite the ability of existing theory to provide an intuitive picture of the origin of LSs current understanding does not apply to the latter situation. As is well established, additive white noise induces random motion of LSs but ultimately leads to their destruction [22,23]. This is not the case when the forcing is chaotic, i.e., deterministic [24].

Figure 1 illustrates the dramatic difference between deterministic and stochastic forcing of a one-bump LS described by the bistable Swift-Hohenberg equation. In the absence of forcing [Fig. 1(a)] the structure is stable and motionless. With deterministic but chaotic forcing the structure remains stable but executes lateral motion resembling a random walk [Fig. 1(b)], in stark contrast to the effect of multiplicative white noise forcing that ultimately always destroys the structure [Fig. 1(c)]. As discussed further below, this is a consequence of the fact that white noise ultimately explores a wide range of fluctuations, resulting in a potential *noise-induced transition* [25], while those arising from a deterministic origin are bounded by the size of the attractor. In the following we refer to the trajectory in Fig. 1(b) as a *chaotic walk* to distinguish it from the more commonly studied random walk.

The work that follows is motivated by the striking difference between Figs. 1(b) and 1(c). We begin by describing the model problem we study followed by a description of our simulation results in one spatial dimension together with a semi-analytical understanding of the LS mobility characteristics revealed by these simulations as the forcing amplitude increases. The paper concludes with a brief discussion of the two-dimensional case.

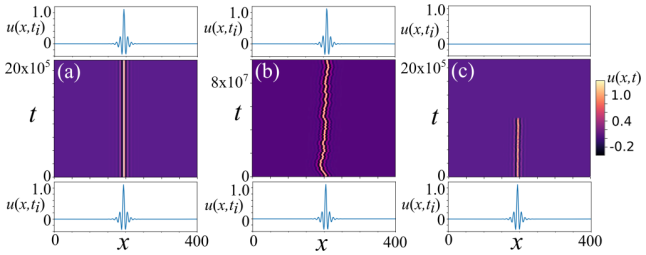

FIG. 1. Spatiotemporal evolution of a one-bump localized solution of the Swift-Hohenberg equation (1) subject to spatiotemporally chaotic forcing with $\mu = 3$ when $\rho = -0.27$, $b = 1.8$ and (a) $\gamma = \eta = 0$, (b) $\gamma = 0.017$, $\eta = 0$, and (c) $\gamma = 0$, $\eta = 5$. The lower and upper panels show the solution profiles at the initial and final times, respectively. Note the much longer timescale in panel (b).

II. THE MODEL

To study the effect of deterministic fluctuations on the dynamics of localized structures, we employ a system of partial differential equations (PDEs) composed of a bistable Swift-Hohenberg (SH) equation subject to multiplicative forcing provided by the Kuramoto-Sivashinsky (KS) equation [24], as described by

$$\partial_t u = \rho u - (1 + \partial_{xx})^2 u + bu^2 - u^3 + \gamma\, \partial_x \psi(x,t) u + \sqrt{\eta}\zeta(x,t)u, \quad (1)$$

together with

$$\partial_t \psi = -\mu \partial_{xx}\psi - (\partial_x \psi)^2 - \partial_{xxxx}\psi. \quad (2)$$

Here $\zeta(x,t)$ is a Gaussian white noise with zero mean, $\langle \zeta(x,t)\rangle = 0$, and correlation $\langle \zeta(x,t)\zeta(x',t')\rangle = \delta(t-t')\delta(x-x')$ and η represents its intensity, while γ specifies the strength of the multiplicative spatiotemporally chaotic fluctuations experienced by the LSs in Eq. (1) which can be tuned by selecting appropriate values of the parameter μ in Eq. (2) [24]. When $\gamma = \eta = 0$ the system reduces to the usual bistable Swift-Hohenberg equation, whose properties are now well-established [9,26]. Figure 1 shows sample results for $b = 1.8$ and (a) $\gamma = \eta = 0$, (b) $\gamma = 0.017$, $\eta = 0$, i.e., for deterministic forcing. In contrast, Fig. 1(c) is computed from Eq. (1) with stochastic forcing only ($\gamma = 0$).

To investigate the effect of spatiotemporally chaotic fluctuations on the behavior of LSs, we have conducted a numerical study of the model Eqs. (1) and (2) with $\gamma > 0$, $\eta = 0$, and μ sufficiently large that Eq. (2) possesses solutions in the form of spatiotemporal chaos [27]. For the sake of simplicity, periodic boundary conditions are used. Integration was implemented using a fourth-order Runge-Kutta scheme in time with step size $dt = 0.01$ and a finite difference scheme in space that uses a centered stencil of seven grid points. Space was discretized into 400 points with grid size $dx = 0.6$. A stable localized one-bump solution of the bistable Swift-Hohenberg equation ($\gamma = 0$, $\eta = 0$) at $b = 1.8$ and $\rho = -0.27$ was taken as initial condition, motivated by the parameter regime studied in Ref. [9]. This solution can be seen in Fig. 1(a).

The spatiotemporal forcing is provided by the Kuramoto-Sivashinsky equation [28,29], whose dynamics are well explored. In particular, it is known that for $\mu = 3$ this equation

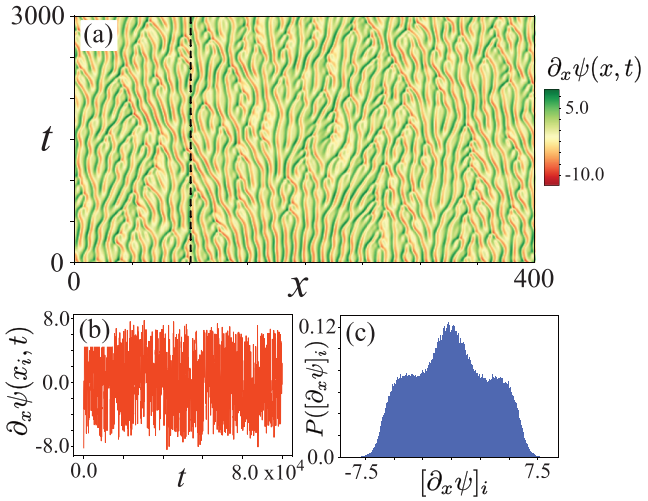

FIG. 2. (a) Spatiotemporal complexity in the Kuramoto-Sivashinsky Eq. (2) at $\mu = 3$. (b) Temporal profile of the fluctuations at the fixed location $x = 100$ [vertical dashed line in (a)] and (c) its probability density function, both at $\mu = 3$.

exhibits spatiotemporally chaotic behavior. Figure 2(a) shows the spatiotemporal chaos at this value of μ while Figs. 2(b) and 2(c) show the resulting forcing amplitude at an arbitrarily selected location $x = 100$ and its probability density function (pdf). It is noteworthy that this density is symmetric with mean zero. Note also that the density has a finite support since the KS attractor is bounded. This is in contrast to white noise.

In the following we employ the parameter values $b = 1.8$ and $\mu = 3$ and vary the parameters ρ, γ while keeping $\eta = 0$ (deterministic forcing). We then compare the results with those for pure stochastic forcing ($\gamma = 0$, $\eta \neq 0$).

III. RESULTS

We now study the effects of the deterministic fluctuations quantified in Section II on the dynamics of the one-bump localized state shown in Fig. 1(a). Figure 3(a) shows the snakes-and-ladders structure of the pinning region when $\gamma = 0$ (blue curves) within the region of bistability between the homogeneous state $u = 0$ (red horizontal line) and the periodic state with 2π wavelength (red curve), both for $b = 1.8$; solid (dashed) lines indicate stable (unstable) states. In the following we call the three lowest stable states LS1, LS2, and LS3, the integer indicating the number of fully developed peaks within the structure. Thus, Fig. 1(a) shows LS1. Superposed on the LS curves are the LS1, LS2, and LS3 states that were found to persist for $t = 10^7$ for three different values of γ and color-coded as follows: $\gamma = 0.006$ (thick red), $\gamma = 0.008$ (thick blue), and $\gamma = 0.015$ (thick yellow), suggesting that in each of these cases these states are in fact stable, albeit in a reduced parameter range: the figure indicates that as the fluctuation amplitude γ increases the snaking zone gradually shrinks but does not disappear. Figures 3(b) and 3(c) portray the surviving snaking zones for $\gamma = 0.006$ and $\gamma = 0.008$, respectively. These results are presented in a different way in Fig. 4 which shows the regions of stable LS1, LS2, and LS3 in the (ρ, γ) plane. Note that as

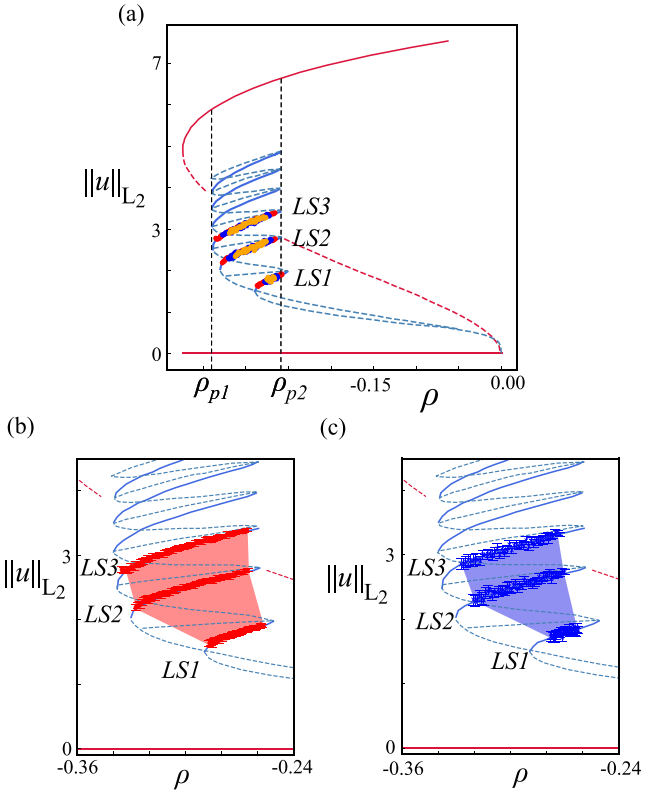

FIG. 3. (a) Snakes-and-ladders structure of the pinning zone when $b = 1.8$ and $\gamma = \eta = 0$ (blue curves) straddling the Maxwell point located at $\rho_M \approx -0.3137$, with superposed stable localized states: $\gamma = 0.006$ (red), $\gamma = 0.008$ (blue), and $\gamma = 0.015$ (yellow), showing the progressive shrinking of the snaking region as γ increases. Dashed lines at ρ_{p1} and ρ_{p2} indicate the width of the pinning zone when $\gamma = \eta = 0$. The corresponding results for (b) $\gamma = 0.006$ and (c) $\gamma = 0.008$ showing, from bottom to top, the branches of stable LS1, LS2, and LS3 as determined from simulations over a time interval $t = 10^7$. In each case the error bars indicate the size of the fluctuations over this timescale.

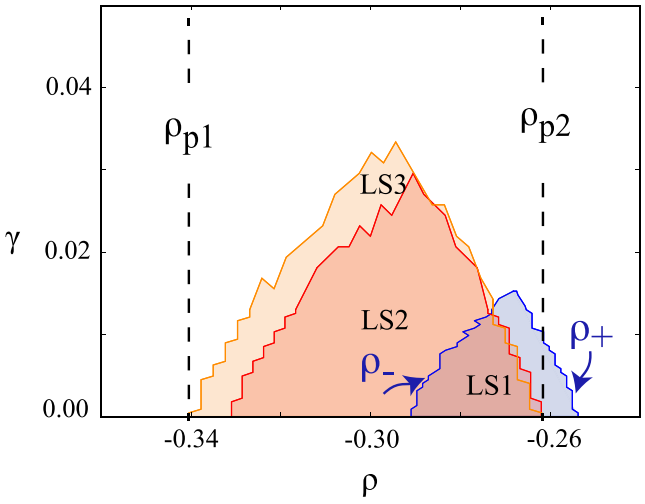

FIG. 4. Regions of stability of LS1, LS2, and LS3 in the (ρ, γ) plane showing that the stability regions become increasingly asymmetrical and in each case close off [at $\gamma = \gamma_c(n)$] when the forcing amplitude γ becomes too large. Dashed lines at ρ_{p1} and ρ_{p2} indicate the width of the pinning zone when $\gamma = \eta = 0$.

γ increases the LSs are eroded more rapidly in the vicinity of the left boundary $\rho = \rho_-(\gamma)$ than near the right boundary $\rho = \rho_+(\gamma)$. This asymmetry arises because the fluctuations near ρ_-, i.e., for values of ρ below the (effective) Maxwell point, favor the homogeneous state, leading to front retraction, while those near ρ_+, i.e., for ρ above the Maxwell point, favor the periodic state and hence front advance. As a result the fluctuations gradually shift the pinning region toward larger values of ρ relative to the case $\gamma = \eta = 0$. We also see that this effect is larger for LSn with small n, and that stable LSn with larger n survive to larger values of γ. As discussed further below this appears to be a consequence of the reduced mobility of larger structures. Figure 5 sheds additional light on this behavior. The left panels show the boundary of the pinning or snaking zone as γ increases across $\gamma_-(\rho)$ [Fig. 5(a)] and across $\gamma_+(\rho)$ [Fig. 5(c)]. Thus, for $\gamma > \gamma_-(\rho)$ the preferred state is $u = 0$ while the opposite is the case for $\gamma > \gamma_+(\rho)$. These observations are reflected in Figs. 5(b) and 5(d) which show that below the pinning region the structure collapses to $u = 0$ [Fig. 5(b)] while above it it gradually nucleates additional wavelengths and so grows in spatial extent [Fig. 5(d)]. Figures 5(a) and 5(c) also show that the lifetime of the localized structures outside their stability region (see Fig. 4) increases rapidly as one approaches the top boundary of the pinning region in the (ρ, γ) plane. We expect that this lifetime increases inversely as the square root of the distance from the boundary of the stability zone much as occurs when $\gamma = 0$ [9].

To explain some aspects of the above results, and in particular the lateral motion of the LSs computed from the PDE system Eqs. (1) and (2), we employ a semianalytical approach, putting the system into the instantaneous comoving frame $z = x - \int_0^t c(t')\,dt'$. Thus, $c(t)$ is the instantaneous velocity

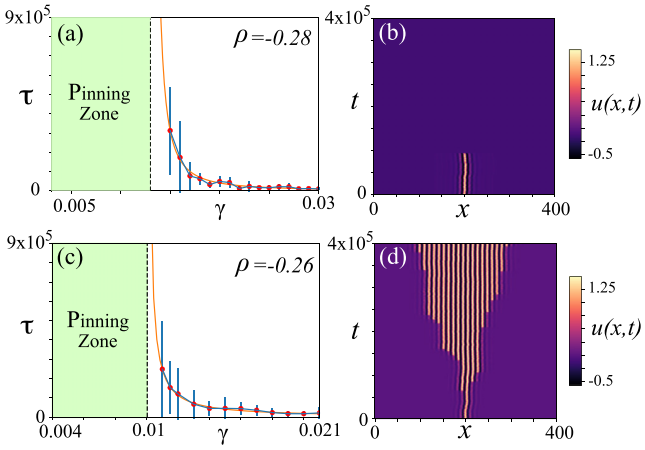

FIG. 5. Lifetimes τ of localized states as a function of γ for $b = 1.8$ and (a) $\rho = -0.28$, (c) $\rho = -0.26$ outside the pinning zone (red dots with error bars). The solid lines represent the fits (a) $\tau = 14.39/(\gamma - 0.013)^{1.6}$, (c) $\tau = 125.9/(\gamma - 0.01)^{1.1}$. (b) Eventual decay of LS1 at $\rho = -0.28$ when $\gamma = 0.0225 > \gamma_-(\rho)$. (d) Gradual growth of LS1 at $\rho = -0.26$ when $\gamma = 0.012 > \gamma_+(\rho)$.

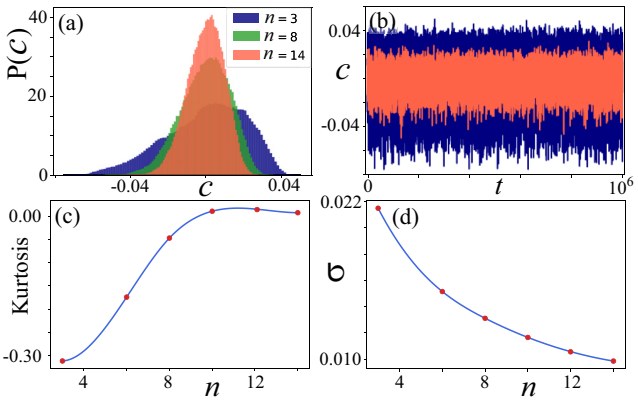

FIG. 6. Characterization of the instantaneous speed $c(t)$ of localized structures as a function of their length n as obtained from Eq. (6) with $b = 1.8$, $\rho = -0.3$, $\gamma = 0.25$, $\eta = 0$, and $\mu = 3$. (a) Probability density function of $c(t)$ for three different values of n. (b) Typical temporal evolution of $c(t)$ for $n = 3$ (dark blue curve) and $n = 14$ (light red curve). The remaining panels show (c) the kurtosis and (d) the standard deviation σ of the pdf of c as functions of n.

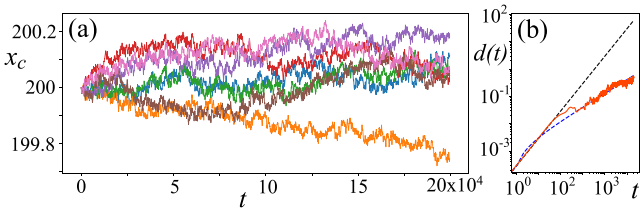

FIG. 7. (a) Position of the centroid $x_c(t)$ for several slightly different one-bump initial conditions when $\rho = -0.27$, $\gamma = 0.001$, $\eta = 0$. (b) Corresponding ensemble-averaged centroid displacement $d(t)$ (red curve). The black-dashed line corresponds to the linear fit $d(t) = 3 \times 10^{-4} t$ to the short-time evolution ($0 \leqslant t \leqslant 100$), while the blue-dashed curve represents the square root fit $d(t) = 0.0013\sqrt{t} - 0.001$ to the subsequent evolution.

of the structure. To simplify the calculation that follows, we use standard bracket notation for the inner product with

$$\langle f | g \rangle = \int_{-\infty}^{\infty} f(x) g(x)\, dx. \tag{3}$$

We suppose that $|u\rangle = |u_0\rangle + |w\rangle$, where $u_0 \equiv u_0(z)$ is an appropriate LS solution and w is a small perturbation comparable in magnitude to both γ and the instantaneous velocity $c(t)$. It follows that

$$-c\partial_z u_0 = \mathcal{L}\,|w\rangle + \gamma\,|(\partial_z \psi) u_0\rangle\,, \tag{4}$$

where $\mathcal{L} \equiv \rho - (1 + \partial_{zz})^2 + 2\beta u_0 - 3u_0^2$. Since $\mathcal{L}$ is a self-adjoint linear operator (i.e., $\mathcal{L} = \mathcal{L}^\dagger$) with a kernel spanned by $\partial_z u_0$ the solvability condition for $w(x, t)$ yields

$$\dot{x}_c(t) \equiv c(t) = -\gamma \frac{\langle \partial_z u_0 |\, (\partial_z \psi) u_0 \rangle}{\langle \partial_z u_0 |\, \partial_z u_0 \rangle}. \tag{5}$$

Since the structure is localized, integration by parts shows that

$$\dot{x}_c(t) = \gamma \frac{\langle \partial_z u_0 |\, \psi\, \partial_z u_0 \rangle}{\langle \partial_z u_0 |\, \partial_z u_0 \rangle}. \tag{6}$$

This equation governs the motion of the centroid, hereafter $x_c(t)$, of the localized structure and shows that motion results from the asymmetry in the projection of $\psi(z, t)$ on the translation mode $\partial_z u_0(z)$. For fluctuations driven by noise alone we have

$$\dot{x}_c(t) = -\sqrt{\eta} \frac{\langle \partial_z u_0 |\, \zeta(z, t) u_0 \rangle}{\langle \partial_z u_0 |\, \partial_z u_0 \rangle} \equiv \sqrt{\eta}\, \xi(t), \tag{7}$$

where $\xi(t)$ is a white noise satisfying

$$\langle \xi(t) \xi(t') \rangle_\zeta = \frac{\langle (\partial_z u_0)^2 |\, u_0^2 \rangle}{(\langle \partial_z u_0 |\, \partial_z u_0 \rangle)^2} \delta(t - t'). \tag{8}$$

Figure 6(a) compares the probability density functions of $c(t)$ for localized structures with $n = 3$, 8, and 14, while Fig. 6(b) shows the corresponding realizations $c(t)$ for $n = 3$ and 14. We see that the distribution of speeds is much broader when n is small than when it is large, and conclude that narrower structures have greater mobility, a conclusion in agreement with related work on colliding LS [30]. We ascribe this effect to the requirement that to move a broader structure one requires a fluctuation with a larger spatial correlation, making larger speeds less likely. Notice also that the distribution function for small n is markedly asymmetric. This is due to the asymmetry in the forcing function $\partial_x \psi$ with respect to spatial reflection $x \to -x$. Inevitably the resulting asymmetry in the pdf of the speed c decreases with increasing length n of the structure. These properties are summarized in Figs. 6(c) and 6(d) which show the kurtosis of the pdf and its standard deviation σ as a function of n.

IV. STATISTICAL CHARACTERIZATION OF LS DISPLACEMENT

To characterize the dynamics of an LS, we fix attention on its centroid, defined by

$$x_c(t) = \frac{\int_{-L}^{L} x u(x, t)\, dx}{\int_{-L}^{L} u(x, t)\, dx}, \tag{9}$$

where $[-L, L]$ is the domain size. Figure 7 shows the location of this centroid for LS1 as a function of the elapsed time t as determined from numerical simulations of the system Eqs. (1) and (2) starting from several slightly different initial conditions (color-coded) obtained by multiplying u and ψ at the same grid points as the solution by independent random vectors of magnitude 10^{-5}. The results evidence the extreme sensitivity of the drift dynamics to initial conditions, as is expected of a chaotic system.

From the dynamics of the centroid, we can extract its displacement $\Delta x(t) \equiv x_c(t + dt) - x_c(t)$ in time dt for each realization of the chaotic process. Figure 8(a) shows this displacement for one such realization. We see that successive displacements may be considered to be uncorrelated, with zero mean. Indeed, the resulting distribution of Δx resembles a Gaussian distribution [Fig. 8(b)], as may be expected of Brownian motion. However, in the present case the distribution is truncated since very large displacements in the time dt are prohibited. This is a consequence of the fact that the displacement is fully deterministic, with each realization drawn from a bounded attractor. Figure 8(c) shows the expected rapid

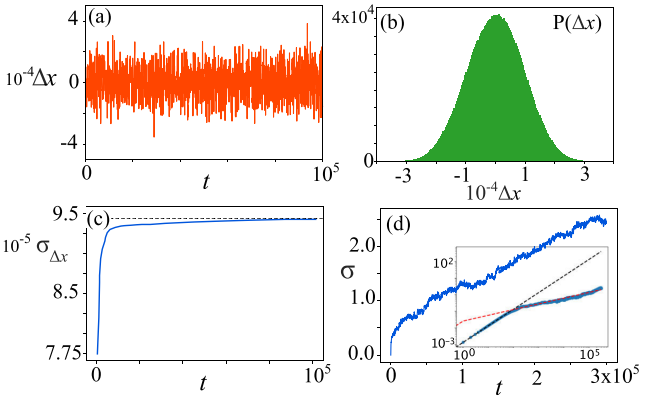

FIG. 8. (a) Displacement Δx of the centroid of a one-bump state as a function of time t in a single realization of the chaotic walk at $\rho = -0.27$ and $\gamma = 0.001$. (b) Associated probability density function $P(\Delta x)$. (c) Evolution of the standard deviation $\sigma_{\Delta x}$ of the resulting displacement dynamics. (d) Ensemble standard deviation $\sigma(t)$ computed over 100 slightly different initial conditions differing by order 10^{-4}. The inset presents the same results on a log-log scale. Initially, a ballistic behavior is observed (exponent 1, $t < 100$, dashed black curve), followed by a crossover to subdiffusive behavior (exponent 0.345, $t > 100$, dashed red curve).

saturation of the standard deviation $\sigma_{\Delta x}(t)$ of Δx. In contrast, Fig. 8(d) shows the cumulative effect of these displacements, i.e., the standard deviation $\sigma(t)$ of the centroid position $x_c(t)$ computed over 100 realizations of the above process, each generated by a small $[O(10^{-4})]$ random perturbation of the initial condition.

Figure 9 shows the corresponding evolution of 3-bump and 14-bump localized states in a space-time diagram. We see that the broader structure has a broader probability distribution function than the shorter structure [Fig. 9(c)]. At first sight this conclusion is in conflict with our mobility calculation. We understand this unexpected result as follows: because broader structures have lower mobility and therefore larger effective inertia, a broader structure, once in motion, will

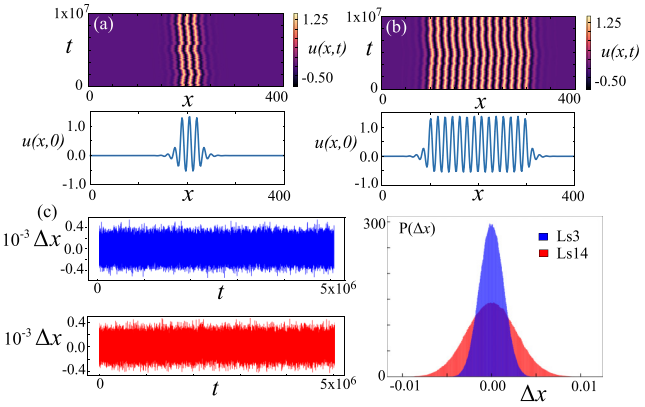

FIG. 9. Space-time evolution of (a) 3-bump and (b) 14-bump localized states when $\rho = -0.28$, $\gamma = 0.012$ showing that the amplitude of the centroid displacement decreases with increasing number of bumps. (c) Displacement Δx of the structures as a function of time together with their pdf.

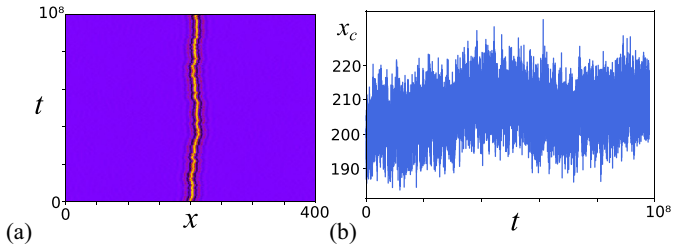

FIG. 10. (a) Spatiotemporal evolution of a one-bump localized solution of the Swift-Hohenberg equation (1) with $b = 1.8$, $\rho = -0.27$, $\eta = 0$ in the presence of additive deterministic fluctuations $\gamma \partial_x \psi(x,t)$ with $\gamma = 0.004$ and $\mu = 3$. (b) Temporal evolution of the centroid position $x_c(t)$.

drift further before it can change direction, resulting in larger typical displacement than for shorter structures.

V. CONCLUSIONS

Based on a prototype model of pattern formation, the Swift-Hohenberg equation, we have shown that localized structures are robust in the presence of multiplicative deterministic fluctuations. This is in contrast to the effect of random fluctuations, which ultimately always destroy such structures. We have seen that in the former case the LSs exhibit complex spatiotemporal behavior we have termed a chaotic walk. This type of walk is highly sensitive to the initial conditions but its properties can nonetheless be described using standard statistical physics approaches including the computation of probability distribution functions. The exploding dissipative solitons studied in Ref. [31] provide a distinct example of a system exhibiting related behavior, where translation is triggered by loss of reflection symmetry. However, in contrast to the system studied here, in this system translation is intermittent and associated with episodic escapes from a reflection-invariant strange attractor as described in Ref. [32]. The resulting walk is thus a chaotic Lévy flight. In contrast our system Eqs. (1) and (2) has no reflection symmetry. As shown in Fig. 10 similar results hold in the case of additive deterministic fluctuations as well.

We have seen that the presence of deterministic fluctuations with increasing amplitude leads to the gradual erosion of the stability zone of different LSs, with shorter structures proving more fragile than broader ones. In addition, the stability zone shifts towards larger values of the parameter ρ because fluctuations at the lower end of the zone tend to eliminate spatial structure while those at the upper end tend to nucleate new structure. For large enough fluctuation amplitude stable LSs are no longer possible.

We have seen that within their zone of stability the LSs execute a chaotic walk. The properties of this walk are determined by the mobility of the structure, and we have shown by explicit calculation that shorter structures have greater mobility, and hence smaller effective inertia. As a result shorter structures change direction more frequently than longer structures, which are therefore characterized by a broader distribution of step sizes.

Similar behavior is found in two spatial dimensions as well. Figure 11(b) shows several examples of chaotic but

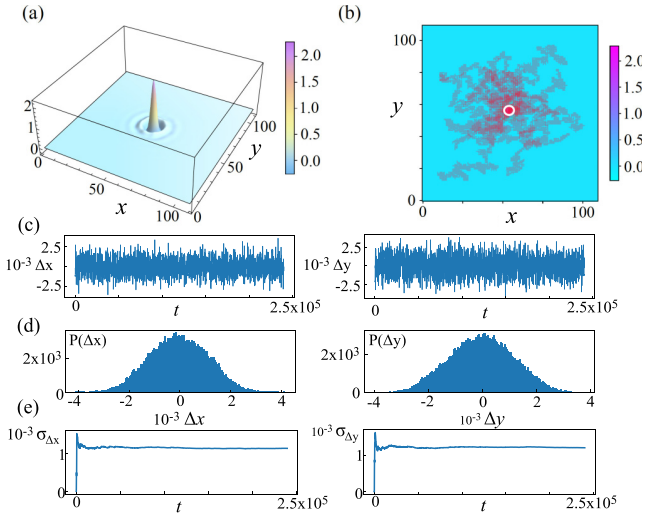

FIG. 11. Chaotic walk in two dimensions of an initially axisymmetric one-bump state (a) for several slightly different initial conditions for Eq. (2) when $b = 2.2$, $\rho = -0.5$, $\gamma = 0.07$, $\eta = 0$ (b). The red dot in (b) shows the location of the structure at $t = 0$. (c) Displacements Δx and Δy of the centroid of a one-bump state in time $dt = 0.01$ as a function of the time t in one realization of the chaotic walk. (d) Associated probability density functions. (e) Evolution of the standard deviations $\sigma_{\Delta x}$, $\sigma_{\Delta y}$ of the resulting displacements.

deterministic walks of a one-bump localized structure [Fig. 11(a)] initially at $(x, y) = (0, 0)$ obtained from different realizations of Eqs. (1) and (2) in two dimensions generated by multiplying u and ψ at each grid point by independent random vectors of magnitude 10^{-3}. No additive noise is included ($\eta = 0$). The figure shows the resulting trajectories in the (x, y) plane while Figs. 11(c) and 11(d) show the statistics of the centroid displacement $(\Delta x, \Delta y)$ in time $dt = 0.01$, defined as in the one-dimensional case, for one of these realizations. These show that the chaotic walk is statistically isotropic with a constant and isotropic standard deviation. Moreover, when averaged over the initial conditions used to generate the different realizations, the distribution of the resulting walks is also isotropic. Thus localized structures in two spatial dimensions undergo similar behavior when subjected to multiplicative deterministic fluctuations as those in one spatial dimension. A detailed study of the properties of these two-dimensional deterministic walks is in progress.

The above results differ fundamentally from those prevailing for Eq. (1) driven stochastically by white noise ($\gamma = 0$). In this case all LSs eventually collapse to either the trivial state $u = 0$ or to a spatially extended state. These two outcomes are separated by an effective Maxwell point that has to be computed as a function of the applied forcing strength η. In fact theoretical interpretations of experimental studies of LSs, in both 1D and 2D [4–6], typically assume that any fluctuations that may be present are of a stochastic nature, and not deterministic. We have shown that a careful examination of the statistical properties of the observed LS dynamics can in principle discriminate between these two possibilities, and provide new insights into the nature of the underlying fluctuations.

Throughout this paper we have adopted periodic boundary conditions. However, it is known that fluctuations in the boundary conditions can in and of themselves lead to unexpected timing jitter in optical signals [33]. A study of the effect of deterministic boundary fluctuations on the dynamics of LSs through their effect on the critical wave number k_c is therefore also of interest, and will be reported on in a future publication.

ACKNOWLEDGMENTS

This work was partially funded by CONICYT-USA Grant No. PII20150011. A.J.A.-S. gratefully acknowledges financial support from Becas CONICYT 2015, Contract No. 21151618.

[1] G. Nicolis and I. Prigogine, *Self-Organization in Nonequilibrium Systems* (J. Wiley & Sons, New York, 1977).
[2] M. C. Cross and P. C. Hohenberg, Rev. Mod. Phys. **65**, 851 (1993).
[3] L. M. Pismen, *Patterns and Interfaces in Dissipative Dynamics*, Springer Series in Synergetics (Springer, Berlin/Heidelberg, 2006).
[4] *Localized States in Physics: Solitons and Patterns*, edited by O. Descalzi, M. Clerc, S. Residori, and G. Assanto (Springer, New York, 2010).
[5] H. G. Purwins, H. U. Bödeker, and Sh. Amiranashvili, Adv. Phys. **59**, 485 (2010).
[6] *Dissipative Solitons: From Optics to Biology and Medicine*, Lecture Notes in Physics 751, edited by N. Akhmediev and A. Ankiewicz (Springer, Heidelberg, 2008).
[7] P. Coullet, Int. J. Bifurcat. Chaos **12**, 2445 (2002).
[8] P. D. Woods and A. R. Champneys, Physica D **129**, 147 (1999).
[9] J. Burke and E. Knobloch, Phys. Rev. E **73**, 056211 (2006).
[10] A. G. Vladimirov, R. Lefever, and M. Tlidi, Phys. Rev. A **84**, 043848 (2011).
[11] D. Turaev, M. Radziunas, and A. G. Vladimirov, Phys. Rev. E **77**, 065201(R) (2008).
[12] K. Staliunas and V. J. Sánchez-Morcillo, Phys. Rev. A **57**, 1454 (1998).
[13] F. Haudin, R. G. Rojas, U. Bortolozzo, M. G. Clerc, and S. Residori, Phys. Rev. Lett. **106**, 063901 (2011).
[14] P. V. Paulau, D. Gomila, T. Ackemann, N. A. Loiko, and W. J. Firth, Phys. Rev. E **78**, 016212 (2008).
[15] A. J. Scroggie, W. J. Firth, and G.-L. Oppo, Phys. Rev. A **80**, 013829 (2009).
[16] M. Tlidi, A. G. Vladimirov, D. Pieroux, and D. Turaev, Phys. Rev. Lett. **103**, 103904 (2009).
[17] A. J. Alvarez-Socorro, M. G. Clerc, and M. Tlidi, Chaos **28**, 053119 (2018).
[18] M. G. Clerc, S. Coulibaly, and D. Laroze, Int. J. Bifurcat. Chaos **19**, 2717 (2009).

[19] B. Schäpers, M. Feldmann, T. Ackemann, and W. Lange, Phys. Rev. Lett. **85**, 748 (2000).
[20] A. Prigent, G. Grégoire, H. Chaté, O. Dauchot, and W. van Saarloos, Phys. Rev. Lett. **89**, 014501 (2002).
[21] D. Barkley and L. S. Tuckerman, Phys. Rev. Lett. **94**, 014502 (2005).
[22] H. Sakaguchi and H. R. Brand, Physica D **97**, 274 (1996).
[23] M. G. Clerc, C. Falcon, and E. Tirapegui, Phys. Rev. E **74**, 011303 (2006).
[24] A. J. Alvarez-Socorro, M. G. Clerc, M. A. Ferré, and E. Knobloch, Phys. Rev. E **99**, 062226 (2019).
[25] W. Horsthemke and R. Lefever, *Noise-induced Transitions* (Springer, Berlin, 1984).
[26] J. Burke and E. Knobloch, Chaos **17**, 037102 (2007).
[27] P. Manneville, *Lecture Notes in Physics*, Vol. 280 (Springer, Berlin, 1994), pp. 319–326.
[28] Y. Kuramoto, Prog. Theor. Phys. Suppl. **64**, 346 (1978).
[29] S. Toh, J. Phys. Soc. Jpn. **56**, 949 (1987).
[30] S. M. Houghton and E. Knobloch, Phys. Rev. E **84**, 016204 (2011).
[31] C. Cartes, J. Cisternas, O. Descalzi, and H. R. Brand, Phys. Rev. Lett. **109**, 178303 (2012).
[32] C. Martel, E. Knobloch, and J. M. Vega, Physica D **137**, 94 (2000).
[33] H. Haus and A. Mecozzi, IEEE J. Quant. Electron. **29**, 983 (1993).

Chapter 9

Conclusions

In this chapter, we summarize the main results presented in this thesis at each chapter as well as some points for further research.

In chapter 2 was revealed how nonvariational effects could affect the dynamics of FKPP fronts, obtaining that FKPP fronts exhibit a pulled-pushed-like transition when parameters weighting nonvariational terms like nonlinear advection and nonlinear diffusion varies. These results were validated in a LCLV experiment with optical feedback, obtaining that the experimental results were in good agreement with the theoretical ones. It is noteworthy that the robustness of the FKPP fronts enables us to extend these results to other contexts such as interfaces in optical and magnetical media, population dynamics and in combustion theory. Moreover, these results open the doors to new questions like the nonvariational effects in discrete and heterogeneous media from a theoretical point of view and the possibility of improving the control of liquid crystal displays, considering nonvariational knob.

In chapter 3 was found a new mechanism for front propagation, as evidenced by putting a bistable nonvariational system at the Maxwell points and varying the nonvariational terms. In this scenario, the mechanism of propagation is purely nonvariational. Moreover, in any point of the parameter space where a normal front exists, the speed depends on two contributions, the difference of energy between the stable states connected by the front and terms that are related to the shape of the front and are related to the nonvariational terms. Bistability, and in general multistability, is a robust phenomenon in nature as well as a nonvariational mechanism. Therefore our work enables mechanism to understand and control front propagation when it is possible to have such kinds of nonvariational terms. The applications range from control of interfaces in liquid crystals, magnetical media, granular media dynamics, as well as population dynamics and opinion dynamics in social media. In the scenario of FKPP fronts, we are also interested in understanding how nonvariational effects are affected by discreteness and heterogeneity in the spatial coupling.

In chapter 4 was presented how nonvariational effects can drive a transition from motionless to motion following a supercritical Pitchfork bifurcation in localized dissipative structures exhibiting a parity breaking transition. From the theoretical point of view, we take the nonvariational Turing-Swift-Hohenberg equation as an archetypical model in pattern formation

exhibiting localized states, where the nonvariational contribution comes from terms like nonlinear advection and nonlinear difussion. Moreover, due to the nonvariational TSH-equation genericity, we expect to observe this kind of propagative bounded localized states in more natural phenomena. On the other hand, from an experimental point of view, this kind of mechanism of propagation of localized structures could be of interest in control of spots in liquid crystals devices, labeled delivery of information in photonic and magnetic storage devices, processors, and the delivery of micro-scale cargoes.

In chapter 5, we found a novel kind of chimera states or chaoticons in continuous media, namely, traveling chimera states. Although the traveling chimera states in discrete media were known, our work presents, to the best of the authors' knowledge, the first example of a traveling chimera state in continuous media. Nonvariational effects drives the emergence of these intriguing states. In our work, we characterize its behavior from a dynamical and statistical perspective and give numerical insights about its bifurcations. As further work, we are investigating possible higher dimensional generalization of these states. As nonvariational terms could be accessible as a physical knob, we expect to find such kinds of states in experiments as well as in nature. In particular, due to the emergence of the Turing-Swift-Hohemberg in disciplines like ecology, chemistry, and social dynamics, we expect to see these states in such systems.

In chapter 6, we exhibit an intriguing kind of propagative chimera state in continuous media, namely, wandering chimera states, characterized by a wandering motion resembling a random walk. We characterize its dynamical and statistical properties. In particular, we consider the centroid displacements as order parameter and characterize the geometry of its displacement, obtain numerically the attractor basin, and reveal its interesting geometrical complexity proper of chaotical systems. In this way, the wandering motion of the localized structure was mapped to a chaotical trajectory of the centroid. Moreover, the leading Lyapunov exponents were calculated, obtaining that its chaotic dynamics are of low-dimensional type. On the other hand, we show evidence of these states in the LCLV experiment. Nevertheless, deeper research about the emergence of this kind of state in the LCLV experiment is needed. Moreover, due to the genericity of the nonvariational Turing-Swift-Hohenberg equation, we expect the observation of these kinds of states in a wide variety of natural and technological systems. Finally, some control strategies were offered to achieve spatial pinning or propagation with a preferential direction of motion, enabling its potential use in designing electro-optical devices for storage and computing and micro energy generators.

Inspired by how Spatio-temporal chaos can drive to wandering motion, in chapter 7, we try to answer a more deep question: how chaotic fluctuations, as another example of nonvariational perturbation, can induce new kinds of dynamical phenomena. In particular, we study how deterministic (or chaotic) fluctuations modify the dynamics of normal fronts and how different are such results when they are compared to the stochastic perturbation scenario. Moreover, our work proposes an interesting question, when external fluctuations can be modelled by stochastic processes?. As a physical motivation, these complex deterministic fluctuations could correspond to a system coupled with a small reservoir bath, defined with a small number of particles, whose dynamics could be modeled by an n-body problem which have chaotical solutions typically. This work creates a bridge to exploring how deterministic fluctuation modifies pre-existing phase transitions or even induces new ones. In this sense,

a complete study of chaos-induced transition is missing and creates an interesting area to explore. An experimental approach to an experiment could use the LCLV experiment in the multistability region (for simplicity bistability) and introduce the Spatio-temporal chaotic perturbations using the SLM device. Such experiments could improve our comprehension of the spatiotemporal chaotic perturbations in spatiotemporal systems and give insights into how randomness can emerge from deterministic systems.

In chapter 8, we studied the effect of deterministic fluctuations in the dynamics of localized states, obtaining in such a way an exciting example of a chaotical particle. The effect of deterministic fluctuations enables a pinning zone in contraposition to the effect of randomness perturbations on localized states in a similar way than the obtained result for deterministic fluctuations in fronts in chapter 7. In both scenarios, the pinning zone is a consequence of the limited (or forbidden) transitions in deterministic systems. In addition, we characterize how this zone depends on the fluctuation intensity parameter, obtaining a shrinking effect of the pinning zone when the intensity increase. When the centroid of the localized structures under chaotic fluctuations is tracked, it exhibits complex spatiotemporal dynamics, namely, a chaotic walk. Meanwhile, its dynamics appears to be qualitatively "similar" to the Brownian particle, it is of deterministic nature and it could be interpreted as an analogous to a particle interacting with a small chaotical thermal bath composed by a n-body system, instead of describing it with the standard stochastic approach. This work opens several questions about the nature of randomness and how it can emerge from determinism. Finally, motivate us to explore in deep a research line in chaos induced transitions and its applications.

Bibliography

[1] Bing-Xiang Li, Rui-Lin Xiao, Sathyanarayana Paladugu, Sergij V Shiyanovskii, and Oleg D Lavrentovich. Three-dimensional solitary waves with electrically tunable direction of propagation in nematics. *Nature communications*, 10(1):1–9, 2019.

[2] Bing-Xiang Li, Rui-Lin Xiao, Sergij V Shiyanovskii, and Oleg D Lavrentovich. Soliton-induced liquid crystal enabled electrophoresis. *Physical Review Research*, 2(1):013178, 2020.

[3] N. Verschueren, U. Bortolozzo, M. G. Clerc, and S. Residori. Spatiotemporal Chaotic Localized State in Liquid Crystal Light Valve Experiments with Optical Feedback. *Physical Review Letters*, 110(10):104101, 2013.

[4] N Verschueren, U Bortolozzo, M G Clerc, and S Residori. Chaoticon: localized pattern with permanent dynamics. *Philosophical Transactions of the Royal Society A: Mathematical, Physical and Engineering Sciences*, 372(2027):20140011, 2014.

[5] Wim Van Saarloos. Front propagation into unstable states. *Physics reports*, 386(2-6):29–222, 2003.

[6] Jack Xin. Front propagation in heterogeneous media. *SIAM review*, 42(2):161–230, 2000.

[7] Marcel Clerc. *Waves called fronts*. Universidad de Chile, 2021.

[8] Michel Remoissenet. *Waves called solitons: concepts and experiments*. Springer Science & Business Media, 2013.

[9] Orazio Descalzi, Marcel Clerc, Stefania Residori, and Gaetano Assanto. *Localized states in physics: solitons and patterns*. Springer Science & Business Media, 2011.

[10] Steven H Strogatz. *Nonlinear dynamics and chaos with student solutions manual: With applications to physics, biology, chemistry, and engineering*. CRC press, 2018.

[11] Robert L Devaney. *A first course in chaotic dynamical systems: theory and experiment*. Chapman and Hall/CRC, 2020.

[12] Arkady Pikovsky, Jurgen Kurths, Michael Rosenblum, and Jürgen Kurths. *Synchronization: a universal concept in nonlinear sciences*. Number 12. Cambridge university

press, 2003.

[13] Steven H Strogatz. *Sync: How order emerges from chaos in the universe, nature, and daily life*. Hachette UK, 2012.

[14] Mark C Cross and Pierre C Hohenberg. Pattern formation outside of equilibrium. *Reviews of modern physics*, 65(3):851, 1993.

[15] Giorgio Bertotti and Isaak D Mayergoyz. *The Science of Hysteresis: Mathematical modeling and applications*, volume 1. Academic Press, 2006.

[16] Herman Haken. Synergetics. *Physics Bulletin*, 28(9):412, 1977.

[17] Gérard Iooss and Daniel D Joseph. *Elementary stability and bifurcation theory*. Springer Science & Business Media, 2012.

[18] John Guckenheimer and Philip Holmes. *Nonlinear oscillations, dynamical systems, and bifurcations of vector fields*, volume 42. Springer Science & Business Media, 2013.

[19] Ronald Aylmer Fisher. The wave of advance of advantageous genes. *Annals of eugenics*, 7(4):355–369, 1937.

[20] Andrei N Kolmogorov. Étude de l'équation de la diffusion avec croissance de la quantité de matière et son application à un problème biologique. *Bull. Univ. Moskow, Ser. Internat., Sec. A*, 1:1–25, 1937.

[21] Alan Turing. The turing digital archive, 2019.

[22] Jonathan H.P. Dawes. After 1952: The later development of Alan Turing's ideas on the mathematics of pattern formation. *Historia Mathematica*, 43(1):49–64, 2016.

[23] Ju Swift and Pierre C Hohenberg. Hydrodynamic fluctuations at the convective instability. *Physical Review A*, 15(1):319, 1977.

[24] John Burke and Edgar Knobloch. Localized states in the generalized swift-hohenberg equation. *Physical Review E*, 73(5):056211, 2006.

[25] John Burke and Jonathan HP Dawes. Localized states in an extended swift–hohenberg equation. *SIAM Journal on Applied Dynamical Systems*, 11(1):261–284, 2012.

[26] A Hariz, L Bahloul, L Cherbi, K Panajotov, M Clerc, M A Ferré, B Kostet, E Averlant, and M Tlidi. Swift-Hohenberg equation with third-order dispersion for optical fiber resonators. *Physical Review A*, 100(2):023816, 2019.

[27] I. Bordeu, M.G. Clerc, R. Lefever, and M. Tlidi. From localized spots to the formation of invaginated labyrinthine structures in a Swift–Hohenberg model. *Communications in Nonlinear Science and Numerical Simulation*, 29(1-3):482–487, 2015.

[28] Yoshiki Kuramoto. Diffusion-Induced Chaos in Reaction Systems. *Progress of Theoretical Physics Supplement*, 64:346–367, 02 1978.

[29] Gregory I Sivashinsky. Nonlinear analysis of hydrodynamic instability in laminar flames—i. derivation of basic equations. *Acta astronautica*, 4(11):1177–1206, 1977.

[30] P Coullet, J Lega, B Houchmandzadeh, and J Lajzerowicz. Breaking chirality in nonequilibrium systems. *Physical review letters*, 65(11):1352, 1990.

[31] Felipe Barra, Orazio Descalzi, and Enrique Tirapegui. Nonvariational effects in nonequilibrium systems. *Physics Letters A*, 221(3-4):193–196, 1996.

[32] Aric Hagberg and Ehud Meron. Pattern formation in non-gradient reaction-diffusion systems: the effects of front bifurcations. *Nonlinearity*, 7(3):805, 1994.

[33] M San Miguel, R Montagne, A Amengual, and E Hernandez-Garcia. Multiple front propagation in a potential non-gradient system. In *Instabilities and Nonequilibrium Structures V*, pages 85–97. Springer, 1996.

[34] Marcel G Clerc, Saliya Coulibaly, and David Laroze. Nonvariational Ising-Bloch transition in parametrically driven systems. *International Journal of Bifurcation and Chaos*, 19(08):2717–2726, 2009.

[35] A. J. Alvarez-Socorro, M. G. Clerc, G. González-Cortés, and M. Wilson. Nonvariational mechanism of front propagation: Theory and experiments. *Physical Review E*, 95(1):010202, 2017.

[36] Donald G Aronson and Hans F Weinberger. Multidimensional nonlinear diffusion arising in population genetics. *Advances in Mathematics*, 30(1):33–76, 1978.

[37] K. P. Hadeler and F. Rothe. Travelling fronts in nonlinear diffusion equations. *Journal of Mathematical Biology*, 2(3):251–263, 1975.

[38] Yves Pomeau. Front motion, metastability and subcritical bifurcations in hydrodynamics. *Physica D: Nonlinear Phenomena*, 23(1-3):3–11, 1986.

[39] Anatole Katok and Boris Hasselblatt. *Introduction to the modern theory of dynamical systems*. Number 54. Cambridge university press, 1997.

[40] LM Pismen. Patterns and interfaces in dissipative dynamics. *Synergetics*, pages 85–105, 2020.

[41] Abdul-Majid Wazwaz. *Partial differential equations and solitary waves theory*. Springer Science & Business Media, 2010.

[42] Dan Anderson. Variational approach to nonlinear pulse propagation in optical fibers. *Physical review A*, 27(6):3135, 1983.

[43] D Krökel, Naomi J Halas, G Giuliani, and D Grischkowsky. Dark-pulse propagation in optical fibers. *Physical review letters*, 60(1):29, 1988.

[44] Aditya Kaushik and Mohan D Sharma. Numerical analysis of a mathematical model

for propagation of an electrical pulse in a neuron. *Numerical Methods for Partial Differential Equations: An International Journal*, 24(4):1055–1079, 2008.

[45] Pedro Parra-Rivas, Saliya Coulibaly, MG Clerc, and Mustapha Tlidi. Influence of stimulated raman scattering on kerr domain walls and localized structures. *Physical Review A*, 103(1):013507, 2021.

[46] Marcel Gabriel Clerc, Saliya Coulibaly, Pedro Parra-Rivas, and Mustapha Tlidi. Nonlocal raman response in kerr resonators: Moving temporal localized structures and bifurcation structure. *Chaos: An Interdisciplinary Journal of Nonlinear Science*, 30(8):083111, 2020.

[47] Mustapha Tlidi, Cristian Fernandez-Oto, MG Clerc, D Escaff, and Pascal Kockaert. Localized plateau beam resulting from strong nonlocal coupling in a cavity filled by metamaterials and liquid-crystal cells. *Physical Review A*, 92(5):053838, 2015.

[48] F Haudin, René G Rojas, U Bortolozzo, MG Clerc, and S Residori. Vortex emission accompanies the advection of optical localized structures. *Physical review letters*, 106(6):063901, 2011.

[49] U Bortolozzo, MG Clerc, and S Residori. Solitary localized structures in a liquid crystal light-valve experiment. *New Journal of Physics*, 11(9):093037, 2009.

[50] Daniel Escaff, Cristian Fernandez-Oto, MG Clerc, and Mustapha Tlidi. Localized vegetation patterns, fairy circles, and localized patches in arid landscapes. *Physical Review E*, 91(2):022924, 2015.

[51] Michael Cross and Henry Greenside. *Pattern formation and dynamics in nonequilibrium systems*. Cambridge University Press, 2009.

[52] Daniel Walgraef. *Spatio-temporal pattern formation: with examples from physics, chemistry, and materials science*. Springer Science & Business Media, 2012.

[53] Philip Ball and Neil R Borley. *The self-made tapestry: pattern formation in nature*, volume 198. Oxford University Press Oxford, 1999.

[54] Agnes Buka and Lorenz Kramer. *Pattern formation in liquid crystals*. Springer Science & Business Media, 2012.

[55] Troy Shinbrot, Celso Grebogi, Jack Wisdom, and James A Yorke. Chaos in a double pendulum. *American Journal of Physics*, 60(6):491–499, 1992.

[56] Tomasz Stachowiak and Toshio Okada. A numerical analysis of chaos in the double pendulum. *Chaos, Solitons & Fractals*, 29(2):417–422, 2006.

[57] Marcel Ausloos and Michel Dirickx. *The logistic map and the route to chaos: From the beginnings to modern applications*. Springer Science & Business Media, 2006.

[58] Samia Ayadi and Olivier Haeberlé. The lorenz model for single-mode homogeneously

broadened laser: analytical determination of the unpredictable zone. *Open Physics*, 12(3):203–214, 2014.

[59] M Clerc, Pierre Coullet, and Enrique Tirapegui. The stationary instability in quasi-reversible systems and the lorenz pendulum. *International Journal of Bifurcation and Chaos*, 11(03):591–603, 2001.

[60] C Sparrow. The lorenz equations. *Edited by Arun V. Holden*, page 111, 1982.

[61] Kunihiko Kaneko. Overview of coupled map lattices. *Chaos: An Interdisciplinary Journal of Nonlinear Science*, 2(3):279–282, 1992.

[62] Giancarlo Benettin, Luigi Galgani, Antonio Giorgilli, and Jean-Marie Strelcyn. Lyapunov characteristic exponents for smooth dynamical systems and for hamiltonian systems; a method for computing all of them. part 1: Theory. *Meccanica*, 15(1):9–20, 1980.

[63] Ch Skokos. The lyapunov characteristic exponents and their computation. In *Dynamics of Small Solar System Bodies and Exoplanets*, pages 63–135. Springer, 2010.

[64] Anna Zakharova. *Chimera Patterns in Complex Networks*. Springer, 2020.

[65] Yoshiki Kuramoto and Dorjsuren Battogtokh. Coexistence of coherence and incoherence in nonlocally coupled phase oscillators. *arXiv preprint cond-mat/0210694*, 2002.

[66] Soumen Majhi, Bidesh K Bera, Dibakar Ghosh, and Matjaž Perc. Chimera states in neuronal networks: A review. *Physics of life reviews*, 28:100–121, 2019.

[67] Kanika Bansal, Javier O Garcia, Steven H Tompson, Timothy Verstynen, Jean M Vettel, and Sarah F Muldoon. Cognitive chimera states in human brain networks. *Science advances*, 5(4):eaau8535, 2019.

[68] Zhenhua Wang and Zonghua Liu. A brief review of chimera state in empirical brain networks. *Frontiers in Physiology*, 11, 2020.

[69] Fabian Böhm, Anna Zakharova, Eckehard Schöll, and Kathy Lüdge. Amplitude-phase coupling drives chimera states in globally coupled laser networks. *Physical Review E*, 91(4):040901, 2015.

[70] Joniald Shena, Johanne Hizanidis, Vassilios Kovanis, and George P Tsironis. Turbulent chimeras in large semiconductor laser arrays. *Scientific reports*, 7(1):1–8, 2017.

[71] André Röhm, Fabian Böhm, and Kathy Lüdge. Small chimera states without multistability in a globally delay-coupled network of four lasers. *Physical Review E*, 94(4):042204, 2016.

[72] Marcel Gabriel Clerc, Saliya Coulibaly, MA Ferré, and Mustapha Tlidi. Two-dimensional optical chimera states in an array of coupled waveguide resonators. *Chaos: An Interdisciplinary Journal of Nonlinear Science*, 30(4):043107, 2020.

[73] Zachary G Nicolaou, Hermann Riecke, and Adilson E Motter. Chimera states in continuous media: Existence and distinctness. *Physical review letters*, 119(24):244101, 2017.

[74] A Kudrolli and Jerry P Gollub. Patterns and spatiotemporal chaos in parametrically forced surface waves: a systematic survey at large aspect ratio. *Physica D: Nonlinear Phenomena*, 97(1-3):133–154, 1996.

[75] Glen D Granzow and Hermann Riecke. Phase diffusion in localized spatiotemporal amplitude chaos. *Physical review letters*, 77(12):2451, 1996.

[76] C David Andereck, SS Liu, and Harry L Swinney. Flow regimes in a circular couette system with independently rotating cylinders. *Journal of fluid mechanics*, 164:155–183, 1986.

[77] M G Clerc, S Coulibaly, M A Ferré, and R G Rojas. Chimera states in a Duffing oscillators chain coupled to nearest neighbors. *Chaos: An Interdisciplinary Journal of Nonlinear Science*, 28(8):083126, 2018.

[78] S Residori, A Petrossian, T Nagaya, and M Clerc. Localized structures and their dynamics in a liquid crystal light valve with optical feedback. *Journal of Optics B: Quantum and Semiclassical Optics*, 6(5):S169, 2004.

[79] S. Residori, A. Petrossian, T. Nagaya, C.S. Riera, and M.G. Clerc. Fronts and localized structures in a liquid-crystal-light-valve with optical feedback. *Physica D: Nonlinear Phenomena*, 199(1-2):149–165, 2004.

[80] M. G. Clerc, A. Petrossian, and S. Residori. Bouncing localized structures in a liquid-crystal light-valve experiment. *Physical Review E*, 71(1):015205, 2005.

[81] T. Tél, R. Graham, and G. Hu. Nonequilibrium potentials and their power-series expansions. *Physical Review A*, 40(7):4065–4071, 1989.

[82] P. G. De Gennes. Short Range Order Effects in the Isotropic Phase of Nematics and Cholesterics. *Molecular Crystals and Liquid Crystals*, 12(3):193–214, 2007.

[83] A.H. Khater, W. Malfliet, D.K. Callebaut, and E.S. Kamel. The tanh method, a simple transformation and exact analytical solutions for nonlinear reaction–diffusion equations. *Chaos, Solitons & Fractals*, 14(3):513–522, 2002.

[84] Abdul-Majid Wazwaz. The tanh method for traveling wave solutions of nonlinear equations. *Applied Mathematics and Computation*, 154(3):713–723, 2004.

[85] I. Andrade-Silva. Interface dynamics in liquid crystals (thesis). *Universidad de Chile*, 2016.

[86] John Scott Russell. *Report on Waves: Made to the Meetings of the British Association in 1842-43*. 1845.

[87] Dmitry Turaev, Mindaugas Radziunas, and Andrei G. Vladimirov. Chaotic soliton walk in periodically modulated media. *Phys. Rev. E*, 77:065201, Jun 2008.

[88] Roberta Zambrini and Francesco Papoff. Signal amplification and control in optical cavities with off-axis feedback. *Phys. Rev. Lett.*, 99:063907, Aug 2007.

[89] F. del Campo, F. Haudin, R. G. Rojas, U. Bortolozzo, M. G. Clerc, and S. Residori. Effects of translational coupling on dissipative localized states. *Phys. Rev. E*, 86:036201, Sep 2012.

[90] K. Staliunas and Víctor J. Sánchez-Morcillo. Spatial-localized structures in degenerate optical parametric oscillators. *Phys. Rev. A*, 57:1454–1457, Feb 1998.

[91] F. Haudin, R. G. Rojas, U. Bortolozzo, M. G. Clerc, and S. Residori. Vortex emission accompanies the advection of optical localized structures. *Phys. Rev. Lett.*, 106:063901, Feb 2011.

[92] P. V. Paulau, D. Gomila, T. Ackemann, N. A. Loiko, and W. J. Firth. Self-localized structures in vertical-cavity surface-emitting lasers with external feedback. *Phys. Rev. E*, 78:016212, Jul 2008.

[93] A. J. Scroggie, W. J. Firth, and G.-L. Oppo. Cavity-soliton laser with frequency-selective feedback. *Phys. Rev. A*, 80:013829, Jul 2009.

[94] M. Tlidi, A. G. Vladimirov, D. Pieroux, and D. Turaev. Spontaneous motion of cavity solitons induced by a delayed feedback. *Phys. Rev. Lett.*, 103:103904, Sep 2009.

[95] O E Omel'chenko. Traveling chimera states. *Journal of Physics A: Mathematical and Theoretical*, 52(10):104001, 2019.

[96] Dawid Dudkowski, Krzysztof Czołczyński, and Tomasz Kapitaniak. Traveling chimera states for coupled pendula. *Nonlinear Dynamics*, 95(3):1859–1866, 2019.

[97] Arindam Mishra, Suman Saha, Dibakar Ghosh, Gregory V. Osipov, and Syamal K. Dana. Traveling Chimera Pattern in a Neuronal Network under Local Gap Junctional and Nonlocal Chemical Synaptic Interactions. *Opera Medica e Physiologica*, 2017.

[98] Bidesh K. Bera, Dibakar Ghosh, and Tanmoy Banerjee. Imperfect traveling chimera states induced by local synaptic gradient coupling. *Physical Review E*, 94(1):012215, 2016.

[99] Christian Bick and Erik A Martens. Controlling chimeras. *New Journal of Physics*, 17(3):033030, 2015.

[100] Andrea Vüllings, Johanne Hizanidis, Iryna Omelchenko, and Philipp Hövel. Clustered chimera states in systems of type-I excitability. *New Journal of Physics*, 16(12):123039, 2014.

[101] Jianbo Xie, Edgar Knobloch, and Hsien-Ching Kao. Multicluster and traveling chimera

states in nonlocal phase-coupled oscillators. *Physical Review E*, 90(2):022919, 2014.

[102] Gautam C. Sethia, Abhijit Sen, and George L. Johnston. Amplitude-mediated chimera states. *Physical Review E*, 88(4):042917, 2013.

[103] J. C. González-Avella, M. G. Cosenza, and M. San Miguel. Localized coherence in two interacting populations of social agents. *Physica A: Statistical Mechanics and its Applications*, 399, 2014.

[104] M. G. Cosenza, M. E. Gavidia, and J. C. González-Avella. Against mass media trends: Minority growth in cultural globalization. *PLoS ONE*, 15, 2020.

[105] Arkady Pikovsky. Chimeras on a social-type network, 2020.

[106] Johanne Hizanidis, Evangelia Panagakou, Iryna Omelchenko, Eckehard Schöll, Philipp Hövel, and Astero Provata. Chimera states in population dynamics: Networks with fragmented and hierarchical connectivities. *Phys. Rev. E*, 92:012915, Jul 2015.

[107] Mark R Tinsley, Simbarashe Nkomo, and Kenneth Showalter. Chimera and phase-cluster states in populations of coupled chemical oscillators. *Nature Physics*, 8(9):662–665, 2012.

[108] Mahesh Wickramasinghe and István Z Kiss. Spatially organized partial synchronization through the chimera mechanism in a network of electrochemical reactions. *Physical Chemistry Chemical Physics*, 16(34):18360–18369, 2014.

[109] Raghu Betha and Rajasekhar Balasubramanian. Particulate emissions from commercial handheld sparklers: Evaluation of physical characteristics and emission rates. *Aerosol and Air Quality Research*, 13, 2013.

[110] Yuri S Kivshar. Dark solitons in nonlinear optics. *IEEE Journal of Quantum Electronics*, 29(1):250–264, 1993.

[111] Yuri S Kivshar and Barry Luther-Davies. Dark optical solitons: physics and applications. *Physics reports*, 298(2-3):81–197, 1998.

[112] Pedro Parra-Rivas, Edgar Knobloch, Damia Gomila, and Lendert Gelens. Dark solitons in the lugiato-lefever equation with normal dispersion. *Physical Review A*, 93(6):063839, 2016.

[113] A Piccardi, A Alberucci, N Tabiryan, and G Assanto. Dark nematicons. *Optics letters*, 36(8):1356–1358, 2011.

[114] Shaozhi Pu, Chunfeng Hou, Kaiyun Zhan, and Chengxun Yuan. Dark and gray solitons in nematic liquid crystals. *Physica Scripta*, 85(1):015402, 2011.

[115] George C Valley, Mordechai Segev, Bruno Crosignani, Amnon Yariv, MM Fejer, and MC Bashaw. Dark and bright photovoltaic spatial solitons. *Physical Review A*, 50(6):R4457, 1994.

[116] A.J. Alvarez-Socorro, M.G. Clerc, and N. Verschueren. Traveling Chimera States in Continuous Media. *Communications in Nonlinear Science and Numerical Simulation*, page 105559, 2020.

[117] Oleh E. Omel'chenko, Matthias Wolfrum, and Yuri L. Maistrenko. Chimera states as chaotic spatiotemporal patterns. *Phys. Rev. E*, 81:065201, Jun 2010.

[118] Jianbo Xie, Edgar Knobloch, and Hsien-Ching Kao. Multicluster and traveling chimera states in nonlocal phase-coupled oscillators. *Phys. Rev. E*, 90:022919, Aug 2014.

[119] Jaime Cisternas, Tony Albers, and Günter Radons. Normal and anomalous random walks of 2-d solitons. *Chaos: An Interdisciplinary Journal of Nonlinear Science*, 28(7):075505, 2018.

[120] Jaime Cisternas, Tony Albers, and Günter Radons. A new kind of chaotic diffusion: Anti-persistent random walks of explosive dissipative solitons. *New J. Phys.*, 21:103034, 2019.

[121] Jaime Cisternas, Carlos Cartes, Orazio Descalzi, Tony Albers, and Günter Radons. Random walks of trains of dissipative solitons. *Chaos: An Interdisciplinary Journal of Nonlinear Science*, 30(7):073134, 2020.

[122] Kramer L. Aranson I. The world of the complex ginzburg–landau equation. *Rev. Mod. Phys.*, 74:99, 2002.

[123] A. J. Alvarez-Socorro, Marcel G. Clerc, Michel Ferré, and Edgar Knobloch. Chaotic motion of localized structures. *Phys. Rev. E*, 101:042212, Apr 2020.

[124] H.-G. Purwins, H.U. Bödeker, and Sh. Amiranashvili. Dissipative solitons. *Advances in Physics*, 59(5):485–701, 2010.

[125] Werner Horsthemke and René Lefever. Noise-induced transitions in physics, chemistry, and biology. *Noise-induced transitions: theory and applications in physics, chemistry, and biology*, pages 164–200, 1984.

[126] Jordi García-Ojalvo and José Sancho. *Noise in spatially extended systems*. Springer Science & Business Media, 2012.

[127] Gladys Jara-Schulz, Michel A Ferré, Claudio Falcón, and Marcel G Clerc. Noise-induced kink propagation in shallow granular layers. *Chaos, Solitons & Fractals*, 134:109677, 2020.

[128] Marcel G. Clerc and Claudio Falcon. Localized patterns and hole solutions in one-dimensional extended systems. *Physica A: Statistical Mechanics and its Applications*, 356(1):48–53, 2005.

[129] George Osipenko. *Dynamical systems, graphs, and algorithms*. Springer, 2006.

[130] M Andrecut. Logistic map as a random number generator. *International Journal of*

Modern Physics B, 12(09):921–930, 1998.

[131] L De Micco, HA Larrondo, A Plastino, and OA Rosso. Quantifiers for randomness of chaotic pseudo-random number generators. *Philosophical Transactions of the Royal Society A: Mathematical, Physical and Engineering Sciences*, 367(1901):3281–3296, 2009.

[132] Osvaldo A Rosso, Laura C Carpi, Patricia M Saco, Martin Gomez Ravetti, Angelo Plastino, and Hilda A Larrondo. Causality and the entropy–complexity plane: Robustness and missing ordinal patterns. *Physica A: Statistical Mechanics and its Applications*, 391(1-2):42–55, 2012.

[133] Felipe Olivares, Angelo Plastino, and Osvaldo A Rosso. Contrasting chaos with noise via local versus global information quantifiers. *Physics Letters A*, 376(19):1577–1583, 2012.

[134] JD Murray. *Mathematical biology II: spatial models and biomedical applications*, volume 3. Springer-Verlag, 2001.

[135] F Haudin, RG Elías, René G Rojas, U Bortolozzo, MG Clerc, and S Residori. Front dynamics and pinning-depinning phenomenon in spatially periodic media. *Physical Review E*, 81(5):056203, 2010.

[136] Benjamin C Ponedel and Edgar Knobloch. Forced snaking: Localized structures in the real ginzburg-landau equation with spatially periodic parametric forcing. *The European Physical Journal Special Topics*, 225(13):2549–2561, 2016.

[137] Yoshiki Kuramoto and Toshio Tsuzuki. On the formation of dissipative structures in reaction-diffusion systems: Reductive perturbation approach. *Progress of Theoretical Physics*, 54(3):687–699, 1975.

[138] Yoshiki Kuramoto and Toshio Tsuzuki. Persistent propagation of concentration waves in dissipative media far from thermal equilibrium. *Progress of theoretical physics*, 55(2):356–369, 1976.

[139] Gregory I Sivashinsky. Instabilities, pattern formation, and turbulence in flames. *Annual Review of Fluid Mechanics*, 15(1):179–199, 1983.

[140] Yoshiki Kuramoto. *Chemical oscillations, waves, and turbulence*. Courier Corporation, 2003.

[141] Uwe Thiele and Edgar Knobloch. Driven drops on heterogeneous substrates: Onset of sliding motion. *Physical review letters*, 97(20):204501, 2006.

[142] Edward N Lorenz. Deterministic nonperiodic flow. *Journal of atmospheric sciences*, 20(2):130–141, 1963.

[143] Hans Fischer. *A history of the central limit theorem: from classical to modern probability theory*. Springer Science & Business Media, 2010.

[144] Morris H DeGroot. *Probability and statistics*. Pearson, 2012.

[145] Kunihiko Kaneko. Globally coupled chaos violates the law of large numbers but not the central-limit theorem. *Physical review letters*, 65(12):1391, 1990.

[146] Arkady S Pikovsky and Jürgen Kurths. Do globally coupled maps really violate the law of large numbers? *Physical review letters*, 72(11):1644, 1994.

[147] Xinxing Wu and Guanrong Chen. Central limit theorem and chaoticity. *Statistics & Probability Letters*, 92:137–142, 2014.

[148] Robert Brown. Xxvii. a brief account of microscopical observations made in the months of june, july and august 1827, on the particles contained in the pollen of plants; and on the general existence of active molecules in organic and inorganic bodies. *The philosophical magazine*, 4(21):161–173, 1828.

[149] Albert Einstein. Über die von der molekularkinetischen theorie der wärme geforderte bewegung von in ruhenden flüssigkeiten suspendierten teilchen. *Annalen der physik*, 4, 1905.

[150] Paul Langevin. Sur la théorie du mouvement brownien. *Compt. Rendus*, 146:530–533, 1908.

[151] A. J. Alvarez-Socorro, Marcel G. Clerc, M. A. Ferré, and Edgar Knobloch. Front depinning by deterministic and stochastic fluctuations: A comparison. *Physical Review E*, 99(6):062226, 2019.

[152] John Burke and Edgar Knobloch. Homoclinic snaking: structure and stability. *Chaos: An Interdisciplinary Journal of Nonlinear Science*, 17(3):037102, 2007.